Contribution of Bone Marrow Derived Cells to Four Mouse Models of Gastrointestinal Tumourigenesis

Author: Arielle Le Brenne

A thesis submitted for examination of the PhD degree

Queen Mary University of London

April 2014

ABSTRACT

Introduction: Houghton and colleagues (2004) demonstrated bone marrow derived cells (BMDCs) to be the origin of epithelial cells in pre-invasive and malignant gastric tumours in *Helicobacter felis* infected mice. However, this has yet to be replicated in any other experimental scenario.

Methods: To clarify the significance of Houghton's observation we examined four mouse models of gastrointestinal tumourigenesis: the *Tff1*$^{-/-}$ mouse model of inflammatory gastric adenocarcinoma, the *Apc*$^{\text{Min/+}}$ and *Apc*$^{\text{1322T}}$ mouse models of familial adenomatous polyposis, and the *Il10*$^{-/-}$ mouse model of colitis-associated colorectal adenocarcinoma, employing sex-mismatched bone marrow (BM) transplantation (male BM to female recipients) followed by the identification of BMDCs in tissues using Y-chromosome *in situ* hybridisation (ISH) detection and immunohistochemical phenotyping of cells. To investigate the mechanism for BMDC recruitment into tissues, osteopontin (*Opn*) mRNA isotopic ISH was employed.

Results: In four mouse models there was not a single instance of a gastric gland or intestinal crypt with a patch of clonal Y-chromosome positive (Y^{+}) cells. Y^{+} cells in the epithelium were very rare and were mostly positive for several markers of immune cells. In contrast, Y^{+} cells were frequently observed in the stroma. Quantification of BMD-myofibroblasts demonstrated increased recruitment into larger *Apc*$^{\text{1322T}}$ mouse tumours and desmoplastic reaction sites in *Tff1*$^{-/-}$ mouse tumours, but not into inflamed non-fibrotic tissues. Similarly, *Opn* mRNA expression was unaffected by inflammation but increased with tumour burden and in desmoplastic reaction sites. In the desmoplastic reaction sites of *Tff1*$^{-/-}$ mouse tumours, increased osteopontin mRNA expression correlated with increased BMD-myofibroblasts, therefore suggesting some chemoattraction was occurring.

Conclusions: In four mouse models of gastrointestinal tumourigenesis BMDCs were not a source of reparative, pre-cancerous, or malignant epithelial cells. Analysis of BM contribution in the stroma demonstrated that BMD-myofibroblast engraftment is driven by increased tumour burden and fibrosis. In addition, the increased presence of BMD-myofibroblasts at desmoplastic reaction sites of *Tff1*$^{-/-}$ mouse tumours correlated with increased *Opn* mRNA expression, indicating that osteopontin may act as chemoattractant in desmoplasia.

ACKNOWLEDGEMENTS

I would like to thank my supervisor Malcolm Alison; Saint Bartholomew's and The Royal London Charitable Foundation for financial sponsorship; Catherine Tomasetto, Marie-Christine Rio, and Olivier Lefebvre (IGBMS) for allowing us to generate the *Tff1*$^{-/-}$ mouse; Annabelle Lewis (Oxford University) for the kindly providing *Apc*^{1322T} mice; Shigeki Bamba for providing the *Apc*$^{Min/+}$ mouse study blocks and *Il10* primers; Cancer Research UK for access to laboratory facilities; Rosemary Jeffery, Richard Poulsom, George Elia, and Chung Yin-Lee (QMUL) for technical assistance with IHC, ISH and fluorescence microscopy; Sir Nicholas Wright (QMUL) and Gordon Stamp (ICL) for their support with histological analysis; Mo Warsame, Nicholas Chisolm, Claire Watkins, Scott Lighterness, Toby Richardson, and Ian Oliver (Biological Resources Unit; CRUK); Emma Nye, Richard Stone, Tamara Bunton, Kornelia Fitch, and Bradley Spencer Dene (Experimental Histopathology; CRUK).

Finally, but certainly not least, this thesis is dedicated to William Otto.

TABLE OF CONTENTS: SUMMARY

FULL CONTENTS LIST: CHAPTER 1

FULL CONTENTS LIST: CHAPTER 2

FULL CONTENTS LIST: CHAPTER 2 (continued)

Section number | **CHAPTER 2: Materials and Methods (continued)** | **Page**

FULL CONTENTS LIST: CHAPTER 3

FULL CONTENTS LIST: CHAPTER 3 (continued)

FULL CONTENTS LIST: CHAPTER 3 (continued)

Section number **CHAPTER 3: Results (continued)** **Page**

FULL CONTENTS LIST: CHAPTER 3 (continued)

FULL CONTENTS LIST: CHAPTER 4

FULL CONTENTS LIST: APPENDIX

LIST OF ABBREVIATIONS

∝-SMA	alpha smooth muscle actin
µl	microlitre
µm	micrometre
A	adenine
AbdPAS	alcian blue/ periodic acid Schiff with diastase pre-treatment
Actb	actin, beta
ANOVA	analysis of variance
Apc	Adenomatous Polyposis Coli
BM	bone marrow
BMD	bone marrow derived
BMDC	bone marrow derived cell
BMTx	bone marrow transplantation
BMTx'd	bone marrow transplanted
bp	base pairs
BrdU	bromodeoxyuridine
BW	body weight
°C	degrees centigrade
C	cytosine
CBC	crypt-base columnar cell
CD	cluster of differentiation
CRC	colorectal cancer
CRUK	Cancer Research UK
CXCR4	C-X-C chemokine receptor type 4
DAB	3,3'-diaminobenzidine
DAPI	diamidinophenylindole
DEPC	diethylpyrocarbonate
dH$_2$0	deionised water
DNA	deoxyribonucleic acid
dNTP	deoxynucleotide triphosphates
DPX	distyrene, plasticizer and xylene
DTT	1,4-dithiothreitol
FAP	familial adenomatous polyposis
FFPE	formalin-fixed paraffin embedded
FISH	fluorescence *in situ* hybridisation
G	guanine
GFP	green fluorescent protein
GI	gastrointestinal
GIT	gastrointestinal tract
GKN2	gastrokine 2
G*v*HD	graft versus host disease
H&E	haematoxylin and eosin

LIST OF ABBREVIATIONS (continued)

HIER	heat-induced epitope retrieval
HSC	hematopoietic stem cell
IBA1	ionized calcium binding adaptor molecule 1
IGBMS	Institut de Génétique et de Biologie Moléculaire
IHC	immunohistochemistry
IL-10	interleukin 10
IMS	industrial methylated spirit
ISH	*in situ* hybridisation
LB-broth	Luria Bertani-broth
LGR5	leucine-rich repeat-containing G-protein coupled receptor 5
M	molar
mm	millimetre
MM	mouse monoclonal
ml	millilitre
MSC	mesenchymal stem cell
mRNA	messenger ribonucleic acid
n	number of observations
NBF	neutral buffered formalin
Neo	neomycin
NF- κB	nuclear factor kappa-light-chain-enhancer of activated B cells
OPN	osteopontin
PBS	phosphate buffered saline
PCR	polymerase chain reaction
PFA	paraformaldehyde
PIER	proteolysis-induced epitope retrieval
POD	peroxidase
RNA	ribonucleic acid
rRNA	ribosomal RNA
rpm	revolutions *per* minute
SAMP	Ser-Ala-Met-Pro
SDF-1	stromal derived factor-1
SEMF	sub-epithelial myofibroblast
SI	small intestine
T	thymine
Taq	*Thermophilus aquaticus* polymerase
TFF	trefoil factor family
T_h	T helper cell
Tris	tris(hydroxymethyl)aminomethane
U	units
UV	ultra violet
WT	wild type

CHAPTER 1

Introduction

1.1 The development of gastrointestinal cancers and the role of stem cells

Cancer is the culmination of a series of genetic changes that confer growth advantages to cells allowing tumour growth (such as self-sufficiency in growth signals and resistance to apoptosis) and eventually the ability to invade the *submucosa* and spread into other tissues (known as invasive carcinoma). This process can be initiated through inherited mutations (hereditary cancer) or somatic mutations (sporadic cancer) of genes that regulate cell-signalling pathways involved in cell proliferation and/or apoptosis. Initial tumours progress to invasive carcinomas through the acquisition of additional somatic mutations or gene silencing from promoter hypermethylation (epigenetic changes).

In addition to mutations, the presence of chronic inflammation plays a major role in carcinogenesis and has been attributed to a fifth of all cancers [1]. This is because increased cellular proliferation resulting from continuous tissue damage and repair seen in chronic inflammation creates an environment advantageous to cancer development and maintenance [1]. In addition, mutations can arise from DNA becoming damaged by free radicals released by macrophages, neutrophils and dendritic cells during inflammation [2].

Another histological hallmark frequently observed in tumours is a heterogeneous cell population. This is often referred to as the cancer stem cell theory, in that a population of cells exhibiting stem-cell like properties (known as cancer stem cells) reside within tumours driving growth in a manner similar to the stem cells tissue stem cell niches, of which *in vivo* experiments have shown this to occur in GI tumours.

As tumours progress to invasive carcinoma, some GI cancers display step-wise patterns of development. Outside of the epithelium, the stroma (or mesenchyme) often also exhibits changes during carcinogenesis. Frequently observed is desmoplasia, which is characterised by an increased presence of myofibroblasts that synthesise abundant collagenous material [3] causing dense fibrosis around the tumour. Experimental studies suggest that tumour-associated myofibroblasts (TAMs) play a role in early tumourigenesis through altered NF-κB [4] and Wnt signalling [5] and in promoting later tumour growth and/or invasion due to their additional secretion of growth factors, MMPs, and chemokines [6-8]. In addition to TAMs, inflammatory infiltrate and tumour vasculature also make up the tumour microenvironment. These cells have been shown to be derived from bone marrow progenitor cells in human and mouse bone marrow transplantation (BMTx) studies. However, the contribution of bone marrow progenitor cells to tumour epithelial cells remains controversial.

This section focuses on the development of cancers in GI tract, the role of altered stem cell dynamics, and contribution of bone marrow derived cells (BMDCs). For brevity, adenocarcinomas will only be discussed as they account for the vast majority of GI cancers observed.

1.1.1 Gastric cancer

The stomach is divided into two functionally distinct parts: the corpus, which secretes hydrochloric acid and the zymogen pepsinogen, and the pyloric antrum that mainly secretes mucus and gastric hormones. Gastric cancer is the fourth most common cause of cancer worldwide with an estimated 990,000 new cases diagnosed in 2008 and is the second most common cause of death from cancer with 740,000 deaths in 2008 [9]. Gastric cancer falls into two histological classifications: diffuse and intestinal-type. Intestinal-type gastric cancer accounts for the majority of gastric cancer cases and is characterised by glandular structures surrounded by desmoplasia with inflammatory infiltrate present. The development of intestinal-type gastric cancer follows a progressive sequence of precancerous lesions: involving an initial transition to chronic gastritis, followed by the development of mucosal atrophy, intestinal metaplasia, dysplasia, and culminating in invasive adenocarcinoma in a lengthy process often referred to as the Correa pathway (Figure 1.1). Additionally, the development of antral-type glands within the corpus, known as spasmolytic polypeptide-expressing metaplasia (SPEM), has also been identified as a precursor lesion [10] (Figure 1.1).

Diffuse gastric cancer is less common and is composed of individual or small groups of neoplastic cells that do not form glandular structures. It is not associated with intestinal metaplasia and no intermediate steps have been observed [11].

Figure 1.1: The Correa sequence for gastric precursor lesions

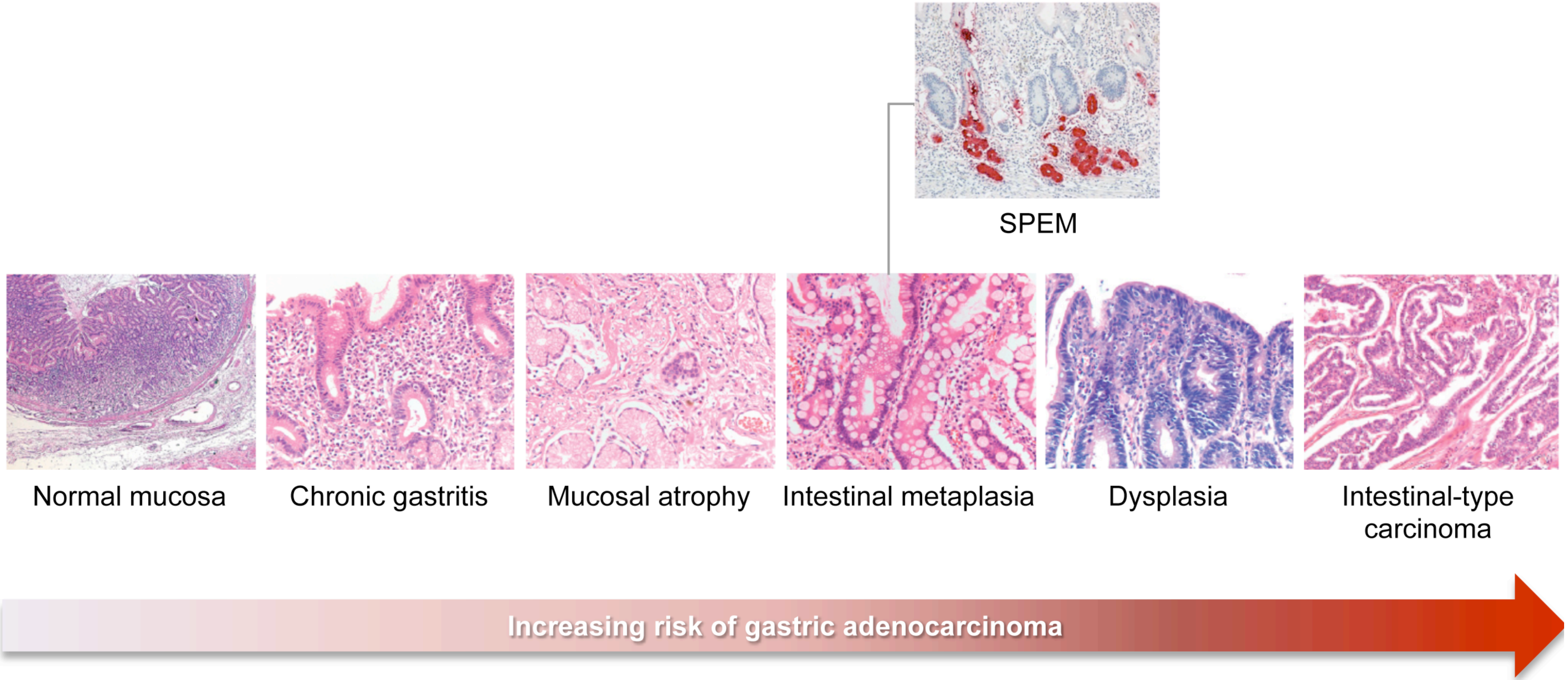

The Correa sequence shows an increasing risk for the development of intestinal-type gastric carcinoma. Spasmolytic polypeptide expressing metaplasia (SPEM) has been recognised as an additional precursor lesion and is identified by TFF2 protein expression (red staining) consistent with antral glands. SPEM image kindly provided by Sir Nicholas Wright; Figure adapted from [11]; No magnifications were provided for the original images.

Risk factors

A major risk factor for both intestinal and diffuse type gastric cancers is *Helicobacter pylori* (*H. pylori*) infection, which accounts for two-thirds of all gastric cancer cases. In contrast, hereditary gastric cancer only accounts for 1-3% of gastric cancer cases where germline mutations in mismatch repair genes [12], serine/threonine kinase 11 (*STK11*) tumour suppressor gene [13], E-cadherin gene (*CDH1*) [14], and the adenomatous polyposis coli (*APC*) gene [15] have all been identified. Other risk factors for gastric cancer include; a high salt diet, a low intake of fruits and vegetables, smoking, and a family history of gastric cancer [16, 17].

Helicobacter-associated gastric cancer

Numerous studies have linked *H. pylori* infection to gastric cancer (reviewed in [18]) and in 1994 the International Agency for Research on Cancer (IARC) classed *H. pylori* as a Group 1 carcinogen. This gram-negative bacterium colonizes the stomach by attaching to the mucosal epithelia. Once attached, its virulence factors (such as CagA) induce inflammation in host cells and immune cells are recruited to the site of infection because of the activation of the transcription of genes responsible for pro-inflammatory cytokines, chemokines, inflammatory modulators, and growth factors [18]. One of transcription factors activated by *H. pylori* virulence factors is NF-κB. NF- κB plays a pivotal role in the inflammatory and immune response by regulating the expression of a wide range of genes including those encoding pro-inflammatory cytokines, numerous chemokines, growth factors, and pro-survival factors. Therefore, it is hardly surprising that aberrant NF- κB activity is observed in a number of human cancers, including gastric cancer [19]. Studies have also attributed the pathogenicity of *H. pylori* to disruption of host cell adhesion and architecture, and decreased gastric acid secretion (reviewed in [18]).

Altered stem cell dynamics

Generation of cell lineages in the pylorus and corpus is maintained by the Wnt and Notch signalling pathways, respectively, as demonstrated *in vivo* [20, 21]. Unsurprisingly these pathways, which are responsible for stem cell differentiation and proliferation, are also implicated in gastric cancer. Patients harbouring *APC* mutations, which affect Wnt signalling (reviewed in Figure 1.2), are 10 times more likely to develop gastric cancer. Indeed, analysis of gastric cancer biopsies frequently observe accumulation of nuclear β-catenin as well as hypermethylation of key components [22] of the Wnt pathway such as DKK Wnt inhibitors [23]. Similarly, the expression of Notch receptors (e.g. Notch1, Notch2 and Notch3) and the Notch ligands such as Jagged1 and Jagged2 is observed human gastric cancer biopsies (see Figure 1.3 for a review of the Notch pathway). In particular, the expression of Notch 1 is observed in intestinal metaplasia and well-differentiated intestinal type of gastric cancer.

Figure 1.2: The Wnt signalling pathway under homeostasis and in presence of an APC truncation

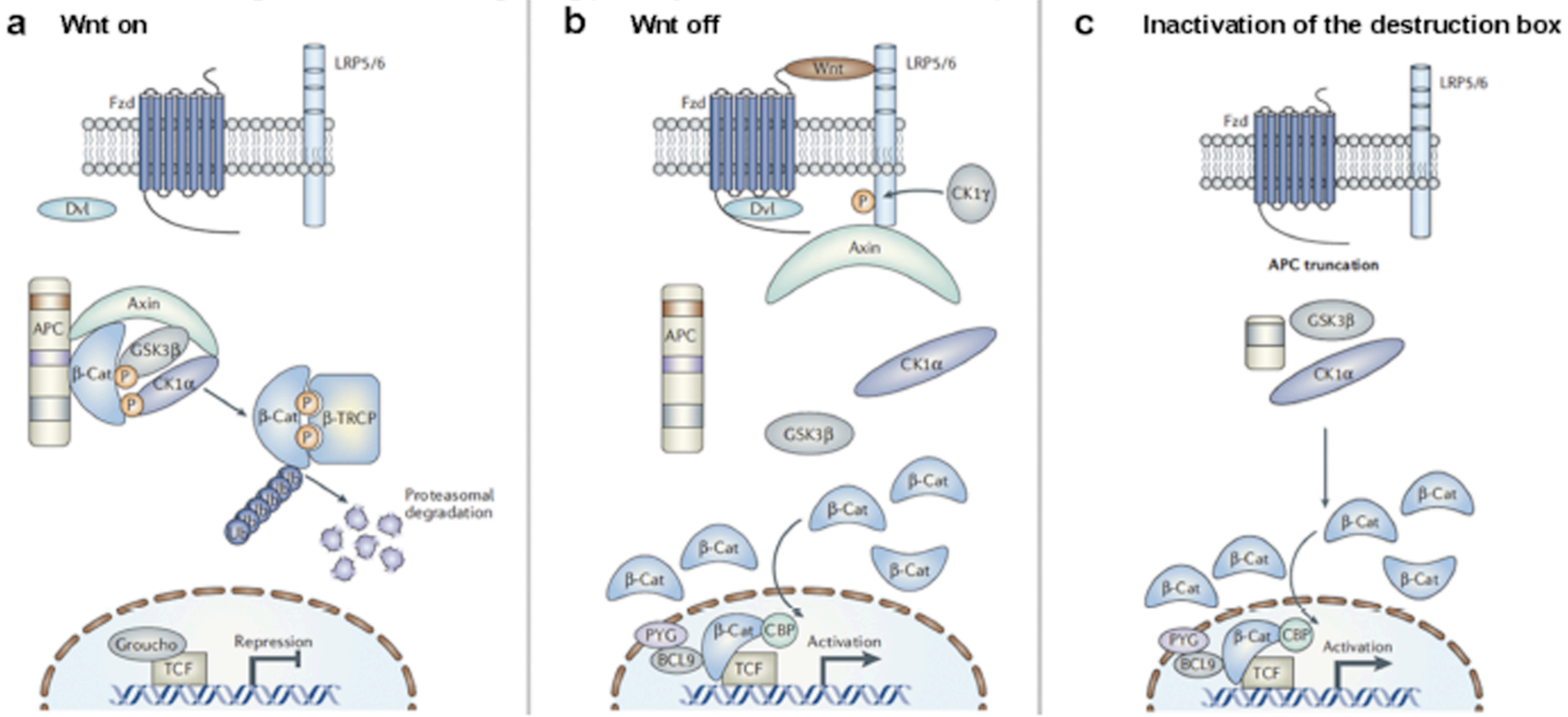

(a) In the absence of Wnt ligand, cytoplasmic β-catenin is captured by APC and axin in a "destruction complex" where Glycogen Synthase Kinase 3 (GSK3) and Casein Kinase 1 (CK1) sequentially phosphorylate a conserved set of serine and threonine residues at the amino terminus of β-catenin. As a result, β–transducin repeat-containing protein (β–TRCP) binds and mediates the ubiquitinylation and proteasomal degradation of β-catenin. The destruction of β-catenin allows T-cell factor (Tcf) DNA binding proteins to block Wnt target gene expression by recruiting transcriptional co-repressors (Groucho/TLE) to their promoters and/or enhancers [24]. (**b**) Wnt ligand initiates Wnt signalling through the Frizzled (Fzd) receptor and lipoprotein-receptor-related proteins 5/6 (LRP5/6) co-receptor. This causes the recruitment of Disheveled (Dvl) to the membrane, triggering the phosphorylation of LRP by CK1γ that facilitates the relocation axin to the membrane, thus inactivating the destruction complex. Consequently, β-catenin builds up and crosses over into the nucleus. There it ousts Groucho/TLE proteins and recruits co-activator proteins such as CREB-binding protein (CBP), B-cell lymphoma 9 (BCL9) and Pygopus (PYG), thus allowing Tcf to transcribe Tcf targets [25]. (**c**) Truncated APC proteins caused by *APC* mutations are unable to bind β-catenin properly, resulting in elevated β-catenin levels due to its ineffective destruction, thus elevating Wnt signalling. Image adapted from [26].

Figure 1.3: Review of the Notch signalling pathway

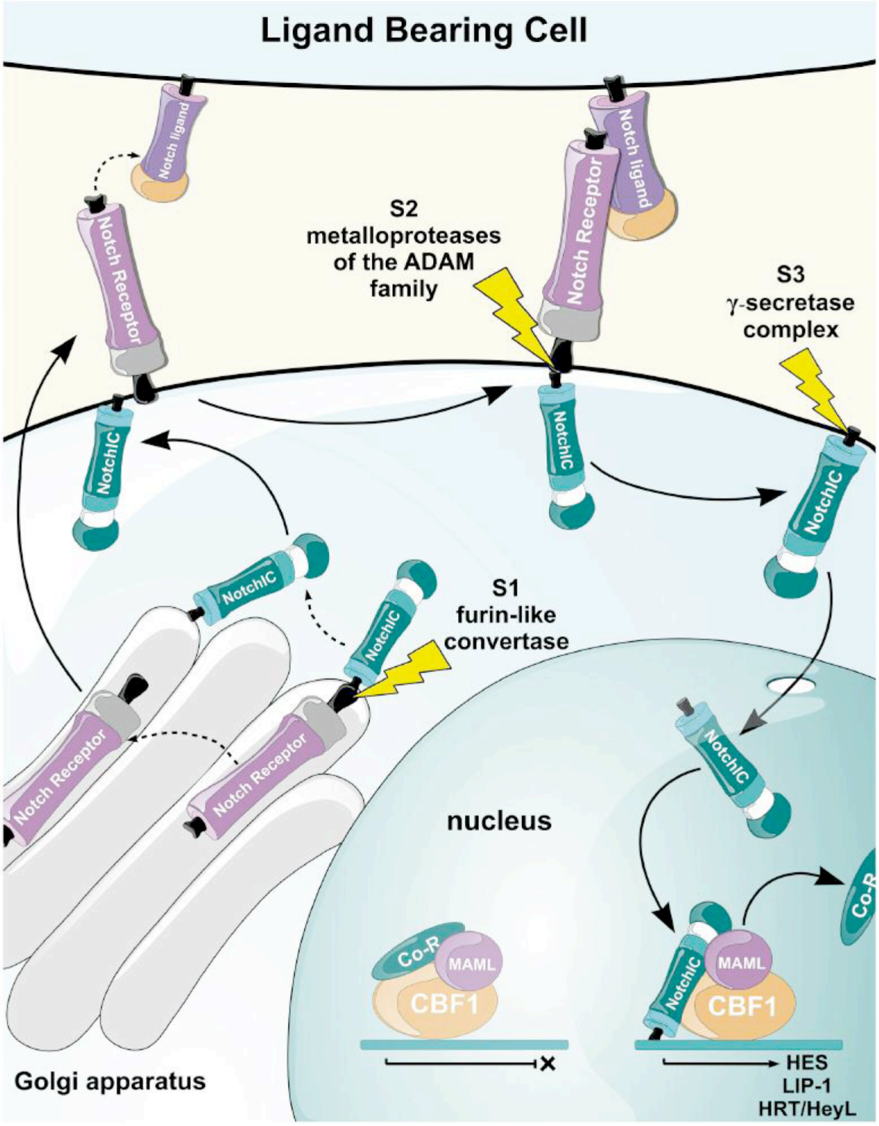

Precursor Notch receptor protein is synthesized in the Golgi apparatus, where it is cleaved by furin-like convertase to generate two subunits: one subunit containing most of the extracellular domain and a second subunit consisting of the remainder of the extracellular domain and a transmembrane domain. Binding of Notch ligand (e.g. Jagged1/2 or Delta-like 1/3/4) onto the EGF-like repeats present on the extracellular domain of a Notch receptor (e.g. Notch 1,2,3, or 4) results in the unfolding of the negative regulatory region (NRR) allowing for cleavage by metalloproteases of the ADAM family [24]. Afterwards, an intramembrane cleavage mediated by γ-secretase complex occurs releasing the Notch intracellular domain (NotchIC). The Notch intracellular domain then translocates to the nucleus where the Mastermind-like family of proteins (MAML1/2/3) have been reported to be required for activation of Notch signalling [25]. MAML, along with C-promoter binding factor-1 (CBF-1), forms a ternary complex with the NotchIC and acts as a transcriptional activator, resulting in the transcription of Notch target genes such as LKB1-interacting protein 1 (LIP-1) and numerous genes involved in the basic helix-loop-helix (bHLH) family. Following Notch activation, transcriptional repressors Hairy/Enhancer-of-Split (HES) and Hairy-Related Transcription factor (HRT), which belong to the bHLH family of proteins, are induced. Image taken from [26].

Research suggests that a stem cell population resides within gastric tumours [27]. Karam and colleagues (2008) observed an expansion of a cell population that expresses all antral cell lineage markers in the antral pyloric adenomas of trefoil factor family peptide 1 (TFF1) null mice [28]. In normal pyloric glands, stem cells at the base that express Wnt target gene and stem cell marker *Lgr5* give rise to all pyloric cell lineages. Barker and colleagues (2010) demonstrated that the deletion of *Apc* in *Lgr5*$^{+}$ pyloric stem cells causes the formation of adenomas in the pylorus, suggesting that *Lgr5*$^{+}$ stem cells are the cell of origin of APC-derived tumours [20, 27].

TFF1

In two-thirds of gastric carcinomas cases, the loss of TFF1 protein expression is observed resulting from either silencing of the *TFF1* gene due to methylation of the *TFF1* promoter region or loss of heterozygosity (LOH) [29] [30]. However, only around 5% of gastric carcinomas harbour mutations in the *TFF1* gene.

The TFF1 protein is secreted by gastric mucosal cells and plays important roles in epithelial restitution and cytoprotection (reviewed in [31]). Studies on *Tff1*-null mice (*Tff1*$^{-/-}$) suggest that this protein plays a further role in tumour suppression. *Tff1*$^{-/-}$ mice develop severe hyperplasia and dysplasia in the antralpyloric gastric mucosa leading to the development of antralpyloric adenomas in all mice [32, 33]. However, only 30% of mice develop multifocal intraepithelial or intramucosal carcinomas by 5 months of age [32]. This indicates that the loss of TFF1 alone is insufficient for malignancy and that further genetic alterations are required [32]. A possibility is the loss gastrokine 2 (GKN2) expression, which is present as a heterodimer with TFF1 in gastric mucosa secretions. A tumour-suppressing role for GKN2 has been suggested following observations of expression loss in human gastric cancer and *H. pylori* infection [34, 35].

Areas of downregulated TFF1 expression in human gastric tumours correlate with activated NF-κB [33]. Soutto and colleagues (2011) demonstrated that TFF1 attenuates the binding of tumour necrosis factor receptor (TNFR)1 to TRAF2 (TNF receptor-associated factor 2) following TNF-α stimulation, therefore suppressing TNF-α-mediated activation of the NF-κB pathway [33] (Figure 1.4). However in *Tff1*$^{-/-}$ mice, this inhibition does not occur resulting in uncontrolled NF-κB-mediated transcription of pro-inflammatory cytokines and chemokines, and pro-survival genes causing chronic inflammation. These findings suggest that, in addition to a possible tumour supressing role, the loss of TFF1 is important in modulating the inflammatory response during gastric tumourigenesis.

Figure 1.4: The role of TFF1 in mediating inflammation in gastric epithelial cells

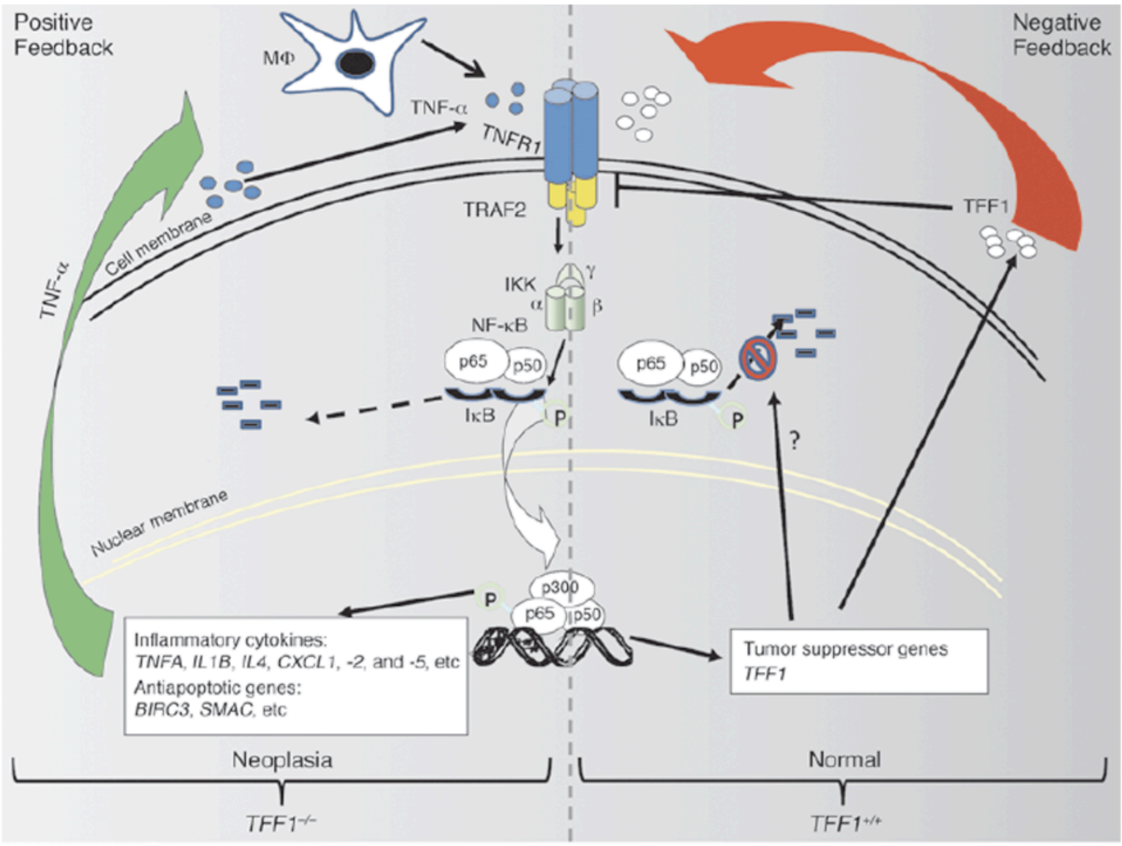

Under normal circumstances TFF1, a transcriptional target of NF-κB, negatively regulates inflammation in gastric epithelial cells by attenuating TNF-α–mediated stimulation of NF-κB (right image). However in *Tff1*$^{-/-}$ mice or in gastric tumours with silenced *TFF1* (either by loss of heterozygosity or hypermethylation) NF-κB transcription of pro-inflammatory cytokines and chemokines, and pro-survival genes goes unregulated (left image). Image: [33].

1.1.1.1 Contribution of BMDCs in gastric cancer

BMDCs have been shown to contribute TAMs and epithelial cells in gastric cancer. Occasional BMD-TAMs have been observed in a gastric adenocarcinoma of a female patient who developed gastric adenocarcinoma after receiving a BMTx using BM from a male donor [36]. Similarly, Quante and colleagues (2011) demonstrated a 20% contribution of BMD-myofibroblasts in *H. felis*-induced gastric dysplasia in BMTx'd mice. In the same study, Quante and colleagues performed FACS analysis of the BM of these mice and demonstrated an expansion of α- smooth muscle actin (SMA)$^{+}$ mesenchymal stem cells (MSCs) when compared to the BM of uninfected mice or mice with early stage dysplasia. This finding suggests that dysplasia modulates the differentiation of BMDCs within BM [37]. Quante and colleagues findings also complement an *in vitro* observation of the chemotactic recruitment of BMD-MSCs *via* chemokines released from *H. pylori* infected GI epithelial cells [38].

Another deleterious consequence of *Helicobacter* infection has been suggested by *in vivo* studies carried out by Houghton *et al.*, (2004) and Varon *et al.,* (2011). In 2004, Houghton and colleagues [39] carried out BMTx experiments in which lethally irradiated mice were transplanted with ROSA26 (that expressed non-mammalian beta-galactosidase) or GFP transgenic BM in order to track the engraftment of BMDCs *via* X-gal staining and fluorescent microscopy, respectively. The transplanted mice would later be infected with *Helicobacter felis* (*H. felis*). Houghton and colleagues observed that the transplanted BMDCs repopulated the stomachs of these mice to the extent that 90% of the gastric mucosa at the squamocolumnar junction was replaced by BMDCs 52 weeks after infection. With time, these cells progressed through metaplasia and dysplasia to intraepithelial cancer. Analysis of neoplastic glands in both groups revealed, for the first time ever, BMD-neoplastic epithelial cells (Figure 1.5).

Figure 1.5: BMD-neoplastic gastric glands, from Houghton *et al.*, 2004

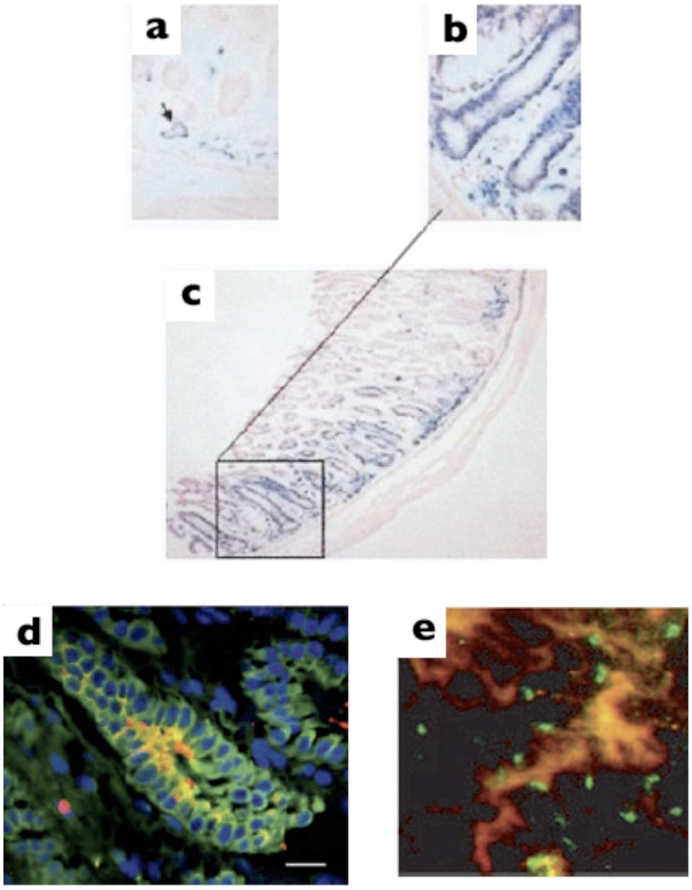

After 20 weeks of *H. felis* infection, few BMD gastric glands are observed (blue; arrow) (**a**). After 12-16 months of chronic *H. felis* infection entire gastric glands were BMD (blue) (**b**). A lower power view demonstrating numerous BMD gastric glands (**c**). BMD-epithelial cells (yellow) in neoplastic gastric glands were detected by co-localisation of pan-cytokeratin (green) and beta-galactosidase expression (red) (**d**; scale bar 40μm). Male GFP^{+} cells in the nuclei (black) of cytokeratin^{+} cells (red) (**e**; no magnification provided). **a**-**c** no magnifications provided, images taken from [40]; **d**,**e** images taken from [39].

A possible explanation for this phenomenon came a year later, when Houghton and colleagues demonstrated increased apoptosis occurring at the isthmus of the gastric glands, the proposed stem cell region of pyloric glands, during early *H. felis* and *H. pylori* infection [40]. A proposed explanation for the observations in both studies is that *Helicobacter* infection resulted in stem cell ablation at the pyloric gland niche (Figure 1.6). Consequently, BMDCs were recruited and engrafted in the gastric stem cell niche where they functioned as stem cells. However, in an abnormal chronically inflamed environment these cells progressed eventually to cancer as opposed to differentiating into the gastric cell lineages. Therefore, it has been proposed that this process may occur in other cancers arising from chronic inflammation [40].

Figure 1.6: A proposed paradigm of gastric epithelial cancer resulting from BMDC engraftment

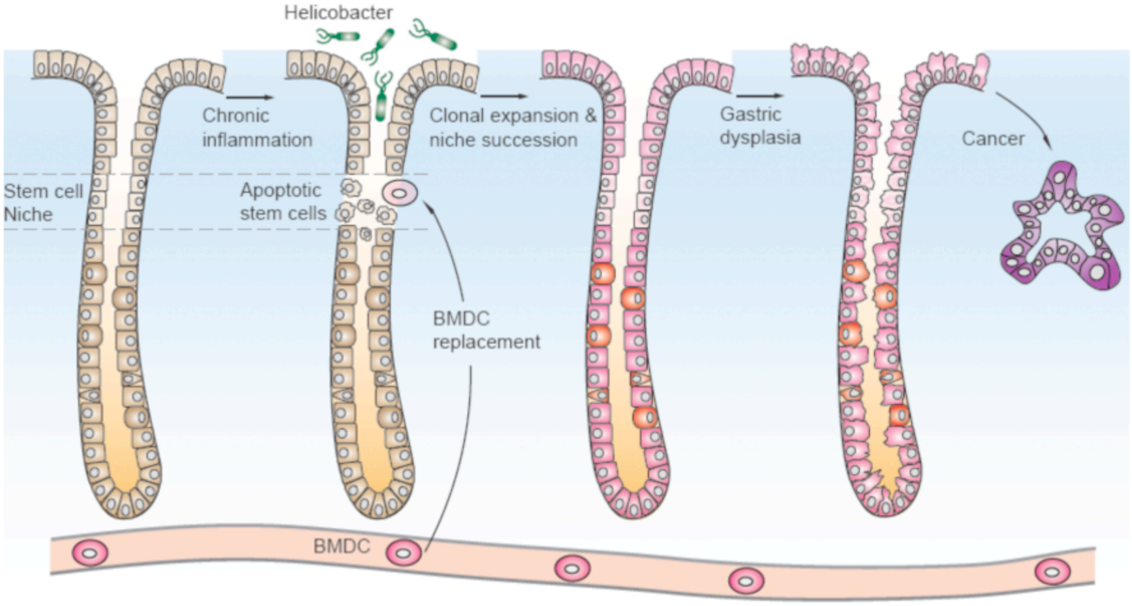

Chronic inflammation and tissue damage in the gastric glands resulting from *Helicobacter* infection results in ablation of the stem cell niche resulting in replacement with BMDCs. These cells subsequently divide to repopulate the entire gastric gland. A mutation in the BMDCs whether genetic or somatically induced by, for example, DNA damage by reactive oxidative species (ROS) by-products of chronic inflammation results in the development of dysplastic gastric glands and subsequent gastric cancer. Figure courtesy of Malcolm Alison.

1.1.2 Intestinal cancer

Colorectal cancer (CRC) is the third most common cancer worldwide with an estimated 1.2 million new cases in 2008 and 608,700 deaths estimated to have occurred in 2008 [41]. In contrast, small intestinal cancer is relatively uncommon with a global incidence of less than 1.0 per 100,000 people [42]. The reason for the discrepancy in small intestinal and CRC incidences is unknown. However, several mechanisms have been hypothesised including: a shorter exposure of mucosa to carcinogens due to a quicker transit time of food in the small intestine (SI), a decreased concentration of potential carcinogens from bile acid breakdown due to a lower bacterial load in the SI, and the generation of less endogenous reactive oxidative species (ROS) in the SI than the colon resulting in less oxidative damage (reviewed in [43]).

Risk factors for intestinal cancer include a high fat diet, inflammatory bowel disease (IBD), and a family history of intestinal cancer (reviewed in [44] and [45]). The development of intestinal cancer can be split into two categories: non-inflammatory and inflammatory mediated.

1.1.2.1 Non-inflammation associated intestinal cancer

The development of adenocarcinoma in the SI and colorectum both follow the Vogelstein adenoma-carcinoma sequence resulting from aberrant Wnt signalling (Figure 1.7). *APC* mutations are causally implicated, observed in around 80% of sporadic colorectal cancers and responsible for the hereditary cancer syndrome, familial adenomatous polyposis (FAP). FAP patients harbour a germline mutation in one *APC* allele, resulting in the development of hundreds to thousands of neoplastic colorectal adenomas (and occasionally in the SI) driven by chronic Wnt signalling [46]. In both FAP and sporadic cases, benign adenomatous polyps resulting from an initial *APC* mutation progress to carcinoma following additional somatic mutations [27]. This progression was suggested to occur in a strict sequence where *APC* mutations are followed by mutations in *KRAS, SMAD4* and lastly *P53* [47], but this may not always be the case. Collectively, these observations have not only identified *APC* as a potent tumour suppressor gene but also as the primary regulator of cell proliferation and survival.

Figure 1.7: The adenoma-carcinoma sequence of sporadic CRC

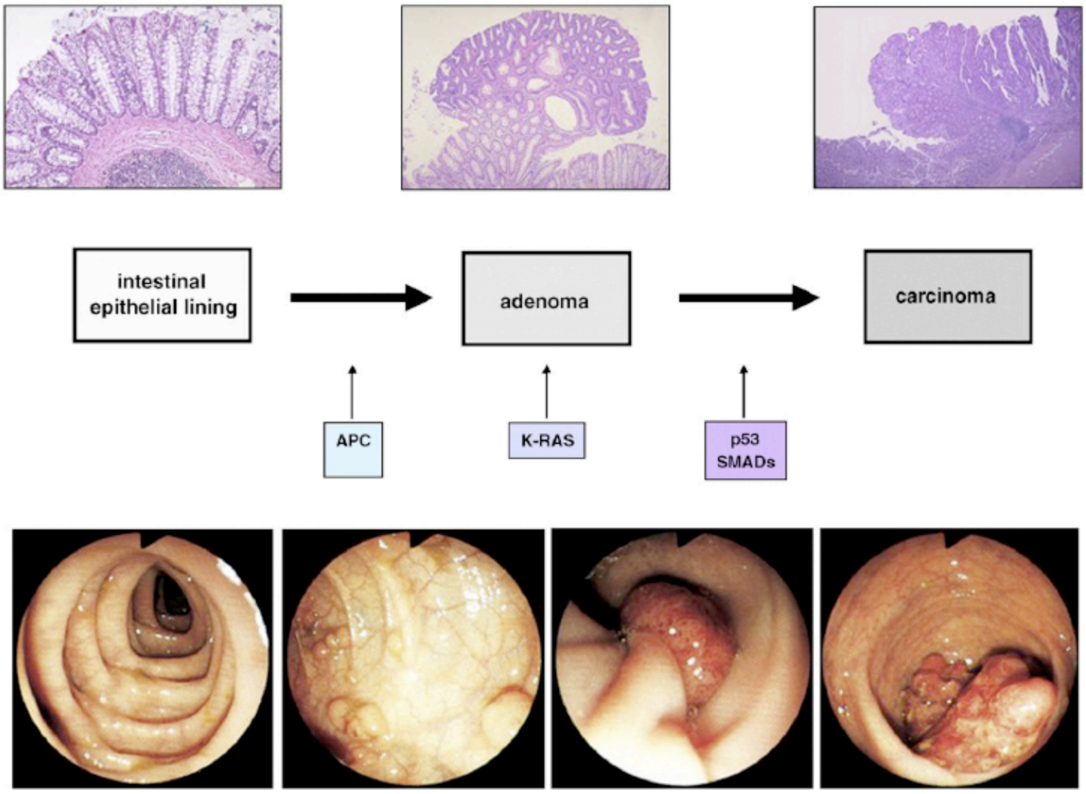

In the adenoma-carcinoma sequence, the development of carcinomas from normal colonic mucosa is the result of key molecular events that result in characteristic histopathological and morphological features (as viewed by colonoscopy). H&E magnifications not provided; figure taken from: [48].

Observations from *Apc* mutant mouse studies

Over the years, several *Apc* mutant mice have been developed to model human polyposis and carcinogenesis. The *Apc*$^{\mathrm{Min/+}}$ mouse was the first FAP model produced bearing a mutation in the *Apc* gene at codon 850 [49]. Homozygous *Apc*$^{\mathrm{Min/Min}}$ mice are non-viable but heterozygous mice develop multiple intestinal neoplasms (Min) within weeks after birth. It is important to note that unlike in human FAP, most tumours in the *Apc*$^{\mathrm{Min/+}}$ mouse are benign small bowel adenomas and do not progress to invasion or metastasis [50]. More recently, the *Apc*$^{\mathrm{1322T}}$ mouse has been generated following the observation that the majority of truncated APC proteins found in human colorectal tumours retain a total of 1-2, 20 amino acid (aa) repeats [51-53]. These repeats play an important role in the Wnt pathway by binding β-catenin and assisting in its degradation [54]. Unlike the *Apc*$^{\mathrm{Min/+}}$ mouse, the *Apc*$^{\mathrm{1322T}}$ mouse retains one of the 20-aa repeats resulting from a stop signal at codon 1322 (Figure 1.8).

Figure 1.8: Diagram of the APC protein and location of germline mutations in *Apc* mouse models

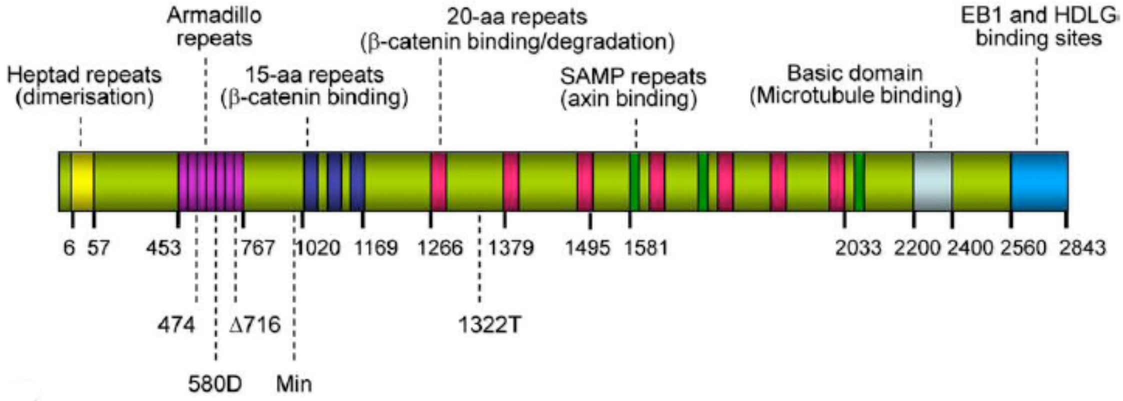

A number of *Apc* mouse models, including the Min (850) model, harbour mutations upstream from the 20-aa repeats in the APC protein. Whereas the 1322T model retains one 20-aa repeat. A mutation at the 1322T codon also means that the 1322T model does not carry any of the Ser-Ala-Met-Pro (SAMP) repeats or binding sites found further downstream of the APC protein as other *Apc* mouse models. Image reproduced from [55].

Compared to *Apc*$^{\mathrm{Min/+}}$ mice, *Apc*$^{\mathrm{1322T}}$ mice have a more severe disease phenotype with an earlier onset, greater percentage of tumours and higher grade of dysplasia [55]. In addition, polyps occur predominately in the proximal SI contrast to the distal SI and colon in the *Apc*$^{\mathrm{Min/+}}$ mice [49, 55]. Moreover, *Apc*$^{\mathrm{1322T}}$ mice develop gastric adenomas. To date, this has only been observed in one other *Apc* mutant, a strain of long-lived Min mice [56]. *Apc*$^{\mathrm{1322T}}$ mouse tumours, as in Min mouse tumours, do not become invasive or metastasize.

Although *Apc*$^{\mathrm{1322T}}$ mice develop a more severe phenotype when compared to *Apc*$^{\mathrm{Min/+}}$ mice, analysis of nuclear β-catenin and active β-catenin levels are consistently lower in *Apc*$^{\mathrm{1322T}}$ mouse adenomas [57]. This is believed due to the 20-aa repeats retained in 1322T mutation allowing for the capture of β-catenin [55]. Using microarray analysis, Lewis and colleagues (2011) demonstrated that this translates to lower levels of Wnt target gene expression in *Apc*^{1322T} mouse adenomas compared to *Apc*$^{Min/+}$ mouse adenomas. However, mRNA expression of Wnt target gene and stem cell marker *Lgr5* increased nearly threefold in *Apc*^{1322T} adenomas compared to *Apc*$^{Min/+}$ mouse adenomas and mRNA expression Wnt regulators such as Wnt inhibitory factor 1 (*Wif1)*, bone morphogenetic protein (*Bmp) 2*, and *Bmp4* were significantly lower compared to expression in *Apc*$^{Min/+}$ mouse adenomas [57]. Furthermore, *Lgr5* mRNA isotopic *in situ* hybridisation (ISH) and protein analysis of BMI1 and MSI1 stem cell markers *via* immunohistochemistry (IHC) revealed increased expression in normal crypts and adenomas of *Apc*^{1322T} mice compared to *Apc*$^{Min/+}$ mice. These findings lead to the conclusion that the severe phenotype seen in *Apc*^{1322T} mice was due to an increased number of stem cells [57].

1.1.2.2 Inflammation-associated intestinal cancers

Chronic inflammation is strongly associated with cancer development at sites of inflammation in various organs, particularly in the intestine. For example, inflammation restricted to the SI in coeliac or Crohn's disease is associated with up to an 80-fold increased risk of small intestinal adenocarcinoma compared to the general population (reviewed in [1]). Similarly, patients with IBD-associated colitis (either Crohn's disease or ulcerative colitis) are six times more likely to develop colorectal cancer (CRC) than the general population [58]. A key difference however is that small bowel adenocarcinoma is rare, whereas

CRC accounts for 10-15% of deaths in IBD patients. Therefore this section will focus on IBD-associated CRC.

IBD-associated CRC does not follow the adenoma-carcinoma sequence seen in sporadic CRC. Instead, dysplastic lesions arise from inflamed epithelium, which progress in severity and culminate in carcinoma (Figure 1.9). Moreover, the timing and frequency of mutations in IBD-associated CRC differs from sporadic CRC [59]. For example, *APC* mutations are often an early event in sporadic CRC but occur later in the development of dysplasia and carcinomas in IBD-associated CRC. Similarly, *p53* LOH is often seen in early dysplastic lesions in IBD, whereas p53 LOH is observed as a later event in sporadic CRC (reviewed in [59]).

Risk factors for IBD-associated CRC include colitis duration, severity of inflammation, and a family history of sporadic CRC (reviewed in [45]).

Figure 1.9: The inflammation-dysplasia-carcinoma sequence of IBD-associated CRC

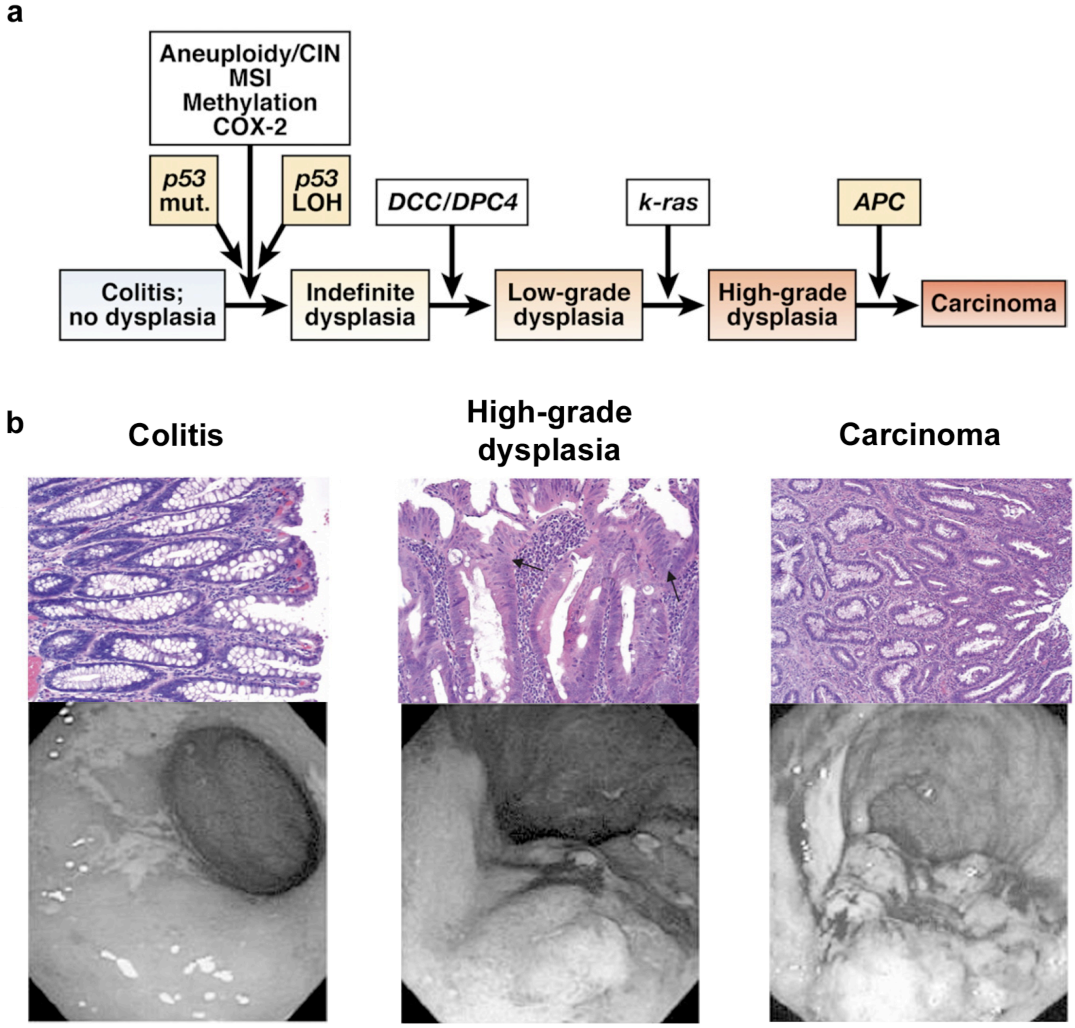

(**a**) Molecular pathogenesis of IBD-associated CRC. (**b**) The histopathological (top left and centre images; 200x, top right image; 100x) and morphological (as viewed by colonoscopy) features of the inflammation-dysplasia-carcinoma sequence in IBD-associated CRC. (**a**) Figure adapted from [59]. (**b**) H&E images taken from [60]**,** colonoscopy images courtesy of Gerald Dryden.

IBD genetic factors

Familial studies have suggested a genetic predisposition to IBD [61]. In addition, race and ethnicity studies have indicated a difference in the occurrence of IBD subtypes and disease severity [62]. An early onset of colitis is correlated with homozygous mutations in the interleukin 10 receptor *IL10RA* and *IL10RB* genes, that encode the IL10R1 and IL10R2 subunit proteins, resulting in restricted IL-10 induced signalling [63].

The role of IL-10

Interleukin 10 (IL-10) is a potent cytokine essential to mucosal immunoregulation, particularly in the intestine. Secreted by almost all leukocytes [64] as well as keratinocytes [65] and epithelial cells [66], IL-10's primary role is to restrict excessive immune responses, thus limiting their damage (see Table 1.1 for a selection). This is particularly important for the intestine, where antigens from bacterial flora and ingested food can elicit an immune response and inflammation and therefore must be constantly checked.

Table 1. 1: Immune responses regulated by IL-10

Immune response	**Role of IL-10**
Release of pro-inflammatory cytokines	Down regulates the expression of pro-inflammatory cytokines such as TNF-α and IL-12. Increases expression of soluble TNF receptors and IL-1R antagonist [67].
Antigen presentation/ T cell activation	Down regulates the expression of MHC antigens, intercellular adhesion molecule-1 (ICAM-1), and co-stimulatory molecules CD80 and CD86 present on APCs [68].
Release of MMPs	Inhibits the production of MMP2 and MMP9. Induces expression of tissue inhibitor of MMP1 (TIMP1) [69].

Emerging evidence suggests that immunosuppressive and anti-inflammatory effects of IL-10 is the result of the activation of signal transducer and activator of transcription 3 (STAT3) by IL-10 binding to its receptor (Figure 1.10). A large scale sequencing study demonstrated STAT3-induced transcription of most genes involved in Th17 cell differentiation and regulation of genes involved in CD4^{+} T cell survival and proliferation [70] confirming earlier *in vivo* [71] and *in vitro* [72, 73] observations.

Figure 1.10: Interaction of IL-10 with its receptor

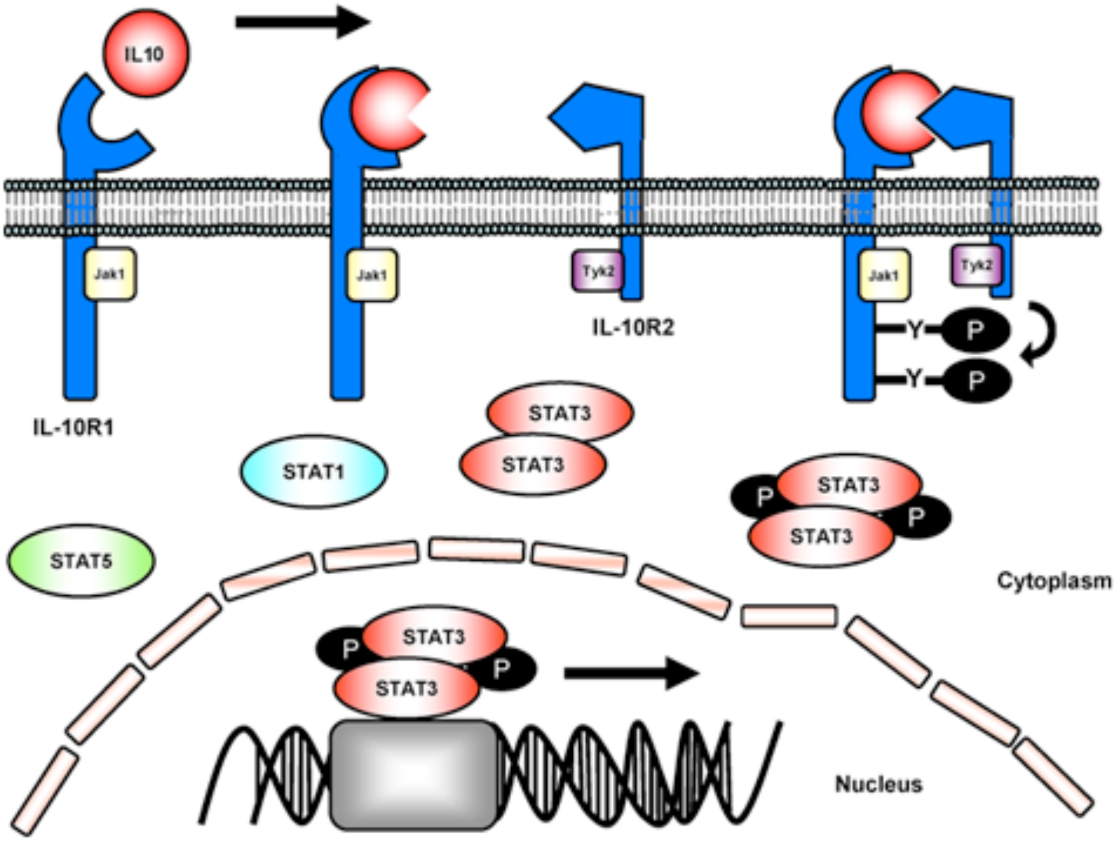

IL-10 first binds to IL-10 receptor 1 (IL-10R1) causing a conformational change in IL-10 thus creating a binding site for IL-10R2. Once bound to IL-10R2, receptor-associated Janus kinases Jak1 (IL-10R1) and Tyk2 (IL-10R2) activate each other. Following tyrosine phosphorylation of IL-10R1, STAT3 molecules bind to and become phosphorylated by the Janus kinases. In certain cells STAT1 and STAT5 molecules are activated. STAT homo- or heterodimers enter the nucleus where they bind to promoters and induce gene transcription. Image reproduced from [74].

Observations from the *Il10*$^{-/-}$ model of IBD

IL-10 as an essential intestinal immunoregulator was first noted in *Il-10* null (*Il10*$^{-/-}$) mice. These mice develop T$_h$-1 type chronic enterocolitis characterized by discontinuous transmural lesions and infiltration of lymphocytes, activated macrophages and neutrophils [75]. By six months of age, 29–60% of *Il10*$^{-/-}$ mice develop colorectal adenocarcinoma. However, this incidence is dependent on which genetic background *Il10*$^{-/-}$ mice are generated on. For example, whilst 60% of *Il10*$^{-/-}$ mice on a 129/SvEv background develop colorectal adenocarcinoma, *Il10*$^{-/-}$ mice on a C57BL/6 background do not develop colorectal adenocarcinomas. Underscoring the relationship between inflammation and carcinogenesis, *Il10*$^{-/-}$ mice on a 129/SvEv background exhibit the most severe enterocolitis compared to other *Il10*$^{-/-}$ mice on different genetic backgrounds, [76]. This difference in enterocolitis severity according to genetic background echoes differences in IBD disease severity from aforementioned racial and ethnicity studies.

Interestingly, restoration of *Il10* through adenoviral vectors [77] or transplantation of wild-type (WT) bone marrow has been shown to reverse colitis *Il10*$^{-/-}$ mice [78]. The potential therapeutic effect of *IL10* gene transfer has yet to be carried out in patients, however, restoration of IL-10 through haematopoietic stem cell transplantation has been shown to induce long-term remission in a majority of patients with active severe Crohn's disease [79].

1.1.2.3 Contribution of BMDCs in colitis and intestinal cancer

In 2006 Bamba and colleagues demonstrated that an influx of IL-10 expressing myeloid cells from transplanted WT bone marrow could ameliorate colitis in *Il10*$^{-/-}$ mice. The amelioration of colitis also involved the repair and regeneration of the damaged mucosa, possibly mediated by BMD-myofibroblasts. Analysis of the colonic crypts of these mice demonsrated up to 30% of subepithelial myofibroblasts (SEMFs) being of BM origin. In comparison, the inflamed mucosa of *Il10*$^{-/-}$ mice that received *Il10*$^{-/-}$ BM in the same study had up to 45% colonic SEMFs being of BM origin, emphasizing the important role of these cells in tissue regeneration in inflammation [78].

How BMD-myofibroblasts would have contributed to the tumour stroma of colitis-associated tumours in *Il10*$^{-/-}$ mice is unknown as the *Il10*$^{-/-}$ mice used by Bamba and colleagues were on a C57/BL10 genetic background that do not develop colorectal adenocarcinoma. However, observations in non-inflammatory colonic tumours indicate a BM contribution to tumour stroma is highly likely. BMD-TAMs have been observed in a rectal adenoma that developed in a female patient after she had received a BMTx using BM from a male donor [36]. Observations by Davies and colleagues (2011) in the *Apc*$^{\mathrm{Min/+}}$ mouse also suggest that BMDCs may preferentially engraft in the tumour stroma of colonic tumours compared normal nearby tissue [80]. However that study did not identify the cell lineages of engrafted cells or quantify engraftment.

1.1.3 Overview of BMTx experiments, controversies, and theories of the mechanisms behind BMDC mobilisation and engraftment

Over the last decade, several research groups have investigated the role of stem cells from the bone marrow (bone marrow derived cells) in GI tumourigenesis. From human and mouse BMTx studies, it is understood that BM can contribute differentiated epithelial, endothelial and stromal cell lineages to numerous tissues that are capable of replication; and that this contribution increases when there is increased regenerative demand in tissues [81-83]. However, how this translates in the setting of carcinogenesis remains controversial.

This section focuses on methodology used in BMTx experiments, the issues that arise from such experiments, and the mechanisms for BMDC mobilisation and engraftment.

Identification of BMDCs

BM houses three stem cell types; haematopoietic stem cells (HSCs) which give rise to all blood cells, mesenchymal stem cells (MSCs) which can possibly give rise to adipocytes, chondrocytes, osteocytes, myocytes and neurons, and endothelial progenitor cells (EPCs) which give rise to endothelial cells.

HSCs are readily identified by their expression of the cluster of differentiation (CD) 34 antigen. In humans, these cells occur at an estimated frequency of 1 in 10,000 BM cells and 1 in 100,000 peripheral blood cells [84]. In contrast, there is no single marker for MSCs. Instead these cells are defined by their ability to adhere to plastic, expression of CD73, CD90 and CD105, and the absence of haematopoietic markers CD34, CD45, CD14, and human leukocyte antigen (HLA)-DR and by differentiation into adipocytes, chondrocytes, and osteocytes *in vitro* [85]. MSCs occur more rarely with an estimated frequency of 1 in 100,000 BM cells [86]. The presence of a significant number MSCs in peripheral blood has been controversial [87, 88]. However, MSCs isolated from peripheral blood that could be expanded *in vitro* has been recently reported by Chong et al., (2012), albeit limited in number when compared to BM [89]. There are a number of markers for EPCs including fetal liver kinase 1 (Flk-1), Von Willebrand factor (vWF), vascular endothelial (VE)-cadherin, CD31, tyrosine kinase with immunoglobulin-like and EGF-like domains (Tie)1, Tie2, c-Kit, CD34, CD133, stem cell antigen (Sca)-1 and fms-related tyrosine kinase 1 (Flt)-1 [90]. EPCs have been identified in peripheral blood, however establishing the number of EPCs in peripheral blood has been difficult as these cells, along with mature endothelial cells (e.g. endothelial cells that do not express CD133) make up between 0.01% and 0.0001% of mononuclear cells in healthy individuals [91]. Analysis of BMDC engraftment in tissues *in vivo* has mostly been *via* experimental mouse studies, while analysis in human tissue comes from rare clinical cases of BMTx patients that received a sex mismatched BM graft. Sex-mismatched BMTx has been used extensively in mouse studies where BMDCs can be traced using X and/or Y-chromosome ISH. Other approaches used to trace BMDCs in mouse studies include the transplantation of green fluorescent protein (GFP) or ROSA26-expressing BM. Other mouse studies have been carried out by injecting purified MSCs or HSCs directly into an affected tissue/organ, however this section focuses on BMTx studies as they are the most relevant to this study.

In BMTx studies BMDCs are identified in tissues or biopsies through a two-pronged approach: identification of donor markers and phenotyping of cells. To phenotype cells, cell marker immunohistochemistry (IHC) is carried out. Figure 1.11 demonstrates the identification of BMD-myofibroblasts through Y-chromosome ISH and α-smooth muscle actin (SMA) IHC.

Figure 1.11: BMD-myofibroblasts in the tumour stroma of a pancreatic insulinoma, from Direkze *et al.*, 2004

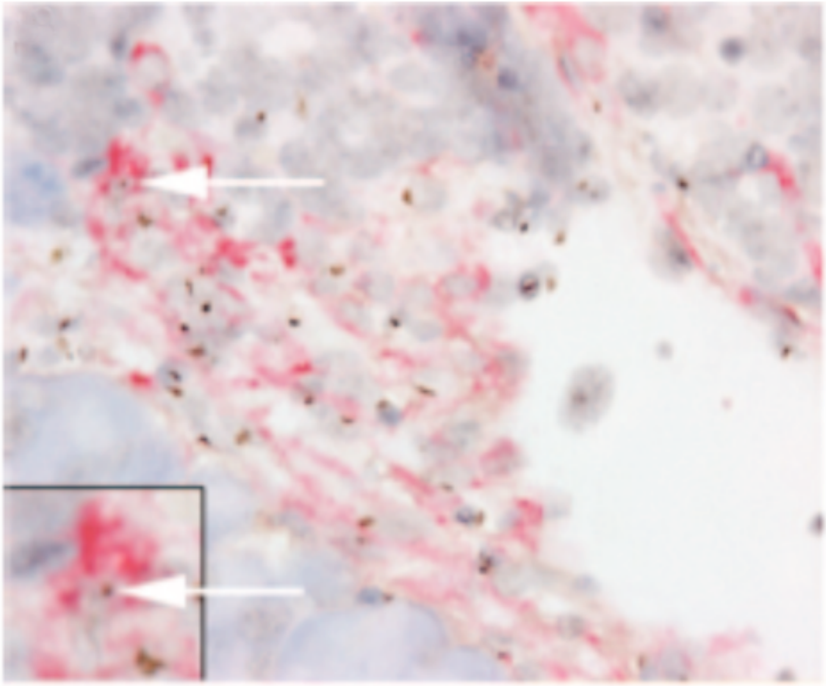

BMD-myofibroblasts at the junction between the tumour and surrounding pancreas are demonstrated through α-SMA positivity (red staining) and Y chromosome positivity (brown dot; x20). A donor-derived myofibroblast is shown enlarged (x60; white arrow, inset). Image taken from [92].

Issues surrounding BMTx experimentation

When assessing the contribution of BMDCs to tissues in BMTx studies, particularly in the GI tract, it is important to remember that BMTx itself can contribute to tissue damage and potentially instigate or advance carcinogenesis. A complication of allogeneic BMTx (e.g. BMTx where the donor and recipient are genetically different) is graft-versus-host disease (G*v*HD), in which donor T cells attack host tissues of which the skin, liver, and GI tract are the major targets. Indeed, BMDCs were identified in biopsies from patients suspected having G*v*HD where intestinal epithelial damage resulting from acute GvHD increases the contribution of BMD stromal and epithelial cells [83, 93]. Moreover, the engraftment of BMD-epithelial cells increased 5-50 fold in G*v*HD damaged epithelium compared to unaffected epithelium [83].

In addition to G*v*HD, ionising radiation can damage tissues. Prior to transplantation, ionizing radiation is administered, causing double-strand DNA breaks leading to the apoptosis of haematopoietic cells (known as myeloablation). Moreover, mitotically active intestinal epithelial cells are susceptible to damage as well. Clinically and experimentally this is avoided by using a radiation dose that allows for myeloablation but prevents tissue damage. Additionally, DNA damage incurred may cause DNA mutations that can lead to the development of tumours. Indeed, the development of secondary tumours has been observed years after patients had undergone BMTx to treat haematopoietic malignancies (reviewed in [94]).

Using BMTx experimentally to assess the contribution of BMDCs to GI tumourigenesis presents numerous potential challenges as touched upon previously. Any intestinal epithelium damage creates an additional stimulus for BMDC recruitment. Moreover, DNA damage caused by ionising radiation can accelerate the development of tumours. Therefore, histological comparison of tumours and pathology with untransplanted mice is necessary to demonstrate that the contribution observed is not merely a result of radiation.

Evidence and controversy surrounding the BM contribution

Whilst there is consensus that BMDCs contribute fully functional immune cells and TAMS to the tumour microenvironment (reviewed in [95]), there is controversy regarding the contribution of BMDCs to the tumour vasculature and epithelium. Several *in vivo* studies suggest that BMDCs play an important role in tumour angiogenesis [96, 97]. These studies have demonstrated a contribution of endothelial progenitor cells (EPCs) [98, 99] [100] and pericytes [101] [102] to tumour endothelium. However, the magnitude of this BMDC-contribution to endothelial cells varies greatly from undetectable [103-107] [108-110] or low [111], to half [112], to nearly all [100] endothelial cells lining tumour vessels.

More controversial is the contribution of BMDCs to tumour epithelial cells. As with BMD-endothelial cells, estimates of the contribution of BMDCs to the tumour epithelial cell population vary greatly. For example, in human BMTx studies this can vary from occurring at low frequencies (<10%) [113, 114] to nearly all malignant cells in one patient that developed a gingival squamous carcinoma [115]. However, whether these cells are playing an active role in tumourigenesis remains unknown.

Mechanisms of BMDC mobilisation

The recruitment of BMDCs into the tumour microenvironment and the demonstration of BMD neoplastic cells, raises an interesting conundrum: do circulating BMDCs engraft as a result of the inflammation/increased regenerative demand present in these areas, or are tumours actively siphoning stem cells from host cell reservoirs such as BM?

Under normal circumstances, BMDCs are recruited into tissues *via* chemotaxis in which cells move towards areas of an increased extracellular signal. Chemokines and growth factors (such as vascular endothelial growth factor [VEGF]) released by epithelial and stromal cells are active participants in this process. Recently, CXC12 and osteopontin have emerged as two key players in BMDC recruitment, particularly during tumourigenesis. CXCL12 (formally known as stromal derived factor 1 [SDF-1]) is a α-chemokine secreted by osteoblasts, BM endothelium, endothelial and smooth muscle progenitor cells and stromal fibroblasts. There are two known receptors for CXCL12: CXCR4 and, recently discovered, CXCR7. Binding of CXCL12 to the CXCR4 receptor (known as the CXC12/CXCR4 axis) present on HSCs and circulating white blood cells activates numerous cell signalling pathways responsible for chemotaxis, cell proliferation, and survival of CXCR4^{+} cells [116] (Figure 1.12). The role of CXCR7 in immune processes remains unknown.

CXCL12 expression by osteoblasts and BM endothelium is crucial to the homing and retention of CXCR4^{+} HSCs in the BM; and has been exploited therapeutically, where inhibition of CXCL12 binding with Plerixafor (AMD-3100) has been shown to significantly increase the mobilisation of HSCs for autologous stem cell transplantation [117-119].

Figure 1.12: CXCL12/CXCR4 intracellular cell signalling pathways

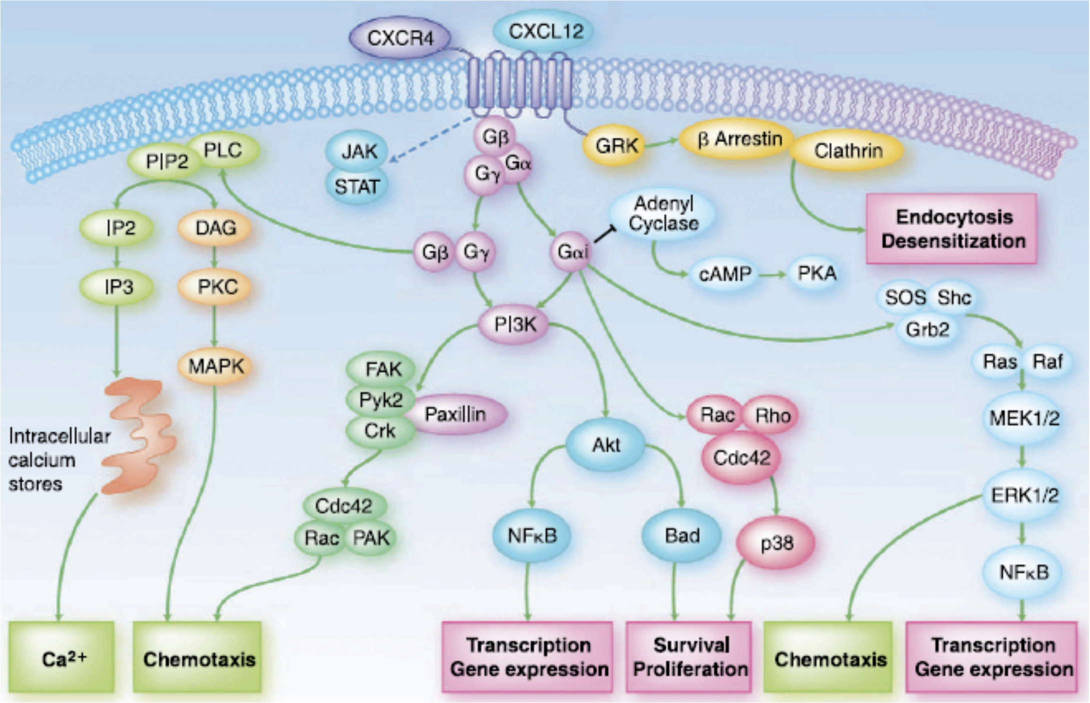

Binding of CXCL12 to G protein coupled receptor CXCR4 initiates numerous cell signalling pathways. This figure illustrates some of the key signalling pathways thought to be involved in CXCR4 signal transduction including P13 Kinase-mediated chemotaxis, gene transcription and cell proliferation. Figure taken from [120]

In the GI tract, CXCL12 is expressed by intestinal epithelial cells (IECs) stromal T cells and peripheral blood T cells. In IBD patients, an increase in CXCR4^{+} cells is observed in the intestinal stroma and peripheral blood [121]. In addition, CXCL12 expression is upregulated on IBD-IECs compared to normal IECs [121]. Indeed, blocking the CXCL12/CXCR4 axis ameliorates DSS-induced colitis in mice [122]. In these experiments, CXCR4 expression on CD4-positive cells significantly increased after the start of DSS administration compared with normal mice, and CXCL12 expression was significantly higher in the colonic tissue of DSS colitic mice than in normal mice.

The functional role of CXC12 and CXCR4 expression in the GI tract depends on whether inflammation is present. For instance, expression in normal IECs mediates cell migration, barrier maturation and restitution through cAMP-mediated cellular functions [121]. Whilst *in vitro* studies suggest that the upregulation CXCL12 in IBD serves to attract peripheral blood T cells and stromal T cells to inflammation sites- thus increasing inflammation [123].

In cancer, increased CXCR4 expression is observed on malignant epithelial cells and is correlated with increased metastasis that is believed to occur through the migration of CXCR4$^+$ malignant cells to tissues that express CXCL12 [124]. Furthermore, expression of CXCR4$^+$ on endothelial cells may contribute to tumour vascularisation [120]. The recruitment of BMDCs through the CXCL12/CXCR4 axis may be important for the role of BMDCs in GI tumourigenesis. Takemoto and colleagues (2011) demonstrated that an increase of circulating CD34$^+$ BMDCs following gastrectomy led to the increased growth of implanted tumours and tumour microvessel density compared to unoperated mice [96]. Blocking of CXCL12 with AMD-3100 negated these changes. Quante and colleagues (2011) also blocked CXCL12 and observed a decrease in gastric α-SMA$^+$ myofibroblasts and inhibition of gastric dysplasia in mice infected with *H. felis* [37]. Observation of CXCL12 expression in *Apc*$^{\mathrm{Min/+}}$ mice revealed that expression occurred solely in intestinal tumours and not normal tissues; this correlated with increased BMDC engraftment (Figure 1.15)

[80]. Collectively these findings indicate that the CXCL12/CXCR4 axis plays an important role in the BM- contribution to tumour vasculature and desmoplasia.

Like CXCL12, osteopontin (OPN) has also been implicated in the recruitment of BMDCs. OPN is an acidic glycoprotein that through its interaction with integrins present on other cells or with its receptor CD44, activates various cell signalling pathways involved in cell-cell interactions, angiogenesis, cell migration, proliferation, and survival (Figure 1.13). OPN can exist both extracellularly and intracellularly, free or bound, and secreted by numerous cell types including bone, BM cells, immune cells (such as B and T lymphocytes), macrophages, smooth muscle cells, and epithelial cells.

Figure 1.13: OPN induced cell signalling pathways

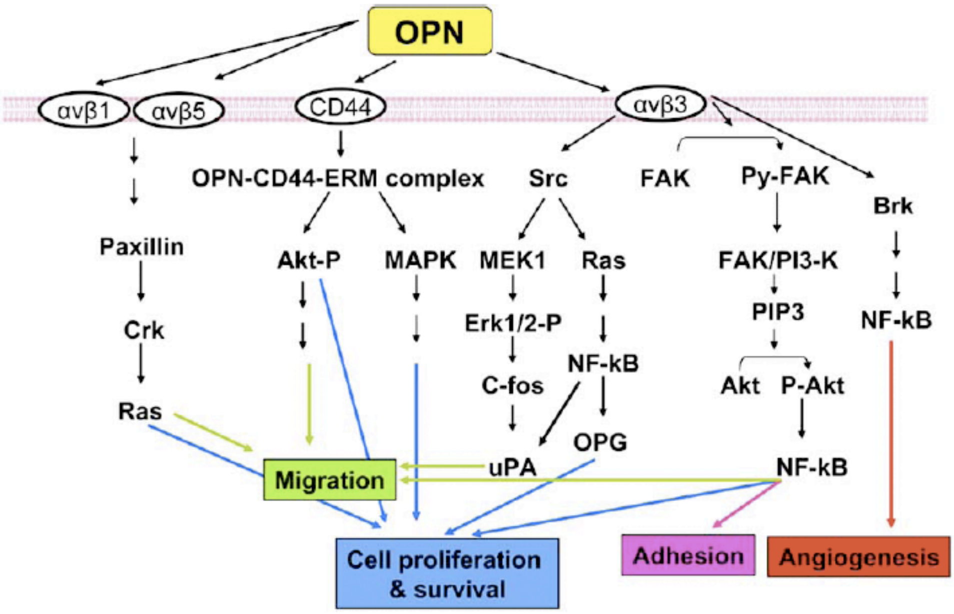

By interacting with integrins (such as a_vb1, a_vb5, or a_vb3) or its receptor CD44 on the surface of cells, osteopontin can act on numerous cell signalling pathways affecting cell migration, proliferation and survival, adhesion and angiogenesis. Figure adapted from [125].

In vitro and *in vivo* studies have shown that OPN is a key maintainer of the BM niche. This occurs through the homing of HSCs to the BM niche and their retention through the regulation of HSC proliferation [126]. Thrombin-cleaved OPN, which is abundant in human and mouse BM, has been demonstrated *in vivo* to be a key regulator of human and mouse HSCs *via* interactions with $\alpha_9\beta_1$ and $\alpha_4\beta_1$ integrins present on HSCs [127].

In the GI tract, IBD and tumourigenesis are associated with an increase in OPN [128, 129]. In various cancers (not just those in the GI tract) OPN is overexpressed on tumour cells (reviewed in [125]). Moreover, high levels of OPN is observed in the blood of patients with metastatic cancers [130]. *In vitro* and *in vivo* studies implicate OPN in every step of tumourigenesis [125], from increased migration *via* overexpression of integrins on cancer cells [131-133] to the apoptotic resistance in cancer cells due to the interaction of OPN with CD44 activating Src-mediated cell signalling [134]. One burgeoning theory is that the increased OPN expression in tumourigenesis disrupts the regulation of the BM (see Figure 1.14) [135]. McAllister and colleagues (2008) demonstrated *in vivo* that OPN produced from aggressive tumours increased BMDC recruitment into neighbouring indolent tumours, and that small hairpin RNA (shRNA) suppression of *Opn* mRNA resulted in a significant decrease in BMDC recruitment into indolent tumours [136]. *In vivo* studies by Davis and colleagues (2011) demonstrated frequent OPN expression on the BMD-HSCs present in tumour stroma but not in the BMD-HSCs present in normal intestinal stroma (Figure 1.15). Moreover, they observed increased BMDC engraftment in tumour stroma compared to the normal intestinal stroma [80]; however which cell lineages the BMDCs contributed to was not investigated.

These findings suggest a role of OPN in BMDC recruitment during tumourigenesis. Whether aberrant OPN expression in tumours is solely associated with the recruitment of HSCs or whether MSCs or EPCs become involved remains unknown.

Figure 1.14: Proposed paradigm of OPN instigated BMDC recruitment into secondary tumour sites

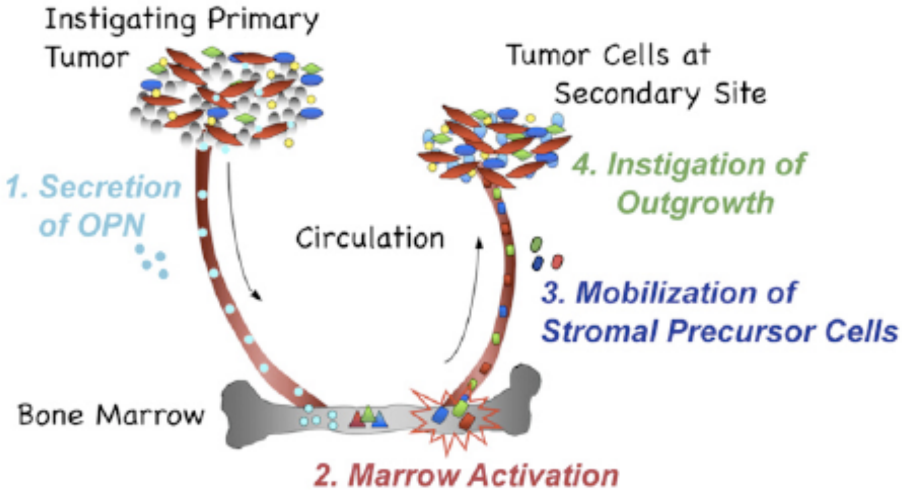

OPN secreted by an instigating primary tumour disrupts normal HSC regulation causing the mobilisation of activated BMDCs into the circulation that eventually incorporate into the tumour stroma of distant tumours. Figure taken from [136].

Figure 1.15: OPN and CXCL12 expression in *Apc*$^{Min/+}$ mouse tumours, from Davis *et al.*, 2011

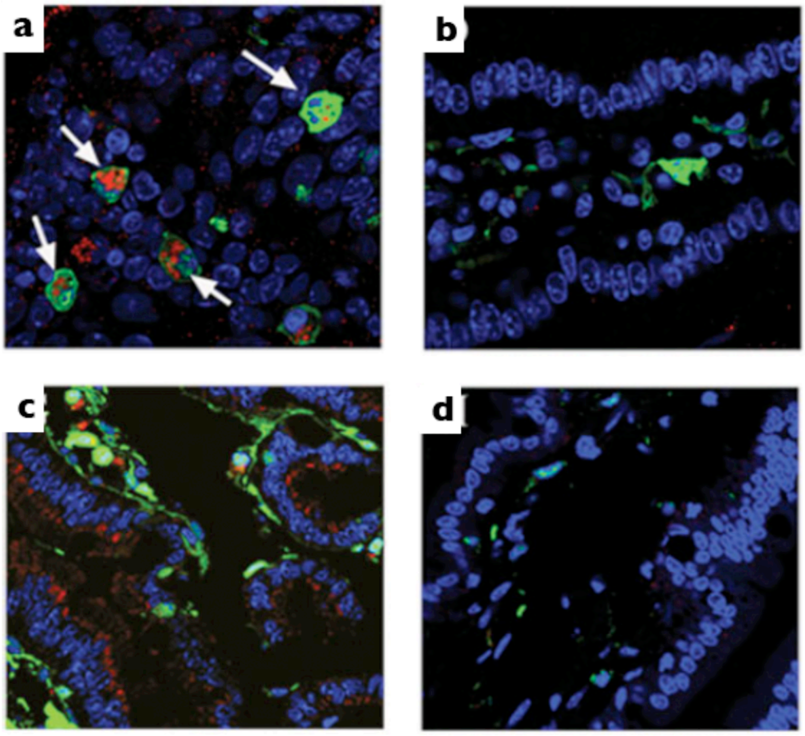

Fluorescent *in situ* hybridisation for OPN protein (red) demonstrates co-expression in eGFP (green) BMDCs in a small intestinal tumour (**a**) but similar expression is not observed in normal SI (**b**). Similarly, CXCL12 protein expression (red; **c**) is observed in an intestinal tumour (**c**) but not in normal intestine. Blue; DAPI. Magnifications were not provided in the paper. Figure taken from [80].

Mechanisms proposed for BMD-epithelial cell engraftment

The presence of BMD-epithelial cells and tumours cells has led to a debate as to how these cells engraft, with two competing theories: BM plasticity and cell fusion. For example with BM plasticity, a fraction of cytokeratin 19$^+$ BMD-MSCs can differentiate into epithelial cells, as demonstrated to occur with gastric epithelial cells *in vivo* [137]. A competing theory is that BMDCs fuse with somatic cells. Cell fusion events occur as part of mammalian development, for example macrophage fusion to produce osteoclasts [138]. Cell fusion in BMTx experiments is the result of the nuclear fusion of donor and host cells, identified by either the combination of donor and host cell markers or chromosomes, demonstrated by fluorescence *in situ* hybridisation (FISH). Chromosomal analysis has demonstrated that fused cells are synkaryons (e.g. containing a single nucleus), stable, and non-proliferating containing chromosomes from different cell types [139, 140]. However, loss of chromosomes has been shown to occur following nuclear fusion (cytoreductive division), which would then make demonstrating cell fusion impossible due to the loss of chromosomes and genetic markers [141].

BMDCs have been reported to stably fuse with various cell types *in vivo* [139, 142-149] including intestinal cells [150]-[151] at low frequencies. Moreover, cell fusion-mediated tissue repair has also been reported *in vivo* [152, 153]. However, evidence from several *in vivo* mouse [39, 154, 155] and human BMTx studies [83] [82] have cast doubt on the contribution of cell fusion to intestinal tract epithelial cells. Most recently, de Jong and colleagues (2012) presented what could be defining research on BMDC cell fusion. By tracking GFP and inducible diphtheria toxin receptor (iDTR) expression in BMTx'd mice, they concluded that cell fusion events were rare, occurring at a rate of around 1 in 1000 cells and that they were isolated incidences in the crypt. Moreover, DSS-induced intestinal damage did not increase cell-fusion events. In these experiments a novel Cre-Lox BMTx model was created in which inducible diphtheria toxin receptor (iDTR)/GFP BM harbouring a LoxP site was transplanted into CMV-Cre mice. Therefore, fused cells would express both GFP and DTR. Using semi-quantitative PCR analysis of the iDTR locus to analyse the biological contribution of cell fusion to tissue repair, diphtheria toxin (DT) was routinely injected into a group of mice following DSS-induced damage of intestinal epithelium, while another group remained untreated. DSS-induced damage and inflammation did not result in a significant increase in cell fusion events, while the DT treated group displayed no difference in histology compared to the untreated group, indicating that cell fusion was not necessary for intestinal epithelial repair [156].

Therefore, a question that arises is if cell fusion is a rare event how could one explain the past studies demonstrating a significant contribution of cell fusion? One possible explanation is the horizontal DNA transfer *via* phagocytosis of apoptotic bodies as recently demonstrated by Waterhouse *et al.,* (2011) [157]. Nevertheless, cell fusion remains a controversial theory for explaining BMDC engraftment in the gastrointestinal tract.

1.2 Aims and hypotheses of this study

1.2.1 Overview

Sex-mismatched BMTx was utilised to investigate the contribution of BMDCs to GI tumourigenesis in the following four different mouse models: the *Tff1*$^{-/-}$ mouse model of inflammation-associated gastric tumourigenesis, the *Apc*$^{\mathrm{Min/+}}$ and *Apc*$^{\mathrm{1322T}}$ mouse models of adenomatous polyposis, and the *Il10*$^{-/-}$ mouse model of chronic enterocolitis with a predisposition to colorectal adenocarcinoma. The aim was to conduct a comprehensive study of the contribution of BMDCs to tumour epithelium and stroma; comparing engraftment in inflammatory and non-inflammatory associated neoplasia, early dysplasia to later adenocarcinoma, and the effect of increased tumour burden.

1.2.2 Major aims and hypotheses

The overall remit of this study was to investigate whether BMDC-tumours, as demonstrated by Houghton *et al.*, (2004) [39], could occur in absence of *Helicobacter* infection. To this, we utilised IHC to identify putative donor-derived epithelial cells with Y-chromosome ISH.

As chronic inflammation from *Helicobacter* infection was a key feature of the Houghton *et al.*, (2004) study, we aimed to determine whether inflammation alone could drive the creation of BMDC-crypts and glands. Therefore, the *Il10*$^{-/-}$ and *Tff1*$^{-/-}$ mouse models were chosen as these models develop tumours in an inflammation context. From this, a hypothesis developed was that engraftment of BMD-epithelial cells would be significantly higher in the *Il10*$^{-/-}$ and *Tff1*$^{-/-}$ mouse models compared to *Apc*$^{Min/+}$ and *Apc*^{1322T} mouse models, which do not develop chronic inflammation as part of their pathology.

As BMD recruitment appears to correlate with increased regenerative demand [78], another hypothesis was that engraftment of BMD-epithelial cells would be higher in *Apc*^{1322T} mice which have a greater tumour burden than *Apc*$^{\mathrm{Min/+}}$ mice.

1.2.3 Minor aims and hypotheses

Several minor hypotheses and aims were developed to further investigate BMD-myofibroblast contribution and recruitment to tumour stroma, stem cell dynamics within tumours, cell fusion events, and whether BMTx could reverse the pathology observed in *Apc*$^{Min/+}$ and *Tff1*$^{-/-}$ mice.

In addition, the development of SPEM in WT mice of the *Tff1*$^{-/-}$ mouse crossover study let to the formation of additional hypotheses which are discussed in Section 1.2.3.1.

BMD-myofibroblast contribution and recruitment to tumour stroma

In this study, we aimed to understand whether increases in inflammation or tumour burden would impact on BMDC myofibroblast recruitment using α-SMA IHC/ Y-chromosome ISH identification of BMD myofibroblasts. A hypothesis was that BMD-myofibroblasts would home into areas of increased inflammation or increased tumour burden.

Despite previous studies that have demonstrated a significant contribution of BMD-myofibroblasts to inflammation and to tumour stroma [78, 92], little is known about the mechanisms of BMD-myofibroblast recruitment. To improve our understanding of this, isotopic ISH was carried out to identify and compare *Opn* mRNA expression in tumours, areas of inflammation and normal surrounding tissues. *Opn* was chosen based on the findings from McAllister *et al.,* (2008) and Davis *et al.,* (2011) that suggested a role in the recruitment of

BMDCs into the tumour stroma [80, 136]. Therefore we propose that aberrant *Opn* mRNA expression in tumours and/or inflammation correlates with increased BMDC engraftment.

Stem cell dynamics within tumours

Numerous studies have indicated that stem cell dynamics are altered within tumours. For example, strong mRNA expression of the Wnt target gene *Lgr5* has been described in a number of human tumours [158] [159] and in *Apc*$^{\mathrm{Min}/+}$ and *Apc*$^{1322\mathrm{T}}$ mouse SI adenomas [57]. Therefore, we aimed to compare *Lgr5* mRNA expression in the tumours and normal tissues of *Tff1*$^{-/-}$ and *Il10*$^{-/-}$ mouse models that do not harbour *Apc* mutations.

In addition, a stem cell origin of *Tff1*$^{-/-}$ mouse invasive gastric carcinomas has been suggested by Karam *et al.,* (2008) [28]. Therefore, a hypothesis in this study is that the highly proliferative, heterogeneous cell populations observed in *Tff1*$^{-/-}$ mouse adenocarcinomas are the result of aberrant Wnt signalling. To investigate this we employed *Lgr5* mRNA isotopic ISH to compare expression in WT mouse pyloric antrum with expression in *Tff1*$^{-/-}$ mouse adenocarcinomas.

Of particular interest is a proposed paradigm of BMDC engraftment developed by Houghton and colleagues (2005) in which BMDCs could engraft in an ablated stem cell niche and function as stem cells [40]. We aimed to use isotopic ISH to analyse *Lgr5* mRNA expression to investigate whether BMD-epithelial cells could adopt stem-like properties. A hypothesis was that if BMDCs could adopt stem-like properties, these cells would strongly express the Wnt target gene *Lgr5* and be capable of replication producing clones of cells recognisable in tissue sections as donor-derived. However, we did not observe engraftment of putative BMD-epithelial cells in the stem cell niche of any tissues analysed.

Cell fusion events

Fusion of BMDCs with normal and neoplastic intestinal cells has been reported as the means of BMDC engraftment [150, 151], eliciting much controversy. Based on these studies, if cell fusion events do occur they would correlate with tumours and/or areas of inflammation with a relatively low frequency of cell fusion events occurring in nearby normal tissue [141]. We attempted to optimise X/Y-chromosome FISH (as well as the detection of other mouse chromosomes with the Y-chromosome) and the use of pancentromeric probes to demonstrate cell fusion. We were unable to find a reliable method of demonstrating cell fusion; discussed Section A.1 in the Appendix.

BMTx-induced alteration of pathology

Amelioration of colitis in *Il10*$^{-/-}$ mice following transplantation of wild-type (WT) mouse BM has been described previously and therefore was not repeated with the *Il10*$^{-/-}$ mice of this study. However, this (WT mouse BMTx) was repeated for the *Apc*$^{\mathrm{Min}/+}$ and *Tff1*$^{-/-}$ mice. In other words, not only were these mice transplanted with similar mutant BM (e.g. *Tff1*$^{-/-}$ BM transplanted into *Tff1*$^{-}$

$^{/-}$ mice) but also these mutant mice were transplanted with WT BM. We did not expect transplantation of mutant or WT mouse BM into mutant mice to have an observable effect on pathology. This is because the enterocolitis observed in *Il10*$^{-/-}$ mice is due to a mutation that affects immune cells, therefore replacement of these cells with WT immune cells *via* BMTx would ameliorate colitis. Whereas the pathology observed in *Apc*$^{\mathrm{Min}/+}$ and *Tff1*$^{-/-}$ mice is due to mutations that effect epithelial cells. In addition to these transplantations, mutant mouse BM was transplanted into WT mice to investigate whether this BMTx of cells harbouring mutations could have a deleterious effect. In carrying out these crossover studies, our aim was to understand what effects BMTx could have on pathology and on BMDC recruitment.

1.2.3.1 Aims and hypotheses formed during this study

SPEM was observed in WT mice transplanted with either WT or *Tff1*$^{-/-}$ mouse BM in the *Tff1*$^{-/-}$ mouse crossover study from 6 months post BMTx. At the time that this study was being carried out, one hypothesis as to why SPEM occurred was that there was an expansion of TFF2 protein expressing progenitor (stem) cells. In addition, rare *Lgr5* expressing cells in the oxyntic mucosa have been occasionally shown to give rise to oxyntic mucosal cell lineages [20]. Therefore, we aimed to investigate whether *Lgr5* expression is altered during SPEM by utilising isotopic ISH to analyse *Lgr5* mRNA expression. A hypothesis formed was that there would be an increase in *Lgr5* mRNA in SPEM tissues as a result of increased Wnt signalling to create SPEM lineages.

In the histological examination of SPEM tissues inflammatory infiltrate was always observed. As with an earlier hypothesis that BMDC engraftment in epithelium and stroma would be driven by inflammation, we utilised the same methods described in Sections 1.2.2 and 1.2.3 to investigate the contribution of BMD-putative epithelial cells and myofibroblasts, respectively, in inflamed SPEM tissues. Similarly, we also investigated *Opn* mRNA expression in SPEM tissues using isotopic ISH based on previous reports of increased *Opn* mRNA expression in inflamed tissues [78].

CHAPTER 2

Materials and methods

2.1 Overview of experiments and rationale

All incubations were carried out at room temperature unless otherwise stated. Water refers to Milli-Q purified water unless otherwise stated.

To investigate the contribution of BMDCs to tumourigenesis, sex-mismatched BMTx (male BM into female recipient mice) was carried out in the *Tff1*$^{-/-}$, *Apc*$^{\mathrm{Min}/+}$ *Apc*^{1322T} and *Il10*$^{-/-}$ mouse studies. BMTx involved the use of ionising radiation which ablated the recipient mouse's BM to allow for the reconstitution with haematopoietic stem cells harvested from donor male BM.

A consequence of irradiation is that the recipient mice are immuno-compromised and thus susceptible to infectious pathogens. Therefore, it is common practice to administer antibiotics to mice and humans pre- and post-BMTx, to minimise pathogen infection and reduce the risk of systemic infection from gastrointestinal bacteria. However, there are several limitations to administering antibiotics such as the risk of antibiotic resistance development [160]. In this study we did not administer antibiotics to BMTx'd mice and instead relied upon the following common animal husbandry practices to reduce the risk of pathogen infection:

- Mice were fed acidified water two weeks prior to BMTx which continued for 6 weeks after BMTx. This served two purposes. The first was to cleanse the GI tract of pathogens prior to BMTx. The second was to reduce the likelihood of bacterial contamination from water bottles post BMTx [160].

- Mouse chow and water, cages and water bottles were autoclaved to reduce the likelihood of bacterial and fungal infection.
- Mice were kept in HEPA-filtered individually ventilated cages and handled only under a HEPA-filtered flow hood to remove aerolised bacteria and fungal spores [160].
- Screening for common mouse colony bacterial and parasitic infections (such as *Streptococcus* spp. and *Giardia)* was carried out post BMTx.

Following BMTx, mice were monitored daily and then culled at determined time points. Prior to culling, mice were administered Vincristine and BrdU to analyse for mitotic activity and DNA synthesis, respectively. Tissues were then harvested, fixed in formalin, embedded into paraffin blocks. Tissue blocks were cut into serial sections, with the first section stained with haematoxylin and eosin (H&E) to be used as a guide and the remaining sections to be used for special stains and immunohistochemistry. Sections to be analysed for *Opn*, *Lgr5*, *Tff*1, *Tff*2, and *Tff*3 mRNA expression *via* isotopic ISH were cut under RNase free conditions a day prior to the experiment to provide optimal results.

To analyse the contribution of BMDCs in tissues, an IHC/Y-chromosome ISH assay was carried out on a single section for either α-SMA (to analyse for myofibroblasts) or lymphocytic cells and macrophages, followed by Y-chromosome ISH. The presence of BMD-myofibroblasts in the processed sections was then quantitated using Nikon microscope/image analysis software and quantified using PRISM statistical software.

Statement on experimental collaborations

This study contained a number of collaborations. Paraffin embedded *Apc*$^{Min/+}$ mouse crossover study tissues were presented as a kind gift from Shigeki Bamba. *Apc*^{1322T} mice were presented as a kind gift from Annabelle Lewis (University of Cambridge). Genotyping of *Apc*$^{Min/+}$ crossover study mice was carried out by Alison Martin (CRUK) and genotyping of *Apc*^{1322T} mice was performed by Annabelle Lewis. The author was responsible for the genotyping of *Il10*$^{-/-}$ and *Tff1*$^{-/-}$ mouse crossover study mice.

The Biological Resources Unit (Cancer Research UK) was responsible for animal husbandry and carried out whole-body irradiation of mice *Apc*^{1322T}, *Il10*$^{-/-}$ and *Tff1*$^{-/-}$ mouse crossover study mice. The author carried out bone marrow collection, processing, and stem cell transplantation. Microbiological screening for bacterial and parasitic infections was carried out by Minal Panya (Cancer Research UK), whilst screening for *Helicobacter* species in mice was performed by Harlan Laboratories. The author was responsible for monitoring, culling, and harvesting and processing of mouse tissues.

The Experimental Histopathology laboratory (Cancer Research UK) carried out tissue paraffin embedding and sectioning; and H&E and Alcian blue/diastase/PAS staining. Nicholas Wright (Pathologist; QMUL) performed a histological assessment of *Apc*^{1322T}, *Apc*$^{Min/+}$ and *Tff1*$^{-/-}$ mouse crossover study mouse tissues. Gordon Stamp (Pathologist; ICL) performed a histological assessment of *Il10*$^{-/-}$ mouse tissues.

All immunohistochemistry, Y-chromosome ISH and detection and quantification of BMDCs was carried out by the author.

Both the author and Rosemary Jeffrey (Cancer Research UK) performed *Lgr5, Tff1, Tff2,* and *Tff3* mRNA isotopic ISH experiments. Table 2.1 outlines which experiments were performed by Rosemary Jeffrey and which were performed by the author. The author was responsible for preparation and purification of *Opn* containing plasmids and *Opn* mRNA isotopic ISH. Isotopic ISH for *Tff1* mRNA was carried out only on *Il10*$^{-/-}$ mouse tissues before switching to more time and cost effective TFF1 IHC.

Table 2.1: Delegation of isotopic ISH experiments

Experimental group	**Isotopic ISH experiment**				
	Lgr5 mRNA	*Opn mRNA*	*Tff1 mRNA*	*Tff2 mRNA*	*Tff3 mRNA*
Tff1$^{-/-}$ mouse crossover study	**RJ**: *Tff1*$^{-/-}$→*Tff1*$^{-/-}$ mice group, WT →*Tff1*$^{-/-}$ mice group at 6 months post BMTx, *Tff1*$^{-/-}$→WT mice at 6 months post BMTx **ALB** remaining groups	**ALB**	----	**RJ:** *Tff1*$^{-/-}$→*Tff1*$^{-/-}$ mice at 6 months post BMTx, *Tff1*$^{-/-}$ →WT mice at 6 and 12 months post BMTx **ALB** remaining groups	**RJ**
Apc$^{Min/+}$ mouse crossover study	**ALB**	**ALB**	----	----	----
Apc^{1322T}	**RJ**	**ALB**	**----**	**RJ**	**----**
Il10$^{-/-}$ mice	**RJ**	**ALB**	**RJ**	----	**RJ**

RJ Rosemary Jeffrey; **ALB** Arielle Le Brenne; → mouse BM transplanted into; ---- experiment not performed

2.2 Animals

Il10$^{-/-}$ mice (on a BALB/c background) from the Jackson Laboratory were used to create an experimental colony. *Tff1*$^{-/-}$ mice (on a C57BL/6 background) generated by Lefebvre *et al*. (1996) were used in this study. *Apc*^{1322T} mice (on a C57BL/6 background) mice were a kind gift from Annabelle Lewis.

Husbandry

All mice were maintained under barrier housing at the Biological Resources Unit (London Research Institute, Cancer Research UK) and provided with standard chow diet and water *ad libitum* in accordance with UK Home Office guidelines.

Microbiological screening

Microbiological screening was carried out on a mouse from each cage present in the *Tff1*$^{-/-}$, *Apc*^{1322T}, and *Il10*$^{-/-}$ mouse colonies. This was done a week post BMTx and prior to culling for *Apc*^{1322T} mice and was carried out monthly for the *Tff1*$^{-/-}$ and *Il10*$^{-/-}$ mice. Oral swabs and faecal samples were taken from the mice and analysed by Minal Pandya (Clare Hall, CRUK). *Entamoeba, Giardia, Chilomastix,* and *Tritrichomonas* were detected using a routine faecal smear method [161]. *Streptococci* and *Lactobacilli,* which are present in normal murine flora, were tested for antibiotic sensitivity using disk-diffusion antibiotic testing (the Kirby-Bauer antibiotic testing method) [162]. Testing for *Helicobacter* species was performed by Harlan Laboratories. DNA was extracted from faecal samples, using methods described by Shen *et al*., (1997) [163].

Genotyping

Genotyping of *Apc*^{1322T} mice was carried out by Annabelle Lewis. Genotyping of *Apc*$^{Min/+}$ mice was carried out by Alison Martin. The author carried out genotyping of *Tff1*$^{-/-}$ and *Il10*$^{-/-}$ mice.

All mice were genotyped using PCR and agarose gel electrophoresis. Mouse DNA was extracted from mouse ear or tail snip tissue using manufacturer-supplied instructions and reagents from a DNEasy blood & tissue kit (Qiagen) for *Tff1*$^{-/-}$, *Apc*$^{Min/+}$ and *Il10*$^{-/-}$ mouse genotyping or following the HotSHOT alkaline lysis method [164] for *Apc*^{1322T} mouse genotyping. Extracted DNA and amplified products were then kept at 4°C (or frozen for longer term storage) until use.

Genotyping involved PCR of extracted DNA using a three-primer mix that allowed for the amplification of +/+, -/+, or -/- alleles in mice which can then allow for the determination of mouse genotype by specific molecular weight bands following 1% agarose gel electrophoresis. For example, *Tff1*$^{-/-}$ and *Il10*$^{-/-}$ mice possess a neomycin (Neo) resistance gene that is amplified by a Neo primer produced in any mice possessing a mutated allele(s). Similarly, specific primers bind onto a mutated allele found only in *Apc*$^{Min/+}$ and *Apc*^{1322T} mice, respectively. Genotyping protocols are summarised in Table 2.2.

Table 2.2: Genotyping protocol details

Genotyping protocol and details	Primer sequences		PCR reaction volume	PCR reagents per reaction (concentration; supplier)	PCR Conditions
Tff1$^{-/-}$ Oligonucleotide primer sequences provided by Catherine Tomasetto. William Otto optimised the *Tff1* genotyping PCR protocol.	Neo forward:	5' AGG ATC TCC TGT CAT CTC ACC TTG CTC CTG 3'	25μl	2.5μl 10x magnesium free buffer (1x; Invitrogen), 2.0μl 25mM MgCl$_2$ (2mM; Qiagen), 0.4 μl 10mM dNTP (1.6 mM; Qiagen), 5μl 5X Q solution (1X; Qiagen), 0.5μl 500U/ml *Taq* DNA polymerase (10U/ml; CRUK), 0.5μl 200μM three Il-10 genotyping primers (0.3μM per primer, Sigma-Genosys) 13.1μl water and 1μl extracted DNA to be analysed	Initialization at 95°C for 4 minutes, denaturing at 95°C for 1 minute, annealing at 60°C for 1 minute, and elongation at 72°C for 1 minute. Forty amplification cycles were performed. A final elongation step at 72°C for 15 minutes was performed.
	Tff1 forward:	5' CCA TGA CTC ACC CTG CTT TT 3'			
	Tff1 reverse:	5' CCC CTA CTG TGC TGA GAG ATG 3'			
Apc$^{Min/+}$ Oligonucleotide primer sequences and a PCR protocol provided by the Jackson Laboratory	Wild type:	5' GCC ATC CCT TCA CGT TAG 3'	12μl	1.55μl 10x AB PCR Buffer II (1.29x; Applied Bioscience), 1.15μl 25mM MgCl$_2$ (2.40mM; Qiagen), 1.15μl 2.5mM dNTP (0.24mM each; Qiagen), 0.89μl 20μM wild type primer (1.48μM), 0.90μl 20μM common primer (1.50μM), 0.72μl mutant primer (1.20mM), 1.66μl 5mM DNA Loading Dye (0.69mM; Applied Bioscience), 0.20μl 5U/μl *Taq* DNA polymerase+*Taq*Start AB (1:1) [0.02U/μl; Applied Biosciences], 1.78μl water and 2μl extracted DNA to be analysed.	Initialization at 94°C for 3 minutes, denaturing at 94°C for 30 seconds, annealing at 55°C for 30 seconds, and elongation at 72°C for 1 minute. Thirty-five amplification cycles were performed. A final elongation step at 72°C for 2 minutes was performed
	Common:	5' TTC CAC TTT GGC ATA AGG C 3'			
	Mutant:	5' TTC TGA GAA AGA CAG AAG TTA 3'			

Table 2.2: Genotyping protocol details (continued)

Genotyping protocol and details	**Primer sequences**		**PCR reaction volume**	**PCR reagents per reaction** (concentration; supplier)	**PCR Conditions**
Apc ^{1322T} Oligonucleotide primer sequences designed by Patrick Pollard.	Wild type:	5’ TGG GTT TGG CTC TAG CAT TC 3’	50μl	5μl 10x Bioline reaction buffer (1x; Bioline), 3μl 50mM MgCl$_2$, 4μl dNTP (0.2mM each; Amersham), 10μl 5x Q solution (1x; Qiagen), 0.5μl 5U/μl *Taq* DNA polymerase (2.5U/μl; Bioline), 1μl mixture of three *Apc*^{1322T} genotyping primers (0.3μM per primer), 26μl water, and 2μl of extracted DNA to be analysed.	Initialization at 95°C for 4 minutes, denaturing at 94°C for 1 minute, annealing at 55°C for 1 minute, and elongation at 72°C for 1 minute. Thirty-five amplification cycles were performed. A final elongation step at 72°C for 15 minutes was performed.
	Common:	5’ CCC TCC ATC AAC CAA GAA AC 3’			
	Mutant:	5’ AAG AGT GCC TCC CAA AAT GA 3’			
Il10 $^{-/-}$ Oligonucleotide primers and PCR protocol optimised by Shigeki Bamba.	Neo Reverse:	5’ AAT CCA TCT TGT TCA ATG GCC GAT C 3’	25μl	2.5μl 1x magnesium free buffer (Invitrogen), 2.0μl 25mM MgCl$_2$ (2mM; Qiagen), 2.0μl 10mM dNTP (0.8mM; Qiagen), 5μl 5x Q solution (1x; Qiagen), 0.5μl 500U/ml *Taq* DNA polymerase (10U/ml; CRUK), 0.5μl mixture of three Il-10 genotyping primers (0.3μM per primer), 11.5μl water, and 1μl extracted DNA to be analysed.	Initialization at 94°C for 3 minutes, denaturing at 94°C for 30 seconds, annealing at 58°C for 1 minute, and elongation at 72°C for 1 minute. Thirty-five amplification cycles were performed. A final elongation step at 72°C for 2 minutes was performed.
	Il10 forward:	5’ GCC TTC AGT ATA AAA GGG GGA CC 3’			
	Il10 reverse:	5’ GTG GGT GCA GTT ATT GTC TTC CCG 3’			

Amplified PCR products were separated on a 1% agarose gel containing ethidium bromide. A 150ml agarose gel was made by adding 1.5g molecular biology grade agarose to 150ml 1x TBE and heating in a microwave until the agarose fully dissolved (~3 minutes). The melted agarose was allowed to cool for ~2 minutes and 1.5μl of ethidium bromide was then added, mixed and poured into a gel-casting tray with a comb(s) inserted in order to create sample wells. The gel was allowed to set (~30 minutes) before the combs were removed and the gel tray was placed into a gel tank filled with 1x TBE buffer. 5μl amplified PCR product was mixed with 2μl 5x loading buffer and loaded into respective wells in the gel. 6μl of 100bp DNA ladder was run alongside in order to determine fragment size (see Table 2.3 for PCR product sizes of each genotyping protocol). The gel was run at 400V for 40 minutes, then placed under UV light to visualise DNA and a digital image was taken (See Figure 2.1 and 2.2).

Table 2.3: PCR product sizes of *Tff1*$^{-/-}$, *Apc*$^{Min/+}$, *Apc*^{1322T} and *Il10*$^{-/-}$ mouse genotyping

	PCR product size (base pairs) for each genotype		
Genotyping protocol	**+/+**	**-/+**	**-/-**
Tff1$^{-/-}$	200	200 and 500	500
Apc$^{Min/+}$	600	340 and 600	----
Apc^{1322T}	217	217 and 433	----
Il10$^{-/-}$	200	200 and 450	450

Figure 2.1: Separation of *Tff1* genotypes on agarose gel

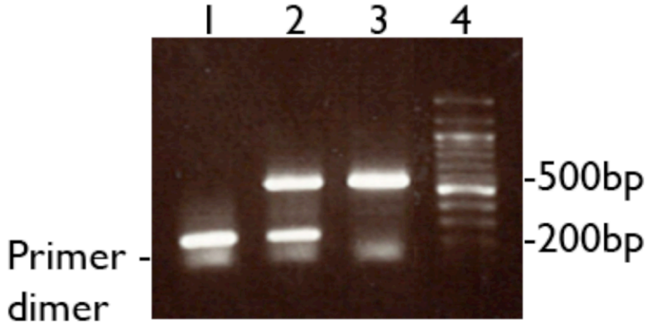

A digital photograph of *Tff1*$^{+/+}$ (**1**), *Tff1*$^{-/+}$ (**2**) and *Tff1*$^{-/-}$ (**3**) mouse DNA separated on a 1% agarose gel. A 100bp ladder (**4**) was run alongside to determine the molecular weight of the samples.

Figure 2.2: Separation of *Il10* genotypes on agarose gel

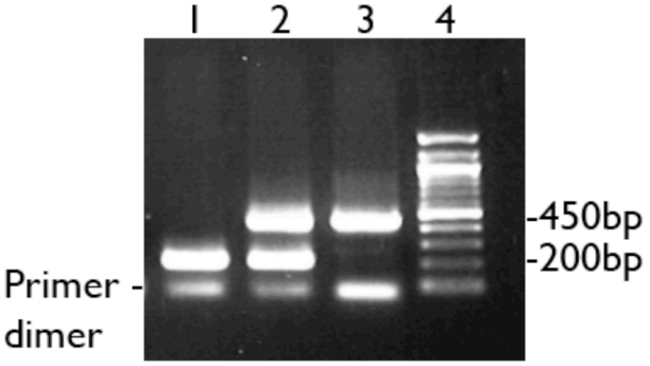

A digital photograph of *Il-10*$^{+/+}$ (**1**), *Il-10*$^{-/+}$ (**2**) and *Il10*$^{-/-}$ (**3**) mouse DNA separated on a 1% agarose gel. A 100bp ladder (**4**) was run alongside to determine the molecular weight of the samples.

Bone marrow transplantation

Female mice that underwent transplantation were housed under conventional conditions. A week prior to transplantation, these mice were fed acidified water (pH2.5-3.0), as previously described [160]. *Apc*$^{\mathrm{Min}/+}$, *Il10*$^{-/-}$ and *Tff1*$^{-/-}$ mice of at least six weeks of age to a maximum of 2 months of age were subjected to a total of 12 Gray whole body gamma-irradiation divided into two doses three hours apart to allow for BM ablation. *Apc*^{1322T} mice received a similar transplantation protocol except these mice received a total of 10 Gray whole body gamma-irradiation. A lower radiation dose was given to these mice due to their severe phenotype as a 12 Gray dose resulted in their death within a week of transplantation.

Within 4 hours after the second dose of irradiation, female recipient mice were injected with 1 x 10^6 whole BM cells from litter matched male donors (one donor being sufficient to reconstitute 3 recipients). BM was flushed from both the femurs and tibias of donor mice using sterile PBSA in a 5ml syringe. The cells were then centrifuged at 400g for 5 minutes and re-suspended in 5ml sterile PBSA. Re-suspended cells were then needled (using 19, 23, and 27 gauge needles) to disaggregate the cells and filtered using a 40μm filter. The number of nucleated cells was counted using a haemocytometer. Donor BM was injected *via* the tail vein (cell injection volume equal 5ml/kg mouse weight) at 2 x 10^6 cells in 100μl PBS.

Post-transplantation mice were kept on acidified water for 6 weeks. Mice were monitored daily and weighed weekly.

Experimental groups

A crossover study was carried out for both *Tff1*$^{-/-}$ and *Apc*$^{Min/+}$ mouse models. *Il10*$^{-/-}$ mice were not studied in a crossover design, due to the findings of Bamba and colleagues (2006) [78]. In addition, due to a small number of *Apc*^{1322T} mice available from Annabelle Lewis, a crossover study could not be carried out on this mouse model. For the crossover study groups, WT mice on the same genetic background as mutant mice were used as controls. Table 2.4 summarises the experimental groups and culling time points for each mouse model.

Table 2.4: Experimental groups for the four mouse models used in this study

Mouse model	**Total number of mice**	**Experimental groups** (number of mice)	**Time points culled**
Tff1$^{-/-}$	72	WT mouse BM→WT mice (*n*=18)	Six mice from each experimental group were culled at 6, 12, or 18 months post BMTx
		Tff1$^{-/-}$ mouse BM→WT mice (*n*=18)	
		Tff1$^{-/-}$ mouse BM→*Tff1*$^{-/-}$ mice (*n*=18)	
		WT mouse BM→*Tff1*$^{-/-}$ mice (*n*=18)	
Apc$^{\text{Min/+}}$	48	WT mouse BM→WT mice (*n*=12)	Six mice from each experimental group were culled 1 or 2 months post BMTx
		Apc$^{\text{Min/+}}$ mouse BM →WT mice (*n*=12)	
		Apc$^{\text{Min/+}}$ mouse BM→*Apc*$^{\text{Min/+}}$ mice (*n*=12)	
		WT mouse BM→*Apc*$^{\text{Min/+}}$ mice (*n*=12)	
Apc$^{\text{1322T}}$	4	*Apc*$^{\text{1322T}}$ mouse BM→*Apc*$^{\text{1322T}}$ mice (*n*=4)	All mice were culled 4 weeks post BMTx
Il10$^{-/-}$	12	*Il10*$^{-/-}$ mouse BM → *Il10*$^{-/-}$ mice (*n*=12)	Six mice were culled 3 or 5 months post BMTx

→ transplanted into

Analysis of cell proliferation prior to tissue harvesting

BrdU and Vincristine were injected into mice (except for BM donors) prior to culling in order to assess cell proliferation. BrdU is a thymidine analogue that incorporates into DNA during DNA synthesis [165] while Vincristine arrests mitoses in metaphase by binding to microtubules.

Mice (with the exception of BM donors) were administered Vincristine and bromodeoxyuridine (BrdU) prior to culling. BrdU (50μg/g BW) and vincristine (1μg/g BW) were administered *via* intraperitoneal (IP) injection one and two hours, respectively, prior to the culling of transplanted and control mice. All mice were killed by cervical dislocation.

Tissue harvesting, fixation and processing

All organs of the gastrointestinal tract (stomach, intestines, liver, pancreas, spleen, kidneys) were fixed in 10% neutral buffered formalin (NBF) for 24 hours, transferred to 70% ethanol and then embedded in paraffin wax the same day. Organs were then sectioned at 4μm. Serial sections were used for analysis and a representative H&E stained section was used as a guide.

2.3 Special stains and IHC

2.3.1 All experiments

Buffers and solutions are described in Table 2.5. Formalin-fixed, paraffin embedded sections were dewaxed in xylene with two 5 minute washes, changing to fresh xylene for each wash. Sections were then rehydrated in 100% industrial methylated spirit (IMS) for 5 minutes. If IHC using an avidin/biotin/peroxidase complex was to be carried out, endogenous peroxidases were then blocked with a 1.5% hydrogen peroxide in methanol solution for 15 minutes. If IHC using a biotin/streptavidin/alkaline phosphatase was used, a block for endogenous alkaline phosphatases (20% acetic acid in methanol at 4°C for 15 minutes) was carried out. Sections were them re-immersed in 100% IMS for 5 minutes then rehydrated through graded alcohols (95%; 70%; 5 minutes each) to PBS.

Heat-induced epitope retrieval (HIER) or proteolytic enzyme induced epitope retrieval (PIER) was carried out if antigenic retrieval was required. HIER was performed by microwaving de-waxed sections in boiling 0.01M sodium citrate buffer at pH6.0 for 10 minutes at full power then quenching in cold running tap water prior to carrying out the standard IHC protocol, unless otherwise specified. PIER was performed by immersing de-waxed sections in 0.04% pepsin in 0.1M HCl for 30 minutes at 37°C then quenching 0.2% glycine in PBS prior to carrying out the standard IHC protocol.

All serum/ antibody incubations were carried out in a humidified chamber at room temperature. A block using normal serum from the host of the secondary antibody was applied onto sections for 30 minutes at the start of the IHC protocol to prevent non-specific staining. Primary antibody was replaced with 1% bovine serum albumin (BSA) in PBS for negative controls. Blocking serum and all antibodies and were made up in 1% BSA in PBS. 0.1% Tween® 20 in PBS was used to wash sections in between antibody layers.

Light microscopy involved the use of an avidin/biotin/peroxidase complex or a biotin/streptavidin/alkaline phosphatase complex with chromogenic visualisation. For both complexes a biotinylated secondary antibody was used. The third and final layer involved the use of either an avidin-peroxidase conjugated layer (VECTASTAIN® Elite ABC kit) for an avidin/biotin/peroxidase complex or a streptavidin-alkaline phosphatase conjugated layer for a biotin/streptavidin/alkaline phosphatase complex.

3,3'-Diaminobenzidine (DAB) was used to develop an avidin/biotin/peroxidase complex whilst Vector Red® was used to develop a biotin/streptavidin/alkaline phosphatase complex. Both substrates were prepared following manufacturer's instructions and development was monitored microscopically. Generally, Vector Red® development took 10 minutes while DAB development took 1 minute. DAB was washed off using dH_20. Vector Red® was washed using PBS. Tissue sections were then counterstained using light haematoxylin, dehydrated through graded alcohols, cleared in xylene and mounted using DPX mounting medium.

For immunofluorescence, sections were placed into PBS during the final antibody layer washes. Any excess was tipped off and a small amount of VECTASHIELD HardSet Mounting Medium with DAPI (Vector Labs) was applied and slides were kept refrigerated at 4°C.

Table 2.5: Buffers and solutions used in IHC experiments

Buffer/solution	**Details/Reference number**
Citrate buffer pH6.0	2.94g tri-sodium citrate (BDH) dissolved in 1l water and adjusted to pH6.0 with 10x HCl
0.04% pepsin in 0.1M HCl	0.08g pepsin (6887; Sigma) dissolved in 200ml 0.1M HCl at 37°C
VECTASTAIN® Elite ABC kit	Prepared according to manufacturer's instructions. SK-4100; Vector Labs
Alkaline phosphatase streptavidin	Diluted 1:50. Incubated for 30 minutes. SA-5100; Vector Labs
DAB	Prepared according to manufacturer's instructions. SK-4100; Vector Labs
Vector Red®	Prepared according to manufacturer's instructions. SK-5100; Vector labs
VECTASHIELD HardSet Mounting Medium with DAPI	H-1200; Vector Labs

2.3.2 Combined Alcian blue/diastase/PAS demonstration of mucins

Stomach sections from the *Tff1*$^{-/-}$ mouse crossover study were stained by the Experimental Histopathology Laboratory (CRUK) using the combined Alcian blue/diastase/PAS method. This was to demonstrate changes in mucin expression due to TFF1 deficiency and/or disease progression. Combined Alcian blue and Periodic Acid-Schiff's with diastase pre-treatment (ABdPAS) is a pan-mucin detection stain. Alcian blue is a cationic dye that forms reversible electrostatic bonds with anionic sites in acid mucins. Neutral mucins and Nacetyl sialomucins contain a reactive hexose component that is stained by the PAS reaction. The PAS reaction is a two-step process in which periodic acid causes oxidative cleavage of carbon-to-carbon bonds in 1.2-glycols or their amino derivatives forming dialdehydes. Then Schiff's reagent is applied causing the aldehydes to combine with the fuchsin-sulfurous acid and pararosaniline present in the reagent forming a magenta coloured compound [166]. As the PAS reaction stains glycogen as well, a diastase pre-treatment is carried out to digest glycogen prior to Alcian blue staining. Therefore only neutral mucins will be stained by the PAS reaction. This combined method results in acid mucins stained blue and neutral mucins stained magenta (Figure 2.3).

The ABdPAS protocol is as follows; tissue section slides were dewaxed then rinsed in tap water. Sections were incubated in 0.5% α-amylase for 30 minutes at 37°C. Sections were stained in Alcian Blue for 5 minutes and then washed under running deionised water for 5 minutes. Sections were then treated with 1% periodic acid for 5 minutes and washed as before. Sections were then immersed in Schiff's reagent for 15 minutes. Afterwards sections were washed as before. Sections were then counterstained in haematoxylin for 5 minutes and differentiated in 1% acid alcohol for 10 seconds. Sections were then washed under running tap water for 5 minutes. Afterwards sections were dehydrated and cleared (in xylene) and then mounted using DPX.

Figure 2.3: ABdPAS staining of mouse stomach and duodenum

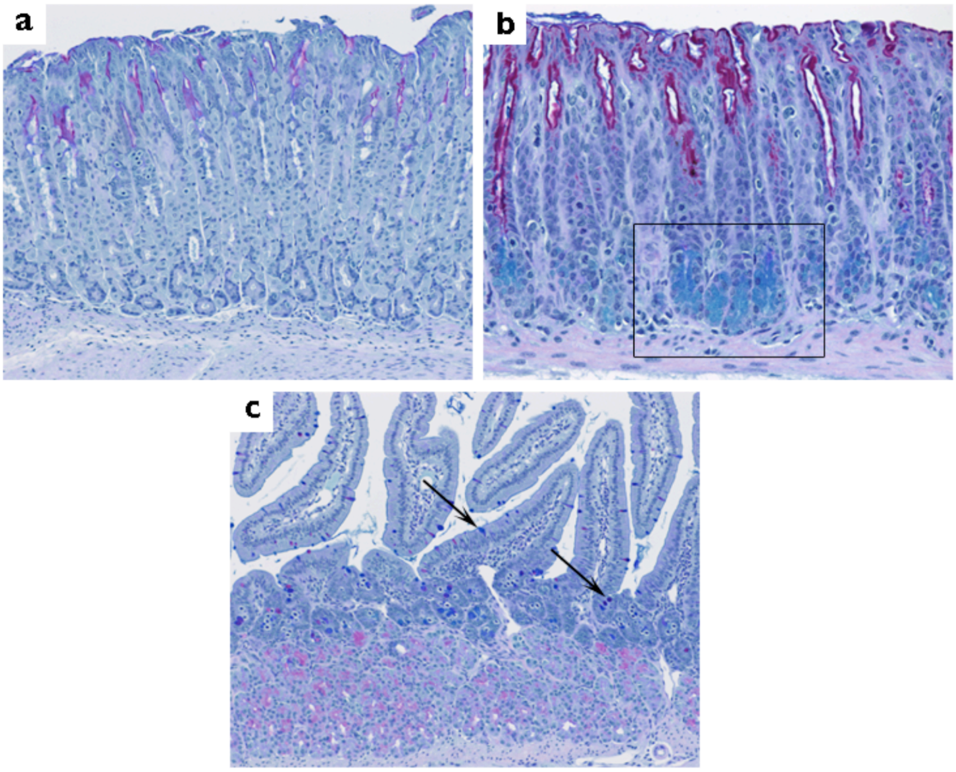

Alcian blue/diastase/PAS (ABdPAS) staining of the stomach and duodenum of a WT mouse transplanted with WT mouse BM 6 months post BMTx. The mucosal surface of the fundus (**a**; x10) and pylorus (**b**; x20) stains positive for PAS while the basal region of the pylorus is positive for Alcian blue (rectangle; **b**). In the duodenum (**c**; x10), Brunner's glands are PAS positive while goblet cells are identified by their Alcian blue positivity and morphology (arrows).

2.3.3 IHC for BrdU, GKN2, H^+/K^+ ATPase, pepsinogen, and TFF1

BrdU IHC was carried out on the four mouse models to identify where cell proliferation was occurring. IHC for GKN2, H^+/K^+ ATPase, pepsinogen and TFF1 gastric markers was carried out on stomach sections of the *Tff1*$^{-/-}$ mouse crossover study mice, to investigate which gastric cell lineages were affected by the BMTx and/or tumourigenesis and their expression patterns. Parietal cells were identified with an antibody against H^+/K^+ ATPase, chief cells were identified with an anti-pepsinogen antibody and foveolar cells were identified with anti-GKN2 and anti-TFF1 antibodies. We attempted TFF3 IHC (as an alternative to *Tff3* isotopic ISH) but at the time of this study were unable to find a suitable commercially available anti-TFF3 antibody for mouse tissues.

Monoclonal antibodies to BrdU and H^+/K^+ ATPase and polyclonal antibodies to pepsinogen, GKN2 and TFF1 were obtained. Details of antibodies and substrates used are shown in Table 2.6. Indirect immunohistochemistry was carried out using an avidin/biotin/peroxidase for all antibodies except for GKN2, which was detected using a streptavidin/biotin/alkaline phosphatase complex. This was performed to allow for comparison of TFF1 and GKN2, which share a similar expression pattern.

Table 2.6: Details of BrdU, GKN2, H^+/K^+ ATPase, pepsinogen and TFF1 antibodies

Antibody	**Details/ Reference number**	**Dilution**	**Incubation time (min)**	**Epitope retrieval**	**Source**
BrdU	**MM** Fab fragments with POD conjugated specific to BrdU Ref: 11 585 860 011	1:5	60	**C**	Roche
GKN2	**RP** IgG raised against synthesised GKN2 with an additional cysteine at the N-terminus Ref: [167]	1:250	60	----	Courtesy of Dr. William Otto, CRUK
H^+/K^+ ATPase	**MM** clone 2G11 raised against the 34 kDa core peptide of t the β-subunit of H^+/K^+ ATPase. Ref: A-274	1:6000	35	**C**	Sigma-Aldrich
Pepsinogen	**SP** IgG specific to human pepsinogen II. Ref: PC132	1:4000	35	**P**	Binding Site
TFF1	**RP** IgG raised against aa 5-87 mapping at the C-terminus of mouse TFF1 Ref: SC-28926	1:250	60	----	Santa Cruz

Key: **MM** mouse monoclonal; **RP** rabbit polyclonal; **SP** sheep polyclonal; **P** PIER with 0.04% pepsin for 30 minutes; **C** HIER with sodium citrate

2.4 Combined IHC/Y-chromosome ISH detection of male donor-derived cells

2.4.1 Overview

Rationale

Combined IHC/Y-chromosome ISH (the combined detection protocol) allows for the detection and immunohistochemical phenotyping of donor-derived cells in formalin-fixed paraffin embedded tissue sections. This method takes advantage of IHC using a biotin/streptavidin/alkaline phosphatase complex followed by indirect Y-chromosome ISH to detect whether any myofibroblasts, lymphocytes, macrophages or epithelial cells are donor-derived. Indirect Y-chromosome ISH utilises anti-fluorescein antibodies to bind onto the hybridised fluorescein isothiocyanate (FITC) labelled Y-chromosome in cells (Figure 2.4). The indirect method was chosen over the direct method due to the stability of DAB that was required for lengthy quantifications.

A criticism of the indirect Y-chromosome ISH with anti-fluorescein is that the DAB end-product can sometimes stain nucleoli resulting in small light brown dots inside the nucleus upon DAB development. However, when this cell is compared with one containing a Y-chromosome signal there are very clear differences. The Y-chromosome signal is larger, at the edge of the nucleus and very dark brown (Figure 2.5).

The methods used in IHC phenotyping will be discussed in this section. Y-chromosome ISH controls were male spleen hybridised with either the Y-chromosome probe (positive control) or with hybridisation buffer instead (negative control).

Figure 2.4: Y-chromosome detection using an anti-fluorescein peroxidase conjugated antibody

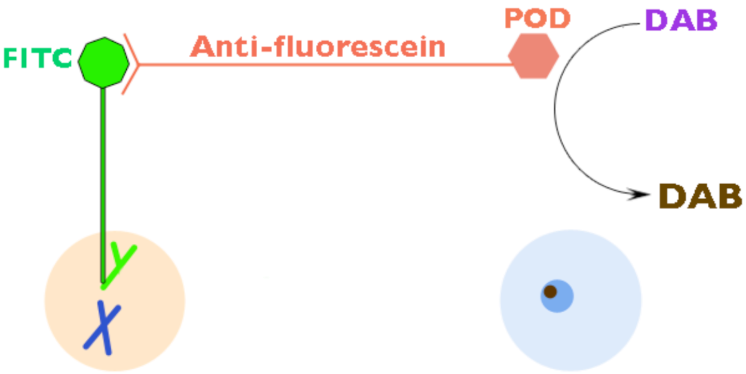

Post ISH, FITC-labelled chromosome probe is bound onto any Y-chromosome present in cells. An anti-fluorescein antibody is applied and binds onto the fluorescein present in the FITC. As this antibody is peroxidase (POD) conjugated, bound antibody can be visualised by the DAB substrate. The POD binds the DAB oxidising it, resulting in a brown coloured insoluble reaction product in the nuclei of cells containing a Y-chromosome.

Figure 2.5: Comparison of Y-chromosome signal and DAB-stained nucleoli

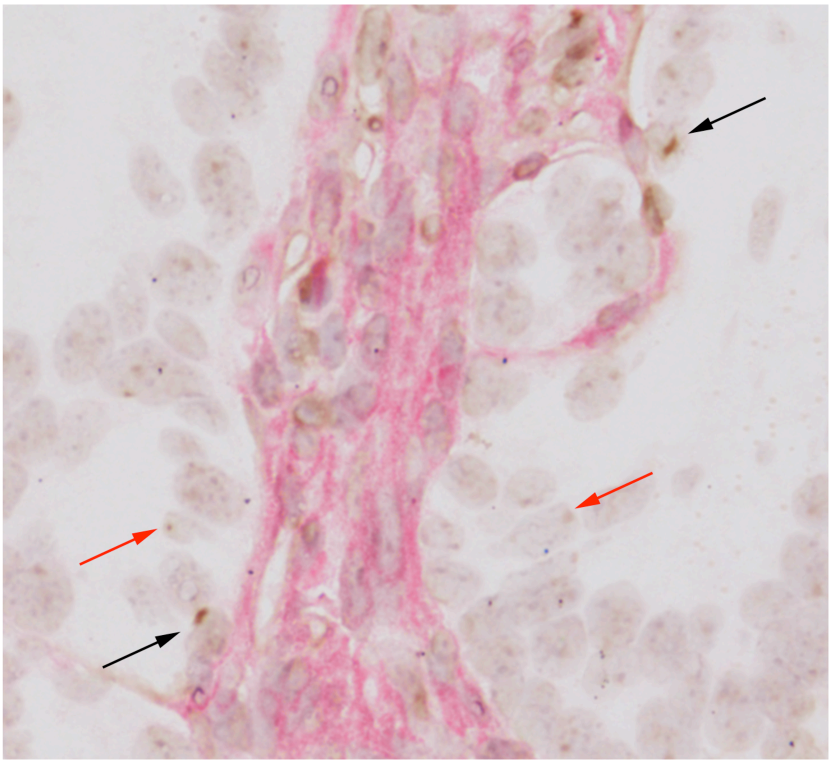

Y-chromosome signal appears as a dark brown rice-shaped signal (black arrows. In comparison, DAB-stained nucleoli (red arrows) appear as smaller dots which are lighter in colour. Image magnification: x40.

Statement on external validation of interpretation and scoring of donor-derived myofibroblasts

External validation of the author's scoring and interpretation of donor-derived myofibroblasts was carried out by Malcolm Alison. The number of donor-derived myofibroblasts (e.g. Y-chromosome positive cells which are ∝-SMA positive [Y$^+$/∝-SMA$^+$]) and the total number of ∝-SMA$^+$ cells (e.g. Y$^+$/∝-SMA$^+$ cells and Y-chromosome negative cells which are ∝-SMA positive [Y$^-$/∝-SMA$^+$]) were counted in five different x20 images by Malcolm Alison and the author. A Wilcoxon signed-rank test was performed determine whether the counted number of donor-derived myofibroblasts and the total number of ∝-SMA$^+$ cells was significantly different between Malcolm Alison and the author (Table 2.7). This non-parametric test was chosen as it is used to compare two related samples.

There was no significant difference in the number of donor-derived myofibroblasts counted (P=0.22). However, there was a significant difference in the counted total number of ∝-SMA$^+$ cells (P=0.04). This finding suggests that the author undercounted the total number of ∝-SMA$^+$ cells, or conversely, that Malcolm Alison overcounted these cells. Analysis of the percentage of BMD-myofibroblasts, derived from dividing the number of Y$^+$/∝-SMA$^+$ cells by the total number of ∝-SMA$^+$ cells, which was used to quantify BMD-myofibroblast engraftment in this study (see Section 2.4.5), revealed that the difference in counted cells amounted to a percentage difference of less than 2%.

Table 2.7: Statistical analysis of scoring and interpretation of donor-derived myofibroblasts

	Number of donor-derived myofibroblasts (Y^{+}/∝-SMA^{+})		**Total number of ∝-SMA^{+} cells**		**Percentage of BMD-myofibroblasts**		**Percentage difference**
	MA	**ALB**	**MA**	**ALB**	**MA**	**ALB**	
Image 1	118	103	4	3	3	3	0
Image 2	107	97	9	9	8	9	1
Image 3	193	131	21	13	11	10	1
Image 4	144	115	9	7	6	6	0
Image 5	100	95	9	10	9	11	2
P value	0.04		0.22				

MA Malcolm Alison; **ALB** Arielle Le Brenne

Statement on method development

This study utilised a ∝-SMA IHC/Y-chromosome ISH method for identifying donor-derived myofibroblasts that had been previously described [78, 92]. Similarly, a previously described method of identifying BMD-epithelial cells using CD45 and *Dolichos biflorus agglutinin* (DBA) IHC/ Y-chromosome ISH was attempted [155]. However the method was unable to be successfully carried out, most likely as it was optimised for tissues fixed in methanol rather than NBF. Therefore in order to investigate the occurrence of BMD-epithelial cells, a dual-staining IHC method was developed with the following aims:

- To identify gastrointestinal epithelial cells using an epithelial cell marker.
- Use anti-lymphocytic markers to exclude possible intraepithelial lymphocytes (IELs).

- To take into account the possibility of macrophages fusing with BMD-epithelial cells as reported to occur in the liver [168], IBA1, an anti-macrophage antibody was included (the marker also identified dendritic cells) was included in the cocktail of anti-lymphocytic antibodies.

I attempted to optimise a dual immunohistochemical staining method for cytokeratin 8 (expressed throughout the GI tract and in GI cancers) and a mixture of lymphocytic, macrophage, dendritic cell (immune cell) markers. However, the Y-chromosome signal could not be visualised (either directly or indirectly) in dual stained sections (Figure 2.6). On the other hand, Y-chromosome signal was easily detected in tissues that had only been stained with cytokeratin 8 or immune cell markers. This discrepancy could have been the result of the extra microwaving steps required for dual IHC causing DNA damage. With this in mind, immune cell marker IHC /Y-chromosome ISH was utilised to identify putative BMD-epithelial cells. The rationale behind this was that of a process-of-elimination. That is, if Y-chromosome positive cells present in the epithelium were negative for lymphocytic, macrophage and dendritic cell markers, what else could they be?

Figure 2.6: Attempted optimisation of epithelial cell IHC/Y-chromosome ISH

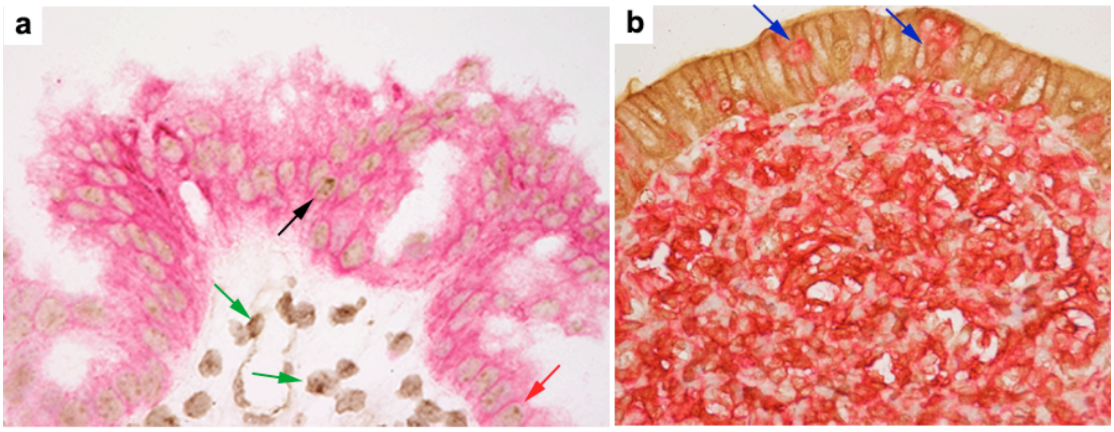

(**a**) Cytokeratin 8 IHC/Y-chromosome ISH on a gastric adenoma of a *Tff1*$^{-/-}$ mouse transplanted with *Tff1*$^{-/-}$ mouse BM at 12 months post BMTX. Epithelial cells were identified by cytokeratin 8 staining (pink). Y-chromosome signal (dark brown nuclear dots) identified donor-derived stromal cells (green arrows) and a putative donor-derived epithelial cell (black arrow). A red arrow points to DAB-stained nucleoli. (**b**) Double IHC for cytokeratin 8 and lymphocytic markers was carried out on Si tissue of a 12 month-old male stock *Tff1*$^{-/-}$ mouse. Epithelial cells were identified by cytokeratin 8 staining (brown staining) and lymphocytic cells are identified with lymphocytic markers (pink staining). Blue arrows point to IELs. Magnifications: **a**; x40, **b**; x20.

2.4.2 α-SMA IHC detection of myofibroblasts

A monoclonal antibody to α-SMA was used to detect myofibroblasts. Details of antibodies and reagents used can be found in Table 2.8. Positive controls for α-SMA IHC were mouse intestinal sections.

Table 2.8: Antibodies and reagents used in α-SMA IHC

Antibody/ reagent	**Details/ Reference number**	**Dilution**	**Incubation time (min)**	**Source**
α-SMA	**MM** IgG2a specific to α-smooth muscle actin. Ref: A2547	1:4000	35	Sigma-Aldrich
Rabbit anti-mouse biotinylated IgG	Ref: E0354	1:250	35	Dako
Normal rabbit serum	Ref: 10510	1:10	30	Invitrogen

MM mouse monoclonal

2.4.3 Immune cell marker IHC detection of putative BMD-epithelial cells

Monoclonal antibodies to CD45R/B220 were used to identify B cells and polyclonal antibodies to CD3 and IBA1 were used to identify donor derived T cells, B cells and macrophages and dendritic cells. Details of antibodies and reagents used can be found in Table 2.9.

Positive controls for the immune cell IHC were mouse spleen and intestinal Peyer's patches. For negative controls, the antibody (with the exception of goat anti-rabbit) was omitted from the primary and secondary antibody layers. Sections required HIER using boiling 0.01M sodium citrate buffer at pH6.0 for 15 minutes on medium power followed quenching in cold running tap water prior to carrying out the protocol. Following goat serum incubation, both CD3 and IBA1 antibodies were applied onto sections and incubated. Following standard washes, CD45R/B220 and goat anti-rabbit biotinylated antibodies were applied onto sections. The protocol then proceeded as described in Section 2.3.1. The resultant staining patterns of immune cell IHC on GI tissue samples can be found in Figure 2.7.

Table 2.9: Antibodies and reagents used in immune cell marker IHC

Antibody/ Reagent	**Details/ Reference number**	**Dilution**	**Incubation time (min)**	**Source**
CD3	**RP** IgG raised against a synthetic peptide corresponding to the intracellular part of the ε-chain of human CD3. Ref: A0452	1:150	60	DAKO
CD45R/ B220	**RM** IgG2a, κ. RA3-6b2 antibody. Specific to an epitope of mouse CD45 conjugated with biotin Ref: 553086	1:200	45	BD Pharmin-gen
IBA1	**RP** IgG raised against a synthetic peptide corresponding to C-terminus of IBA1. Ref: 019-19741	1:200	60	Wako
Goat anti-rabbit biotinylated IgG	Ref: B7389	1:250	45	Sigma
Normal goat serum	G9023	1:10	30	Sigma

RP Rabbit polyclonal; **RM** Rat monoclonal

Figure 2.7: Immune cell marker IHC

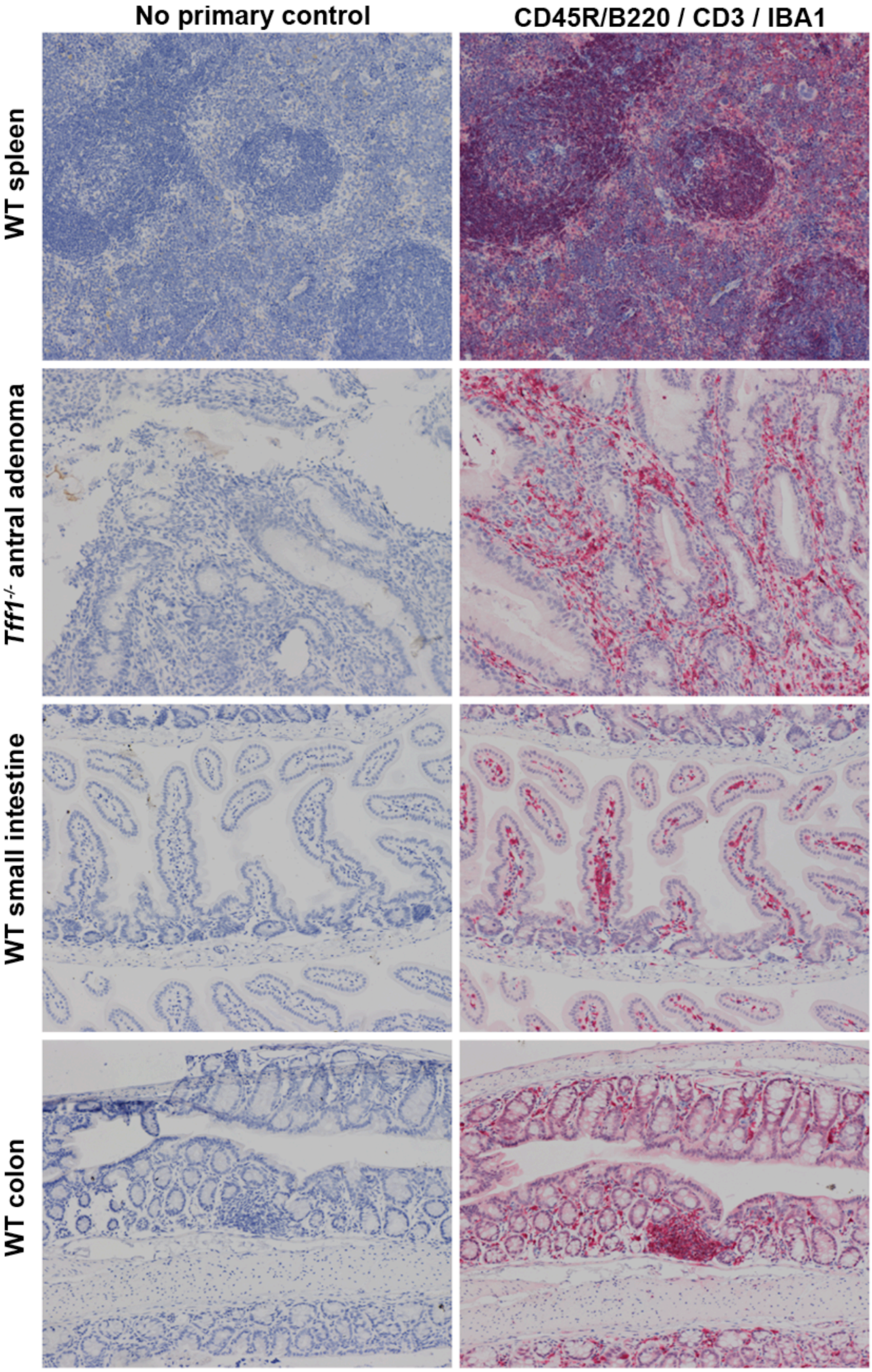

CD45R/B220 /CD3 / IBA1 IHC is shown by red staining. Magnification: x10.

2.4.4 Y-chromosome ISH identification of donor-derived cells

Immediately following IHC phenotyping, sections were placed into 0.1M sodium thiocyanate for 10 minutes at 80°C. However, this step was omitted for sections that had undergone immune cell IHC to avoid loss of tissue integrity. Afterwards, sections were washed in PBS for 5 minutes with 3 changes. Sections were then incubated in freshly made 0.4% pepsin at 37°C for an optimised digestion time determined beforehand.

Pepsin digestion was quenched using 0.1% glycine for 5 minutes and then washed in PBS. Sections were then post-fixed in 4% paraformaldehyde (PFA) for 2 minutes followed by PBS washes. Following this, sections were then dehydrated to absolute alcohol and allowed to air dry. FITC Y-chromosome probe paint was applied to sections and the slides were then coverslipped and sealed with vulcanizing rubber solution. Negative controls were incubated with hybridisation buffer alone. Sections were then denatured at 60°C for 10 minutes and then transferred to a humidified chamber and allowed to incubate overnight at 37°C.

The following morning, the coverslips were carefully removed and slides were washed in 0.5x SSC solution for 5 minutes at 37°C and then rinsed in PBS. Fluorescein labelled chromosomes were detected using sheep anti-fluorescein-peroxidase applied onto sections and incubating them in a humidified chamber for 35 minutes followed by PBS washes. The Y-chromosome was visualised by DAB staining. Sections were washed in distilled water for 5 minutes and then counterstained with light haematoxylin. Afterwards, sections were rinsed, dehydrated, cleared (in xylene) and then mounted in DPX.

Details of reagents and buffers can be found in Table 210.

Table 2.10: Reagents and buffers used in Y-chromosome ISH

Buffer/solution	Details
Sodium thiocyanate	16g sodium thiocyanate (251410; Sigma) dissolved in 200ml water at 80°C
0.4% pepsin	0.8g pepsin (P-6887; Sigma) dissolved in 0.1M HCl for 30 minutes at 37°C
4% paraformaldehyde (PFA)	8g PFA dissolved in 200 ml boiling PBS until clear and immediately cooled on ice.
0.1% glycine	10 PBS tablets (P-4417; Sigma), 2g glycine dissolved in 1l water.

2.4.5 Quantification and statistical analysis

Quantification of donor-derived myofibroblasts

There have been various methods of quantifying donor-derived cell engraftment described in previous BMTx studies. Donor-derived cells have been counted in one high power (e.g. x40) objective field [92] [169], three high power objective fields [78] or 15-25 high power objective fields [170], or within a defined measured area [171]. Some studies would then divide the percentage of donor-derived cells by a correction factor taken from the percentage of Y-chromosome positive cells in a male spleen control to account for loss of part of the nucleus resulting from tissue sectioning [78] [92, 172]. In this study, donor-derived cells were quantified in a 150,000μm^2 area of either lamina propria or epithelium. This area was used as it was the first area to fall within 5% of the standard error of the mean (SEM) following a quantitation of the number of donor-derived myofibroblasts in the lamina propria in different areas of lamina propria (Figure 2.8). This area was used to quantify putative donor-derived epithelial cells as a similar counting optimisation could not be carried out in the epithelium as the number of donor-derived cells was so low.

Figure 2.8: Optimisation of counting donor-derived myofibroblasts within a defined area

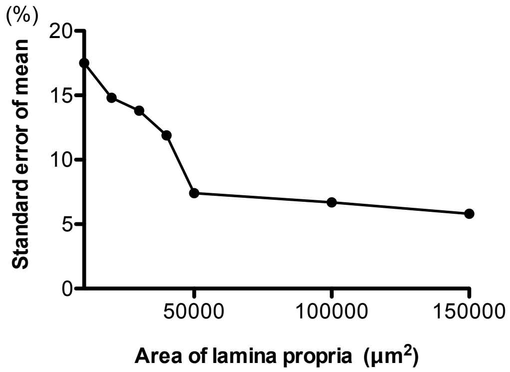

Donor-derived myofibroblasts were counted in three measurements of lamina propria within the gastric adenomas of *Tff1*$^{-/-}$ mice transplanted with *Tff1*$^{-/-}$ mouse BM at 12 months post BMTx (*n*=6). In each measurement, donor-derived myofibroblasts were counted in areas of lamina propria ranging from 10,000 to 150,000μm^2. The standard error of mean (SEM) was calculated for each area and it was found that counting within a 150,000μm^2 area was closest to 5% of SEM.

To quantify donor-derived myofibroblasts or epithelial cells, stained sections were photographed and analysed using a Nikon microscope system. This comprised of a digital camera used to capture images from a connected microscope. The captured images were then viewed and calibrated in μm using the Nikon NIS Elements software. From the calibrated images, a 150,000μm^2

area was measured using the region of interest (ROI) option of the software. Cells were counted using the taxonomy option.

A donor-derived myofibroblast was identified by dark pink α–SMA cytoplasmic staining encircling a nucleus with a dark brown dot representing the Y-chromosome (Y^+). The degree of engraftment was quantified by counting the number of α–SMA^+ cells with and without a Y-chromosome signal within 150,000μm^2 of lamina propria beneath the epithelium. Then the number of Y^+/ α–SMA^+ cells was divided by the total number of α–SMA^+ cells and multiplied by 100 to derive the percentage of donor-derived myofibroblasts.

Quantification of putative donor-derived epithelial cells

A putative donor-derived epithelial cell was identified as being negative for immune cell markers and containing a Y^+ nucleus. The degree of engraftment was quantified by counting the number of epithelial cells with and without a Y chromosome signal in a 150,000μm^2 area of epithelium. The number of Y^+/immune cell marker negative cells was then divided by the total number epithelial cells counted and multiplied by 100 to derive the percentage of putative donor-derived epithelial cells.

Statistical analysis

The statistical significance of differences between measurements was determined by a Student's t-test and differences between groups was determined by ANOVA, both using GraphPad Prisim software (Version 5.0c). Differences resulting in *P* values of less than 0.05 were considered statistically significant.

2.5 Assessment of *Lgr5, Tff2, Tff3* and *Opn* mRNA distribution in normal and diseased mouse tissue using isotopic ISH

Isotopic ISH allows for the specific localisation of mRNA in formalin-fixed paraffin embedded (FFPE) tissues using antisense RNA probes labelled with ^{35}S-UTP. The methods used were based on those previously described by Senior *et al*, (1988), with modifications [173]. As a control to assess mRNA presence, an RNA probe to rat β-actin (*Actb*) control was used in each assay.

Growth of plasmid containing *E. coli* cultures

Labelled RNA probes were produced through *in vitro* transcription of cDNA template linearised from plasmid vectors. *Opn* IMAGE clones arrive pre-transfected into *E. coli* hosts. Plasmids were prepared by growing transfected *E. coli* cultures in the presence of an antibiotic to allow for the selection of plasmid vectors harbouring a gene conferring resistance to that antibiotic.

Agar was melted in a microwave at full power for 5-8 minutes in one-minute bursts. 2ml stock ampicillin (Table 2.11) was added to 400ml cooled agar and gently mixed. The ampicillin-containing agar was poured into the base of 8 clean petri dishes and covered with their lids before being allowed to set for 1 hour at room temperature. Agar plates were then transferred to an incubator set a 37°C and incubated for 1 hour to remove condensation by partially covering the plate with its lid.

Using an aseptic technique, 50μl *E. coli* culture was pipetted onto agar plates and spread by placing 5-10 autoclaved glass beads and gently shaking the covered plates. The beads were then carefully transferred to a new clean labelled plate and the previous plate was covered with its lid to prevent contamination. This process was repeated for the remaining labelled plates. Plates were then inverted (e.g. agar side up) and incubated overnight a 37°C.

The following day, L-Broth was prepared to grow bacterial colonies by adding 4ml stock ampicillin to 400ml L-Broth warmed to 37°C. 10ml was added to a glass screw top tube. Using an aseptic technique, a single colony was picked off using a flame-sterilised wire hoop and transferred to the tube. The tube was then transferred onto a heated rotor plate and incubated for 5 hours at 37°C. Unused L-broth was transferred to a 37°C incubator to maintain temperature. Afterwards, the contents of the tube was tipped into a flask filled with 250ml ampicillin containing L-Broth at 37°C. The flask was stopped with a foam stopper and covered with aluminium before being transferred to a heated rotor plate to be incubated overnight at 37°C. The following day, the entire contents of the flask were tipped into a centrifugation container and centrifuged at 6000g at 4°C for 15 minutes. The supernatant was tipped out and the pellet was re-suspended in 10ml P1 buffer from the QIAGEN plasmid maxi kit. From this step plasmid purification was performed.

Table 2.11: Reagents used for the growth of *E. coli* culture

Reagent	**Details**
Agar	Prepared in-house; CRUK
Ampicillin stock solution	0.2g Ampicillin (Sigma) in 20ml 50% ethanol
Luria Broth (L-Broth)	Prepared in-house; CRUK

Plasmid purification and determination of plasmid DNA concentration

Plasmids were purified from *E. coli* bacteria using a QIAGEN plasmid maxi kit following manufacturer-supplied instructions. Plasmid DNA concentration was determined using UV spectroscopy using a NanoDrop 2000 spectrophometer connected to a computer running the NanoDrop 2000 software programme. 1 μl of purified plasmid DNA sample was pipetted onto the pedestal of the NanoDrop spectrophotometer and the machine arm was closed forming sample column in which the sample was exposed to ultraviolet (UV) light at 260nm and 280nm to measure the concentration of DNA and possible protein contamination (detected at 280nm). The A_{260} and A_{280} measurements, DNA concentration (in ng/μl) and an A_{260}/A_{280} ratio were calculated by the NanoDrop 2000 software programme and printed off and recorded. Samples with a A_{260}/A_{280} ratio less than 1.8 were not used due to protein contamination.

Template preparation from purified plasmids

50μg of plasmid DNA was linearised using restriction enzyme digestion (Table 2.12) for 2 hours in a water bath set at 37°C. A 5μl sample was taken prior to the addition of the restriction enzyme. Following digestion, the sample was mixed and a 5μl sample was taken. 340μl bottom phase phenol chloroform (Invitrogen) was added and the sample was mixed for 30 seconds and then centrifuged for 5 minutes at 16,000 relative centrifugal force (RCF). The top phase was then transferred to a new tube. 330μl bottom phase phenol chloroform was added to the top phase and then mixed and centrifuged as before. The top phase was transferred to a new tube and 320μl bottom phase chloroform isoamyl alcohol (Fluka) was added and then mixed and centrifuged. The top phase was transferred to a new tube where 150μl 7.5M ammonium acetate and 1.125ml absolute ethanol was added. The sample was mixed and allowed to precipitate for 30 minutes. The sample was then centrifuged as before. The supernatant was discarded into a spare tube and kept in case of error. The pellet was washed with 70% alcohol and then the supernatant was removed taking care not to disturb the pellet. The pellet was dried at 37°C until all residual ethanol evaporated. The dried pellet was dissolved in 25μl 10mMTris/0.1mM EDTA and a 1μl sample was taken. The template (dissolved pellet) was then stored at -20°C. To check the quality and quantity of the template, the pre-digest, post-digest, cleaned template, and a 10kb molecular weight ladder were loaded onto a 1% agarose gel and run at 100V for 2 hours

Table 2.12: Regents used for plasmid linearization

Reagent	**Details**
Rat *Actb*	EcoRI restriction enzyme and 10x buffer
Mouse *Lgr5*	HindII restriction enzyme and 10x buffer
Mouse *Opn*	EcoRI restriction enzyme and 10x buffer
Mouse*Tff1*	and 10x buffer
Rat *Tff2*	HindII restriction enzyme and 10x buffer
Rat *Tff3*	EcoRI restriction enzyme and 10x buffer
Plasmid linearization digestion mix	1x restriction enzyme buffer 4-fold restriction enzyme to plasmid DNA concentration water to make up to 350μl

Preparation of ^{35}S labelled RNA probes

^{35}S labelled RNA probes to rat *Tff2*, rat *Actb*, mouse *Opn*, and mouse *Lgr5* were prepared using *in vitro* transcription using linearised DNA templates. For each probe required, DNA template was added to a prepared mastermix containing an appropriate RNA polymerase (Table 2.13). The reaction was mixed well, centrifuged for 10 seconds to ensure thorough mixing and then incubated at 37°C for 60 minutes. The template was then destroyed using 1μl of 1U/μl RNAse-free DNAse I (Boehringer or Promega Quality Grade) to each reaction. Again the tubes were mixed and centrifuged for 10 seconds. The tubes were then incubated at 37°C for 15 minutes. Following the incubation, the reaction was diluted with a mixture of 25μl DTT and 1.5μl ribosomal RNA (10mg/ml). 1μl of diluted reaction was then mixed with 50μl water and 4ml scintillant (Ultima Gold; Perkin Elmer) in scintillation vials.

The remaining diluted reaction was purified using a CHROMA SPIN™-30 column (Biorad) to remove DNA/RNA fragments smaller than 40bp. First, the column was prepared by centrifuging at 1000g or equivalent for 2 minutes at 15°C and discarding the eluate. A new collection tube was prepared containing 4μl RNAsin and 6μl DTT (10 mM) and the column was placed into the tube. The diluted reaction was added to the column and then centrifuged for 4 minutes. The resultant eluate containing the purified probe was stored at -20°C for no more than 48 hours or used immediately.

1μl of probe was added to 50μl water and 4ml scintillant in scintillation vials. This aliquot and the unpurified aliquot were then assessed for the total ^{35}S-UTP incorporation into the probe using a Beckman LS6500 scintillation counter. Successful incorporation of ^{35}S-UTP results in counts for the purified sample of between 40-80% of the counts recorded for the unpurified control and sufficient to give 1x10^6 cpm per slide in the subsequent hybridisation.

To assess probe quality, a sample of purified probe containing 1x10^6 cpm was loaded onto a prepared 6% TBE-urea gel (Invitrogen) and run for 35 minutes at 250V. To calculate the amount needed to load 1x10^6cpm onto the gel, the total cpm of the purified riboprobe was divided by 1x10^6. This amount was then made up to 10μl using 5x loading buffer. The sample was loaded onto the gel alongside a nucleic acid standard ladder (Novagen Perfect RNA Marker Template Mix, 0.1-1Kb).

Once the gel had run, it was then fixed in 10% acetic acid for 10 minutes and then rinsed for a further 10 minutes in tap water. The gel was then gently placed onto blotting paper and covered with cellulose film leaving the edges exposed. The gel and paper were dried at 80°C in a vacuum slab gel dryer (Hoefer GD2000, Amersham Biosciences) for 90 minutes. The cellulose film was removed and under an X-ray safe light in a darkroom, the dried gel and adherent paper were taped to the bottom of an X-ray film cassette (Hypercassette TM, Amersham Life Sciences) and an X-ray film (Hyperfilm MP, Amersham Life Sciences 28906844) was placed on top. The cassette was closed and locked and left to expose for 15 minutes. Afterwards, under an X-ray safe light in a darkroom as before, the cassette was opened and the film was removed and processed using an automatic X-ray film processor (Lungwon Precision Industrial Co. Korea JP-33). A good quality probe is defined as a strong single band of the expected molecular weight (Figure 2.9). On the other hand, probes of poor quality are often a mixture of different molecular weight transcripts (due to either degradation or poor quality template DNA) or have high molecular weight bands due to incomplete plasmid linearization.

Figure 2.9: Purified ^{35}S labelled RNA probes on a 6% TBE-urea gel

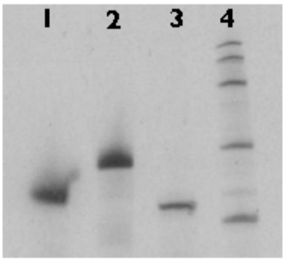

1 million counts of ^{35}S labelled RNA probes to rat *Actb* (**1**), mouse *Opn* (**2**), and rat *Tff2* (**3**) are run alongside a nucleic acid standard ladder (**4**) to give the expected molecular weights of ~250bp, ~500bp, and ~150bp respectively.

Table 2.13: Reagents used for ^{35}S labelled RNA probe production

Reagent	Details	Polymerase
Rat *Actb* template	Rat partial *Actb* cDNA PCR product inserted into the EcoRV site of pBSIIKS Ref: [173] Obtained from Rebecca Chinery	T3-specific bacterial RNA polymerase (P208C; Promega)
Mouse *Lgr5* template	562bp from 5' UTR to exon 5 (UCSC chr10: 114, 915,553-115,024,557, introns excluded). Amplified from polyp cDNA from an *Apc*$^{Min/+}$ mouse, sequenced to exclude mutations. Cloned into pGEM3Z. Ref: [57] Obtained from Stephanie Shier	SP6-specific bacterial RNA polymerase (Promega P108B)
Mouse *Opn* template	IMAGE clone 1382028, anti-sense from mouse *Opn* cloned into pT7T3D-PacI Ref: [78] Obtained from Shigeki Bamba	T3 (as above)
Mouse *Tff1*	Full length 435nt sequence of the mouse *Tff1* gene. Ref:[174] Obtained from Richard Poulsom	T3
Rat *Tff2* template	270 nt sequence of positions 149–419 of the rat *Tff2* gene. Ref: [175] Obtained from Richard Poulsom	T7-specific bacterial RNA polymerase (P207B; Promega)
Rat *Tff3* template	Full length coding region of the rat *Tff3* gene inserted into the EcoRV site of Bluescript II KS+. Ref: [176] Obtained from Richard Poulsom	T3
Mastermix	1X Promega Transcription Buffer 1.5 U/µl Promega 20U/µl RNAsin 11.2mM DTT (D9779; Sigma) 1mM each ATP, GTP, CTP 14µM ^{35}S-UTP (40383; Amersham SJ)+ 5.6mM DTT	-----

Isotopic ISH

For each assay, one section was cut for the rat *Actb* control. There were two sections cut for each probe to be analysed, one for a first (initial) exposure the other for a second exposure. Sectioning was carried out under RNAse-free conditions. 5µm thick serial sections were cut onto water treated with the

RNAse inhibitor diethylpyrocarbonate (DEPC) and collected onto clean SuperFrost slides. Cut sections were stored for a maximum of 24 hours prior to labelling. Reagents used are detailed in Table 2.14.

Sections were de-waxed in xylene, rehydrated through graded alcohols (100%, 80%, 60% and 30%), treated with 0.1% DEPC, and washed in DEPC-treated phosphate-buffered saline (PBS+). Sections were then permeabilised with 20μg/ml proteinase K in PBS for 10 minutes at 37°C, quenched in 2x PBS+ containing 0.2% (w/v) glycine for 5 minutes, and then rinsed in PBS+ for 5 minutes (with two changes). Post-fixation was carried out using freshly prepared 4% PFA for 10 minutes followed by three rinses in PBS+ of 5 minutes each. Sections were then acetylated with litre 0.1M triethanolamine + 2.5 acetic anhydride added and mixed well just before immersing the slides for 10 minutes. Afterwards sections were rinsed three times in PBS+, dehydrated to absolute ethanol/0.1% DEPC and air dried overnight.

The same day, ^{35}S-labelled probes were diluted with enough hybridisation buffer to allow for 1×10^6 cpm in 20μl. Diluted probe was denatured at 80°C for 1 minute and immediately placed on ice. 20μl of probe was then added onto each tissue section and covered with an RNAse-free glass coverslip. Slides were then placed in slide racks in sealed humidified boxes containing paper towels saturated with 1X salts mix/50% formamide and incubated overnight at 55°C to allow hybridisation.

The following day, the slides were removed from boxes in a fume hood. The coverslips were carefully removed and the slides were placed into a clean rack. The rack was then immersed in 50% formamide buffer at 55°C and incubated at 55°C for 3 hours on a rocking platform with 3 evenly spaced changes of 50% formamide buffer. Formamide was then removed with TNE buffer with changes every 5 minutes totalling to 9 washes at 37°C on a rocking platform. RNAse A stock solution was thawed at room temperature and added to 1l TNE buffer at 37°C. The slides were then incubated in RNAse A/TNE for 1 hour at 37°C in order to remove all unbound probe. RNAse contaminated gloves were removed to avoid laboratory contamination. Probe fragments were removed with washes in 2X and then 0.5X SSC for 30 minutes, each at 65°C. Finally, slides were dehydrated through graded alcohols containing 0.3M ammonium acetate (to ensure bound probes remain bound to mRNA) and air dried overnight.

Table 2.14: Reagents used for isotopic *in situ* hybridisation

Reagent	**Details/ Reference number**
Acetic anhydride	Commercially prepared. A6404; Sigma
Ammonium acetate 5M stock	96.25g ammonium acetate (A1542; Sigma) in 1l distilled H_2O. Autoclaved prior to use
Denhardt's solution in 10X salts	Denhardt's solution (D9905; Sigma) comes prepared in 50mg vials containing BSA, Ficoll® and polyvinylpyrollidine. 5ml Denhardt's solution was dissolved in 20ml 10X salts solution to produce a 0.2% solution. Stored at -20°C in 300μl aliquots.
DEPC	Commercially prepared (D9779; Sigma). Stored at 4°C. Add to make 0.1% in treated solutions.
Dextran sulphate	50g dextran sulphate (D8906; Sigma) dissolved in 10ml autoclaved water at 80°C. Stored at -20°C.
0.2M EDTA stock	14.88g EDTA dissolved in 200ml water and adjusted to pH 8.0 with 1.0 M NaOH.
Formamide (deionised) for hybridisation buffer.	20g AG 501-X8 resin (20–50 mesh size fully regenerated; 143-7424;BioRad) dissolved in 400ml formamide (BDH). Stirred overnight in fume hood, filtered to remove resin using a No 1 filter paper (Whatman) and stored at -20°C in 1ml aliquots.
50% Formamide buffer	250ml 10X salt solution added to 1250ml non de-ionised formamide and made to 2.5l with autoclaved DEPC-treated water.
0.2% Glycine	2g glycine (G5516; Sigma) dissolved in 2X PBS. Autoclaved afterwards.
Hybridisation buffer	100µl Denhardt's solution in 10X salts (used to buffer pH and osmolarity), 500µl deionised formamide, 30µl ribosomal RNA (which acts as a probe carrier, 200µl dextran sulphate, 10µl 1M DTT, 160μl DEPC treated water (wetting agent with added RNase inhibiton).
4% PFA	40g PFA dissolved in 1l PBS at 80°C. Cooled on ice once completely dissolved.
10mg/ml Proteinase K stock	200mg Proteinase K (4914; Sigma) added to 20ml TE buffer and stored at -20ºC in 1ml aliquots.
20μg/ml Proteinase K solution for permeabilisation	1ml aliquot of 10mg/ml Proteinase K stock to 500ml TE buffer.
RNAse A	500mg RNAse A (Sigma; R5503g in 100mls 10mm NaAc pH5.2
rRNA	rRNA (R5502; Sigma) comes in 50units (17.7 units/mg) vials. 283µl DEPC-treated water was added directly to the vial to give a 10mg/ml final concentration.

Table 2.14: Reagents used for isotopic *in situ* hybridisation (Contd.)

Reagent	**Details/ Reference number**
10X Salts mix	14.2g Na_2HPO_4 (Fisher) dissolved in 50ml water and adjusted to pH6.8. Then 176.2g NaCl (BDH), followed by 100ml 1M Tris/HCl and 250ml 0.2M EDTA. Mixed and made up to 1l. The concentrations in the final volume were; 3M NaCl, 100mM Na_2HPO_4, 100mM Tris/HCL, 50mM EDTA.
20X stock Standard saline citrate (SSC)	Prepared in-house; CRUK.
TNE buffer	146g NaCl added to 50ml 1M Tris/HCl and 25ml 0.2M EDTA and made to 5l with water and pH adjusted to 7.2-7.6. Stored overnight at 37ºC prior to use.
0.1M Triethanolamine	37.5g triethanolamine (T1502; Sigma) made to 2l with DEPC-treated water. Autoclaved and stored at room temp.
TE buffer for proteinase K permeabilisation	200ml 1M Tris/HCl added to 100ml 0.2M EDTA and made up to 4l with water, pH7.6. Autoclaved and stored at room temperature.

Autoradiography

Principles of autoradiography: this technique facilitates the hybridised labelled probe to be visualised. Post-hybridisation tissue sections are immersed in Ilford K5 scientific emulsion, which contains silver halide crystals dispersed in a gelatine matrix. When the emulsion comes into contact with bound labelled probe, the ionising radiation causes clusters of silver atoms to be produced from the silver halide crystals present in the emulsion. The same process occurs if the emulsion is exposed to light, therefore autoradiography and development are carried out under "safe" 902 (orange) filtered light and slides were left to expose in complete darkness. When the emulsion is developed, the developer reduces the clusters of silver atoms to metallic silver allowing them to be visualised. As the development reaction is pH dependent, it is stopped by immersing the sections in an acidic environment (here 1% acetic acid). Fixation with 10% sodium thiocyanate is carried out to remove any residual silver halide leaving only metallic silver. This is done as any remaining silver halide will eventually turn brown and degrade the image. The sections are then extensively washed in water to remove all the silver thiosulphate complexes present as any remaining complexes will eventually turn brown and degrade the image. Reagents are detailed in Table 2.15.

Method: a glass measuring cylinder containing 25ml water was warmed to 42°C in a water bath. Ilford K5 scientific emulsion was added to give a volume of 40ml, mixed well with a glass rod and allowed to melt for 15 minutes with gentle stirring every 5 minutes. Emulsion was then transferred to a dipping vessel and the consistency of the emulsion was determined by immersing a test slide and assessing coverage and whether air bubbles are present. Slides were dipped in emulsion to completely cover the tissue section and excess on the bottom and back of the slide was wiped off. Then the slides were placed onto pre-cooled metal plates emulsion side up and allowed to dry for 2.5 hours in the dark until the emulsion was set. After drying, slides were placed into plastic slide racks and then into black boxes that were placed into black plastic bags, sealed with tape and incubated at 4°C.

Two exposures were performed at 7 days (initial exposure) and up to 14 days depending on the strength of the first exposure signals compared to the rBAC control. To develop slides, plastic racks containing the slides were immersed in

Kodak D19 developer for 4 minutes. The reaction was stopped by quickly transferring racks into 1% acetic acid for 30 seconds and then rinsed in tap water for 30 seconds. Fixation was carried out in 30% sodium thiosulphate for 8 minutes and then finally slides were washed in running tap water for 1 hour. Sections were then counterstained with Giemsa solution, dehydrated, air dried at 37°C and then mounted in DPX ready for microscopy.

Table 2.15: Reagents used in autoradiography

Reagent	**Details**
Emulsion	Comes in gel form. Stored at 4ºC : Ilford; K5
Kodak D19 developer	Prepared according to manufacturer's instructions (1464593; Kodak)
1% acetic acid	10ml glacial acetic acid dissolved in 10l water
30% sodium thiosulphate	1kg sodium thiosulphate dissolved in 3.3l water
Stock Giemsa counterstain	10ml Giemsa (35086; BDH) added to 20ml acetate buffer*, 50ml acetone and 320ml water
*200mM Acetate buffer	442µl glacial acetic acid, 359mg sodium acetate trihydride, made to 100ml with dH_2O, pH4.2. Stored at 4°C.

Scoring and assessment of mRNA expression

Sections were examined with both transmitted light (bright field) and epi-illumination (dark field) using a Nikon Eclipse ME600 microscope equipped with a digital camera (Q Imaging MicroPublisher 5.0 RTV) by Richard Poulsom and the author. Images were captured using QCapture Pro 6 software (QImaging) and using Photoshop (Adobe, CS3), were processed to remove shadows using methods described by Marty *et al*., (2007) [177].

mRNA labelling was assessed by distribution pattern, frequency and intensity in tissue sections compared to positive rat β-actin controls and negative controls using a semi-quantitative and qualitative scoring system based on several histopathological scoring systems. Each examined area (i.e. small adenomas in *Apc*^{1322T} mice) was given a score for the frequency and a score for intensity of mRNA signal. The two scores were then added together to produce a derived score value between 0 and 6 which were indicated by a symbol score of either a minus or up to three plusses (see Table 2.16).

Table 2.16: Scoring and interpretation of mRNA expression following isotopic ISH

Frequency Score (F)*		**Intensity Score (I)**		**Derived Score (F+I)**	**Symbol Score**
Negative	0	Negative	0	0	-
Focal	1	Weak	1	1-3	+
Patchy	2	Moderate	2	4	++
Diffuse	3	Strong	3	5-6	+++

***Frequency**

Focal	< 25% cells showing expression
Patchy	25-75% cells showing expression
Diffuse	> 75% cells showing expression

The average scores for each examined area was rounded to the nearest whole number.

CHAPTER 3

Results

3.1 Summary of pathological findings

All representative *Tff1*$^{-/-}$ mouse crossover study, *Apc*^{1322T} or *Il10*$^{-/-}$ samples tested negative for *Entamoeba, Giardia, Chilomastix, Tritrichomonas*, antibiotic resistant *Streptococci* or *Lactobacilli*, or any of the *Helicobacter* species.

Representative H&E-stained tissue sections from *Apc*^{1322T}, *Apc*$^{Min/+}$ and *Tff1*$^{-/-}$ mouse crossover study mice were histologically assessed by Nicholas Wright and Gordon Stamp performed a histological assessment of H&E-stained *Il10*$^{-/-}$ mouse tissues. Analysis of *Apc*$^{Min/+}$ and *Apc*^{1322T} mouse tissues revealed pathology consistent with observations by Moser *et al*., (1990) and Pollard *et al*., (2009), respectively (see Figure. 3.1 and 3.2) [49, 55]. The same however cannot be said for analysis of the other two mouse models. For example, *Il10*$^{-/-}$ mice of this study exhibited moderate-to-severe colitis as *Il10*$^{-/-}$ mice of the same genetic background (e.g. BALB/c) and age as described by Berg *et al*., (1996) [76] (Figure 3.3). However, there was not a single instance of colitis progressing to colonic adenocarcinoma by six months of age in the *Il10*$^{-/-}$ mice of this study (e.g. at 5 months post BMTx) as had been reported to occur in 29% of *Il10*$^{-/-}$ mice on a BALB/c background by six months of age by Berg and colleagues (1996) [76]. An important point to note is that micrographs demonstrating enterocolitis and adenocarcinoma in the *Il10*$^{-/-}$ mouse on a BALB/c genetic background are absent from the original Berg *et al*., (1996) publication and in the literature to date, therefore it is difficult to compare the pathology observed in this study with previous studies.

Tff1$^{-/-}$ mice of this study developed antral pyloric adenomas and occasional intramucosal carcinoma similar to that described by Karam *et al*., (2008) [28] and Soutto *et al*., (2011) [33] (Figure 3.4). We also observed similar histology to what has been previously described as adenocarcinoma invading the submucosa by Karam *et al*., (2008) [28] (Figure 3.5). However, in both instances it was identified as herniation by Nicholas Wright due to an absence of a stromal or inflammatory reaction. We also observed a loss of GKN2 protein expression in *Tff1*$^{-/-}$ mouse group adenomas (further discussed in Section A.2 in the Appendix).

There was additional unexpected pathology in the *Tff1*$^{-/-}$ mouse crossover experimental groups. WT mice that had been transplanted with either WT or *Tff1*$^{-/-}$ mouse BM occasionally developed spasmolytic polypeptide expressing metaplasia (SPEM), also known as oxyntic atrophy. SPEM is characterised by fundic glands becoming populated with spasmolytic polypeptide (TFF2) expressing cells and is associated with *Helicobacter* infection [178]. However none of these mice, or any of the mice of this study for that matter, tested positive for *Helicobacter* species. SPEM was initially identified through the loss of parietal and chief cells in fundic glands (Figure 3.6a), both hallmarks of SPEM. Isotopic ISH for *Tff2* mRNA confirmed the presence of SPEM in the fundic glands with parietal cell loss (Figure 3.6b). ABdPAS staining demonstrated a loss of PAS^+ neutral mucins on the mucosal surface and the presence of AB^+ acid mucins in *Tff2* mRNA expressing cells in regions of SPEM, consistent with previous observations by Goldenring *et al.*, 2000 [179] (Figure 3.6b). In addition, SPEM was also associated with decreased GKN2 protein expression (Figure 3.6b), which has been previously observed in experimental models of SPEM [180, 181]. Analysis of cell proliferation revealed that there was no uptake of the BrdU label by *Tff2* mRNA expressing cells in regions of SPEM, suggesting that these cells were not actively proliferating (Figure 3.6b) as has been reported by Nam and Colleagues (2010) [182]. However, unlike the group's observations, we did not observe a modulation of cell proliferation with increased inflammation. Comparison of *Tff2* mRNA expression in the WT groups suggests that WT mice transplanted with $Tff1^{-/-}$ BM had an earlier onset and more severe SPEM than their WT counterparts (Table 3.1). SPEM was not observed in $Tff1^{-/-}$ mouse groups (e.g. transplanted with either WT or $Tff1^{-/-}$ mouse BM), $Apc^{Min/+}$ mouse crossover study mice, Apc^{1322T} or $Il10^{-/-}$ mice.

The development of SPEM in WT mice was the only incidence where our observations suggested BMTx may have played a role in disease outcome. Allogeneic BMTx had no histologically observable effect on any of the $Apc^{Min/+}$ crossover experimental groups. Similarly the transplantation of WT mouse BM into $Tff1^{-/-}$ mice did not ameliorate inflammation or affect tumourigenesis.

Figure 3.1: Comparison of *Apc*$^{Min/+}$ mouse intestinal tumour pathology reviewed by Yamada and Mori (2006) with BMTx'd *Apc*$^{\mathrm{Min/+}}$ mouse pathology

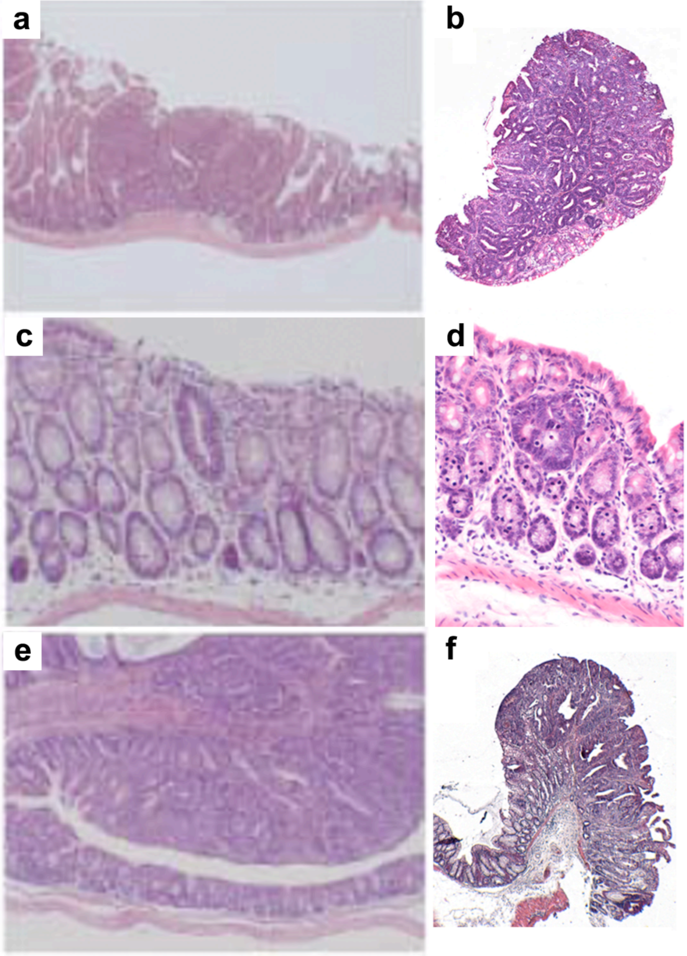

Polyps in the SI (**a**,**b**), occasional microadenomas in the colon (**c**,**d**), and large colonic adenomas (**e**,**f**) were observed in *Apc*$^{Min/+}$ mice reviewed by Yamada *et al*., (2006) [**a**,**c**,**e**] in *Apc*$^{\mathrm{Min/+}}$ mice at 1 month post BMTx from this study (**b**,**d**,**f**). (**a**,**c**,**e**) Images taken from [183]; no magnifications were provided; **b**: x10; **b**, **f**; x1.

Author's note: Images from the original Moser *et al*., (1990) publication were not used as they were of low resolution.

Figure 3.2: Comparison of *Apc*^{1322T} mouse GI pathology described by Pollard *et al*., (2009) with BMTx'd *Apc*^{1322T} mouse pathology

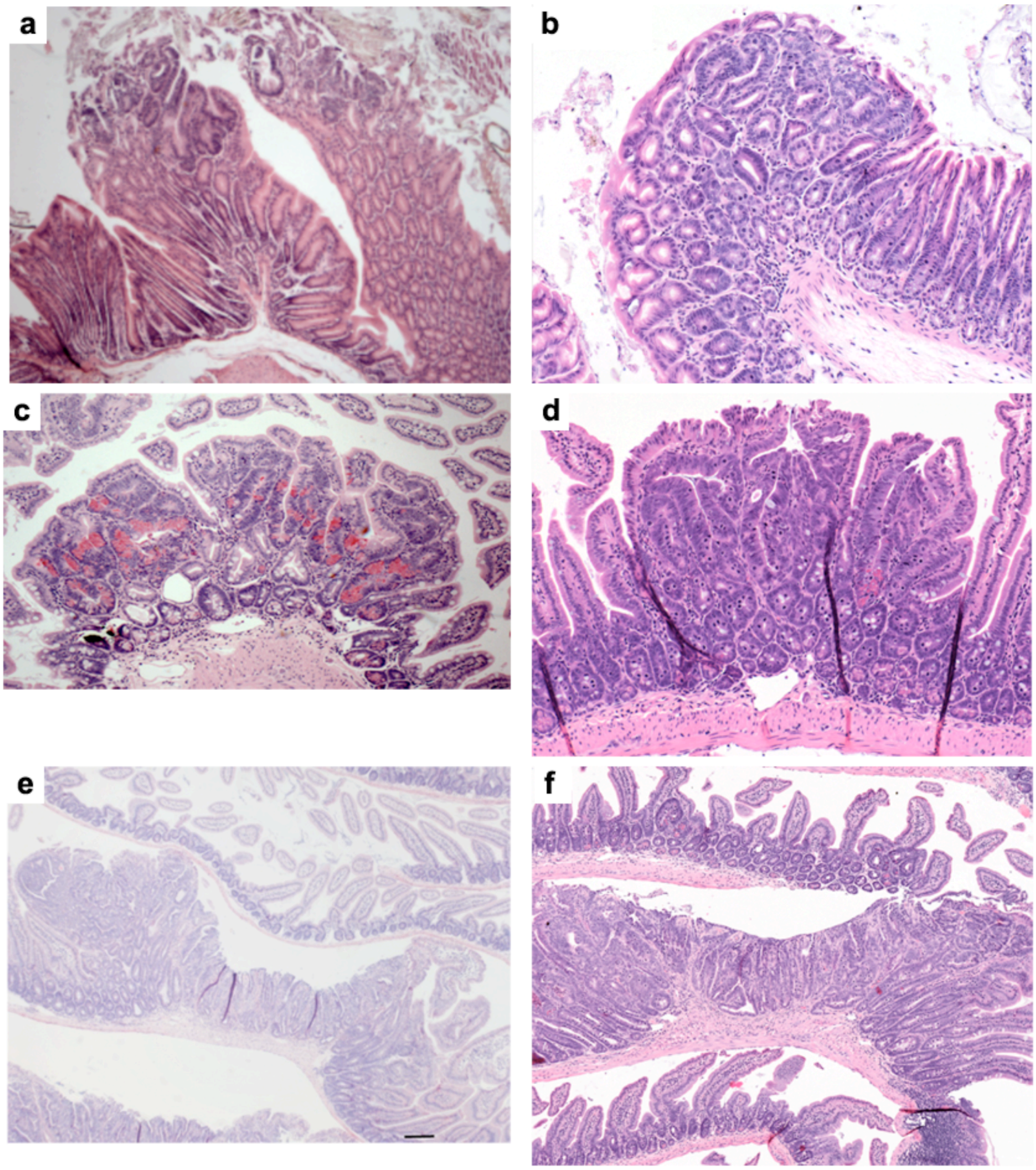

Occasional adenomas in the pyloric antrum (**a**,**b**), small polyps in the SI (**c**,**d**), and large adenomas in the SI (**e**,**f**) were observed in *Apc*^{1322T} mice described by Pollard *et al*., (2009) [**a**,**c**,**e**] and *Apc*^{1322T} mice transplanted with *Apc*^{1322T} mouse bone marrow at 1 month post BMTx from this study (**b**,**d**,**f**). (**a**,**c**) Images taken from [55]; no magnifications were provided; **b**,**d**: x10; (**e**) Image kindly provided by Annabelle Lewis; scale bar=100 μm; **f**: x4.

Figure 3.3: Comparison of *Il10*$^{-/-}$ mouse pathology described by Berg *et al*., (1996) with BMTx'd *Il10*$^{-/-}$ mouse pathology

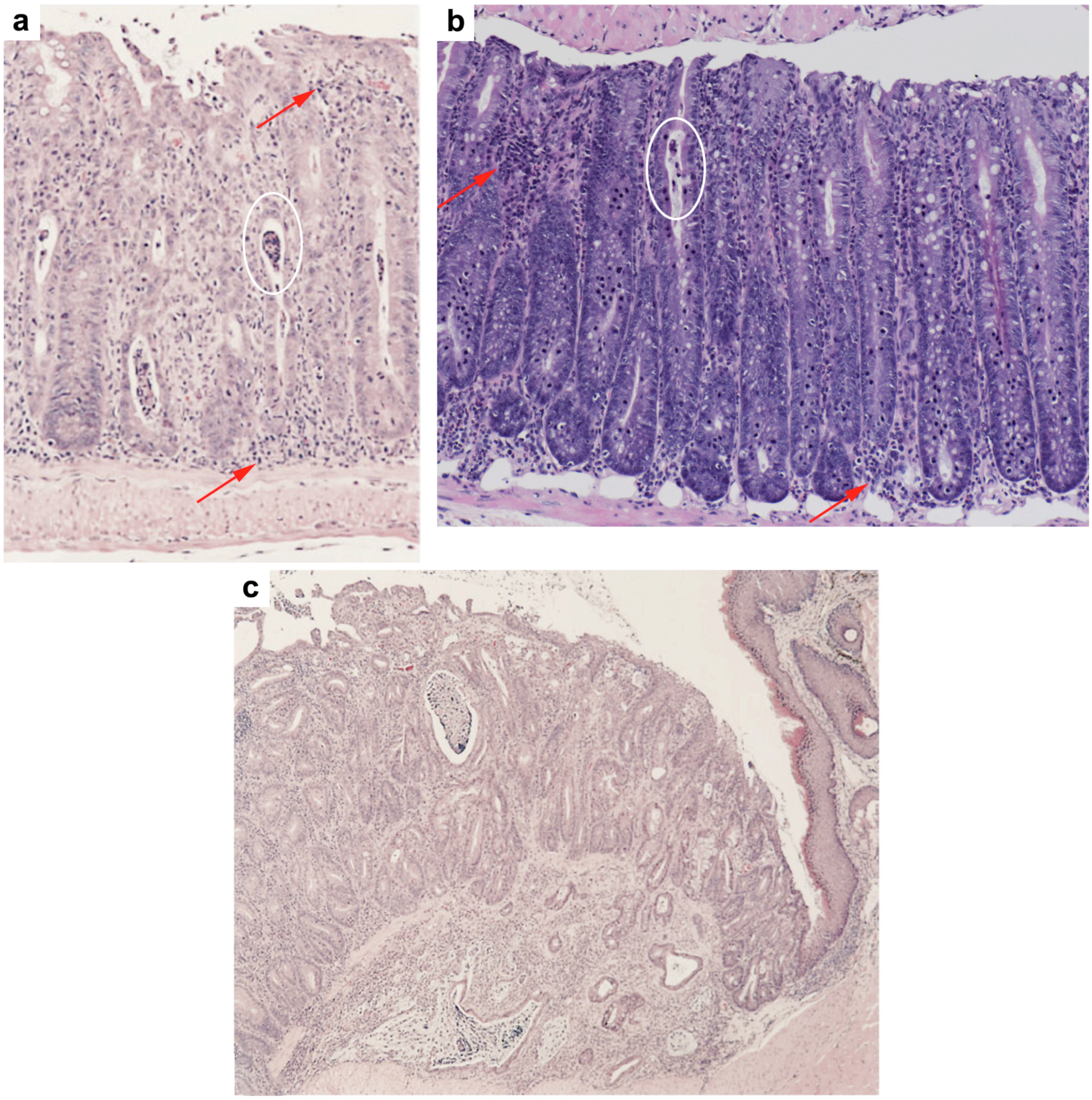

Similar colitis-associated histological features such as crypt hyperplasia, inflammatory infiltrate (red arrows), and crypt abscesses (white circles) were observed in a *Il10*$^{-/-}$ mouse described by Berg *et al*., (1996) [**a**; 140x] with an *Il10*$^{-/-}$ mouse transplanted with *Il10*$^{-/-}$ mouse bone marrow at 5 months post BMTx from this study (**b**; x10) revealed. However, we did not identify colonic adenocarcinoma (**c**; 50x) which has been described in certain strains of the *Il10*$^{-/-}$ mouse. (**a**,**c**) Images taken from [76].

Figure 3.4: Comparison of *Tff1*$^{-/-}$ mouse pathology observed by Karam *et al*., (2008) and Soutto *et al*., (2011) with BMTx'd *Tff1*$^{-/-}$ mouse pathology

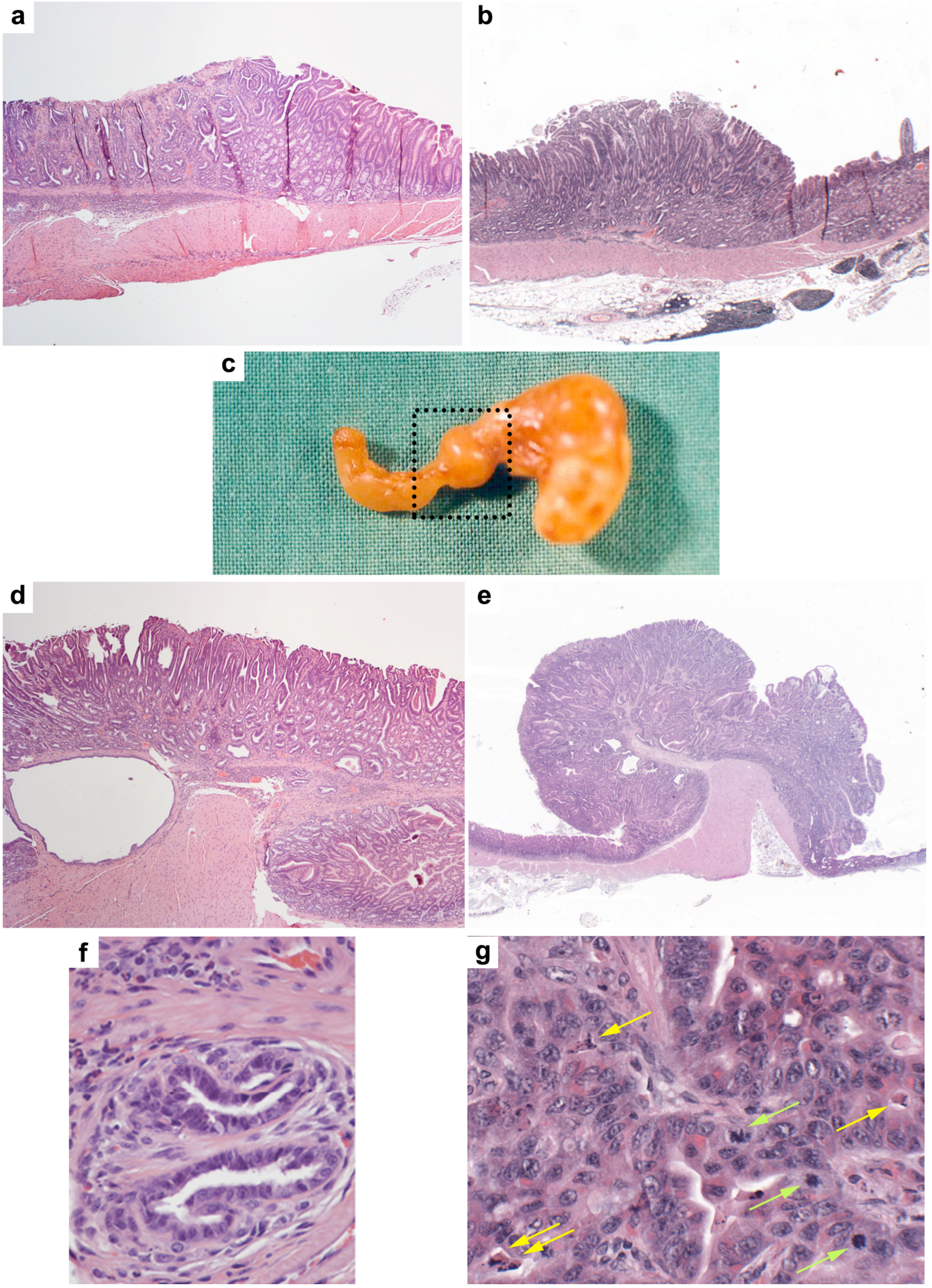

(continued on the next page)

Figure 3.4: Comparison of *Tff1*$^{-/-}$ mouse pathology observed by Karam *et al*., (2008) and Soutto *et al*., (2011) with BMTx'd *Tff1*$^{-/-}$ mouse pathology [continued]

High-grade dysplasia in the antrum was observed in a 6 month old *Tff1*$^{-/-}$ mouse by Soutto *et al*., (2011) (**a**; x4) and a *Tff1*$^{-/-}$ mouse transplanted with *Tff1*$^{-/-}$ mouse BM 6 months post BMTx (8 months of age) in this study (**b**; x4). Antral pyloric adenomas were observed in untransplanted *Tff1*$^{-/-}$ mice at 12 months of age (**c**; no magnification,**d**; x4) and in a *Tff1*$^{-/-}$ mouse transplanted with *Tff1*$^{-/-}$ mouse BM 12 months post BMTx (14 months of age) in this study (**e**; x1). Adenocarcinoma in an untransplanted *Tff1*$^{-/-}$ mouse reported by Soutto *et al*., (2011) [**g**; no magnification given]. Intramucosal carcinoma in a *Tff1*$^{-/-}$ mouse transplanted with *Tff1*$^{-/-}$ mouse BM at 16 months post BMTx (**f**; x40). Mitotic cells are indicated by green arrows. Apoptotic cells are indicated by yellow arrows. (**a**,**d**) Images kindly provided by Wael El-Rifai. (**f**) Image taken from [33]. (**c**) Image kindly provided by Catherine Tomasetto.

Figure 3.5: Comparison of histology in a BMTx'd *Tff1*$^{-/-}$ mouse adenoma with invasive adenocarcinoma described by Karam *et al.,* 2008

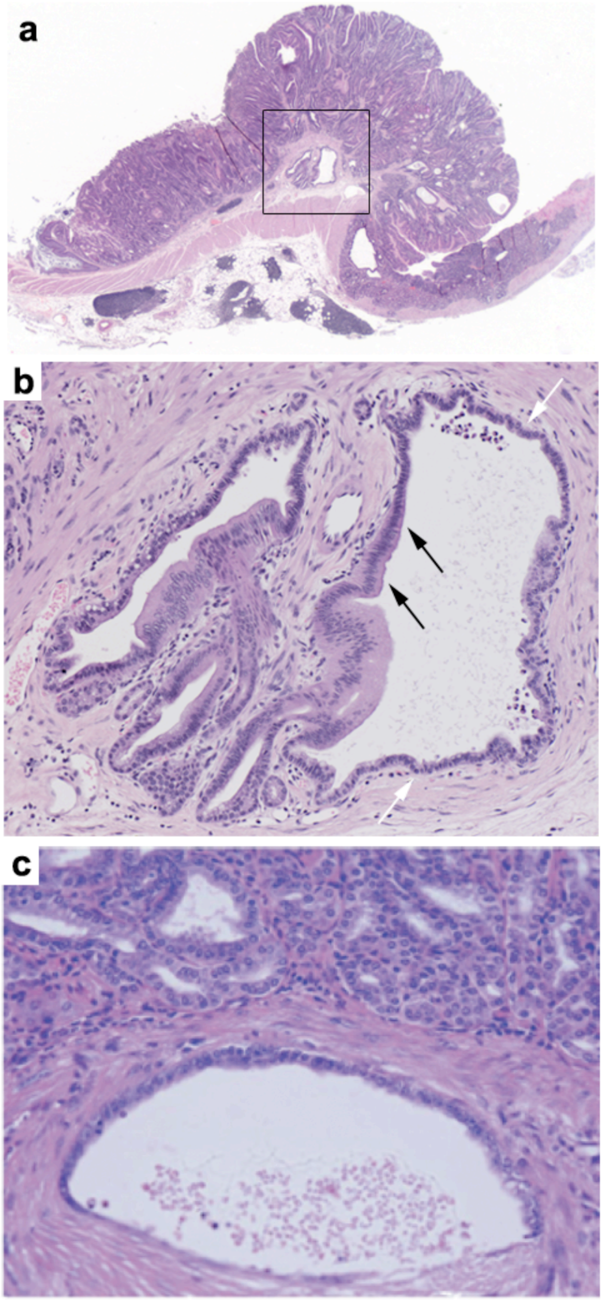

Herniation of adenomatous cells into the submucosa is observed in an antral adenoma of a *Tff1*$^{-/-}$ mouse transplanted with *Tff1*$^{-/-}$ mouse BM at 12 months post BMTx (boxed in **a**; x1). Magnification reveals that neoplastic cells (black arrows) and normal (white arrows) epithelial cells are surrounded by muscle (**b**; x10). There is an absence of stromal and inflammatory reaction. (**c**) Similar pathology was reported as invasive adenocarcinoma in a 12 month old *Tff1*$^{-/-}$ mouse by Karam *et al*., 2008 (no magnification given in the publication) [28].

Figure 3.6a: Comparison of fundic pathology in WT mouse groups at 6 months post BMTx

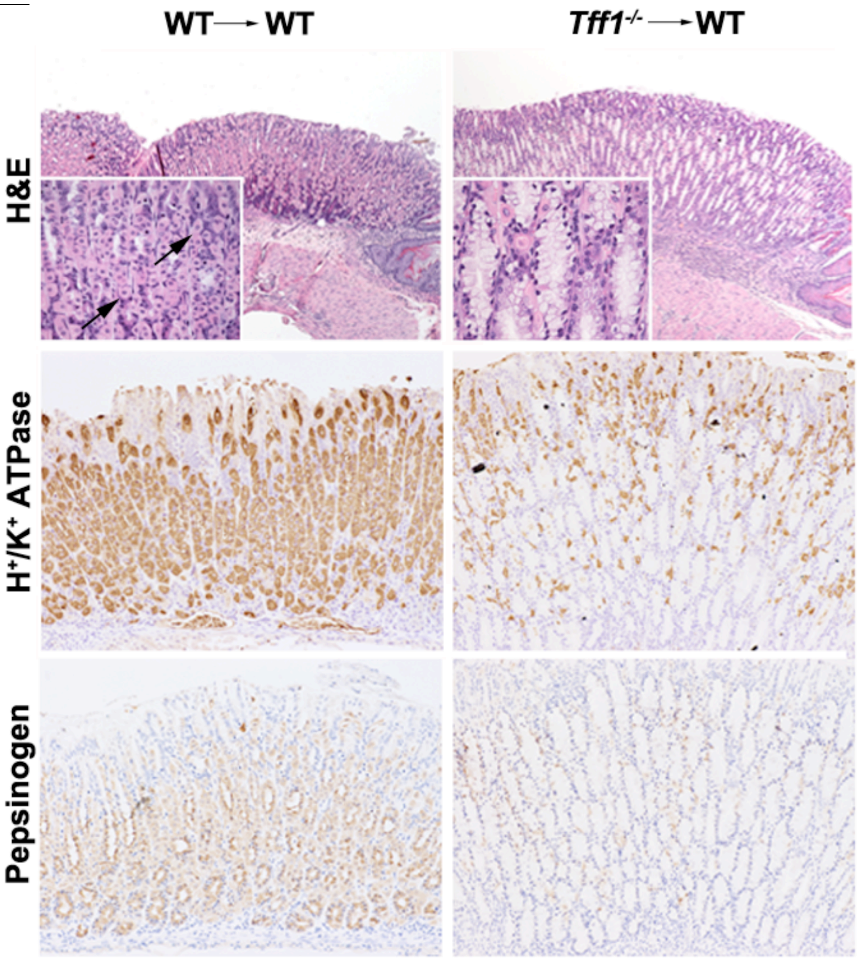

Parietal cells (black arrows) are observed in a WT mouse transplanted with WT mouse BM (WT→WT) at 6 months post BMTx whereas parietal cell loss occurred in a WT mouse transplanted with *Tff1*$^{-/-}$ mouse BM (*Tff1*$^{-/-}$→WT) at 6 months post BMTx (H&E images, x4 with x40 insets). H$^+$/K$^+$ ATPase IHC identifies parietal cells in the WT→WT mouse (brown staining). In areas of parietal cell loss in the *Tff1*$^{-/-}$→WT mouse, H$^+$/K$^+$ ATPase is only expressed by remaining parietal cells. Similarly, IHC for pepsinogen demonstrated chief cells at the base of fundic glands (brown staining) in the WT→WT mouse but no expression in the base of fundic glands affected by parietal cell loss was observed in the *Tff1*$^{-/-}$→WT mouse. Magnification of H$^+$/K$^+$ ATPase and pepsinogen IHC images: x10, → BM transplanted into.

Figure 3.6b: Comparison of fundic pathology in WT mouse groups at 6 months post BMTx

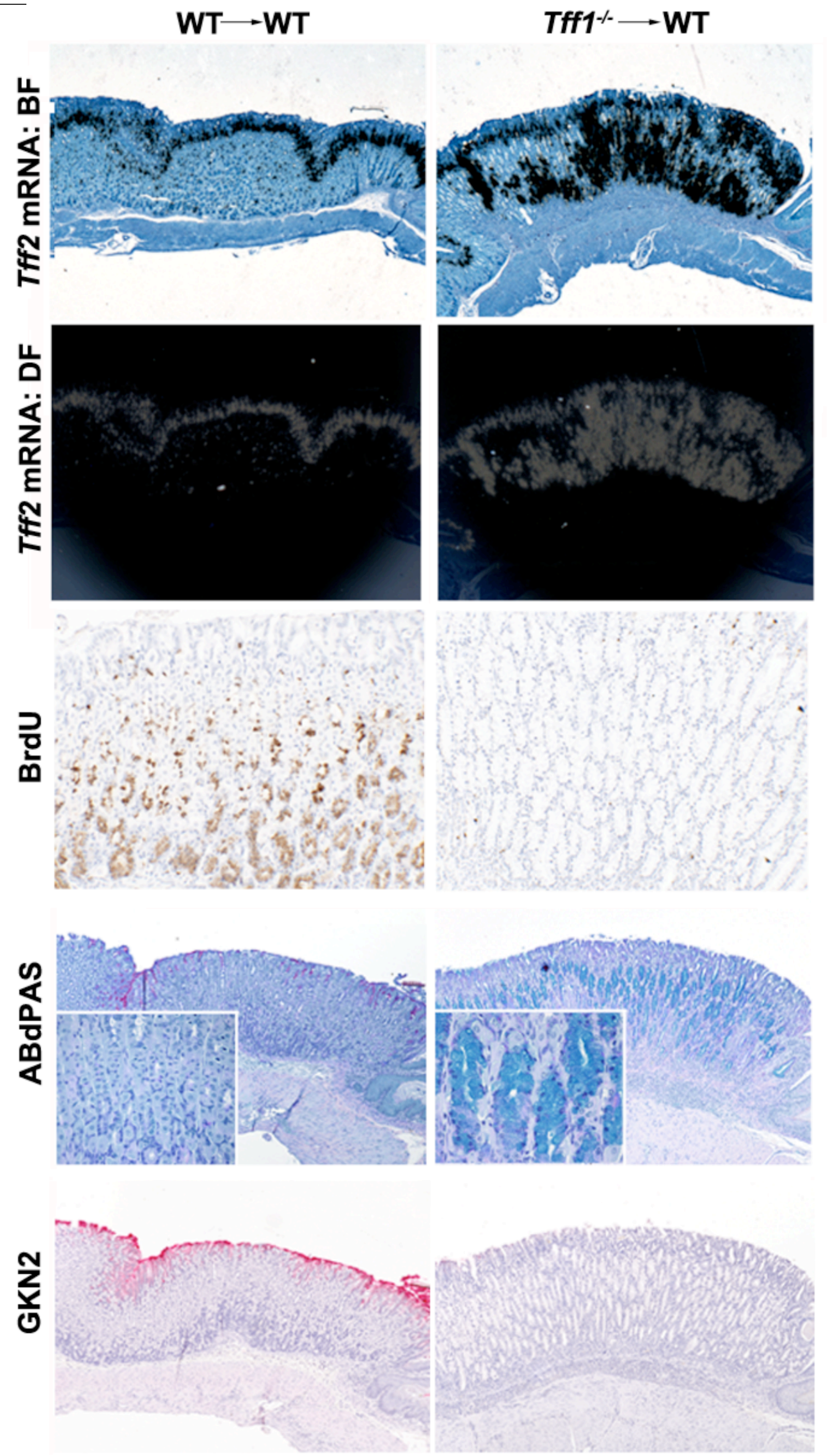

(continued on the next page)

Figure 3.6b: Comparison of fundic pathology in WT mouse groups at 6 months post BMTx (continued)

Isotopic ISH for *Tff2* mRNA demonstrated expression in the mucous neck region of the fundus of the WT→WT mouse. In the *Tff1*$^{-/-}$→WT mouse an abnormal expansion of *Tff2* mRNA expression confirmed SPEM. Comparison of cell proliferation revealed rare BrdU^{+} (brown staining) cells in the region of SPEM of the *Tff1*$^{-/-}$→WT mouse (BrdU images; x10). There were no BrdU^{+}, *Tff2* mRNA expressing cells in regions of SPEM. Analysis of ABdPAS staining demonstrated that the mucous neck region does not stain with either Alcian blue or PAS (magenta) in normal fundus, whereas Alcian blue positive mucous secreting cells (aqua staining in inset) were observed in areas of parietal cell loss in a WT mouse transplanted with *Tff1*$^{-/-}$ mouse BM (*Tff1*$^{-/-}$→WT) at 6 months post BMTx (ABdPAS images, x4 with x40 insets). GKN2 (pink staining) protein are strongly expressed by foveolar cells in the fundus of the WT→WT mouse but decreased in the *Tff1*$^{-/-}$→WT mouse. *Tff2* mRNA expression appears as black grains in bright field images (BF) and white grains in dark field images (DF); *Tff2* mRNA isotopic ISH and GKN2 IHC images: x4,→ BM transplanted into.

Author's note regarding *Apc*$^{\mathrm{Min/+}}$ mouse crossover study tissues

Analysis of BMD-myofibroblast engraftment in *Apc*$^{\mathrm{Min/+}}$ tissues was limited by the following factors:

- Paraffin-embedded tissues from 5 mice were missing from the *Apc*$^{\mathrm{Min/+}}$ mouse BM transplanted into *Apc*$^{Min/+}$ mice group at 2 months post BMTx and the paraffin-embedded tissues from 1 mouse was missing from the WT mouse BM into WT mice group at the same time point. Therefore, we were unable to carry out a statistically valid comparison of engraftment at 1 and 2 months post BMTx.
- For each mouse, a single longitudinal section of SI and colonic tissue was available. Perhaps as result, very few microadenomas, polyps, or adenomas were available to analyse.

Based on these considerations, we did not attempt to draw any conclusions regarding BMD-myofibroblast contribution in *Apc*$^{\mathrm{Min/+}}$ mouse adenomas (see Figure 3.16 in Section 3.4.3), as there were only 3 adenomas available from the entire cross over study to analyse and therefore would not make a statistically valid observation. Instead, we focused on screening all available *Apc*$^{\mathrm{Min/+}}$ mouse crossover study tissue samples for putative BMD-epithelial cells, as well as analysing *Opn* mRNA expression.

3.2 Contribution of BMDCs in neoplastic and inflamed epithelium

This study analysed over 10^5 crypts, villi and gastric glands and their associated 202 adenomas. There was not a single instance of the Y-chromosome signal occurring in either a dividing cell or a putative stem cell position in either glands or crypts, nor were there any doublets or clusters of Y^+ cells in the epithelium which would indicate clonal expansion from an engrafted cell. Instead, putative BMD-epithelial cells were identified as rare events, whose frequencies were unaffected by the presence of inflammation or adenomas.

3.2.1 Putative BMD-epithelial cells were rare, random events

Putative BMD-epithelial cells were identified in the epithelial layer as immune cell marker-negative (e.g. lacking dark pink staining) with a dark brown nuclear dot representing the Y-chromosome. Putative BMD-epithelial cells appeared as single random events (Figure 3.7). Quantification of putative BMD-epithelial cells was carried out in adenomas of *Tff1*$^{-/-}$ mice transplanted with *Tff1*$^{-/-}$ mouse BM, *Apc*^{1322T} mouse SI and *Il10*$^{-/-}$ mouse colon following the methods described in Section 2.4.5. The frequency of putative BMD-epithelial cells averaged ≤ 1.0% in a 150,000μm^2 area of epithelium (Figure 3.8).

The presence of adenomas in the *Apc*^{1322T} mouse SI or areas of inflammation in *Il10*$^{-/-}$ mouse intestines did not significantly increase the percentage of putative epithelial cells derived from BM compared to nearby normal epithelium in these mice.

Figure 3.7: A putative BMD-epithelial cell in a colonic crypt of an *Il10*$^{-/-}$ mouse

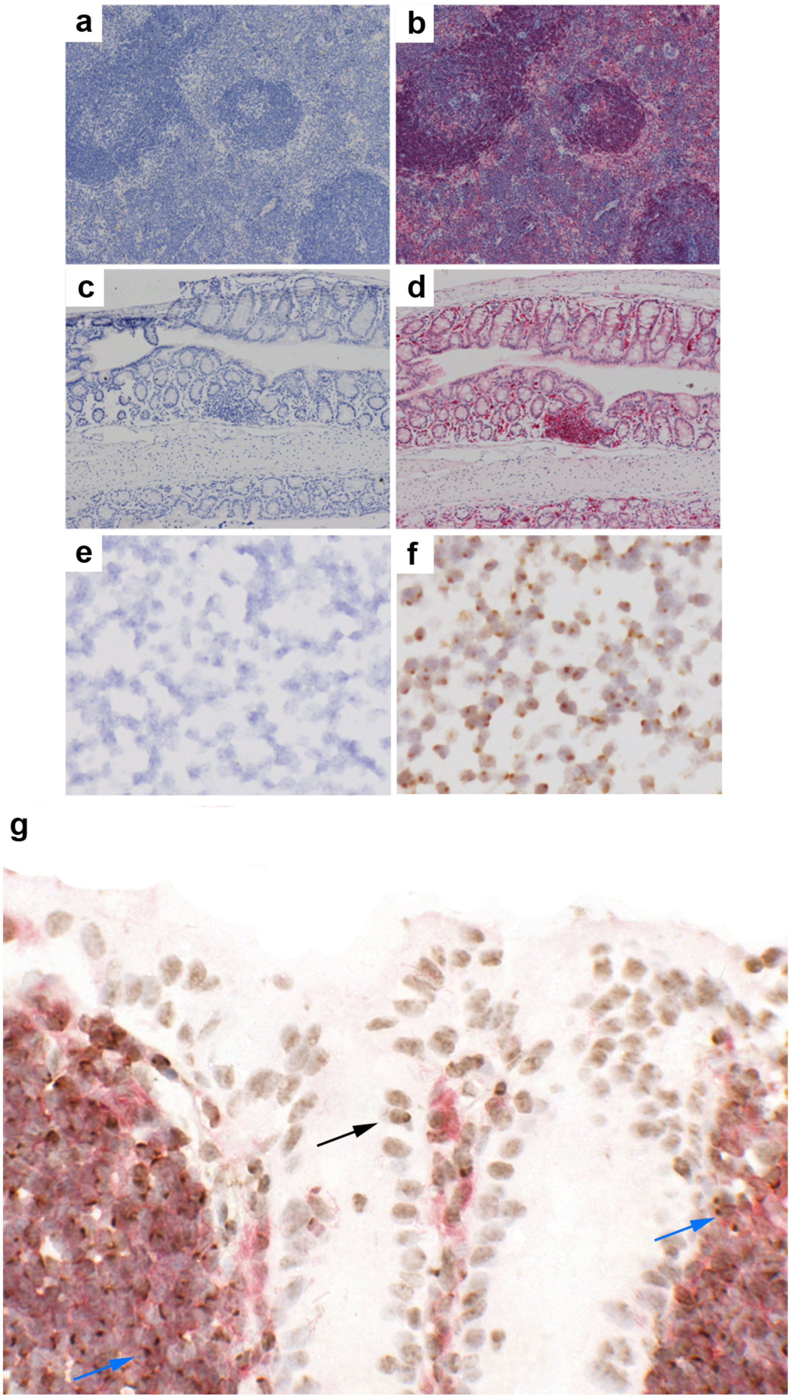

Demonstration of a putative BMD-epithelial cell *via* immune cell marker IHC/Y-chromosome ISH. Negative and positive control splenic (**a**,**b**; x4) and colonic tissue (**c**,**d**: x4) for immune cell marker IHC. Positivity is shown through dark pink staining. Negative and positive control splenic tissue for Y-chromosome ISH (**e**,**f**; x20). Y-chromosome positivity is show by a dark brown nuclear spot. Immune cell IHC/Y-chromosome ISH carried out on inflamed colonic tissue of an *Il10*$^{-/-}$ mouse transplanted with *Il10*$^{-/-}$ mouse BM at 5 months post BMTx (**g**; x60) demonstrates a rare putative BMD-epithelial cell (black arrow) as shown by an absence of immune cell marker staining and Y-chromosome positivity. Blue arrows point to donor-derived immune cells.

Figure 3.8: Comparison of putative BMD-epithelial cell engraftment

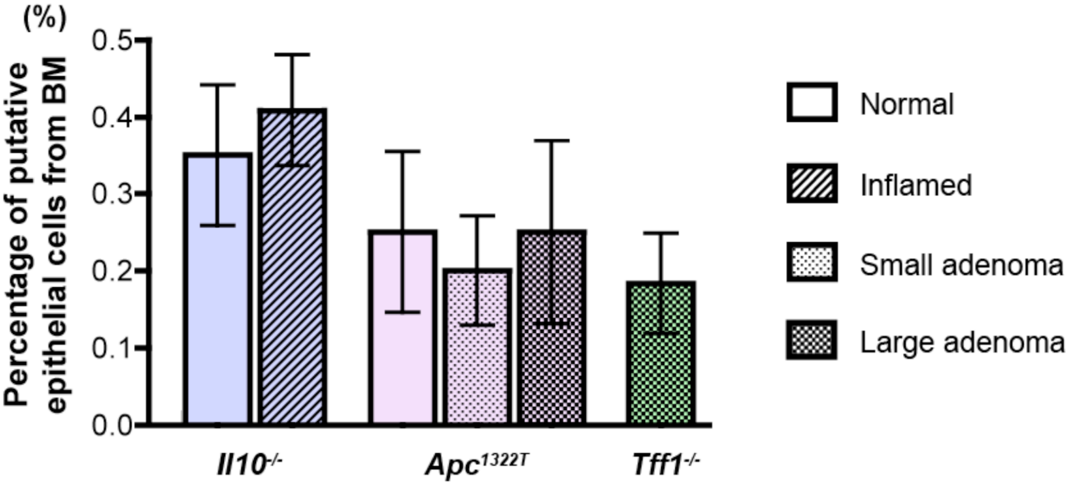

The percentage of putative epithelial cells from BM in 150,000 μm^2 was analysed in normal and inflamed colonic mucosa of *Il10*$^{-/-}$ mice transplanted with *Il10*$^{-/-}$ mouse BM at 3 and 5 months post BMTx (data for the two time points combined), normal and adenomatous SI of *Apc*^{1322T} mice transplanted with *Apc*^{1322T} mouse BM at 1 month post BMTx, and the gastric adenomas of *Tff1*$^{-/-}$ *mice* transplanted with *Tff1*$^{-/-}$ mouse BM at 12 months post BMTx. Mean±SEM. *Il10*$^{-/-}$ *mice*$^{-}$: *n*=12, *Apc*^{1322T} mice: *n*=4, *Tff1*$^{-/-}$ mice*:* *n*=6. All comparisons non significant.

3.3 Analysis of *Lgr5* mRNA expression in neoplastic and inflamed epithelium

We examined the role of altered Wnt signalling in tumourigenesis and inflammation by performing *Lgr5* mRNA isotopic ISH on *Apc*^{1322T} mice, *Tff1*$^{-/-,}$ mouse crossover experimental groups, and *Il10*$^{-/-}$ mouse tissues. We were unable to carry out analysis on *Apc*$^{Min/+}$ mouse crossover study tissues due to the isotopic ISH service closing down. Nevertheless, we observed increased *Lgr5* mRNA expression in adenomas of *Apc*^{1322T} mice as previously described by

Lewis *et al.*, (2010) [57]. In comparison, *Lgr5* mRNA expression in *Tff1*$^{-/-}$ mouse adenomas (either transplanted with WT or *Tff1*$^{-/-}$ mouse BM) was not dissimilar to expression in WT antrum, indicating that any stem cell activity in *Tff1*$^{-/-}$ mouse adenomas was unlikely to be maintained by *Lgr5*-associated Wnt signalling. In addition, *Lgr5* mRNA expression was not observed in SPEM tissues, suggesting that SPEM lineages are also not maintained by aberrant Wnt signalling.

In *Il10*$^{-/-}$ mouse tissues, we were unable to detect *Lgr5* mRNA expression. This was unlikely to be a reflection of experimental error, mRNA degradation or poor tissue quality, as the *Actb* mRNA control was positive and other isotopic ISH assays worked on these tissues. Therefore, one possibility is that, as *Lgr5*-expressing cells have been rarely observed at the base of colonic crypts in Lgr5 cell lineage tracing experiments [184], the mRNA signal from a few cells in *Il10*$^{-/-}$ mouse colonic crypts (which are devoid of an *Apc* mutation that would have caused increased *Lgr5* expression) may have been too feint to be detected.

3.3.1 *Lgr5* mRNA was strongly expressed in adenomatous SI of *Apc*^{1322T} mice

Lgr5 mRNA expression was observed at the crypt base in normal SI of *Apc*^{1322T} mice. Strong *Lgr5* mRNA expression occurred in adenomatous SI as previously described by Lewis *et al.*, 2010 [57] (Figure 3.9). We were unable to analyse *Lgr5* mRNA in *Apc*^{1322T} mouse colons due to time constraints.

Figure 3.9: *Lgr5* mRNA expression in *Apc*^{1322T} mouse SI

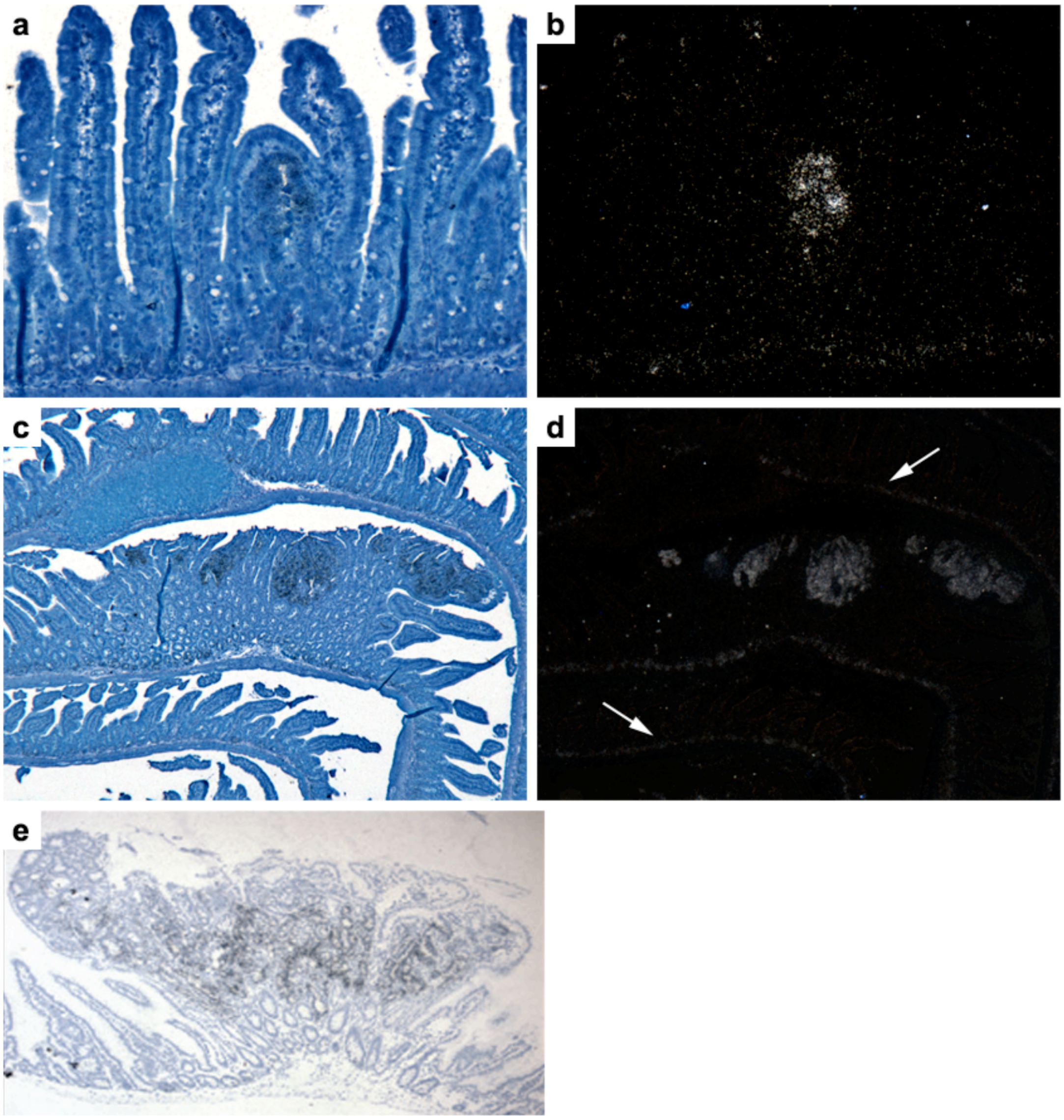

Lgr5 mRNA was strongly expressed in small (**a**,**b**; x4) and large SI adenomas (**c**,**d**; x4) and bottom) in *Apc*^{1322T} mouse transplanted with *Apc*^{1322T} mouse BM at 1 month post BMTx. Strong *Lgr5* mRNA expression in large SI adenomas was also reported by Lewis *et al*., 2010 [57] (**e**; no magnification given). In normal SI expression occurred along crypt bases (white arrows). *Lgr5* mRNA expression appears as black grains in bright field images (**a**,**c**,**e**) and white grains in dark field images (**b**,**d**). Magnification: x4.

3.3.2 Upregulated *Lgr5* mRNA expression was not observed in *Tff1*$^{-/-}$ mouse adenomas

Compared to WT mouse group tissues, *Tff1*$^{-/-}$ mouse group adenomas had an increase in BrdU^{+} cells suggesting increased cell proliferation. In addition, ABdPAS staining demonstrated that *Tff1*$^{-/-}$ mouse adenomas were composed of a heterogeneous mucin cell population (Figure 3.10). In addition, an expansion of *Tff2* mRNA (Figure 3.10) further demonstrated the heterogeneity of *Tff1*$^{-/-}$ mouse adenoma cell population. These findings supported Karam and colleagues (2008) observation of a highly proliferative cell population in *Tff1*$^{-/-}$ mouse adenomas that expressed all cell lineages [28]. However, ISH for *Lgr5* mRNA (Figure 3.11) demonstrated that expression was limited to the base of the adenomatous pyloric glands, similar to basal expression in non-neoplastic pyloric glands. Collectively these findings suggest that whilst *Tff1*$^{-/-}$ mouse adenomas have highly proliferative, heterogeneous cell populations cell populations, these cells do not have upregulated *Lgr5* mRNA expression.

3.3.3 Upregulated *Lgr5* mRNA expression was not observed in SPEM tissues

We investigated whether *Lgr5* expression is altered during SPEM by analyzing *Lgr5* mRNA expression *via* isotopic ISH. As with normal fundic glands we were unable to detect *Lgr5* mRNA in SPEM (data not shown). This suggests that upregulation of *Lgr5* gene expression (and therefore Wnt signaling) is unlikely in SPEM. However, this observation does not rule out the possibility SPEM cell lineages originating from the *Lgr5*$^{+}$ stem cells at the base of oxyntic glands that lost *Lgr5* expression due to differentiation.

Figure 3.10: Comparison of BrdU positivity, ABdPAS staining, and *Tff2* mRNA expression in WT antrum and *Tff1*$^{-/-}$ mouse antral adenomas

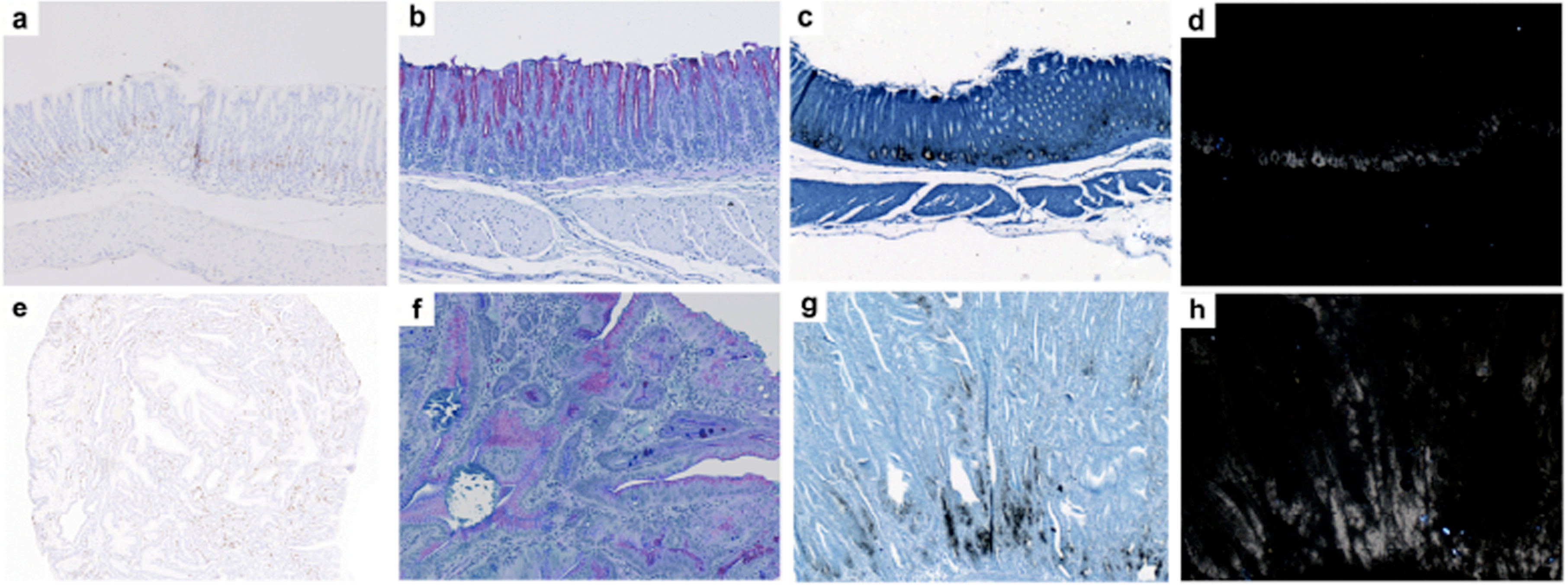

BrdU$^+$ cells appear at the base of pyloric glands in WT mouse pyloric antrum (**a**; x10) whereas, they appear scattered throughout a *Tff1*$^{-/-}$ mouse adenoma (**e**; x4). Comparison of ABdPAS staining in WT mouse antrum (**b**; x10) and *Tff1*$^{-/-}$ mouse adenoma (**f**; x10) reveal that the latter is composed of a mixture of Alcian blue$^+$ and PAS$^+$ mucous-secreting cells. Isotopic ISH for *Tff2* mRNA expression showed basal expression in the normal antrum of a WT mouse (**c**,**d**; x10) and diffuse expression in a *Tff1*$^{-/-}$ mouse adenoma (**g**,**h**; x10). *Tff2* mRNA expression appears as black grains in bright field images (**c**,**g**) and white grains in dark field images (**d**,**h**).

Figure 3.11: Comparison of *Lgr5* mRNA expression in WT mouse antrum and *Tff1*$^{-/-}$ mouse antral adenomas

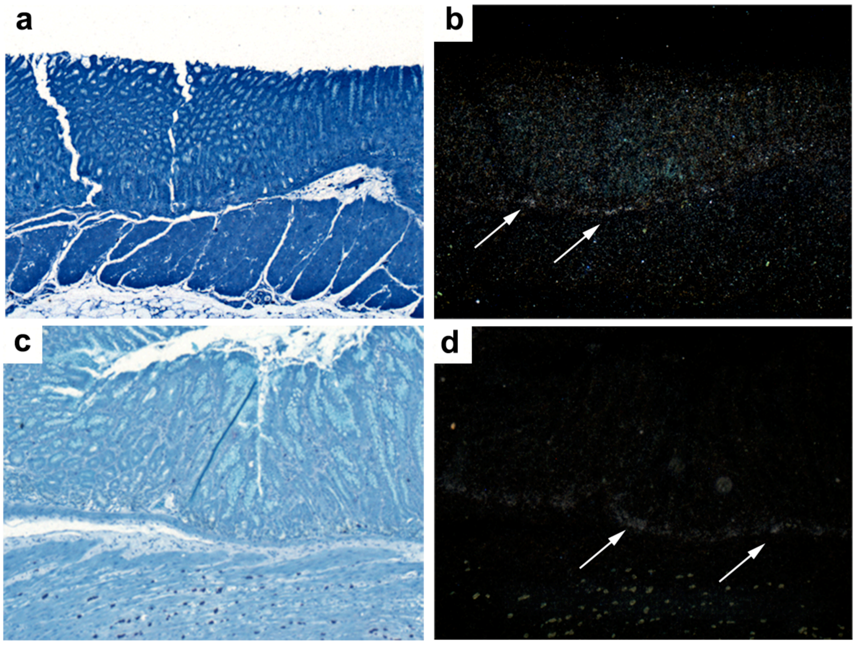

In both WT mouse antrum (**a**,**b**; x10) and *Tff1*$^{-/-}$ mouse adenomas (**c**,**d**; x10), *Lgr5* mRNA expression was limited to the base of antral glands (shown in white arrows) [**a**,**c**: bright field images; **b**,**d**: dark field images].

3.4 Contribution of BMD-myofibroblasts to tumour stroma

BMD-immune cells and myofibroblasts were observed in the tissue stroma of all mouse models. In contrast, BMD-pericytes and endothelial cells were rare and, most often the case, not observed at all. Therefore, only BMD-myofibroblasts were quantified in the stroma.

BMD-myofibroblasts were identified in the stroma by dark pink α–SMA cytoplasmic staining encircling a nucleus with a dark brown dot representing the Y-chromosome (Y^{+}). BMD-myofibroblasts were quantified using the methods described in Section 2.4.5. In brief, the number of α-SMA^{+} cells with and without a Y chromosome signal was counted within a 150,000μm^{2} area of lamina propria beneath the epithelium. Then the number of Y$^+$/α-SMA$^+$ cells was divided by the total number α-SMA$^+$ cells and multiplied by 100 to calculate the percentage of donor-derived myofibroblasts. We demonstrated that fibrosis and tumour burden correlated with a significant increase in BMD-myofibroblasts in *Tff1*$^{-/-}$ and *Apc*^{1322T} mouse tissues.

3.4.1 BMD-myofibroblasts contributed to the desmoplastic response in *Tff1*$^{-/-}$ mouse antral pyloric adenomas

For simplicity, *Tff1*$^{-/-}$ mouse crossover study experimental groups are referred to by shorthand symbols detailed in Table 3.1 in this section.

Table 3.1: Details of shorthand symbols used for *Tff1*$^{-/-}$ mouse crossover study experimental groups in Section 3.4.1

Experimental group	**Code**	**Details of BMTx experiment**
Tff1$^{-/-}$ mouse groups	*Tff1*$^{-/-}$→*Tff1*$^{-/-}$	*Tff1*$^{-/-}$ mouse BM transplanted into *Tff1*$^{-/-}$ mice
	WT→*Tff1*$^{-/-}$	WT mouse BM transplanted into *Tff1*$^{-/-}$ mice
WT mouse groups	WT→WT	WT mouse BM transplanted into WT mice
	Tff1$^{-/-}$→WT	*Tff1*$^{-/-}$ mouse BM transplanted into WT mice

Tff1$^{-/-}$ mouse groups (e.g. *Tff1*$^{-/-}$→*Tff1*$^{-/-}$ and WT→*Tff1*$^{-/-}$) exhibited antral dysplasia at 6 month post BMTx which progressed to adenomas observed at the 12 month and 16 month post BMTx time points. Desmoplasia was observed in *Tff1*$^{-/-}$ mouse adenomas at 12 and 16 months post BMTx. This was identified by increased α-SMA IHC staining, BMD-myofibroblasts, and an increased

presence of BMD inflammatory cells compared to the stroma of dysplastic or normal pyloric antrum of *Tff1*$^{-/-}$ mice at 6 months post BMTx (Figure 3.12). It was noted that normal or SPEM WT mice from the WT groups (e.g. WT→WT and *Tff1*$^{-/-}$→WT) did not develop desmoplasia.

Consistently observed was increased desmoplasia at the top (e.g. towards the lumen) of adenomas. One-way ANOVA demonstrated that the number of Y^+/α-SMA^+ cells and the percentage of gastric SEMFs derived from BM significantly increased at the tops of adenomas compared to the middle or base (Figure 3.13). However, the total number of α-SMA^+ cells in each region was not significantly different. Following the observation of geographical location changes in BMD-gastric SEMF numbers, quantification in *Tff1*$^{-/-}$ mouse gastric adenomas involved counting a 50,000 μm^2 area at the base, middle and top of the adenomatous stroma (totalling 150,000 μm^2) to get an overall assessment of BMD-myofibroblast engraftment in *Tff1*$^{-/-}$ mouse adenomas.

Based on this, BM contributed, on average, 11% of the total number of SEMFs in a 150,000 μm^2 area of adenomatous stroma in the *Tff1*$^{-/-}$ mouse groups at 12 and 16 months post BMTx. In comparison, BM contribution averaged 4% of the total number of SEMFs in the same area of normal stroma in the WT mouse groups at any time point post BMTx (e.g. 6, 12, or 16 months). Engraftment of BMD-myofibroblasts with time after BMTx was analysed using one-way ANOVA with a Bonferroni multiple comparison test. There was a significant increase both in the percentage of gastric SEMFs derived from BM and the number of Y^+/α-SMA^+ cells in the adenomas of *Tff1*$^{-/-}$ mouse groups at 12 and 16 months post BMTx compared to normal antral tissue near dysplastic antrum of the *Tff1*$^{-/-}$ mouse groups at 6 months post BMTx (Figure 3.14).

However, there was no significant difference in the percentage of gastric SEMFs derived from BM or the number of Y^+/α-SMA^+ cells in *Tff1*$^{-/-}$ mouse group adenomas between 12 and 16 months post BMTx. These observations suggest a plateau in BMD-myofibroblast engraftment, reminiscent of the shorter-term experimental data of Lee *et al*., (2011) in the GI tract of RAG2 colitic mice [155]. This could be a consequence of *Tff1*$^{-/-}$ mouse adenomas remaining relatively the same size at 16 months post BMTx as at the 12 month post BMTx time point (see Figure 3.24a and Figure 3.24b in Section 3.5.1). There is evidence that engrafted BMD-myofibroblasts can proliferate *in situ*. Brittan and colleagues (2005) demonstrated that BMD-keratinocytes are able to proliferate *in vivo* and *in vitro* [185], however the plateauing of BMD-myofibroblast numbers in my experiments suggest their proliferation is not a significant factor.

Analysis of the total number of α-SMA^+ cells using a Bonferroni multiple comparison test revealed that overall there was no significant difference between experimental groups or with time (Figure 3.15). However, there was a single instance where a significant difference was observed (Figure 3.15). In context with the other groups and time points however, there appears to be no biological significance to this difference, as the levels of engraftment were broadly constant across groups and time.

3.4.1.1 Allogeneic BMTx had no observable effect on BMD-myofibroblast engraftment in WT and *Tff1*$^{-/-}$ mouse groups

Comparison of the allogeneic and syngeneic BMTx'd groups using a Bonferroni multiple comparison test, revealed that there was no significant difference in the percentage of BMD- gastric SEMFs, the number of Y^+/α-SMA$^+$ or the total number of α-SMA$^+$ cells in the WT and *Tff1*$^{-/-}$ mouse groups at any of the time points.

Figure 3.12: Development of desmoplasia and presence of BMD-myofibroblasts in antral pyloric adenomas in BMTx'd *Tff1*$^{-/-}$ mice

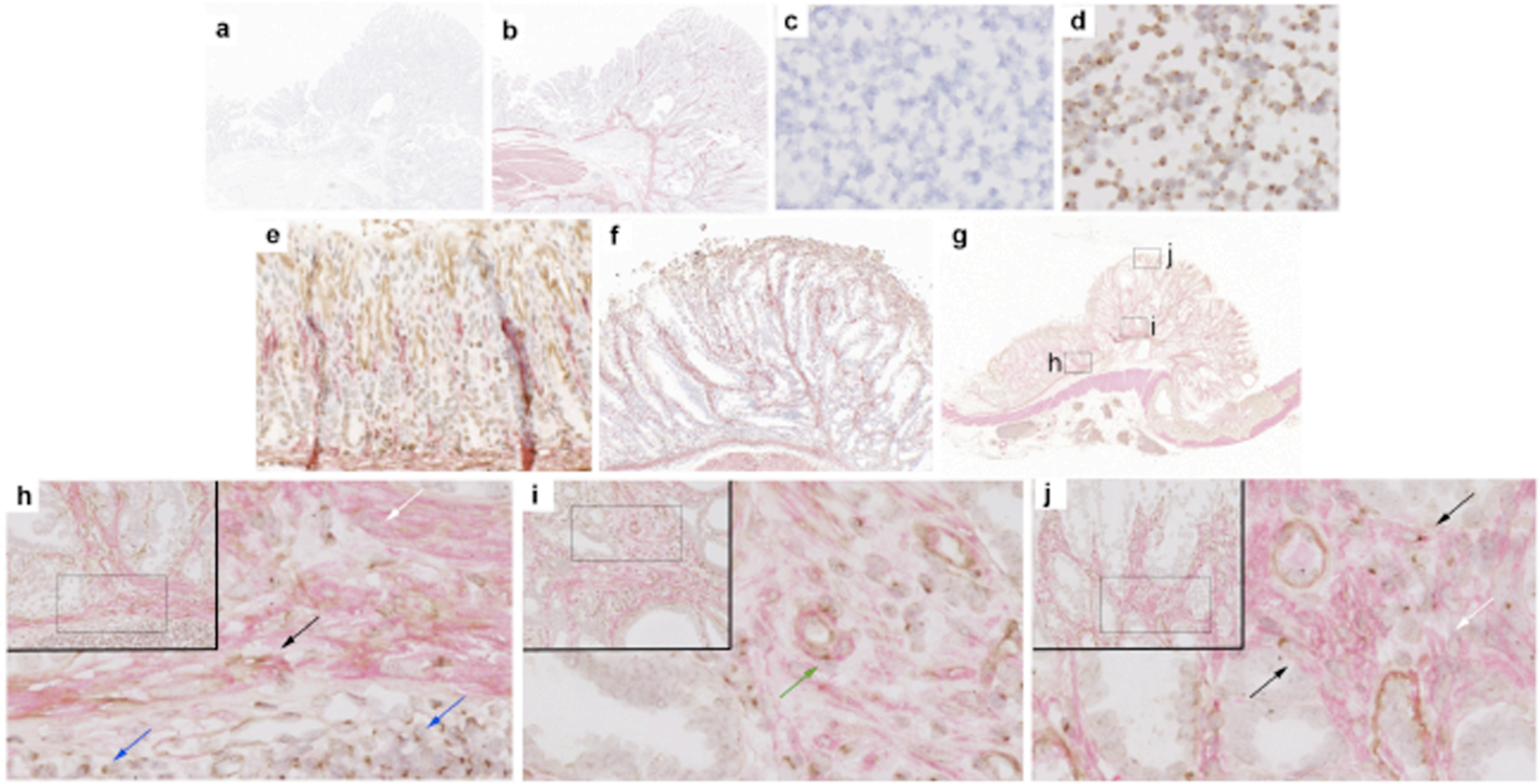

(continued on the next page)

Figure 3.12: Development of desmoplasia and presence of BMD-myofibroblasts in antral pyloric adenomas in BMTx'd *Tff1*$^{-/-}$ mice (continued)

(**a**-**d**) Controls for α-SMA IHC/ Y-chromosome ISH. (**a**,**b**; x4) Gastric adenomatous tissue with α-SMA antibody omitted (**a**; x1) and with (pink staining, **b**; x1). (**c**,**d**; x40) Male spleen control without Y-chromosome probe (**c**; x40) and with (**d**; x40). Y-chromosome positivity is indicated with a dark brown nuclear spot. (**e**-**g**) α-SMA IHC/ Y-chromosome ISH carried out on normal (**e**; x10) and dysplastic (**f**; x10) pyloric antrum at 6 months post BMTx and an antral pyloric adenoma (**g**) at 12 months post BMTx in *Tff1*$^{-/-}$ mouse group mice. (**h**-**j**) Higher magnification images of boxed images in **g**. BMD-myofibroblasts (black arrows) are identified by α-SMA+ cells with Y-chromosome positivity. Y-chromosome negative myofibroblasts are indicated with a white arrow. Within the antral adenoma a rare BMD-blood vessel smooth muscle cell was observed (green arrow). Inflammatory infiltrate is observed in **h** with inflammatory cells indicated by blue arrows. Boxed images: x20.

Figure 3.13: Comparison of BMD-myofibroblast engraftment in different regions of pedunculated gastric adenomas in *Tff1*$^{-/-}\rightarrow$*Tff1*$^{-/-}$ mice at 12 months post BMTx

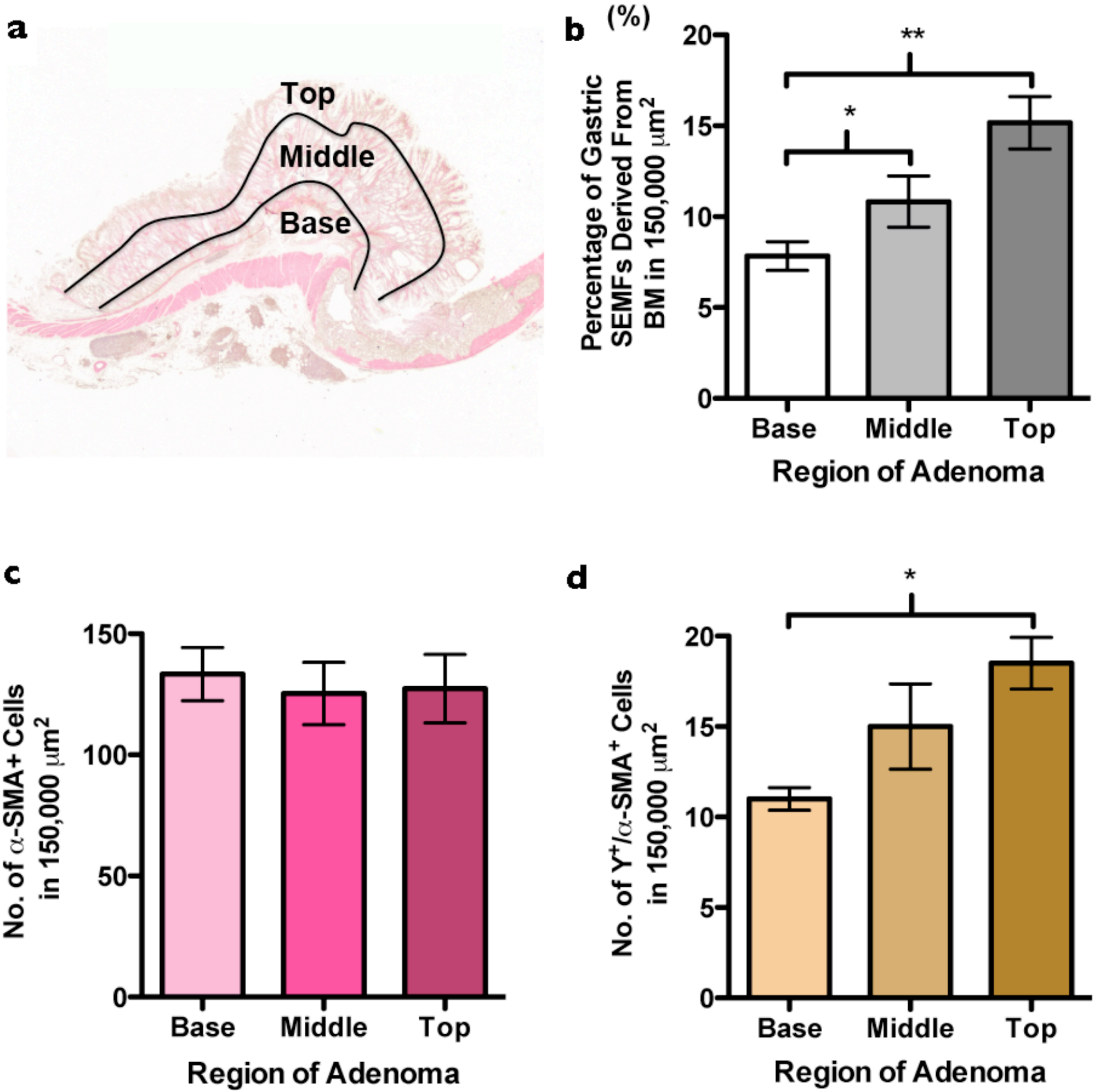

α-SMA^{+} cells were quantified in 150,000 μm^{2} areas at the base, middle and top of pedunculated gastric adenomas of the *Tff1*$^{-/-}\rightarrow$*Tff1*$^{-/-}$ group at 12 months post BMTx (**a**; x1). One-way ANOVA was performed to analyse whether there was a significant difference in percentage of gastric SEMFs derived from BM or the number of Y^{+}/α-SMA^{+} or α-SMA^{+} cells in each region. There was a significant increase in the percentage of gastric SEMFs derived from BM in the top of adenomas *versus* the base ($P<0.01$) and middle of adenomas *versus* the base ($P<0.05$) (**b**). On the other hand, there was no significant increase in the number of α-SMA^{+} cells in these regions (**c**), but there was a significant increase in the number of Y^{+}/α-SMA^{+} cells in the top of adenomas *versus* the base ($P<0.05$) (**d**). Mean±SEM, *$P<0.05$; ** $P<0.01$; $n=6$.

Figure 3.14: BMD-myofibroblast engraftment with time in the *Tff1*$^{-/-}$ mouse crossover study

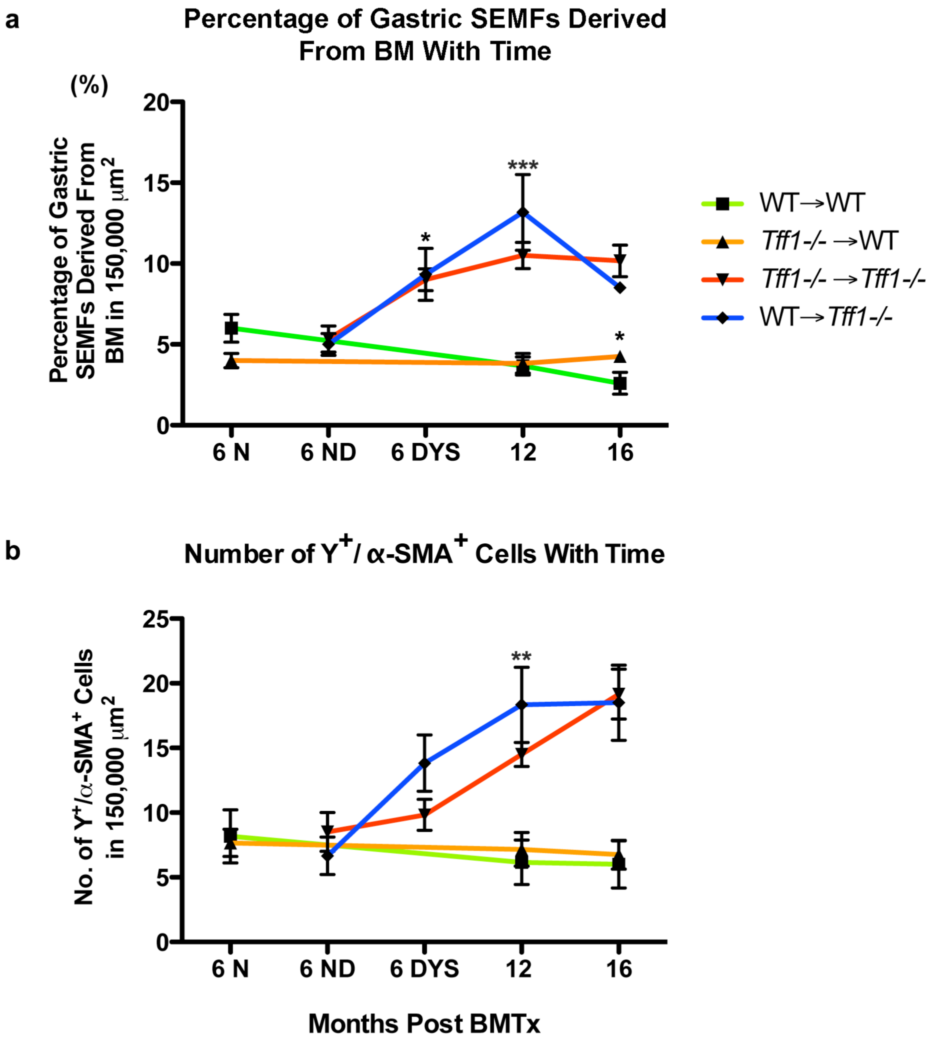

One-way ANOVA with a Bonferroni multiple comparison test was performed to analyse whether there was a significant difference in the percentage of gastric SEMFs derived from BM (**a**) or the number of Y^{+}/α-SMA^{+} cells (**b**) with time in the *Tff1*$^{-/-}$ mouse crossover study.

(**a**) Only the *Tff1*$^{-/-}$→*Tff1*$^{-/-}$ group demonstrated a significant increase in the percentage of gastric SEMFs derived from BM from normal antrum surrounding dysplastic antrum (ND) into dysplastic antrum (DYS) at 6 months post BMTx ($P<0.05$, red line). There was a significant increase in the percentage of gastric SEMFs derived from BM from ND at 6 months post BMTx to adenomatous antrum at 12 months post (*Tff1*$^{-/-}$→*Tff1*$^{-/-}$ [$P<0.01$] WT→*Tff1*$^{-/-}$ [$P<0.001$, blue line]). However, there was no significant increase from 12 to 16 months post BMTX in these groups. A single decrease in the percentage of gastric SEMFs derived from BM in normal antrum was observed from 6 to 16 months in the WT→WT group ($P<0.05$, green line).

(**b**) There was no significant increase in the number of Y^{+}/α-SMA^{+} cells into dysplastic antrum at 6 months post BMTx or adenomatous antrum at 12 months post BMTx from ND at 6 months in the *Tff1*$^{-/-}$→*Tff1*$^{-/-}$ group. A significant increase was observed from ND at 6 months post BMTx to adenomatous antrum at 12 months post BMTx in the WT→*Tff1*$^{-/-}$ group [$P<0.01$]. However, there was no further significant increase from 12 to 16 months post BMTX in the WT→*Tff1*$^{-/-}$ or *Tff1*$^{-/-}$→*Tff1*$^{-/-}$ groups.

Figure 3.14: BMD-myofibroblast engraftment with time in the *Tff1*$^{-/-}$ mouse crossover study (continued)

There was no significant difference in the percentage of gastric SEMFs derived from BM or the number of Y^{+}/α-SMA^{+} cells from 6-16 months post BMTX in the *Tff1*$^{-/-}$→WT mouse group (orange line).

To account for the smaller sample number in the WT→*Tff1*$^{-/-}$ group at 16 months (*n*=4) a non-parametric Kruskal-Wallis test was additionally performed yielding the same results. N normal; ND normal antrum near dysplastic antrum; DYS dysplasia. Mean±SEM; **P*<0.05, ***P*<0.01, *** *P*<0.001.

Figure 3.15: Number of α-SMA^{+} cells in the pyloric antrum with time in the *Tff1*$^{-/-}$ mouse crossover study

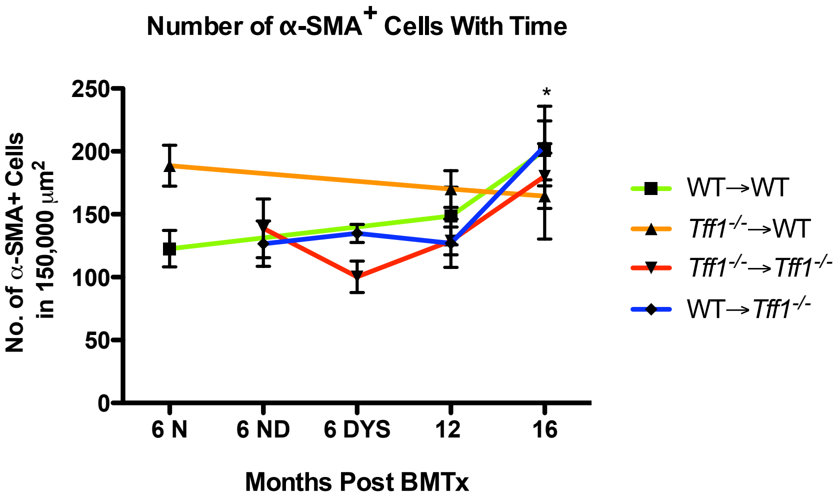

One-way ANOVA with a Bonferroni multiple comparison test demonstrated that in the *Tff1*$^{-/-}$→*Tff1*$^{-/-}$ group there was a significant increase in the number of α-SMA^{+} cells in adenomatous antrum at 16 months post BMTx compared to dysplastic antrum at 6 months post BMTx (*P*<0.05). Mean±SEM; **P*<0.05.

3.4.2 BMD-myofibroblasts were observed in non-fibrotic *Apc*$^{\text{Min/+}}$ mouse tumours

BMDCs frequently contributed to normal and adenomatous SI in *Apc*$^{\text{Min/+}}$ mice. A build-up of tumour stroma was not a feature of *Apc*$^{\text{Min/+}}$ mouse adenomas as demonstrated by little α-SMA immunoreactivity. Despite this, BMD-myofibroblasts were observed in the tumour stroma (Figure 3.16). However, quantification of BMD-myofibroblasts in these tissues was not carried out due to only 3 adenomas being available for analysis that would not allow for statistically valid comparisons.

Figure 3.16: Micrograph of BMDCs in the stroma of normal and adenomatous *Apc*$^{Min/+}$ mouse SI

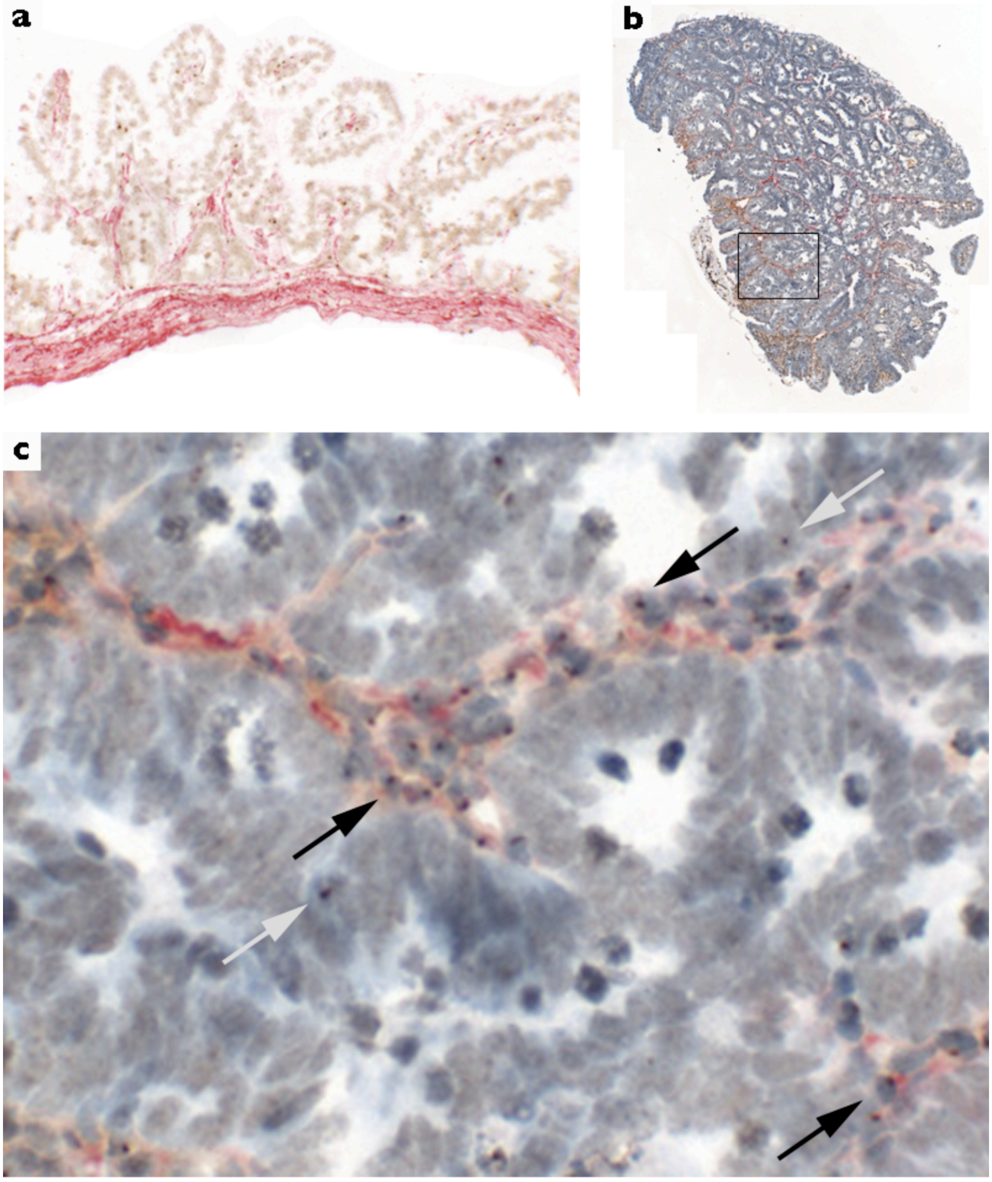

α-SMA IHC (pink staining) of normal SI (**a**; x10) and a small intestinal adenoma (**b**; x1 **c** magnification of boxed image in **b**; x40) in an *Apc*$^{Min/+}$ mouse transplanted with *Apc*$^{Min/+}$ mouse BM at 1 month post BMTx. Within the adenoma, numerous BMD-myofibroblasts (black arrows) were identified as well as rare BMD-cells in the epithelial layer (grey arrow). BMD-myofibroblasts are identified by α-SMA$^+$ cells with a dark brown nuclear spot indicating Y-chromosome positivity.

3.4.3 BMD-myofibroblast engraftment increased with tumour burden in *Apc*^{1322T} mice

BMDCs frequently contributed to the normal and adenomatous SI of *Apc*^{1322T} mice (Figure 3.17). As with *Apc*$^{Min/+}$ adenomas, desmoplasia did not occur. Quantification of BMD-SI SEMF engraftment in small intestinal stroma demonstrated a significantly increased percentage of SI SEMFs derived from BM in small and large SI adenomas compared to normal SI (Figure 3.18). On the other hand, analysis of the number of Y^+/α-SMA$^+$ cells in these tissues did not demonstrate a significant increase into adenomas, though there was a trend which paralleled that of the percentage. However, inspection of Figure 3.18 is an example of this increasing trend into large adenomas.

Analysis of the number α-SMA$^+$ in normal SI and small and large small intestinal adenomas revealed no significant difference (Figure 3.19).

Figure 3.17: Micrograph of BMDCs in the stroma of normal and adenomatous *Apc*^{1322T} mouse SI

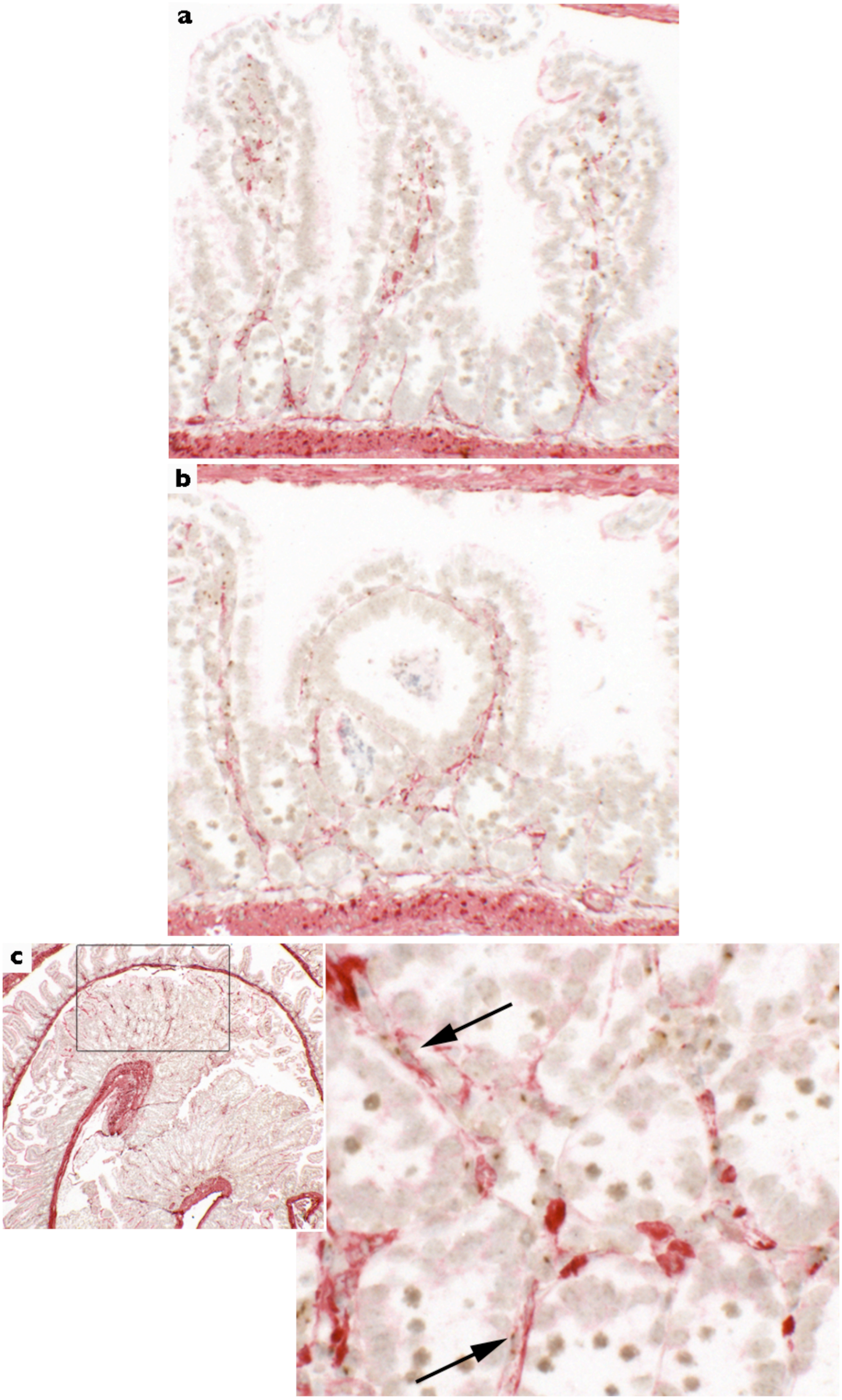

α-SMA IHC (pink staining) of normal SI (**a**; x20), a small adenoma (**b**; x20) and a large adenoma (**c**: left; x4, right; x40) in an *Apc*^{1332T} mouse at 1 month post BMTx. Within the adenoma, numerous BMD-myofibroblasts (black arrows) were identified. BMD-myofibroblasts are identified as α-SMA^{+} cells with a dark brown nuclear spot indicating Y-chromosome positivity.

Figure 3.18: BMD-myofibroblast engraftment in the SI in *Apc*^{1322T} mice transplanted with *Apc*^{1322T} mouse BM at 1 month post BMTX

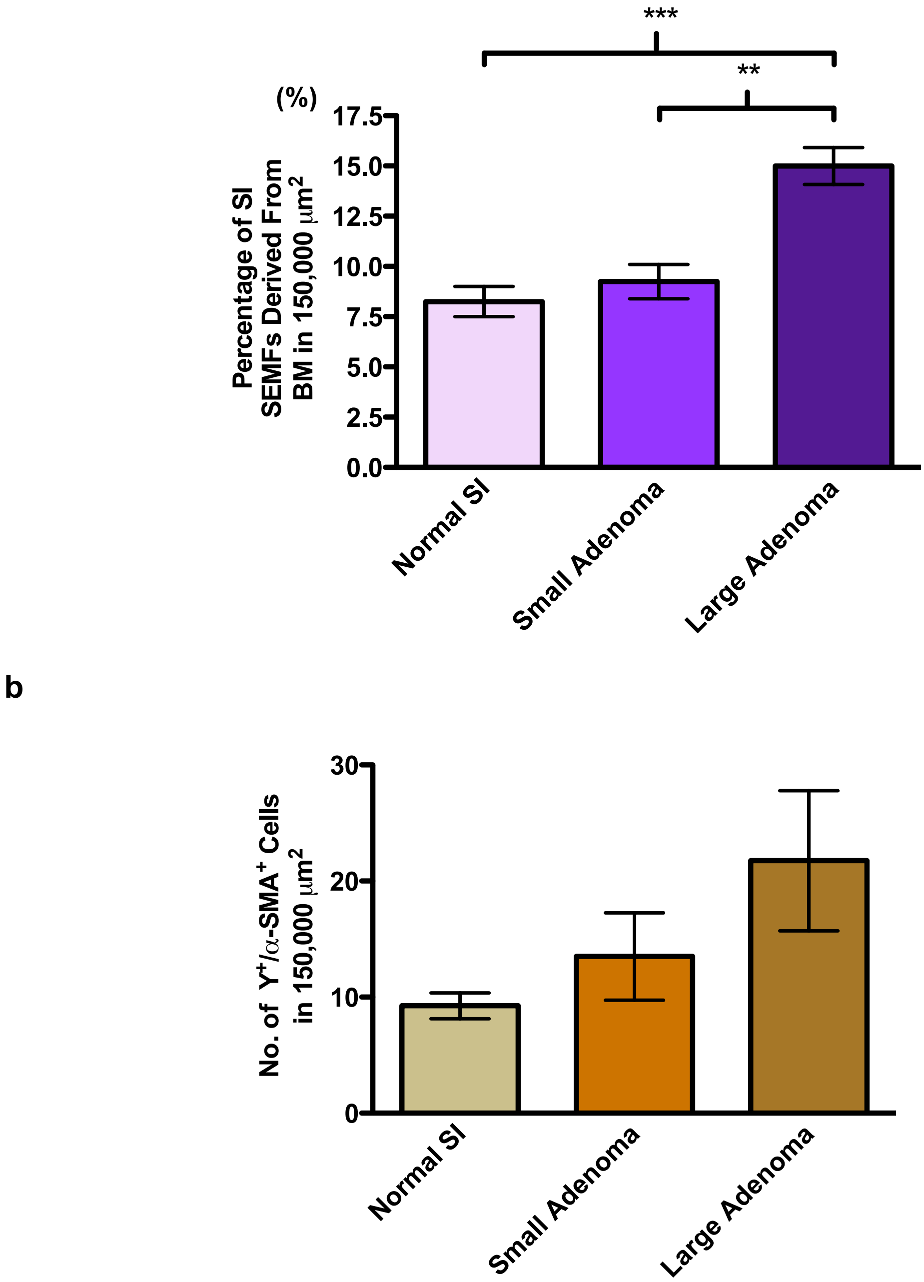

One-way ANOVA with a Bonferroni multiple comparison test was performed to determine whether there was a significant difference in the percentage of gastric SEMFs derived from BM or the number of Y$^+$/α-SMA$^+$ cells in normal and adenomatous SI in in *Apc*^{1322T} mice transplanted with *Apc*^{1322T} mouse BM at 1 month post BMTX. (**a**) The percentage of small intestinal (SI) SEMFs from BM was significantly increased in large adenomas compared to normal SI ($P<0.001$) and small adenomas ($P<0.01$) in *Apc*^{1322T} mice. (**b**) There was no significant increase in the number of Y$^+$/α-SMA$^+$ cells into small or large small intestinal adenomas compared to normal SI. Mean±SEM; ** P<0.01; *** $P<0.001$; $n=4$.

Figure 3.19: Number of α-SMA$^+$ cells in the SI at 1 month post BMTx in *Apc^{1322T}* mice

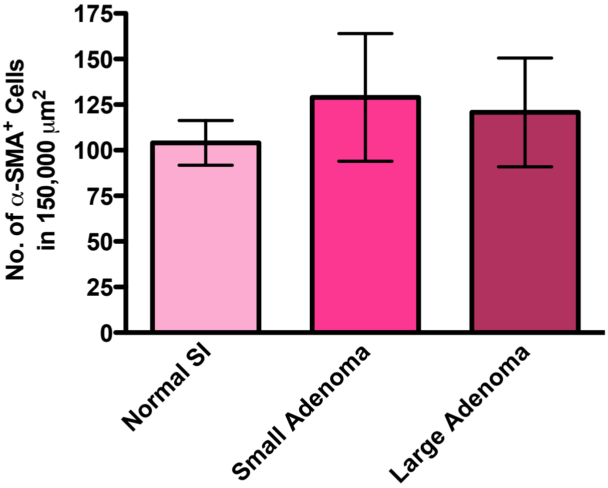

There was no significant difference in the number of α-SMA$^+$ cells in normal SI versus small adenomas or large adenomas. Mean±SEM.

3.4.4 Engraftment of BMD-colonic SEMFs did not increase in areas of inflammation in colitic *Il10$^{-/-}$* mice

The *Il10$^{-/-}$* mouse model exhibited the most inflammation compared to all of the other mouse models used in this study. An abundance of inflammatory infiltrate was observed in the villi and crypt stroma of these mice in H&E stained sections and confirmed by immune cell IHC. Fibrosis was not a feature of pathology in these mice. In fact, very little α-SMA immunoreactivity was observed in the stroma.

As Bamba and colleagues (2006) demonstrated an increase in BMD-colonic SEMFs in inflamed mucosa compared to non-inflamed mucosa in *Il10$^{-/-}$* mice on a C57/BL10 background [78], this led us to suspect that, despite the more severe colitis developed in *Il10*$^{-/-}$ mice on a BALB/c background, BALB/c background mice do not develop fibrosis as a consequence. Indeed, comparison of α-SMA IHC/Y-chromosome ISH in colonic mucosa of C57/BL10 and BALB/c background *Il10*$^{-/-}$ mice shows distinct α-SMA staining patterns (Figure 3.20a). Moreover, immune cell IHC/Y-chromosome ISH demonstrated the predominance of immune cells in the stroma (Figure 3.20b).

In some *Il10*$^{-/-}$ mice of this study, such as the one illustrated in Figure 3.20a and Figure 3.20b, there were very few myofibroblasts present in the inflamed stroma. In this mouse, 31% of colonic SEMFs were derived from BM of inflamed colonic stroma. However, this percentage was derived from counting a total of 49 myofibroblasts in a 150,000m^2 area of stroma, 15 of which were Y-positive. With this is mind, whilst an increasing trend in the percentage of colonic SEMFs was observed both in inflamed mucosa compared to non-inflamed mucosa and with the duration of colitis (Figure 3.21), the number of α-SMA$^+$ cells in these areas decreased (Figure 3.21). This could be because the influx of inflammatory cells in inflamed areas occupied the majority of the stroma.

Figure 3.20a: Comparison of BMD-colonic SEMF engraftment and the presence of immune cells in *Il10*$^{-/-}$ mice on a C57BL/10 and a BALB/c genetic background

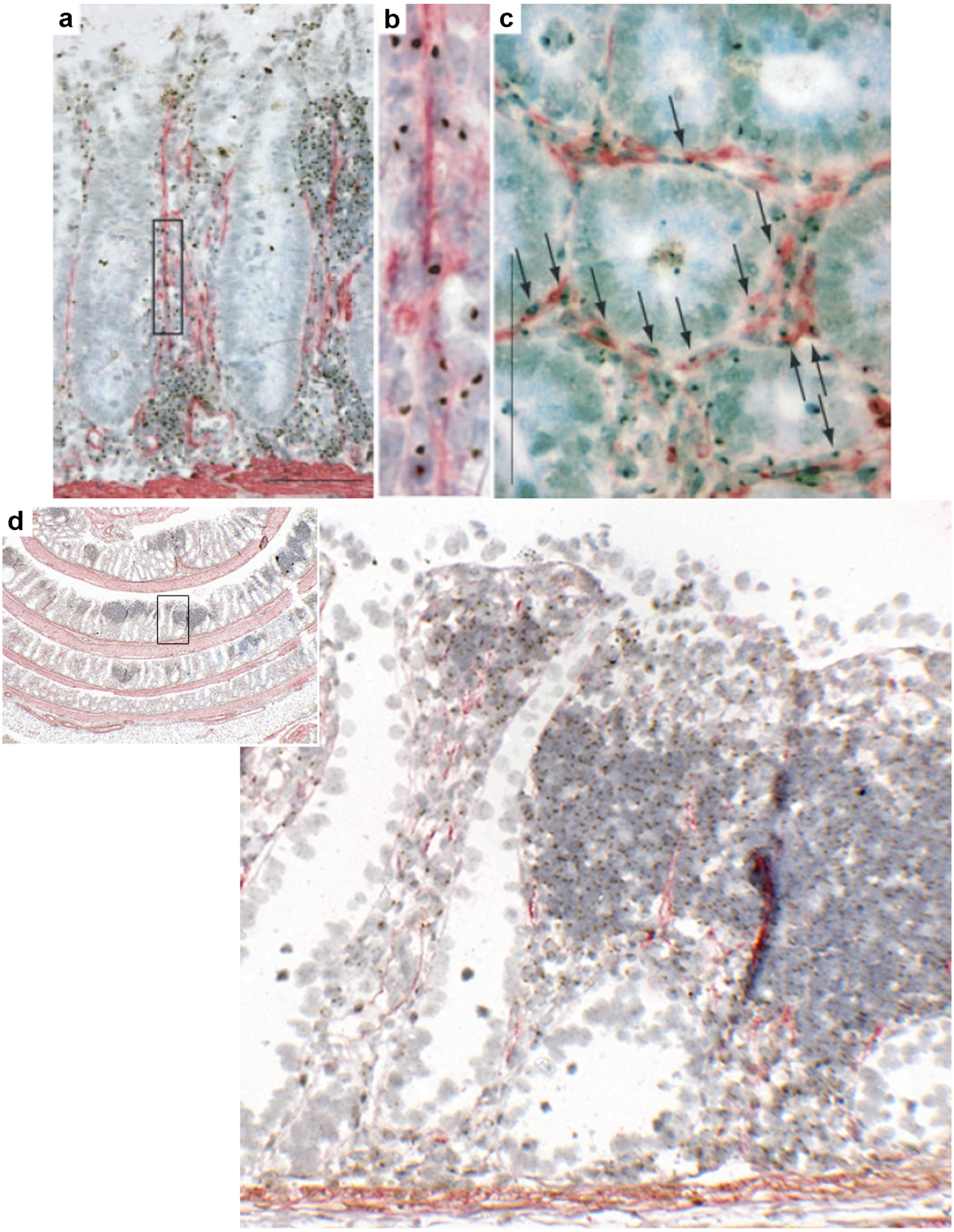

Bamba and colleagues (2006) demonstrated substantial α-SMA immunostaining (**a**) frequently observed BMD-colonic SEMFs (**b**,**c**) in an *Il10*$^{-/-}$ mouse on a C57BL/10 genetic background. In comparison, little α-SMA staining was observed in the inflamed colonic mucosa of an *Il10*$^{-/-}$ mouse on a BALB/c genetic background from this study (**d**). α-SMA is shown as pink staining and a brown dot indicates Y-chromosome positivity. Bar = 0.1mm; **a**-**c** taken from [78]. (**d**) Left hand image: x4; x20 magnification of boxed area is shown in the right hand image.

Figure 3.20b: Comparison of BMD-colonic SEMF engraftment and the presence of immune cells in *Il10*$^{-/-}$ colonic mucosa of mice described by Bamba *et al.,* (2006) and in an *Il10*$^{-/-}$ mouse from this study

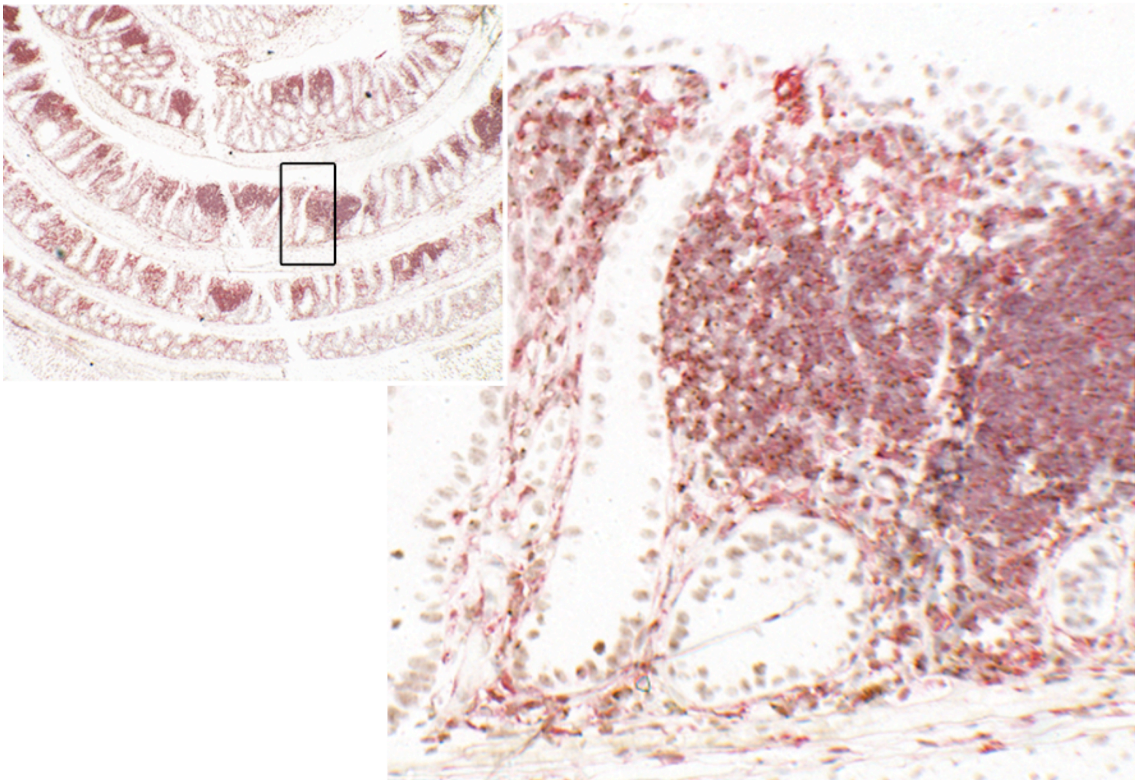

Immune cell IHC/Y-chromosome ISH on another tissue section from the *Il10*$^{-/-}$ mouse in **d** in Figure 3.22a. Here, immune cell marker positivity is shown through pink staining and once again Y-chromosome positivity is indicated by dark brown nuclear dots. Left hand image: x4, x20 magnifications of boxed area is shown in the right hand image.

Figure 3.21: Comparison of BMD-myofibroblast engraftment at 3 months *versus* 5 months post BMTx in *Il10*$^{-/-}$ mice

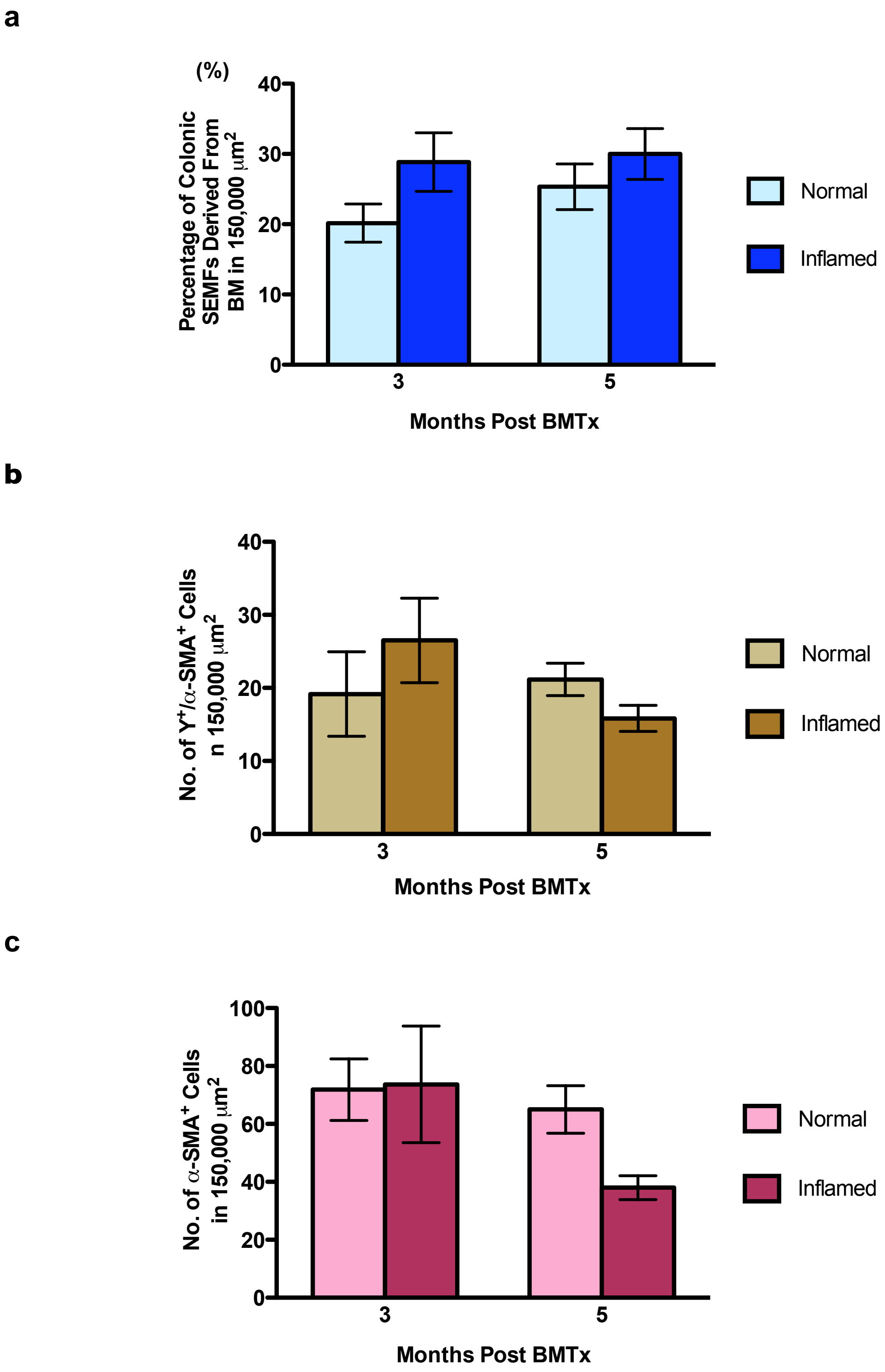

Two-way ANOVA of normal *versus* inflamed colonic mucosa at 3 *versus* 5 months post BMTx in *Il10*$^{-/-}$ mice transplanted with *Il10*$^{-/-}$ mouse BM was carried out for the percentage of colonic SEMFs derived from BM (**a**), the number of Y^+/α-SMA$^+$ (**b**), and the number of SMA$^+$ cells (**c**). A decreasing trend in the number of SMA$^+$ cells in inflamed areas from 3 months post BMTx to 5 months post BMTx is suggested. Mean±SEM, *n*=6.

3.4.5 Engraftment of BMD-gastric SEMFs is not observed in areas of SPEM in WT mice

BMD-inflammatory cells in the mucosa and submucosa were frequently observed in SPEM tissues at 6, 12, and 16 months post BMTx. However, inflammatory fibrosis was not observed as a part of SPEM pathology at any time point. Moreover, little α-SMA immunoreactivity and very few BMD-gastric SEMFs were observed (Figure 3.22). We attempted to quantify BMD-SEMF contribution in these areas but found there was insufficient stroma in both SPEM and normal fundic tissue to make a statistically valid observation.

Figure 3.22: BMDCs in normal and SPEM fundic tissue in WT mice

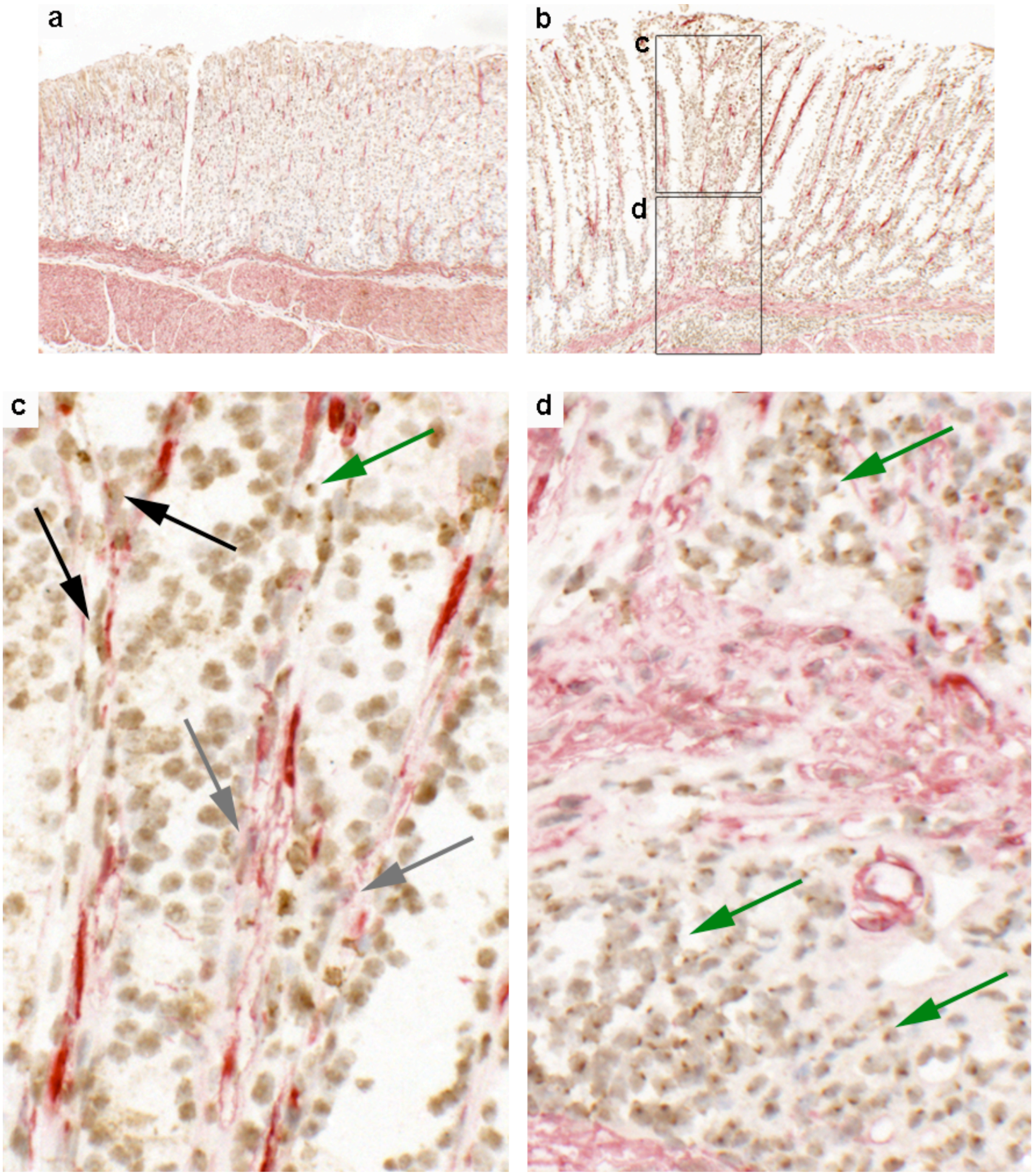

In normal fundic tissue very little stroma (lamina propria) was observed as demonstrated by ∝-SMA IHC (**a**; x10). Similarly, despite the presence of hyperplasia and inflammation in SPEM, fibrosis was not observed (**b**; x10). Few gastric SEMFs (grey arrows) and BMD-gastric SEMFs (black arrows) were observed in the stroma (**c**; x40). Instead, an inflammatory infiltrate in the stroma and submucosa were more commonplace (**d**; x40).

3.5 Summary of the contribution of putative BMD-epithelial cells and BMD-myofibroblasts in four mouse models

Tables 3.2-3.6 summarise the contribution of putative BMD-epithelial cells and BMD-myofibroblasts according to pathology in the *Tff1*$^{-/-}$ mouse crossover study (Tables 3.2 and 3.3), *Apc*$^{\mathrm{Min}/+}$ (Table 3.4), *Apc*$^{1322\mathrm{T}}$ (Table 3.5), and *Il10*$^{-/-}$ mice (Table 3.6).

Table 3.2: Tabulation of results in the pyloric antrum for the *Tff1*$^{-/-}$ mouse crossover study

BMTx details	Months post BMTx	Total number of mice	Pathology	Number of mice affected	Total number of α-SMA^{+} cells in 150,000 μm^2	Percentage of SEMFs derived from BM in 150,000 μm^2	Percentage of putative epithelial cells from BM in 150,000 μm^2
Tff1$^{-/-}$→*Tff1*$^{-/-}$	6	6	Normal histology*	Al mice	139±23	5±0.8	ND
			Antral dysplasia**	All mice	100±12	9±0.7	
	12	6	Single large antral-pyloric adenoma	All mice	129±11	11±0.8	0.2±0.1
	16	6	Single large antral-pyloric adenoma	All mice	198±22	10±1	ND
			Intramucosal carcinoma***	1	90	13	
WT→*Tff1*$^{-/-}$	6	6	Normal histology*	All mice	127±18	5±0.7	
			Antral dysplasia**	All mice	135±7	9±2	
	12	6	Single large antral-pyloric adenoma in each mouse	All mice	127±19	13±2	
	16	4	Single large antral-pyloric adenoma in each mouse	All mice	204±32	9±0.3	
			Intramucosal carcinoma	0	n/a	n/a	
WT→WT	6	6	Normal histology****	All mice	123±14	6±0.9	
	12	6	Normal histology****	All mice	149±23	4±0.6	
	16	5	Normal histology****	All mice	201±23	3±0.7	
Tff1$^{-/-}$→WT	6	6	Normal histology****	All mice	189±16	4±0.4	
	12	6	Normal histology****	All mice	170±15	4±0.6	
	16	4	Normal histology****	All mice	165±34	4±0.3	

* Normal histology was observed in 50-75% of the pyloric antrum in a x1 image. ** Antral dysplasia was observed in 25-50% of the pyloric antrum in a x1 image. *** a single focus of intramucosal carcinoma was observed amounting to less than 10% of the total area in the antral-pyloric adenoma. **** Normal histology was observed throughout the entire pyloric antrum. Key: **ND** not done; **n/a** non-applicable; Mean±SEM

Table 3.3: Tabulation of results in the fundus for the *Tff1*$^{-/-}$ mouse crossover study

BMTx details	Months post BMTx	Total number of mice	Pathology	Number of mice affected	Total number of α-SMA$^+$ cells in 150,000 μm^2	Percentage of SEMFs derived from BM in 150,000 μm^2	Percentage of putative epithelial cells from BM in 150,000 μm^2
Tff1$^{-/-}$→*Tff1*$^{-/-}$	6	6	Normal histology	All mice	Too little stroma in normal fundus or SPEM to allow for analysis		ND
	12	6					
	16	6					
WT→*Tff1*$^{-/-}$	6	6	SPEM*	0			
	12	6					
	16	4					
WT→WT	6	6	Normal histology	All mice			
			SPEM	0			
	12	6	Normal histology	All mice			
			Mild SPEM	1			
			Severe SPEM	1			
	16	5	Normal histology	All mice			
			Moderate SPEM	1			
Tff1$^{-/-}$→WT	6	6	Normal histology	All mice			
			Severe SPEM	1			
	12	6	Normal histology	5			
			Moderate SPEM	1			
			Severe SPEM and **no glands without SPEM were observed in the fundus**	1			
	16	4	Normal histology	All mice			
			Moderate SPEM	1			
			Severe SPEM	1			

Table 3.3: Tabulation of results in the fundus for the *Tff1*$^{-/-}$ mouse crossover study

* SPEM was defined as mild, moderate or severe. Mild SPEM was defined as having over 25% of cells showing mild to moderate *Tff2* mRNA expression in a x4 image of fundic mucosa. Moderate SPEM was defined as having 25%-75% of cells showing moderate to strong *Tff2* mRNA expression in a x4 image of fundic mucosa. Severe SPEM was defined by having over 75% of cells showing strong *Tff2* mRNA expression in a x4 image of fundic mucosa. Key: **ND** not done; Mean±SEM

Table 3.4: Tabulation of results in the SI and colon for the *Apc*$^{Min/+}$ mouse study

BMTx details	**Months post BMTx**	**Total number of mice**	**Pathology**	**Mean number of adenomas***	**Number of mice affected**	**Total number of α-SMA^{+} cells in 150,000 μm^{2}**	**Percentage of SEMFs derived from BM in 150,000 μm^{2}**	**Percentage of putative epithelial cells from BM in 150,000 μm^{2}**
Apc$^{Min/+}$→*Apc*$^{Min/+}$	1	6	Small intestinal adenomas	36±13	All mice	ND	ND	ND
			Colonic adenomas	0.0±0.0	All mice			
WT→ *Apc*$^{Min/+}$	1	6	Small intestinal adenomas	71±42	All mice			
			Colonic adenomas	0.3±0.5	All mice			

* Adenomas were counted in formalin-fixed, methylene blue stained intestine by Shigeki Bamba using a dissection microscope, ALB received tissue blocks from this experiment. Key: **ND** not done; Mean±SEM

Table 3.5: Tabulation of results in the pyloric antrum, SI, and colon for the *Apc*^{1322T} mouse study

BMTx details	Months post BMTx	Total number of mice	Pathology	Number of mice affected	Mean number of dysplastic lesions or tumours*	Total number of α-SMA$^+$ cells in 150,000 μm^2	Percentage of SEMFs derived from BM in 150,000 μm^2	Percentage of putative epithelial cells from BM in 150,000 μm^2
Apc^{1322T}→ *Apc*^{1322T}	1	4	Microadenomas with moderate dysplasia in the pyloric antrum	2	2±1	ND	ND	ND
			Normal SI	All mice	n/a	104±12	8±0.8	0.3±0.1
			Small adenomas in the SI	All mice	12±3	129±35	9±0.9	0.2±0.1
			Large adenomas in the SI	All mice	4±2	121±30	15±0.9	0.3±0.1
			Microadenomas in the colon	2	1±0.8	ND	n/a	ND
			Large adenomas in the colon	0	0	n/a	n/a	n/a

* In each mouse dysplastic lesions and tumours were counted from low-powered micrographs of an H&E stained tissue section of the pyloric antrum, SI, or colon. Key: **ND** not done; **n/a** non applicable; Mean±SEM

Table 3.6: Tabulation of results in the colon for the *Il10*$^{-/-}$ mouse study

BMTx details	**Months post BMTx**	**Total number of mice**	**Pathology**	**Number of mice affected**	**Total number of α-SMA^{+} cells in 150,000 μm^{2}**	**Percentage of SEMFs derived from BM in 150,000 μm^{2}**	**Percentage of putative epithelial cells from BM in 150,000 μm^{2}**
Il10$^{-/-}$→ *Il10*$^{-/-}$	3	6	Normal colonic mucosa*	All mice	72±11	20±3	0.3±0.1
			Colitis score** 1	2	76±57	29±5	0
			Colitis score 2	3	86±24	19±5	0.4±0.1
			Colitis score 3	1	33	43	0.6
	5	6	Normal colonic mucosa*	All mice	65±8	25±3	0.4±0.1
			Colitis score 2	2	33±5	32±7	0.3±0.03
			Colitis score 2.5	1	33	31	0.5
			Colitis score 3	3	49±6	27±6	0.6±0.40

* Normal colonic mucosa was interspersed with inflamed lesions throughout the colon. **Colitis score out of a maximum score of 4. Scoring based on methods described by Berg *et al*., (1996) [76]. Colitis score 1 was defined as having one or a few multifocal mononuclear cell infiltrates in the lamina propria accompanied by minimal epithelial hyperplasia and slight to no depletion of mucus from goblet cells. Colitis score 2 was defined as having lesions that tended to involve more of the intestine than grade 1 lesions, or were more frequent. Typical changes included several multifocal, mild inflammatory cell infiltrates in the lamina propria composed primarily of mononuclear cells with a few neutrophils. Mild epithelial hyperplasia and mucin depletion were also seen. Small epithelial erosions were occasionally present and inflammation rarely involved the submucosa. Colitis score 2.5 was defined as having lesions, inflammation, mucin depletion, and hyperplasia greater or more frequent than grade 2 but not to the same extent as grade 3. Ulcers were not observed. Colitis score 3 was defined as having lesions that involved a large area of the mucosa or were more frequent than grade 2 lesions. Inflammation was moderate and often involved the submucosa but was rarely transmural. Inflammatory cells were a mixture of mononuclear cells as well as neutrophils, and crypt abscesses were sometimes observed. Moderate epithelial hyperplasia and mucin depletion were seen. Ulcers were occasionally observed. Mean±SEM.

3.6 Mechanisms of BMD-myofibroblast recruitment in tumourigenesis and inflammation in all mouse models

To better understand the mechanisms of BMD-myofibroblast recruitment, *Opn* mRNA isotopic ISH was employed in all mouse models of this study. Our findings suggest that *Opn* mRNA at desmoplastic reaction sites at the edges of *Tff1*$^{-/-}$ mouse adenomas was associated with increased BMD-myofibroblast engraftment. In contrast, *Opn* mRNA expression in *Apc*$^{\mathrm{Min/+}}$ and *Apc*$^{\mathrm{1322T}}$ mice tumours was diffuse and did not correlate with increased α-SMA immunoreactivity or an increased presence of BMD-SEMFS. In *Il10*$^{-/-}$ and SPEM mouse tissues, *Opn* mRNA expression varied and did not increase in areas of increased inflammation. Moreover, *Opn* mRNA expression in did not correlate with increased α-SMA immunoreactivity or an increased presence of BMD-SEMFS.

3.6.1 *Opn* mRNA expression in desmoplastic reaction sites in *Tff1*$^{-/-}$ mouse adenomas correlated with an increased frequency of BMD-myofibroblasts

Opn mRNA expression was analysed in normal, dysplastic and adenomatous gastric mucosa in the *Tff1*$^{-/-}$ mouse crossover study (summarised in Table 3.7).

Opn mRNA expression was predominantly epithelial but occasional stromal expression was also observed. In normal pylorus and dysplastic pyloric antrum, *Opn* mRNA was expressed along the base of glands (Figure 3.23). In antral pyloric adenomas, strong *Opn* mRNA expression occurred throughout adenomas with increased expression occurring towards the lumen of adenomas at desmoplastic reaction sites (Figure 3.24a and Figure 3.24b). Increased *Opn* mRNA expression at the top of adenomas was consistent with an increased number of BMD-SEMFs. Figure 3.25 demonstrates an area of increased *Opn* mRNA expression correlating with the increased presence of myofibroblasts and BMD-myofibroblasts. Visual comparison of *Opn* mRNA expression in *Tff1*$^{-/-}$ mouse adenomas at 12 months *versus* 16 months post BMTx suggested a slight decrease in *Opn* mRNA expression in adenomas at 16 months post BMTx.

There was no observable difference in *Opn* mRNA expression in any mice that had received allogeneic BMTx.

Table 3.7: Summary of *Opn* mRNA expression in normal, dysplastic, and adenomatous gastric mucosa in the *Tff1*$^{-/-}$ mouse crossover study

Region of stomach	***Opn* mRNA expression**	***Actb***
Normal pylorus (*n*=15)	+ (3.5) Strong basal expression. Epithelial expression	+++
Normal fundus (*n*=22)	+ (2.6) Focal expression restricted to the lower 2/3 of the gland. Epithelial expression.	+++
Dysplastic antrum (*n*=3)	+ (2.3) Strong basal expression and rare focal expression. Epithelial expression.	+++
Antral adenomas (*n*=8)	++ (4.3) Strong basal and focal expression (particularly towards the lumen) in adenomas. Mainly epithelial and occasional stromal expression.	+++

Symbol scores were allocated according to mean derived numeric scores (bracketed) for each group using the scoring schemes detailed in Table 2.16 in Chapter 2. *Actb*= rat beta-actin mRNA control

Figure 3.23: *Opn* mRNA expression in normal and dysplastic pyloric antrum

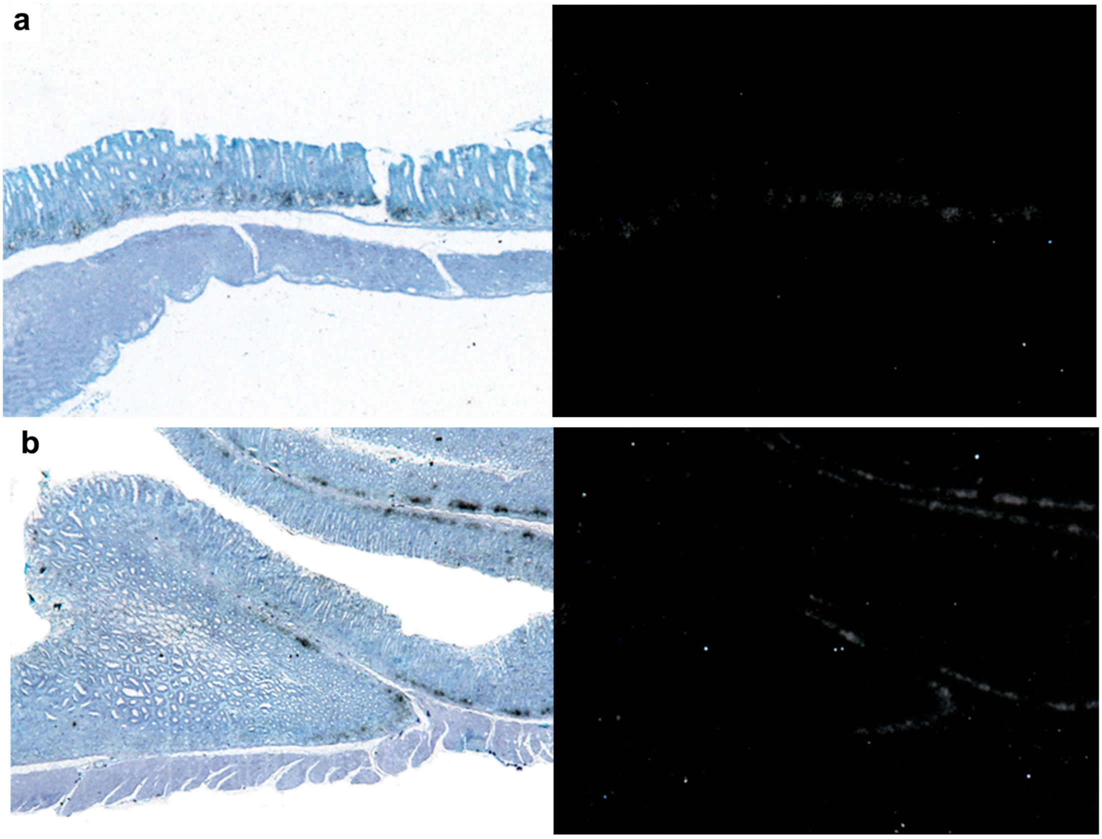

Opn mRNA was expressed throughout the base of normal antral glands of a WT mouse transplanted with WT BM at 6 months post BMTx (**a**; x4) and dysplastic antrum of a *Tff1*$^{-/-}$ mouse transplanted with *WT* mouse BM at six months post BMTx (**b**; x10). *Opn* mRNA expression appeared as black grains in bright field images (left) and white grains in dark field images (right).

Figure 3.24a: *Opn* mRNA expression in gastric adenomas of *Tff1*$^{-/-}$ mice

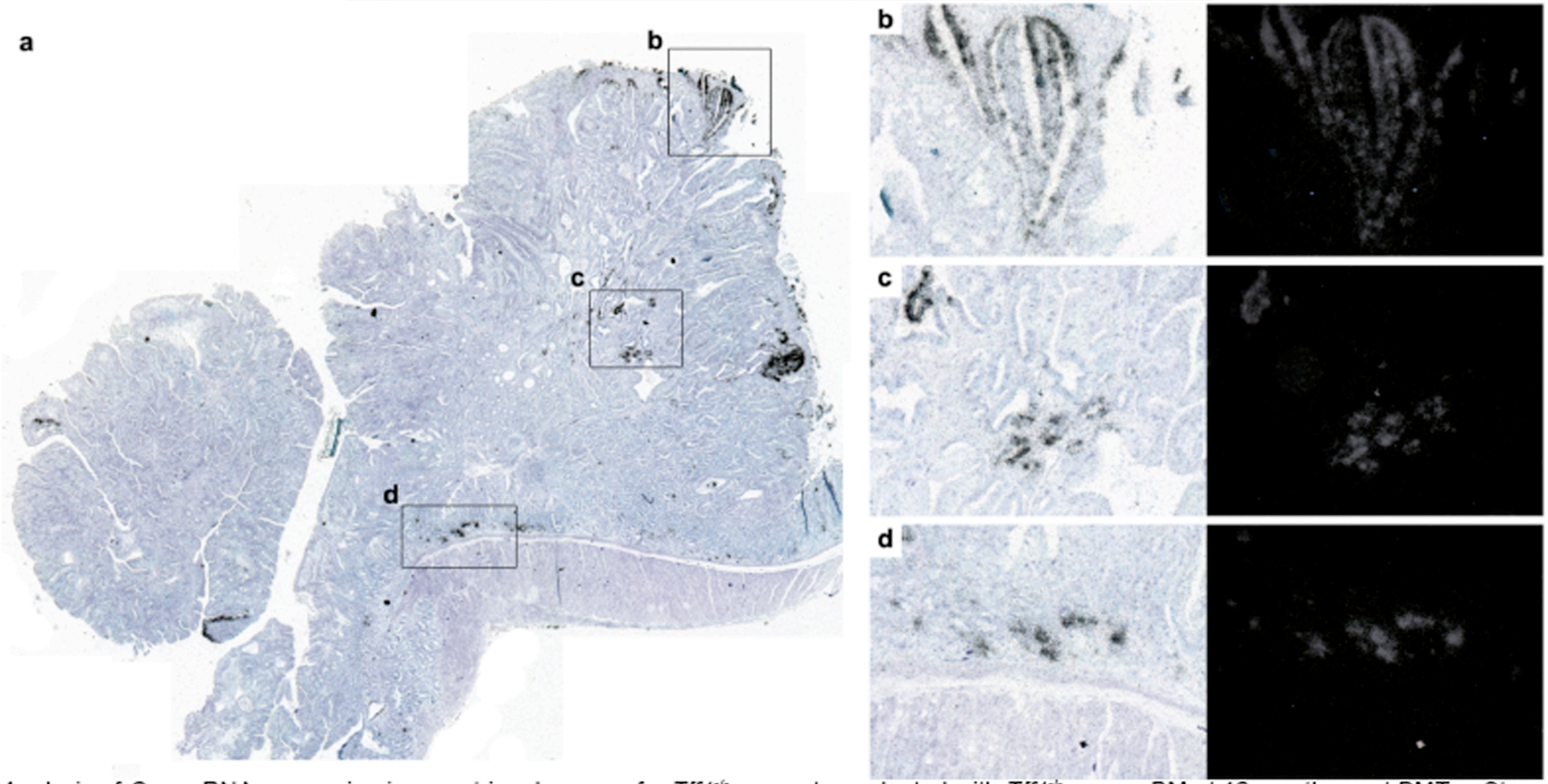

Analysis of *Opn* mRNA expression in a gastric adenoma of a *Tff1*$^{-/-}$ mouse transplanted with *Tff1*$^{-/-}$ mouse BM at 12 months post BMTx. Strong focal *Opn* mRNA was observed in epithelial cells (and occasionally in stromal cells) throughout the adenoma from a *Tff1*$^{-/-}$ mouse (**a**; tiled x4 images), particularly at the adenoma's edges. *Opn* mRNA expression appears as black grains in bright field images (left boxes of **b**,**c**,**d**) and white grains in dark field images (right boxes of **b**,**c**,**d**). **b**,**c**,**d**: bright field and dark field x10 images of boxed areas in adenoma.

Figure 3.24b: *Opn* mRNA expression in gastric adenomas of *Tff1*$^{-/-}$ mice

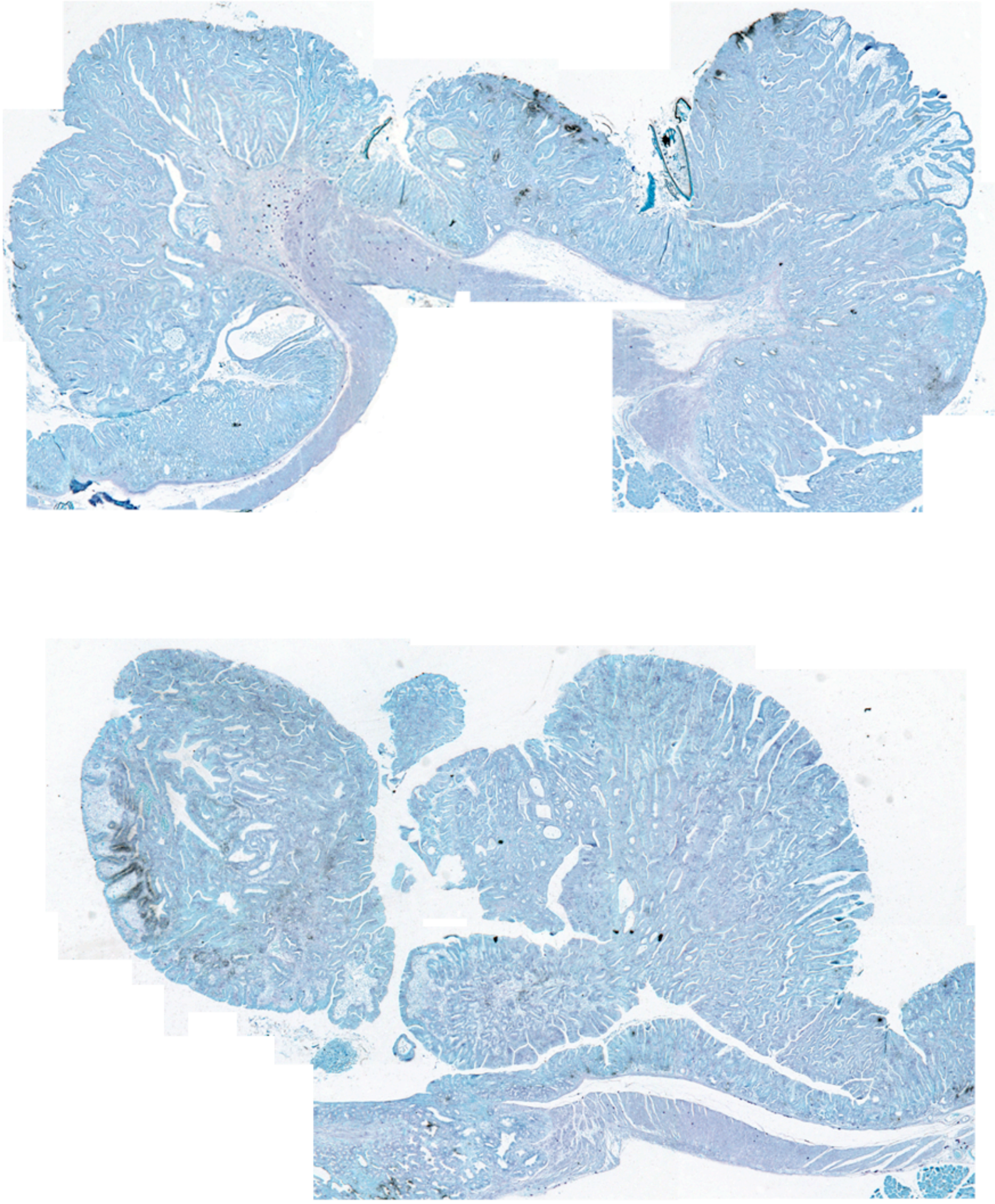

Micrographs of *Opn* mRNA expression in two gastric adenomas of *Tff1*$^{-/-}$ mice that had been transplanted with *Tff1*$^{-/-}$ mouse BM at 16 months post BMTx. Moderate and strong epithelial (and occasional stromal) expression was observed predominantly towards the lumen. *Opn* mRNA expression appears as black grains in bright field images. Tiled x4 images.

Figure 3.25: *Opn* mRNA expression and BMD-myofibroblast engraftment in a *Tff1*$^{-/-}$ mouse gastric adenoma

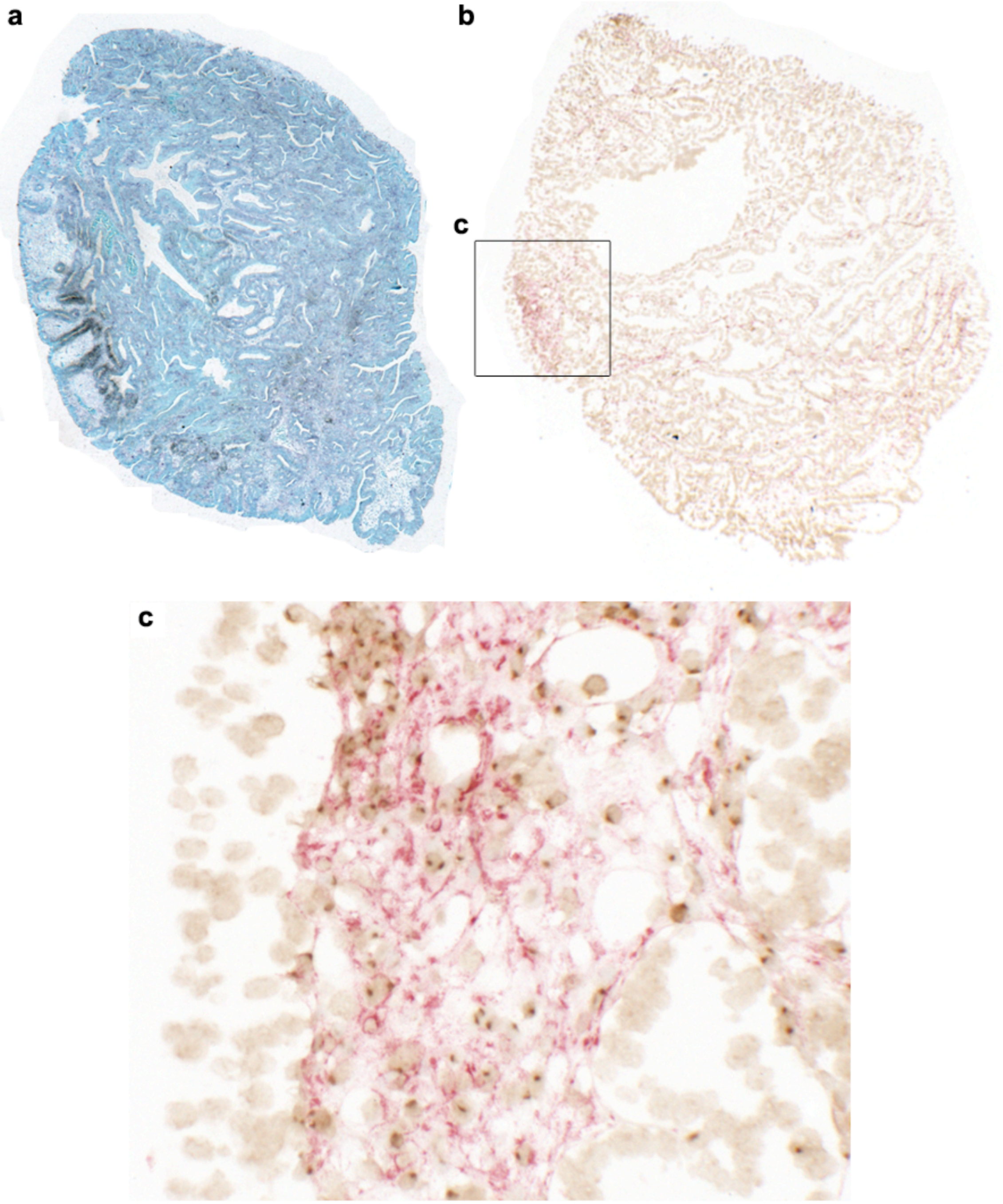

A patch of strong epithelial *Opn* mRNA expression in a gastric adenoma of a *Tff1*$^{-/-}$ mouse transplanted with *Tff1*$^{-/-}$ mouse BM at 16 months post BMTx (black grains in **a**; x4) corresponds to an area with increased α-SMA immunostaining (boxed in **b**; x4). A larger magnification of this area (**c**; x40) shows a concentration of BMD myofibroblasts (pink staining surrounding cells with a brown nuclear dot) and BMD-inflammatory cells (cells with only a brown nuclear dot).

3.6.2 *Opn* mRNA expression in *Apc*$^{Min/+}$ and *Apc*^{1322T} mouse adenomas did not correlate with the increased frequency of BMD-myofibroblasts

In contrast to *Tff1*$^{-/-}$ mouse tissues, *Opn* mRNA expression in *Apc*$^{Min/+}$ and *Apc*^{1322t} mouse tissues was frequently both epithelial and stromal. Expression between *Apc*$^{Min/+}$ and *Apc*^{1322T} mice differed, with *Opn* mRNA expression undetected in normal small intestinal or colonic mucosa of *Apc*$^{Min/+}$ mice, but occasionally detected in the SI and rarely observed in the colonic mucosa of *Apc*^{1322T} mice (summarised in Table 3.8). *Opn* mRNA was also observed in the colonic muscularis propria consistent with reported expression in ganglion cells in the myenteric plexus [186]. However, *Opn* mRNA expression was not observed in the muscularis mucosa of the SI or stomach in *Apc*$^{Min/+}$ and *Apc*^{1322T} mice, or *Tff1*$^{-/-}$ or *Il10*$^{-/-}$ mice for that matter.

Increased, diffuse *Opn* mRNA expression in epithelial and stromal cells was demonstrated in *Apc*$^{Min/+}$ and *Apc*^{1322T} mouse adenomas compared to normal tissues (Figure 3.26 and Figure 3.27). In *Apc*^{1322T} mice there appeared to be increased expression in large adenomas compared to small adenomas in the SI. However, we could not convincingly demonstrate that the *Opn* mRNA expression in *Apc*$^{Min/+}$ and *Apc*^{1322T} mouse adenomas correlated with increased α–SMA immunoreactivity or increased engraftment of BMD-myofibroblasts (Figure 3.28 and Figure 3.29).

Table 3.8: Summary of *Opn* mRNA expression in *Apc*$^{\mathrm{Min/+}}$ and *Apc*$^{\mathrm{1322T}}$ mouse intestinal tissue

Region of Intestine	***Opn* mRNA expression**	***βAC***
Normal *Apc*$^{\mathrm{Min/+}}$ mouse SI	-	+++
Normal *Apc*$^{\mathrm{1322T}}$ mouse SI	+ (2.0) Occasional focal expression. Both epithelial and stromal expression.	+++
Small adenomas of the *Apc*$^{\mathrm{1322T}}$ mouse SI	+ (2.8) Epithelial and stromal expression	+++
Large adenomas of the *Apc*$^{\mathrm{1322T}}$ mouse SI	++ (4.0) As in *Apc*$^{\mathrm{1322T}}$ mouse small adenomas, dispersed throughout adenomas	+++
Normal *Apc*$^{\mathrm{Min/+}}$ mouse colon*	-	+++
Normal *Apc*$^{\mathrm{1322T}}$ mouse colon	+ (2.0) Very rare focal expression. Both epithelial and stromal.	+++
Apc$^{\mathrm{Min/+}}$ mouse colonic adenoma (*n*=1)	+ (4.0) Patchy, more often stromal	+++

Symbol scores were allocated according to mean derived numeric scores (bracketed) for each group using the scoring schemes detailed in Table 2.16 in Section 2.5 of Chapter 2. * strong focal expression occasionally appeared in the muscularis propria.

Figure 3.26: *Opn* mRNA expression in normal and adenomatous *Apc*$^{Min/+}$ mouse intestine

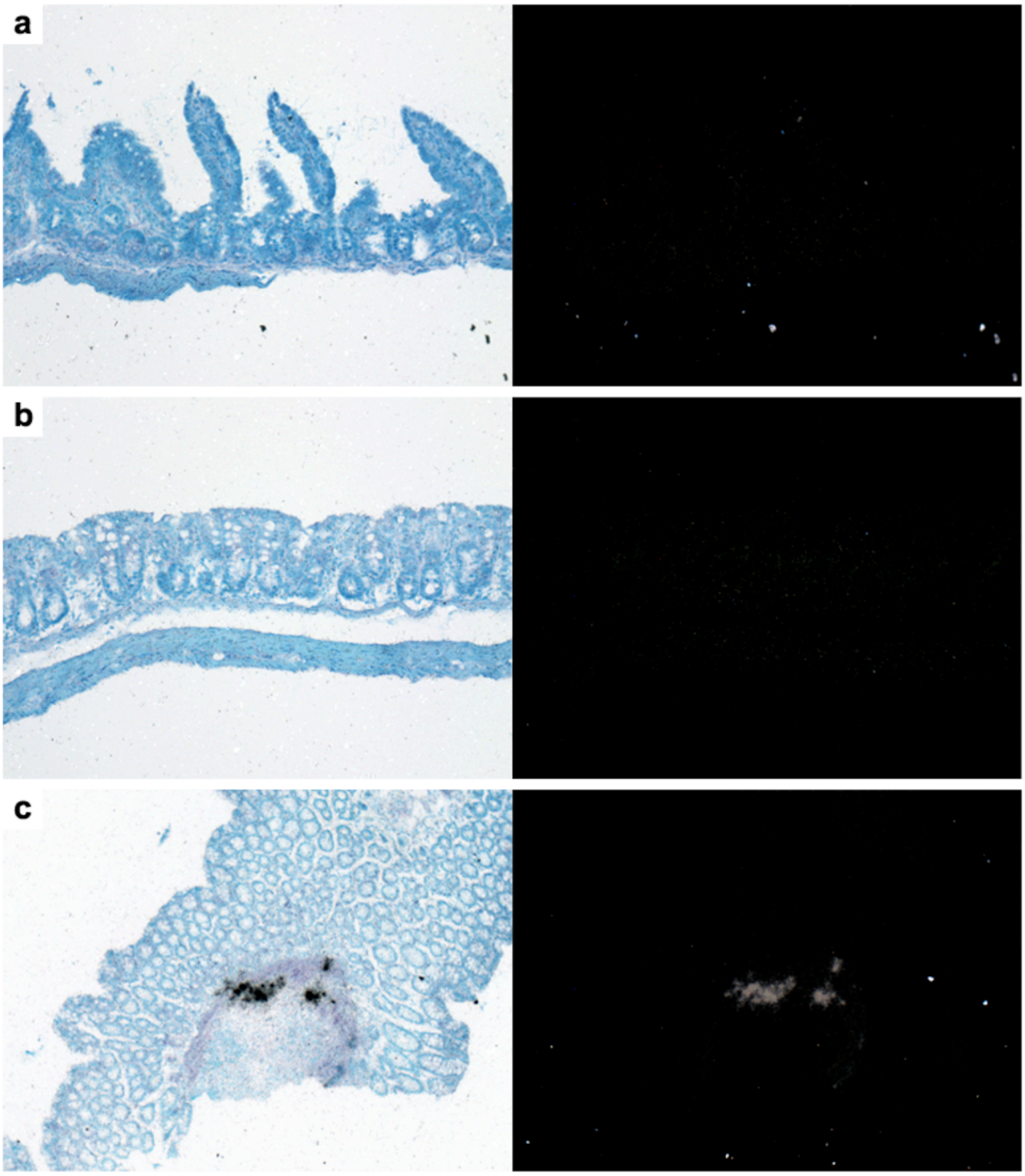

Analysis of *Opn* mRNA expression in an *Apc*$^{Min/+}$ mouse transplanted with *Apc*$^{Min/+}$ mouse BM at 1 month post BMTx. No *Opn* mRNA expression was observed in normal SI (**a**) and colonic (**b**) epithelium. Strong focal expression was observed in the colonic muscularis mucosa and adjacent submucosa (**c**). *Opn* mRNA expression appears as black grains in bright field images (left) and white grains in dark field images (right). Magnification of all images: x10.

Figure 3.27: *Opn* mRNA expression in the normal and adenomatous *Apc*^{1322T} mouse intestine

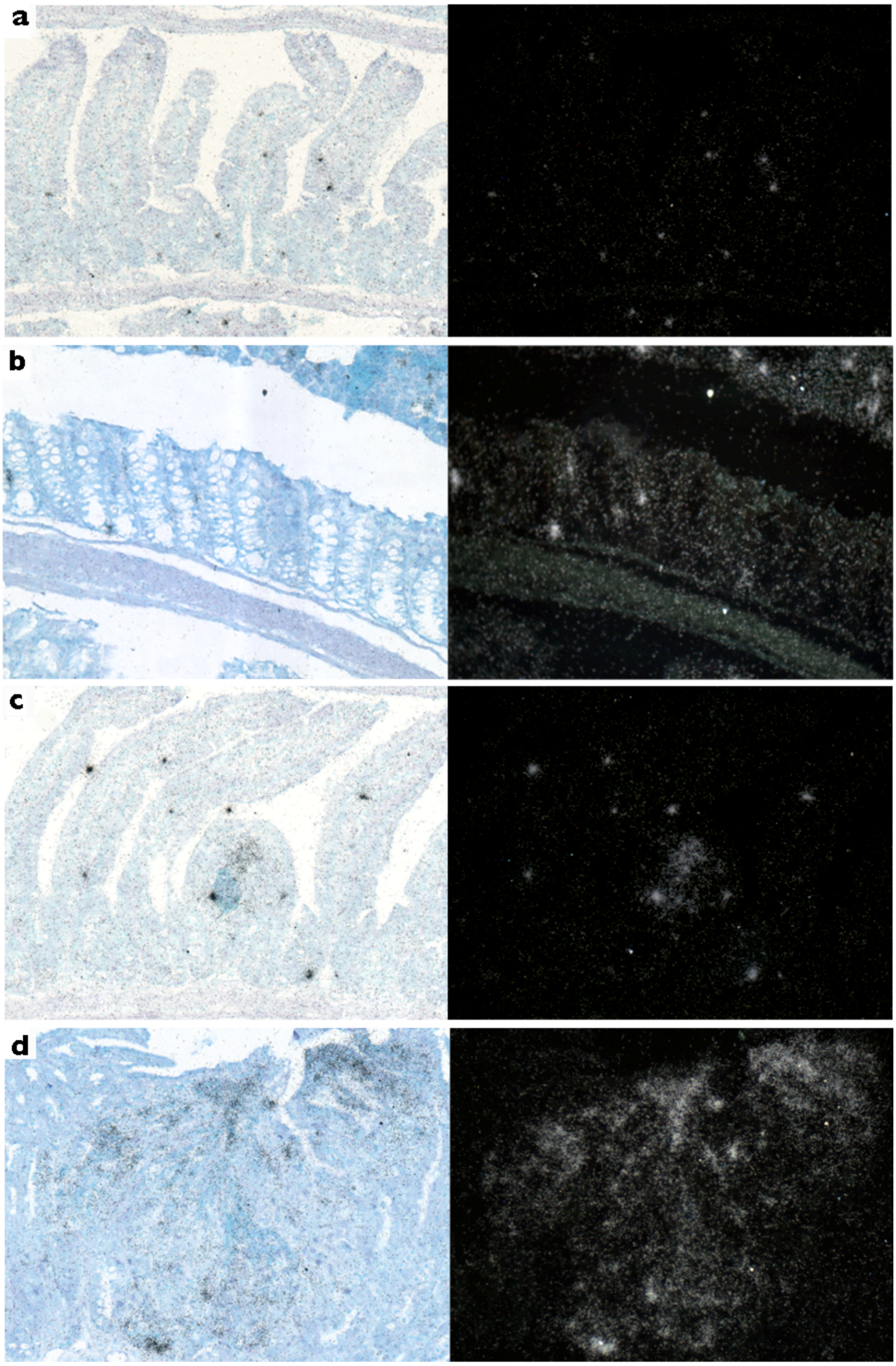

Opn mRNA was occasionally expressed in normal SI (**a**) and rarely expressed in the colon (**b**) in *Apc*^{1322T} mice transplanted with *Apc*^{1322T} mouse BM at 1 month post BMTx. Increased epithelial and stromal *Opn* mRNA expression was observed in small (**c**) and large (**d**) adenomas in the SI. *Opn* expression appears as black grains in bright field images (left) and white grains in dark field images (right). Magnification of all images: x20.

Figure 3.28: *Opn* mRNA expression and BMD-myofibroblast engraftment in an *Apc*$^{\mathrm{Min/+}}$ mouse colonic adenoma

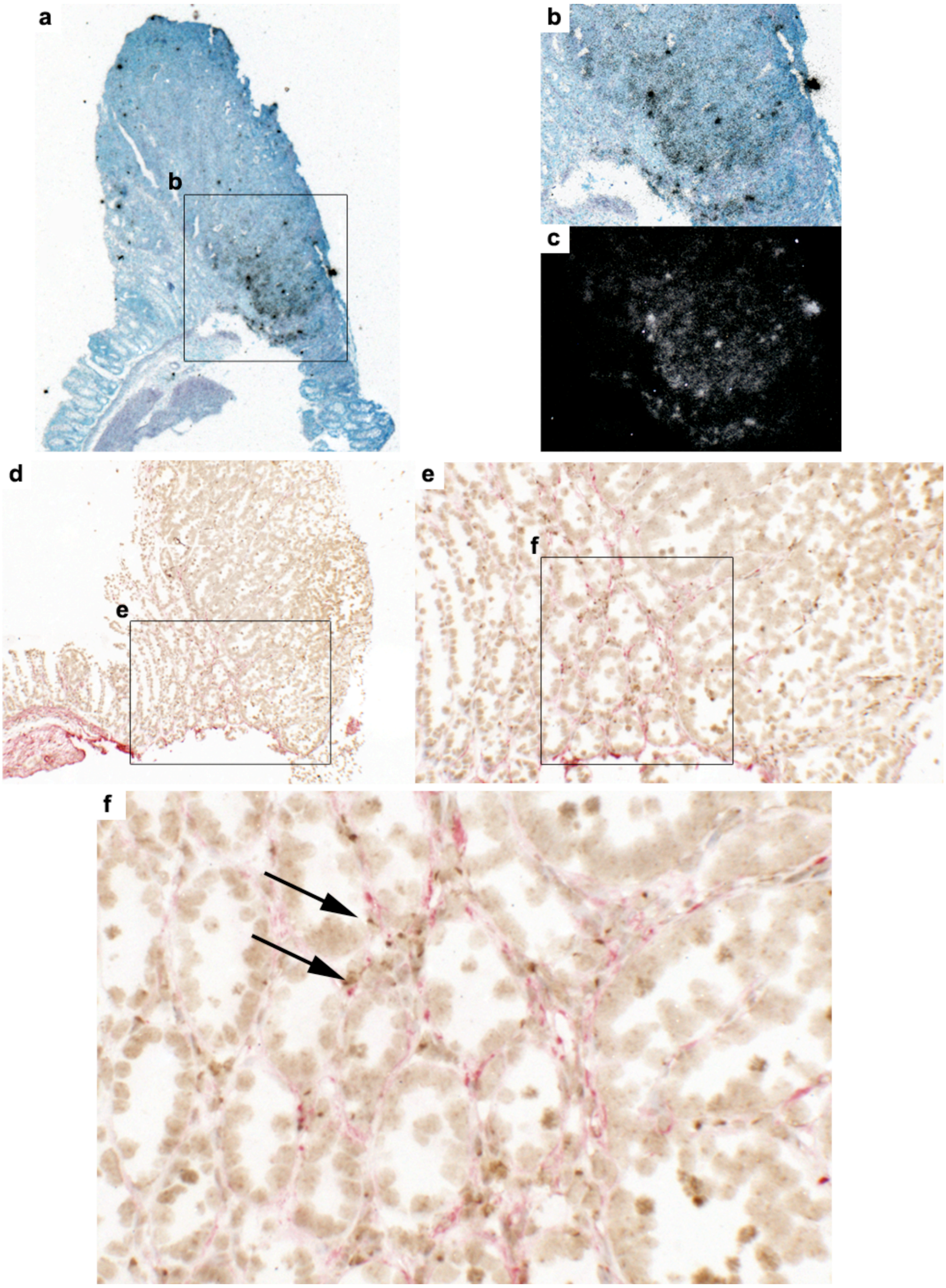

Opn mRNA was expressed by epithelial and stromal cells at the base of a colonic adenoma of an *Apc*$^{\mathrm{Min/+}}$ mouse transplanted with *Apc*$^{\mathrm{Min/+}}$ mouse BM at 1 month post BMTx (boxed; **a**). This corresponded to a nearby area with enhanced α-SMA immunoreactivity (**d**; x4, **e**; x20). However, a higher magnification of this area (**f**; x40) revealed few BMD myofibroblasts (pink staining surrounding cells with a brown nuclear dot). *Opn* mRNA expression appears as black grains in bright field images (**a**; x4 **b**; x20) and white grains in dark field images (**c**; x20).

Figure 3.29: *Opn* mRNA expression and BMD-myofibroblast engraftment in an *Apc*^{1322T} mouse adenoma

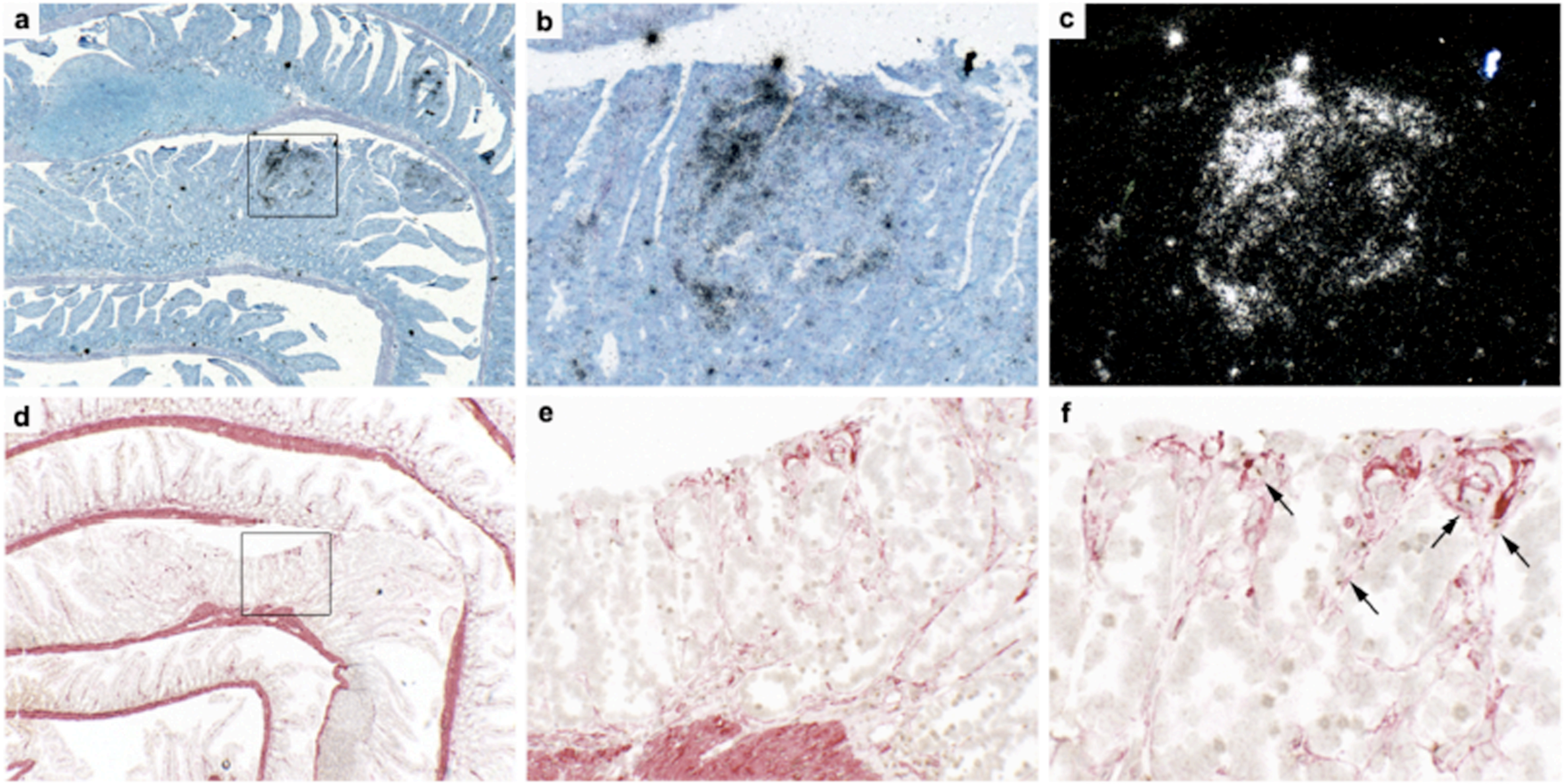

Strong epithelial and stromal *Opn* mRNA expression was observed in a large adenoma of an *Apc*^{1322T} mouse transplanted with *Apc*^{1322T} mouse BM at 1 month post BMTx (**a**; x4, **b**,**c**; x20). α-SMA IHC in a nearby serial section (**d**; x4, **e**; x20, **f**; x40) demonstrated enhanced α-SMA immunoreactivity in this area but few BMD myofibroblasts as demonstrated by α-SMA-positive cells with a brown nuclear dot indicated by arrows. *Opn* mRNA expression appears as black grains in bright field images (**a**, **b**) and white grains in dark field images (**c**).

3.6.3 *Opn* mRNA expression in *Il10*$^{-/-}$ and SPEM mouse tissues did not correlate with increased inflammation

In the inflamed mucosa of *Il10*$^{-/-}$ and SPEM mice, *Opn* mRNA expression was focal and predominantly epithelial (Figure 3.30 and Figure 3.31). Occasional stromal expression was also observed and rare expression in the muscularis propria was also observed. *Opn* mRNA expression did not increase with disease severity or disease duration in either *Il10*$^{-/-}$ or SPEM mouse tissues. As mentioned in Section 3.3.4 and 3.3.5, fibrosis or an increased presence of BMD-myofibroblasts was not observed in these tissues.

Figure 3.30: *Opn* mRNA expression in the colonic mucosa of BMTx'd *Il10*$^{-/-}$ mice

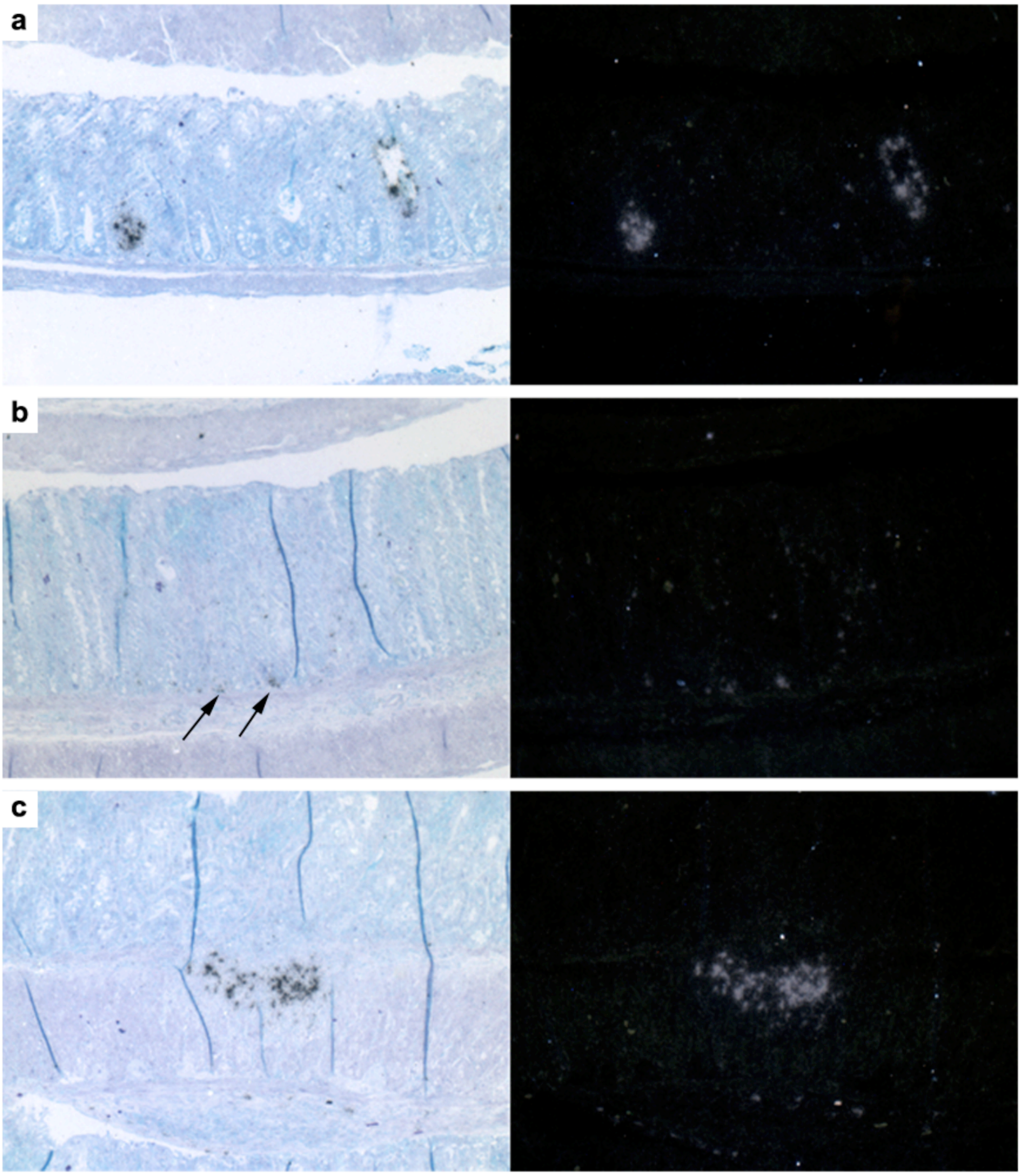

Opn mRNA was expressed in epithelial cells (**a**) and stromal cells (**b**) in the colonic mucosa of an *Il10*$^{-/-}$ mice transplanted with *Il10*$^{-/-}$ mouse BM at 5 months post BMTx. There was with no increase in *Opn* mRNA expression when normal mucosa (**a**) was compared to inflamed mucosa (**b**). Expression occurred mainly in the mucosa, however expression in the muscularis propria was also observed (**c**). *Opn* mRNA expression appears as black grains in bright field images (left) and white grains in dark field images (right). Magnification: x10.

Figure 3.31: *Opn* mRNA expression in SPEM mouse tissues

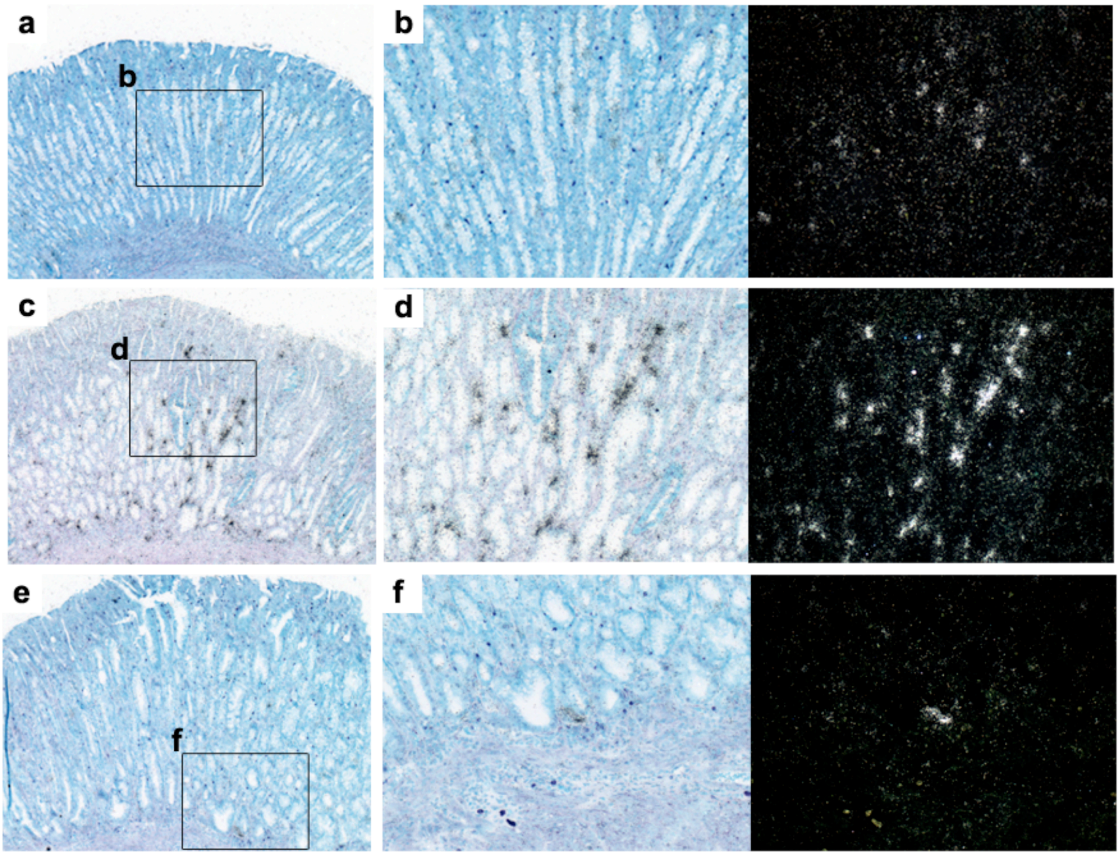

Epithelial *Opn* mRNA was focally expressed in regions of SPEM in a WT mouse transplanted with *Tff1*$^{-/-}$ mouse BM at 6 months post BMTx (**a**; x10, **b**; x20 images) and WT mice transplanted with WT BM at 12 (**c**; x10, **d**; x20 images) and at 16 months (**e**; x10, **f**; x20 images) post BMTx. *Opn* mRNA expression appears as black grains in bright field images (left hand images in **b**,**d**,**f**) and white grains in dark field images (right hand images in **b**,**d**,**f**).

CHAPTER 4

Summary discussion and future directions

Since the demonstration of BMD-neoplastic gastric glands by Houghton *et al.,* in 2004 [39], only recently have Varon *et al.,* (2011) been able to reproduce similar findings. Amid these two studies has been a seven-year endeavour with conflicting reports on the contribution of BMDCs to the intestinal epithelium. Clarifying whether GI tumours are derived from BM is important as it presents an alternative route to neoplasia that can be exploited therapeutically by inhibiting chemotaxis of BMDCs into intestinal/tumour epithelium.

In this study, BMD glands, crypts, or their respective tumours were not identified in four short and long-term mouse models of gastrointestinal tumourigenesis. The percentage of putative epithelial cells derived from BM quantified was ≤1%, concurring with the low frequencies reported in clinical and experimental BMTx studies [82, 156, 187, 188]. We also demonstrated in the inflamed mucosa of *Il10*$^{-/-}$ and *Tff1*$^{-/-}$ mice that inflammation alone does not drive BMD-epithelial engraftment as had been proposed [82]. This led us back to examining the Houghton *et al*., (2004) and Varon *et al*., (2011) studies, of which a unifying factor between the two is *Helicobacter* infection. The mechanisms of BMD- mesenchymal stem cell repopulation of gastric epithelium during *Helicobacter* infection are beginning to be uncovered. One clue lies in the elevated IFN-γ in response to infection [189, 190]. This has been recently demonstrated *in vivo,* where IFN-γ induced the proliferation and recruitment of MSCs to the stomach *via* Shh secretion and signaling [191]. A paradigm of BMD-MSC re-population has also been proposed by Houghton *et al*., (2005) in which ablation of the gastric stem cell niche *via Helicobacter* infection results in engraftment of BMDCs in the stem cell niche conferring stemness and giving rise to gastric cell lineages [40]. We propose that future research could test this theory through targeted ablation of the gastrointestinal stem cell niche in BMTx'd mice. Additional experiments could also investigate whether BMD-tumours are exclusive to pathogen-induced carcinogenesis by BM transplanting mouse models of HPV-induced cervical neoplasia or hepatitis B induced liver tumourigenesis prior to infection and analysing the BMDC contribution throughout the development of neoplasia.

We then turned our attention to examining altered stem cell dynamics within the different mouse models using *Lgr5* mRNA ISH to analyse Wnt signalling in the epithelium. As previously demonstrated, *Lgr5* mRNA was strongly expressed in normal and adenomatous intestinal tissue of $Apc^{Min/+}$ and Apc^{1322T} mice [57]. However in $Tff1^{-/-}$ and $Il10^{-/-}$ mice, which do not harbour *Apc* mutations, *Lgr5* mRNA was either weakly expressed by epithelial cells or, in the case of $Il10^{-/-}$ colonic mucosa, undetected. A possible explanation for this is that weak mRNA expression from slowly cycling $Lgr5^{+}$ cells in these tissues could not be detected by the isotopic ISH technique.

Of particular interest was investigating whether premalignant or malignant gastric lesions would have altered *Lgr5* mRNA expression, possibly associated with stem cell activity. For example, a long-held theory was that SPEM resulted from the expansion of the stem cell zone in the mucous neck region of fundic glands. However, as in normal fundic glands, we could not detect *Lgr5* mRNA in SPEM. As with previous *Lgr5* gene expression studies in human and mouse tissues, we could not demonstrate upregulated *Lgr5* expression in gastric metaplasia [192, 193]. In addition, during this study Nam and colleagues (2011) demonstrated through cell lineage tracing experiments that *Lgr5*$^{+}$ cells at the base of fundic glands do not give rise to SPEM lineages [194]. Moreover, another study from the same group has suggested that SPEM originates from the transdifferentiation of mature *Mist1* expressing chief cells [182].

Similarly, to the findings in SPEM mouse tissues, whilst *Tff1*$^{-/-}$ mouse adenomas exhibited cell heterogeneity and increased proliferation as previously described [28], *Lgr5* mRNA expression did not differ from normal antrum. The absence of *Lgr5* mRNA expression in premalignant and malignant gastric lesions in this study may simply be a reflection of how Wnt pathway mutations, or indications of aberrant Wnt signalling, are rarely observed in human gastric cancers [195]. Therefore, we propose that future experiments could investigate the possibility of inflammation-based gastric tumours being derived from a stem cell population at the base of antral glands that express Villin-promoter (Villin-promoter+). This is because, the normally quiescent Villin-promoter+ stem cells have been demonstrated to become highly proliferative and generate all cell lineages in response to IFN-γ [196]. Analysis in *Tff1*$^{-/-}$ mouse adenomas could be a good starting point to test this hypothesis, as *Tff1*$^{-/-}$ mouse adenomas develop in an inflammatory context as a consequence of absent TFF1 regulation of the NF-KB signalling pathway [33]. Therefore, we envision an experiment with two aims. The first to compare IFN-γ secretion in *Tff1*$^{-/-}$ mouse adenomas compared to normal antrum and the second to examine Villin-promoter mRNA expression in these tissues. Our hypothesis would be that *Tff1*$^{-/-}$ mouse antrum has an elevated level of IFN-γ as a consequence of chronic inflammation which induces the proliferation of Villin-promoter+ stem cells that give rise all antral cell lineages that make up the heterogeneous cell population of *Tff1*$^{-/-}$ mouse adenomas.

Outside of the tumour epithelium, we demonstrated a significant contribution of BMD-myofibroblasts to the tumour stroma, as in previous studies [37, 92]. We demonstrated that tumour burden was a driver of BMD-SEMF recruitment in *Apc*^{1322T} small intestinal adenomas, with increased recruitment into larger adenomas compared to smaller ones. The presence of desmoplasia or fibrosis also appeared to be a driving factor in BMD-myofibroblast engraftment. For example, the presence of BMD-SEMFs increased with the presence of desmoplasia in *Tff1*$^{-/-}$ mouse antral pyloric adenomas. In contrast, we could not demonstrate a significant increase in *Tff1*$^{-/-}$ mouse dysplastic lesions. We also examined whether chronic inflammation, which was also a feature of *Tff1*$^{-/-}$, *Il10*$^{-/-}$, and SPEM mouse pathology, was on its own a contributing factor to BMD-SEMF recruitment. Whilst, increased engraftment of colonic SEMFS has been demonstrated in areas of inflammation in colitic *Il10*$^{-/-}$ by Bamba *et al.*, (2006)[78], we did not observe a significant contribution of BMD-SEMFS in the inflamed tissues of *Il10*$^{-/-}$ and SPEM mice. A clear distinction between these tissues and the inflamed colonic mucosa observed by Bamba *et al.*, (2006) was the absence of fibrosis (as demonstrated by α-SMA immunoreactivity) in the former. The same can be said for comparison with *Tff1*$^{-/-}$ mouse adenomas. This led us to conclude that inflammation without fibrosis was insufficient to drive BMD-myofibroblast recruitment.

To investigate the mechanism of BMD-myofibroblast recruitment in neoplastic and inflamed tissues we utilised isotopic ISH to analyse *Opn* mRNA expression. *Opn* was selected from the literature due to its upregulation in inflammation [197] and malignancies [125]. Furthermore, OPN protein secreted from tumours has been shown to correlate with BMDC engraftment *in vivo* [80, 136]. *Opn* mRNA expression differed between tumours with predominantly stromal expression observed in *Apc*^{1322T} and *Apc*$^{Min/+}$ mouse adenomas and epithelial expression observed in *Tff1*$^{-/-}$ mouse adenomas. We observed increased *Opn* mRNA expression with tumour burden in *Apc*^{1322T} and *Apc*$^{Min/+}$ mouse adenomas. However it was only its expression in desmoplastic reaction sites in *Tff1*$^{-/-}$ mouse adenomas that coincided with increased BMD-myofibroblast engraftment. This particular finding suggests an epithelial-stromal interplay, where OPN secreted from *Tff1*$^{-/-}$ mouse tumour epithelial cells can chemotactically recruit BMD-myofibroblasts to meet the biological demands of the tumour stroma. Uncovering the mechanisms of this interplay is worthwhile as it presents an opportunity for therapeutic treatment in cancers where desmoplasia is a feature of pathology.

In WT mice with SPEM or colitic *Il10*$^{-/-}$ mice, *Opn* mRNA expression was unaffected by increased inflammation. This may be a reflection of a decreased demand for BMD-myofibroblasts in these tissues as *Opn* expression in tissues is strongly associated with inflammatory-associated fibrosis *in vivo* [198]. However, *Opn* mRNA expression in *Il10*$^{-/-}$ colonic mucosa was more frequently observed compared to expression in *Apc*$^{Min/+}$ and *Apc*^{1322T} mouse colonic mucosa. This suggests a global upregulation of *Opn* in *Il10*$^{-/-}$ mouse colonic mucosa where increased secreted OPN protein may play additional roles in immunoregulation and mucosal protection, as has been demonstrated in Crohn's disease patients [128, 129].

A surprising finding of this study was the development of SPEM in WT mice without *Helicobacter* infection or chemical induction. We demonstrated through IHC and ISH that the pathological features of SPEM developed in these mice was consistent with previous experimental observations. However, the reason as to why these mice developed SPEM is unknown as microbiological testing excluded the possibility of *Helicobacter* infection. Therefore, without a repeat study with further experiments, the reason as to why some of the WT mice of this study developed SPEM can only be speculated. A possibility is that damage occurred to the parietal cells of some mice *via* ionising radiation that may have caused the trans-differentiation of mature chief cells into TFF2-

expressing cells. For example, DNA damage within parietal cells may have lead to the expression of splice variant isoforms of CD44 (CD44v). CD44v expression has been demonstrated to occur as a result of SPEM and is associated with the proliferation of metaplastic cells in experimental SPEM models [199]. The latter has been the proposed mechanism behind chief cell transdifferentiation *via* CD44v interaction with xCT (a subunit of cysteine transporter xc), which promotes cysteine uptake for glutathione synthesis, which in turn promotes cell proliferation [199]. Therefore, future experiments could investigate CD44v and Mist1 expression, as well as investigating signalling pathways implicated in SPEM such as EGFR signalling [200] and PGE_2 signaling [201].

An interesting observation in SPEM mouse tissues was the earlier onset and greater disease severity was observed in WT mice that had been transplanted with *Tff1*$^{-/-}$ mouse BM. The *Tff1*$^{-/-}$→*Tff1*$^{-/-}$ and WT→*Tff1*$^{-/-}$ mouse groups did not develop SPEM most likely because they do not express TFF2 in the fundus [202]. So could the absence of TFF1 in BMTx'd immune cells played a role in accelerating SPEM in WT mice? The loss of TFF1 has been shown to result in the activation of NF-κB pathway that TFF1 suppresses [33]. This can lead to chronic inflammation caused by the overproduction of pro-inflammatory cytokines and chemokines [203]. The stimulation of inflammation by *Tff1*-deficient BMD immune cells may have played a role in accelerating and worsening SPEM in the *Tff1*$^{-/-}$→WT mouse group. For now, we can only speculate that SPEM could have arisen from radiation induced parietal cell damage or DNA damage that may have set off a molecular chain of events that led to the transdifferentiation of mature chief cells. Adding to this, we cannot fully exclude the possibility of infection with a new and/or undetected pathogen.

In conclusion the data presented in this study taken together with previous studies strongly suggest that BMD-epithelial cells do not generate tumours beyond *Helicobacter* infection, and that indeed this is an exceedingly rare phenomenon. More commonplace was the contribution of BMD-SEMFs to tumour stroma. Our findings suggest that the biological demand from increased tumour burden and desmoplasia drives engraftment. In the case of desmoplasia, our observation of increased *Opn* mRNA expression in *Tff1*$^{-/-}$ desmoplastic reaction sites coinciding with increased BMD-SEMFs suggest that OPN plays an important role in recruitment of BMD-myofibroblasts into desmoplastic reaction sites. Our observations in *Il10*$^{-/-}$ and SPEM mouse tissues also indicate that inflammation without fibrosis is insufficient to drive OPN-mediated chemotaxis of BMD-myofibroblasts. Some minor findings of this study were the demonstration of unaffected *Lgr5* mRNA expression in SPEM and *Tff1*$^{-/-}$ mouse adenomas and the development of SPEM without *Helicobacter* or chemical induction.

A table comparing the hypotheses generated before and during this study with their experimental findings can be found in Table 4.1 and Table 4.2.

Table 4.1: A comparison of hypotheses formed at the commencement of this study and the conclusions derived from the present studies

Hypothesis at the commencement of this study	**Experimental conclusions**
BMD-glands, crypts, and tumours would occur in absence of *Helicobacter* infection as a result of inflammation or increased tumour burden.	BMD-glands, crypts, and tumours were not observed in any of the mouse models.
BMDCs could contribute to both benign and malignant epithelial cells.	Both benign and malignant epithelial cells were observed (albeit inconclusively identified). However, these were rare events making up ≤ 1.0% of cells in a 150,000μm^2 area of epithelium.
Engraftment of BMD-epithelial cells would be driven by either inflammation or tumour burden.	Neither inflammation or tumour burden affected BMD-epithelial engraftment.
BMD-myofibroblasts would home into areas of increased tumour burden.	In *Apc*^{1322T} tissues, the percentage of SEMFs derived from BM increased in larger adenomas compared to smaller adenomas. This suggests that BMD-myofibroblasts recruitment is determined by tumour burden in some cases.
Opn mRNA expression in tumours would correlate with increased BMD-myofibroblast engraftment.	Increased *Opn* mRNA expression was observed in *Tff1*$^{-/-}$, *Apc*$^{Min/+}$, and *Apc*^{1322T} mouse adenomas. However, whether this correlated with BMD-myofibroblast engraftment was only suggested in *Tff1*$^{-/-}$ mouse adenomas, where *Opn* mRNA expression occurred at desmoplastic reaction sites, which had an increased presence of BMD-myofibroblasts.
Aberrant *Opn* mRNA expression in inflamed tissues would correlate with increased BMD-myofibroblast engraftment.	Increased *Opn* mRNA expression was not observed in areas of increased inflammation or disease severity in *Il10*$^{-/-}$ or SPEM tissues. Moreover, an increase of BMD-myofibroblasts was not observed in areas where *Opn* mRNA expression was identified.

Table 4.1: A comparison of hypotheses formed at the commencement of this study and the conclusions derived from the present studies (continued)

Tff1$^{-/-}$ mouse adenomas would have upregulated *Lgr5* mRNA expression as a result of aberrant Wnt signalling promoting a stem cell phenotype.	Whilst an increased cell proliferation and a heterogeneous cell population were observed in *Tff1*$^{-/-}$ mouse adenomas, isotopic ISH demonstrated that *Lgr5* mRNA expression was limited to the base of adenomatous pyloric glands. This finding suggests two possibilities. The first is that adenomatous cells originating from the stem cell niche at the base of antral glands differentiated and ceased expressing *Lgr5.* The second possibility is that any stem-cell activity in *Tff1*$^{-/-}$ mouse adenomas is the result of the increased proliferation of Villin-promoter^{+} stem cells in the isthmus in response to increased IFN-γ due to the inflammation present in *Tff1*$^{-/-}$ mouse adenomas.

Figure 4.2: A comparison of hypotheses formed during this study and the conclusions derived from the present studies

Hypothesis formed during this study	**Experimental conclusions**
Lgr5 mRNA expression would increase in SPEM mouse tissues compared to normal fundic tissue in mice.	*Lgr5* mRNA expression could not be detected in SPEM fundic glands.
BMD-gastric SEMF engraftment would increase in SPEM due to the inflammation present.	Very little lamina propria was observed in SPEM tissues indicating that fibrosis was not a part of the disease pathology. Very few BMD-myofibroblasts were observed.
Opn mRNA expression would increase in SPEM tissues due to the inflammation present.	Opn mRNA expression in SPEM tissues was unaffected by inflammation severity or disease duration.

APPENDIX

A.1 Method development: fluorescent *in situ* hybridisation to demonstrate cell fusion

We attempted to investigate whether cell fusion-mediated BM engraftment of cells occurs in our mouse models using fluorescent *in situ* hybridisation (FISH). Various mouse chromosome probes and pancentromere probes were tested using FISH with the aim that one of these probes could be combined with Y-chromosome FISH to demonstrate polyploidy (Table A.2). The standard *in situ* hybridisation protocol (described in Section 2.4.4) was used with the following changes:

- A pepsin digestion time trial was carried out for each tissue block and for each probe tested. This would entail pepsin digestion of different sections of the same tissue blocks at various time points (for example, 5, 10, and 15 minutes).
- Sections were denatured at 80°C for pancentromeric probes.
- Mounted slides were kept refrigerated at 4°C in the dark until viewing with fluorescent microscopy.

The author and other collaborators were unable to demonstrate that X-chromosome, various chromosomes, or the use panentromeric probes as reliable methods of demonstrating cell fusion. Figure A.3 demonstrates the inconsistent results of X and Y-chromosome FISH carried out by the author and Rosemary Jeffrey. However, considering the reliability of the mouse Y-chromosome probe, future experiments to analyse cell fusion using sex mismatched BMTX may be facilitated by engineering the expression of GFP or beta galactosidase in host cells. Fused cells therefore would then express both the Y-chromosome and the host cell marker.

Table A.1: Details of FISH DNA probes tested as cell fusion markers

Probe	Supplier	Conclusions	Tester
Chromosome 1	Cambio	Unreliable. Chromosome signal often bulky and difficult to interpret.	RJ
Chromosome 3	Cambio		RJ
Chromosome 17	Cambio		RJ
X-chromosome	Cambio	Inconsistent, unreliable	ALB, CYL, RJ
	ID labs		ALB, RJ
Y-chromosome FITC labelled	Cambio	Reliable.	ALB, CYL, RJ
Y-chromosome IDYE495 labelled	ID labs	To be used only for fluorescence. Cannot be used in place of Cambio FITC-labelled Y chromosome for combined immunohistochemistry/Y-chromosome *in situ* hybridisation.	ALB, RJ
Pancentromeres	Cambio	Not useful for demonstrating cell fusion.	ALB
Pancentromeres	ID labs		

ALB Arielle Le Brenne; **CYL** Chung Yin Lee; **RJ** Rosemary Jeffery

Figure A.1: Testing of X and Y-chromosome FISH

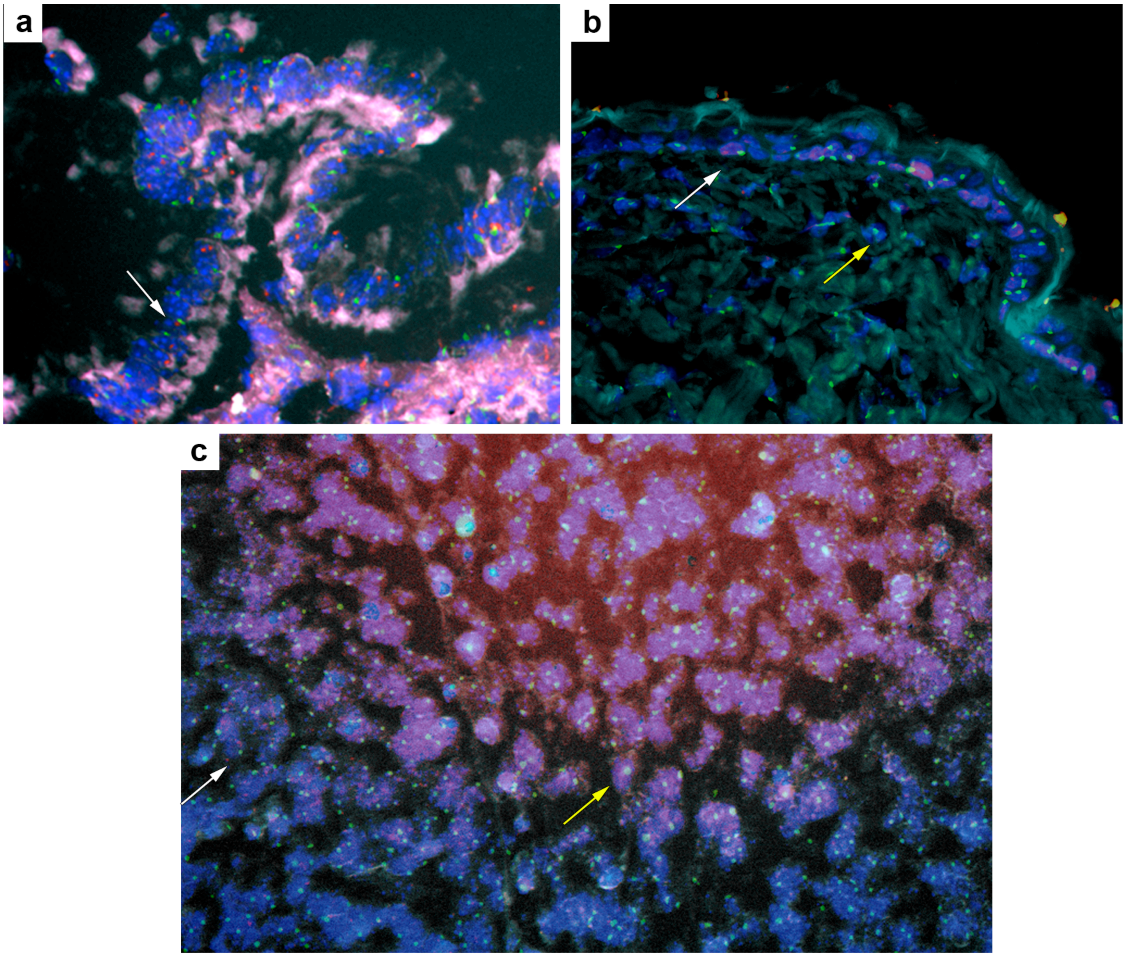

X/Y-chromosome FISH carried out by the author (**a**, **b**) and Rosemary Jeffrey (**c**). (**a**,**b**) X/Y-chromosome FISH on small intestinal tissue of a male stock WT mouse. In one assay (**a**; x10) X and Y-chromosomes are easily identified (red and green dots, respectively), whereas in another (b; x40) very few cells contain cells with both X and Y (white arrow) and the majority of cells contain only the Y-chromosome (yellow arrow). (**c**; x10) Combined X/Y-chromosome FISH on spleen of female mouse transplanted with male BM. Y-chromosome is observed throughout, whereas cells containing X-chromosome occurs only occasionally (red dots; yellow arrow). Image in **c** kindly provided by Rosemary Jeffery.

A.2 GKN2 protein expression is gradually lost with the progression of dysplasia to adenomas in *Tff1*$^{-/-}$ mice

Analysis of GKN2 protein, which exists as a heterodimer with TFF1 protein in gastric secretions, revealed a gradual loss of GKN2 from 6 months post BMTx onwards (Figure A.2).

Figure A.2: GKN2 protein expression in the gastric mucosa of BMTx'd WT and *Tff1*$^{-/-}$ mice

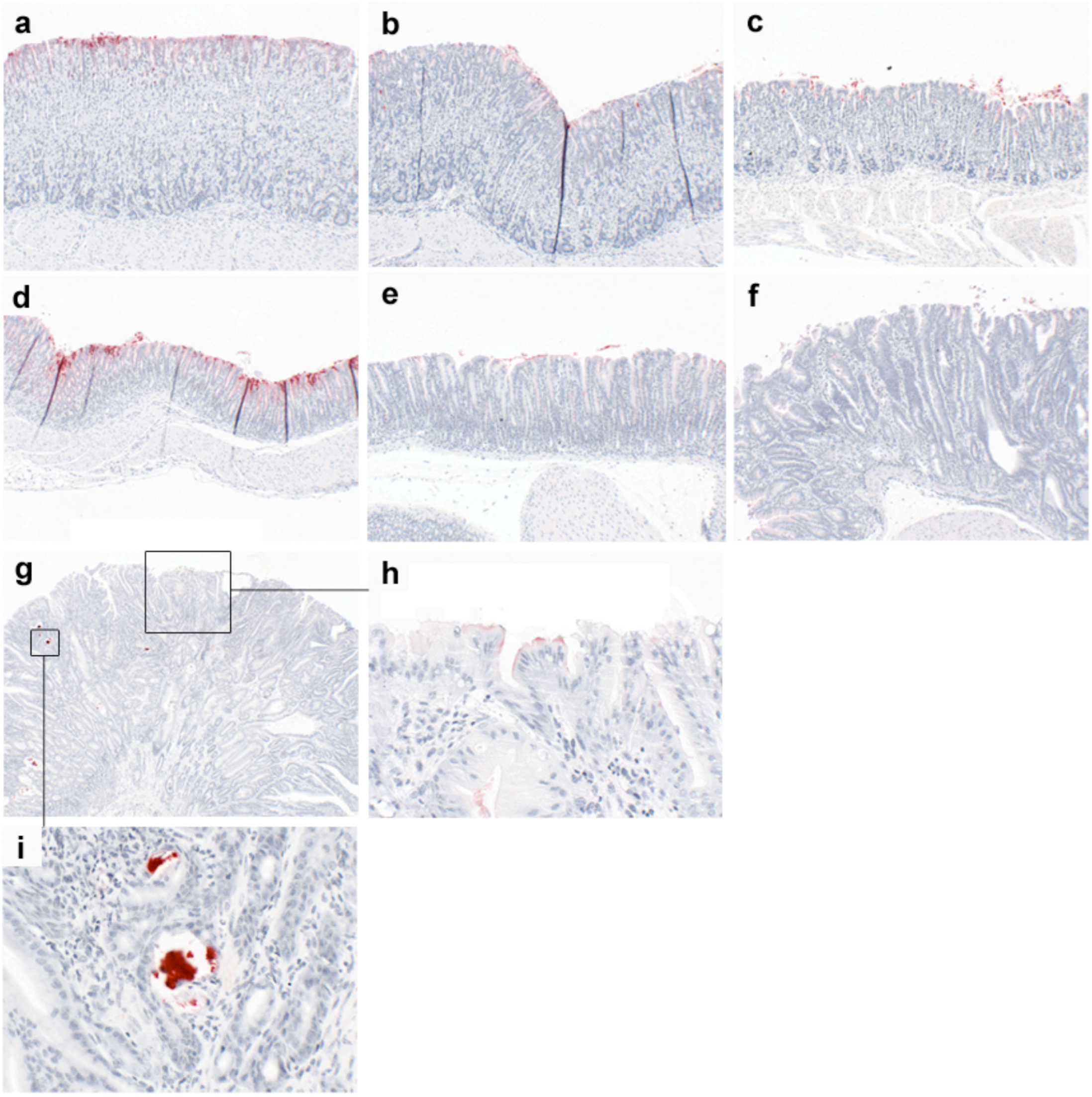

In a WT mouse transplanted with WT mouse BM at 6 months post BMTx, GKN2 protein (pink staining) is expressed by foveolar cells along the fundus (**a**) pylorus (**d**). A slight decrease in GKN2 expression was observed in the fundus of a *Tff1*$^{-/-}$ mice mouse transplanted with *Tff1*$^{-/-}$ mouse BM at 6 months (**b**) and 12 months (**c**) post BMTx. The decrease in GKN2 expression is more pronounced in the antrum, where there is significant decrease in normal (**e**) and dyplastic (**f**) antrum in a *Tff1*$^{-/-}$mouse transplanted with *Tff1*$^{-/-}$ mouse BM 6 months post BMTx. In an antral pyloric adenoma of a *Tff1*$^{-/-}$ mouse transplanted with *Tff1*$^{-/-}$ mouse BM at 12 months post BMTx (**g**), GKN2 is expressed in rare foci (**h**) or pooled in cysts (**i**). **a**-**f**: x10, **g**: x4, **h**: x40.

A.2.1 Discussion and conclusions

A minor finding of this study was the observation of a significant decrease in GKN2 protein expression in the fundus and normal antrum of *Tff1*$^{-/-}$ mouse groups. As dysplastic lesions progressed into adenomas in *Tff1*$^{-/-}$ mice a successive loss of GKN2 protein was observed. One explanation for this finding is that as TFF1 and GKN2 are co-secreted as a heterodimer, the decrease of GKN2 in absence of TFF1 may be due to destabilisation of the protein or decreased resistance against proteolysis or gastric acid. To our knowledge the loss of GKN2 has not been reported in *Tff1*$^{-/-}$ mice to date. However, our findings support observations from *in vivo* and human gastric tumour studies. For example, a significant decrease in *Gkn2* mRNA expression has also been observed in the antral tumours of the *Gp130*$^{F/F}$ mouse model of gastric tumourigenesis [181]. In human gastric adenocarcinoma, GKN2 and TFF1 are downregulated with decreased GKN2 observed in very early tumours [34, 35]. Moreover, expression of TFF1 in gastric tumours in the absence of GKN2 is associated with lymph node metastasis and poor clinical outcome [34]. To the point, overexpression of TFF1 has been frequently observed in tumour cells [204]. It has been suggested the pro-migratory and anti-apoptotic effects conferred by TFF1 that are necessary for mucosal restitution under normal conditions are responsible for the migration of tumour cells when TFF1 is aberrantly expressed. These studies suggest that the formation of the GKN2-TFF1 heterodimer is necessary for the tumour suppressor activity of TFF1 or that GKN2 itself acts as a gastric tumour suppressor. If the latter is the case, then the decrease in GKN2 resulting from TFF1 deficiency in *Tff1*$^{-/-}$ mice may be the cause of the development of antral pyloric adenomas in these mice.

BIBLIOGRAPHY

1. Westbrook, A.M., A. Szakmary, and R.H. Schiestl, *Mechanisms of intestinal inflammation and development of associated cancers: lessons learned from mouse models.* Mutation research, 2010. **705**(1): p. 40-59.

2. Schetter, A.J., N.H. Heegaard, and C.C. Harris, *Inflammation and cancer: interweaving microRNA, free radical, cytokine and p53 pathways.* Carcinogenesis, 2010. **31**(1): p. 37-49.

3. Abbas, O. and M. Mahalingam, *Desmoplasia: not always a bad thing.* Histopathology, 2011. **58**(5): p. 643-59.

4. Erez, N., et al., *Cancer-Associated Fibroblasts Are Activated in Incipient Neoplasia to Orchestrate Tumor-Promoting Inflammation in an NF-kappaB-Dependent Manner.* Cancer cell, 2010. **17**(2): p. 135-47.

5. Vermeulen, L., et al., *Wnt activity defines colon cancer stem cells and is regulated by the microenvironment.* Nature cell biology, 2010. **12**(5): p. 468-76.

6. Orimo, A., et al., *Stromal fibroblasts present in invasive human breast carcinomas promote tumor growth and angiogenesis through elevated SDF-1/CXCL12 secretion.* Cell, 2005. **121**(3): p. 335-48.

7. Yang, F., et al., *Stromal expression of connective tissue growth factor promotes angiogenesis and prostate cancer tumorigenesis.* Cancer research, 2005. **65**(19): p. 8887-95.

8. Olumi, A.F., et al., *Carcinoma-associated fibroblasts direct tumor progression of initiated human prostatic epithelium.* Cancer research, 1999. **59**(19): p. 5002-11.

9. Ferlay J, et al. *GLOBOCAN 2008 v1.2*. Cancer Incidence and Mortality Worldwide 2010 November 2012]; IARC CancerBase No. 10 [Available from: http://globocan.iarc.fr. .

10. Correa, P. and J. Houghton, *Carcinogenesis of Helicobacter pylori.* Gastroenterology, 2007. **133**(2): p. 659-72.

11. Hartgrink, H.H., et al., *Gastric cancer.* Lancet, 2009. **374**(9688): p. 477-90.

12. Gylling, A., et al., *Is gastric cancer part of the tumour spectrum of hereditary non-polyposis colorectal cancer? A molecular genetic study.* Gut, 2007. **56**(7): p. 926-33.

13. Vasovcak, P., et al., *Mutations in STK11 gene in Czech Peutz-Jeghers patients.* BMC medical genetics, 2009. **10**: p. 69.

14. Blair, V., et al., *Hereditary diffuse gastric cancer: diagnosis and management.* Clinical gastroenterology and hepatology : the official clinical practice journal of the American Gastroenterological Association, 2006. **4**(3): p. 262-75.

15. Radulescu, S., et al., *Acute WNT signalling activation perturbs differentiation within the adult stomach and rapidly leads to tumour formation.* Oncogene, 2012.

16. Forman, D. and V.J. Burley, *Gastric cancer: global pattern of the disease and an overview of environmental risk factors.* Best practice & research. Clinical gastroenterology, 2006. **20**(4): p. 633-49.

17. Brenner, H., D. Rothenbacher, and V. Arndt, *Epidemiology of stomach cancer.* Methods in molecular biology, 2009. **472**: p. 467-77.

18. Lamb, A. and L.F. Chen, *Role of the Helicobacter pylori-induced inflammatory response in the development of gastric cancer.* Journal of cellular biochemistry, 2013. **114**(3): p. 491-7.

19. Chaturvedi, M.M., et al., *NF-kappaB addiction and its role in cancer: 'one size does not fit all'.* Oncogene, 2011. **30**(14): p. 1615-30.

20. Barker, N., et al., *Lgr5(+ve) stem cells drive self-renewal in the stomach and build long-lived gastric units in vitro.* Cell Stem Cell, 2010. **6**(1): p. 25-36.

21. Kim, T.H. and R.A. Shivdasani, *Notch signaling in stomach epithelial stem cell homeostasis.* The Journal of experimental medicine, 2011. **208**(4): p. 677-88.

22. Schepers, A. and H. Clevers, *Wnt signaling, stem cells, and cancer of the gastrointestinal tract.* Cold Spring Harbor perspectives in biology, 2012. **4**(4): p. a007989.

23. Sato, H., et al., *Frequent epigenetic inactivation of DICKKOPF family genes in human gastrointestinal tumors.* Carcinogenesis, 2007. **28**(12): p. 2459-66.

24. Koch, U. and F. Radtke, *Notch and cancer: a double-edged sword.* Cellular and molecular life sciences : CMLS, 2007. **64**(21): p. 2746-62.

25. Kopan, R. and M.X. Ilagan, *The canonical Notch signaling pathway: unfolding the activation mechanism.* Cell, 2009. **137**(2): p. 216-33.

26. Brzozowa, M., et al., *Role of Notch signaling pathway in gastric cancer pathogenesis.* Contemporary oncology, 2013. **17**(1): p. 1-5.

27. Vries, R.G., M. Huch, and H. Clevers, *Stem cells and cancer of the stomach and intestine.* Mol Oncol, 2010. **4**(5): p. 373-84.

28. Karam, S.M., C. Tomasetto, and M.C. Rio, *Amplification and invasiveness of epithelial progenitors during gastric carcinogenesis in trefoil factor 1 knockout mice.* Cell Prolif, 2008. **41**(6): p. 923-35.

29. Carvalho, R., et al., *Loss of heterozygosity and promoter methylation, but not mutation, may underlie loss of TFF1 in gastric carcinoma.* Lab Invest, 2002. **82**(10): p. 1319-26.

30. Tomita, H., et al., *Inhibition of gastric carcinogenesis by the hormone gastrin is mediated by suppression of TFF1 epigenetic silencing.* Gastroenterology, 2011. **140**(3): p. 879-91.

31. Kjellev, S., *The trefoil factor family - small peptides with multiple functionalities.* Cell Mol Life Sci, 2009. **66**(8): p. 1350-69.

32. Lefebvre, O., et al., *Gastric mucosa abnormalities and tumorigenesis in mice lacking the pS2 trefoil protein.* Science, 1996. **274**(5285): p. 259-62.

33. Soutto, M., et al., *Loss of TFF1 is associated with activation of NF-kappaB-mediated inflammation and gastric neoplasia in mice and humans.* J Clin Invest, 2011. **121**(5): p. 1753-67.

34. May, F.E., S.M. Griffin, and B.R. Westley, *The trefoil factor interacting protein TFIZ1 binds the trefoil protein TFF1 preferentially in normal gastric mucosal cells but the co-expression of these proteins is deregulated in gastric cancer.* The international journal of biochemistry & cell biology, 2009. **41**(3): p. 632-40.

35. Moss, S.F., et al., *Decreased expression of gastrokine 1 and the trefoil factor interacting protein TFIZ1/GKN2 in gastric cancer: influence of tumor histology and relationship to prognosis.* Clinical cancer research : an official journal of the American Association for Cancer Research, 2008. **14**(13): p. 4161-7.

36. Worthley, D.L., et al., *Human gastrointestinal neoplasia-associated myofibroblasts can develop from bone marrow-derived cells following allogeneic stem cell transplantation.* Stem Cells, 2009. **27**(6): p. 1463-8.

37. Quante, M., et al., *Bone marrow-derived myofibroblasts contribute to the mesenchymal stem cell niche and promote tumor growth.* Cancer cell, 2011. **19**(2): p. 257-72.

38. Ferrand, J., et al., *Helicobacter pylori infection of gastrointestinal epithelial cells in vitro induces mesenchymal stem cell migration through an NF-kappaB-dependent pathway.* PloS one, 2011. **6**(12): p. e29007.

39. Houghton, J., et al., *Gastric cancer originating from bone marrow-derived cells.* Science, 2004. **306**(5701): p. 1568-71.

40. Houghton, J. and T.C. Wang, *Helicobacter pylori and gastric cancer: a new paradigm for inflammation-associated epithelial cancers.* Gastroenterology, 2005. **128**(6): p. 1567-78.

41. Jemal, A., et al., *Global cancer statistics.* CA: a cancer journal for clinicians, 2011. **61**(2): p. 69-90.

42. Curado, M., et al., *Cancer Incidence in Five Continents* 2007, IARC Scientific Publication: Lyon.

43. Pan, S.Y. and H. Morrison, *Epidemiology of cancer of the small intestine.* World journal of gastrointestinal oncology, 2011. **3**(3): p. 33-42.

44. Lin, O.S., *Acquired risk factors for colorectal cancer.* Methods in molecular biology, 2009. **472**: p. 361-72.

45. Dyson, J.K. and M.D. Rutter, *Colorectal cancer in inflammatory bowel disease: what is the real magnitude of the risk?* World journal of gastroenterology : WJG, 2012. **18**(29): p. 3839-48.

46. Barker, N. and H. Clevers, *Mining the Wnt pathway for cancer therapeutics.* Nat Rev Drug Discov, 2006. **5**(12): p. 997-1014.

47. Fearon, E.R. and B. Vogelstein, *A genetic model for colorectal tumorigenesis.* Cell, 1990. **61**(5): p. 759-67.

48. Cardoso, J., et al., *Expression and genomic profiling of colorectal cancer.* Biochimica et biophysica acta, 2007. **1775**(1): p. 103-37.

49. Moser, A.R., H.C. Pitot, and W.F. Dove, *A dominant mutation that predisposes to multiple intestinal neoplasia in the mouse.* Science, 1990. **247**(4940): p. 322-4.

50. Boivin, G.P., et al., *Pathology of mouse models of intestinal cancer: consensus report and recommendations.* Gastroenterology, 2003. **124**(3): p. 762-77.

51. Albuquerque, C., et al., *The 'just-right' signaling model: APC somatic mutations are selected based on a specific level of activation of the beta-catenin signaling cascade.* Hum Mol Genet, 2002. **11**(13): p. 1549-60.

52. Lamlum, H., et al., *The type of somatic mutation at APC in familial adenomatous polyposis is determined by the site of the germline mutation: a new facet to Knudson's 'two-hit' hypothesis.* Nat Med, 1999. **5**(9): p. 1071-5.

53. Crabtree, M., et al., *Refining the relation between 'first hits' and 'second hits' at the APC locus: the 'loose fit' model and evidence for differences in somatic mutation spectra among patients.* Oncogene, 2003. **22**(27): p. 4257-65.

54. Rubinfeld, B., et al., *Loss of beta-catenin regulation by the APC tumor suppressor protein correlates with loss of structure due to common somatic mutations of the gene.* Cancer Res, 1997. **57**(20): p. 4624-30.

55. Pollard, P., et al., *The Apc 1322T mouse develops severe polyposis associated with submaximal nuclear beta-catenin expression.* Gastroenterology, 2009. **136**(7): p. 2204-2213 e1-13.

56. Tomita, H., et al., *Development of gastric tumors in Apc(Min/+) mice by the activation of the beta-catenin/Tcf signaling pathway.* Cancer research, 2007. **67**(9): p. 4079-87.

57. Lewis, A., et al., *Severe polyposis in Apc(1322T) mice is associated with submaximal Wnt signalling and increased expression of the stem cell marker Lgr5.* Gut, 2010. **59**(12): p. 1680-6.

58. Mattar, M.C., et al., *Current management of inflammatory bowel disease and colorectal cancer.* Gastrointestinal cancer research : GCR, 2011. **4**(2): p. 53-61.

59. Ullman, T.A. and S.H. Itzkowitz, *Intestinal inflammation and cancer.* Gastroenterology, 2011. **140**(6): p. 1807-16.

60. Gillespie, E., et al., *Plasminogen activator inhibitor-1 is increased in colonic epithelial cells from patients with colitis-associated cancer.* Journal of Crohn's & colitis, 2013. **7**(5): p. 403-11.

61. Nunes, T., et al., *Familial aggregation in inflammatory bowel disease: is it genes or environment?* World J Gastroenterol, 2011. **17**(22): p. 2715-22.

62. Basu, D., et al., *Impact of race and ethnicity on inflammatory bowel disease.* Am J Gastroenterol, 2005. **100**(10): p. 2254-61.

63. Glocker, E.O., et al., *Inflammatory bowel disease and mutations affecting the interleukin-10 receptor.* N Engl J Med, 2009. **361**(21): p. 2033-45.

64. Wolk, K., et al., *Cutting edge: immune cells as sources and targets of the IL-10 family members?* J Immunol, 2002. **168**(11): p. 5397-402.

65. Liu, B., S.L. Tonkonogy, and R.B. Sartor, *Antigen-presenting cell production of IL-10 inhibits T-helper 1 and 17 cell responses and suppresses colitis in mice.* Gastroenterology, 2011. **141**(2): p. 653-62, 662 e1-4.

66. Unutmaz, D. and B. Pulendran, *The gut feeling of Treg cells: IL-10 is the silver lining during colitis.* Nat Immunol, 2009. **10**(11): p. 1141-3.

67. Joyce, D.A., et al., *Two inhibitors of pro-inflammatory cytokine release, interleukin-10 and interleukin-4, have contrasting effects on release of soluble p75 tumor necrosis factor receptor by cultured monocytes.* Eur J Immunol, 1994. **24**(11): p. 2699-705.

68. Asadullah, K., W. Sterry, and H.D. Volk, *Interleukin-10 therapy--review of a new approach.* Pharmacol Rev, 2003. **55**(2): p. 241-69.

69. Lacraz, S., et al., *IL-10 inhibits metalloproteinase and stimulates TIMP-1 production in human mononuclear phagocytes.* J Clin Invest, 1995. **96**(5): p. 2304-10.

70. Durant, L., et al., *Diverse targets of the transcription factor STAT3 contribute to T cell pathogenicity and homeostasis.* Immunity, 2010. **32**(5): p. 605-15.

71. Takeda, K., et al., *Enhanced Th1 activity and development of chronic enterocolitis in mice devoid of Stat3 in macrophages and neutrophils.* Immunity, 1999. **10**(1): p. 39-49.

72. El Kasmi, K.C., et al., *General nature of the STAT3-activated anti-inflammatory response.* J Immunol, 2006. **177**(11): p. 7880-8.

73. Williams, L., et al., *Signal transducer and activator of transcription 3 is the dominant mediator of the anti-inflammatory effects of IL-10 in human macrophages.* J Immunol, 2004. **172**(1): p. 567-76.

74. Sabat, R., et al., *Biology of interleukin-10.* Cytokine Growth Factor Rev, 2010. **21**(5): p. 331-44.

75. Kuhn, R., et al., *Interleukin-10-deficient mice develop chronic enterocolitis.* Cell, 1993. **75**(2): p. 263-74.

76. Berg, D.J., et al., *Enterocolitis and colon cancer in interleukin-10-deficient mice are associated with aberrant cytokine production and CD4(+) TH1-like responses.* J Clin Invest, 1996. **98**(4): p. 1010-20.

77. Lindsay, J.O., et al., *Local delivery of adenoviral vectors encoding murine interleukin 10 induces colonic interleukin 10 production and is therapeutic for murine colitis.* Gut, 2003. **52**(7): p. 981-7.

78. Bamba, S., et al., *Bone marrow transplantation ameliorates pathology in interleukin-10 knockout colitic mice.* J Pathol, 2006. **209**(2): p. 265-73.

79. Panes, J., I. Ordas, and E. Ricart, *Stem cell treatment for Crohn's disease.* Expert Rev Clin Immunol, 2010. **6**(4): p. 597-605.

80. Davis, C., et al., *Hematopoietic derived cell infiltration of the intestinal tumor microenvironment in Apc Min/+ mice.* Microsc Microanal, 2011. **17**(4): p. 528-39.

81. Brittan, M., et al., *A regenerative role for bone marrow following experimental colitis: contribution to neovasculogenesis and myofibroblasts.* Gastroenterology, 2005. **128**(7): p. 1984-95.

82. Matsumoto, T., et al., *Increase of bone marrow-derived secretory lineage epithelial cells during regeneration in the human intestine.* Gastroenterology, 2005. **128**(7): p. 1851-67.

83. Okamoto, R., et al., *Damaged epithelia regenerated by bone marrow-derived cells in the human gastrointestinal tract.* Nat Med, 2002. **8**(9): p. 1011-7.

84. Ng, Y.Y., et al., *Isolation of human and mouse hematopoietic stem cells.* Methods in molecular biology, 2009. **506**: p. 13-21.

85. Dominici, M., et al., *Minimal criteria for defining multipotent mesenchymal stromal cells. The International Society for Cellular Therapy position statement.* Cytotherapy, 2006. **8**(4): p. 315-7.

86. Caplan, A.I., *Adult mesenchymal stem cells for tissue engineering versus regenerative medicine.* Journal of cellular physiology, 2007. **213**(2): p. 341-7.

87. Kassis, I., et al., *Isolation of mesenchymal stem cells from G-CSF-mobilized human peripheral blood using fibrin microbeads.* Bone marrow transplantation, 2006. **37**(10): p. 967-76.

88. Wexler, S.A., et al., *Adult bone marrow is a rich source of human mesenchymal 'stem' cells but umbilical cord and mobilized adult blood are not.* British journal of haematology, 2003. **121**(2): p. 368-74.

89. Chong, P.P., et al., *Human peripheral blood derived mesenchymal stem cells demonstrate similar characteristics and chondrogenic differentiation potential to bone marrow derived mesenchymal stem cells.* Journal of orthopaedic research : official publication of the Orthopaedic Research Society, 2012. **30**(4): p. 634-42.

90. Khoo, C.P., P. Pozzilli, and M.R. Alison, *Endothelial progenitor cells and their potential therapeutic applications.* Regenerative medicine, 2008. **3**(6): p. 863-76.

91. Khan, S.S., M.A. Solomon, and J.P. McCoy, Jr., *Detection of circulating endothelial cells and endothelial progenitor cells by flow cytometry.* Cytometry. Part B, Clinical cytometry, 2005. **64**(1): p. 1-8.

92. Direkze, N.C., et al., *Bone marrow contribution to tumor-associated myofibroblasts and fibroblasts.* Cancer Res, 2004. **64**(23): p. 8492-5.

93. Spyridonidis, A., et al., *Evidence for a graft-versus-mast-cell effect after allogeneic bone marrow transplantation.* Bone marrow transplantation, 2004. **34**(6): p. 515-9.

94. Roziakova, L., et al., *Secondary malignancies after hematopoietic stem cell transplantation.* Neoplasma, 2011. **58**(1): p. 1-8.

95. Alison, M.R., S. Lim, and J.M. Houghton, *Bone marrow-derived cells and epithelial tumours: more than just an inflammatory relationship.* Current opinion in oncology, 2009. **21**(1): p. 77-82.

96. Takemoto, Y., et al., *Operative injury accelerates tumor growth by inducing mobilization and recruitment of bone marrow-derived stem cells.* Surgery, 2011. **149**(6): p. 792-800.

97. Younes, R.N., A. Rogatko, and M.F. Brennan, *The influence of intraoperative hypotension and perioperative blood transfusion on disease-free survival in patients with complete resection of colorectal liver metastases.* Annals of surgery, 1991. **214**(2): p. 107-13.

98. Spring, H., et al., *Chemokines direct endothelial progenitors into tumor neovessels.* Proceedings of the National Academy of Sciences of the United States of America, 2005. **102**(50): p. 18111-6.

99. Nolan, D.J., et al., *Bone marrow-derived endothelial progenitor cells are a major determinant of nascent tumor neovascularization.* Genes & development, 2007. **21**(12): p. 1546-58.

100. Lyden, D., et al., *Impaired recruitment of bone-marrow-derived endothelial and hematopoietic precursor cells blocks tumor angiogenesis and growth.* Nature medicine, 2001. **7**(11): p. 1194-201.

101. Rajantie, I., et al., *Adult bone marrow-derived cells recruited during angiogenesis comprise precursors for periendothelial vascular mural cells.* Blood, 2004. **104**(7): p. 2084-6.

102. Song, S., et al., *PDGFRbeta+ perivascular progenitor cells in tumours regulate pericyte differentiation and vascular survival.* Nature cell biology, 2005. **7**(9): p. 870-9.

103. De Palma, M., et al., *Targeting exogenous genes to tumor angiogenesis by transplantation of genetically modified hematopoietic stem cells.* Nature medicine, 2003. **9**(6): p. 789-95.

104. Gothert, J.R., et al., *Genetically tagging endothelial cells in vivo: bone marrow-derived cells do not contribute to tumor endothelium.* Blood, 2004. **104**(6): p. 1769-77.

105. Machein, M.R., et al., *Minor contribution of bone marrow-derived endothelial progenitors to the vascularization of murine gliomas.* Brain pathology, 2003. **13**(4): p. 582-97.

106. Purhonen, S., et al., *Bone marrow-derived circulating endothelial precursors do not contribute to vascular endothelium and are not needed for tumor growth.* Proceedings of the National Academy of Sciences of the United States of America, 2008. **105**(18): p. 6620-5.

107. Shinde Patil, V.R., et al., *Bone marrow-derived lin(-)c-kit(+)Sca-1+ stem cells do not contribute to vasculogenesis in Lewis lung carcinoma.* Neoplasia, 2005. **7**(3): p. 234-40.

108. Voswinckel, R., et al., *Circulating vascular progenitor cells do not contribute to compensatory lung growth.* Circulation research, 2003. **93**(4): p. 372-9.

109. Wickersheim, A., et al., *Endothelial progenitor cells do not contribute to tumor endothelium in primary and metastatic tumors.* International journal of cancer. Journal international du cancer, 2009. **125**(8): p. 1771-7.

110. Ziegelhoeffer, T., et al., *Bone marrow-derived cells do not incorporate into the adult growing vasculature.* Circulation research, 2004. **94**(2): p. 230-8.

111. Peters, B.A., et al., *Contribution of bone marrow-derived endothelial cells to human tumor vasculature.* Nat Med, 2005. **11(3)**: p. 261-2.

112. Garcia-Barros, M., et al., *Tumor response to radiotherapy regulated by endothelial cell apoptosis.* Science, 2003. **300**(5622): p. 1155-9.

113. Avital, I., et al., *Donor-derived human bone marrow cells contribute to solid organ cancers developing after bone marrow transplantation.* Stem cells, 2007. **25**(11): p. 2903-9.

114. Cogle, C.R., et al., *Bone marrow contributes to epithelial cancers in mice and humans as developmental mimicry.* Stem cells, 2007. **25**(8): p. 1881-7.

115. Arai, Y., et al., *A solid tumor of donor cell-origin after allogeneic peripheral blood stem cell transplantation.* American journal of transplantation : official journal of the American Society of Transplantation and the American Society of Transplant Surgeons, 2006. **6**(12): p. 3042-3.

116. Kucia, M., et al., *CXCR4-SDF-1 signalling, locomotion, chemotaxis and adhesion.* Journal of molecular histology, 2004. **35**(3): p. 233-45.

117. Flomenberg, N., et al., *The use of AMD3100 plus G-CSF for autologous hematopoietic progenitor cell mobilization is superior to G-CSF alone.* Blood, 2005. **106**(5): p. 1867-74.

118. DiPersio, J.F., et al., *Plerixafor and G-CSF versus placebo and G-CSF to mobilize hematopoietic stem cells for autologous stem cell transplantation in patients with multiple myeloma.* Blood, 2009. **113**(23): p. 5720-6.

119. DiPersio, J.F., et al., *Phase III prospective randomized double-blind placebo-controlled trial of plerixafor plus granulocyte colony-stimulating factor compared with placebo plus granulocyte colony-stimulating factor for autologous stem-cell mobilization and transplantation for patients with non-Hodgkin's lymphoma.* Journal of clinical oncology : official journal of the American Society of Clinical Oncology, 2009. **27**(28): p. 4767-73.

120. Teicher, B.A. and S.P. Fricker, *CXCL12 (SDF-1)/CXCR4 pathway in cancer.* Clinical cancer research : an official journal of the American Association for Cancer Research, 2010. **16**(11): p. 2927-31.

121. Werner, L., H. Guzner-Gur, and I. Dotan, *Involvement of CXCR4/CXCR7/CXCL12 Interactions in Inflammatory bowel disease.* Theranostics, 2013. **3**(1): p. 40-6.

122. Mikami, S., et al., *Blockade of CXCL12/CXCR4 axis ameliorates murine experimental colitis.* The Journal of pharmacology and experimental therapeutics, 2008. **327**(2): p. 383-92.

123. Dotan, I., et al., *CXCL12 is a constitutive and inflammatory chemokine in the intestinal immune system.* Inflammatory bowel diseases, 2010. **16**(4): p. 583-92.

124. Cojoc, M., et al., *Emerging targets in cancer management: role of the CXCL12/CXCR4 axis.* OncoTargets and therapy, 2013. **6**: p. 1347-1361.

125. Shevde, L.A., et al., *Osteopontin: an effector and an effect of tumor metastasis.* Current molecular medicine, 2010. **10**(1): p. 71-81.

126. Haylock, D.N. and S.K. Nilsson, *Osteopontin: a bridge between bone and blood.* British journal of haematology, 2006. **134**(5): p. 467-74.

127. Grassinger, J., et al., *Thrombin-cleaved osteopontin regulates hemopoietic stem and progenitor cell functions through interactions with alpha9beta1 and alpha4beta1 integrins.* Blood, 2009. **114**(1): p. 49-59.

128. Gassler, N., et al., *Expression of osteopontin (Eta-1) in Crohn disease of the terminal ileum.* Scandinavian journal of gastroenterology, 2002. **37**(11): p. 1286-95.

129. Sato, T., et al., *Osteopontin/Eta-1 upregulated in Crohn's disease regulates the Th1 immune response.* Gut, 2005. **54**(9): p. 1254-62.

130. Furger, K.A., et al., *The functional and clinical roles of osteopontin in cancer and metastasis.* Current molecular medicine, 2001. **1**(5): p. 621-32.

131. Liaw, L., et al., *The adhesive and migratory effects of osteopontin are mediated via distinct cell surface integrins. Role of alpha v beta 3 in smooth muscle cell migration to osteopontin in vitro.* The Journal of clinical investigation, 1995. **95**(2): p. 713-24.

132. Seftor, R.E., E.A. Seftor, and M.J. Hendrix, *Molecular role(s) for integrins in human melanoma invasion.* Cancer metastasis reviews, 1999. **18**(3): p. 359-75.

133. Varner, J.A., et al., *Inhibition of angiogenesis and tumor growth by murine 7E3, the parent antibody of c7E3 Fab (abciximab; ReoPro).* Angiogenesis, 1999. **3**(1): p. 53-60.

134. Lee, J.L., et al., *CD44 engagement promotes matrix-derived survival through the CD44-SRC-integrin axis in lipid rafts.* Molecular and cellular biology, 2008. **28**(18): p. 5710-23.

135. Johnston, N.I. and M.K. El-Tanani, *Osteopontin: a new role for a familiar actor.* Breast cancer research : BCR, 2008. **10**(6): p. 306.

136. McAllister, S.S., et al., *Systemic endocrine instigation of indolent tumor growth requires osteopontin.* Cell, 2008. **133**(6): p. 994-1005.

137. Okumura, T., et al., *Identification of a bone marrow-derived mesenchymal progenitor cell subset that can contribute to the gastric epithelium.* Laboratory investigation; a journal of technical methods and pathology, 2009. **89**(12): p. 1410-22.

138. Oren-Suissa, M. and B. Podbilewicz, *Cell fusion during development.* Trends in cell biology, 2007. **17**(11): p. 537-46.

139. Alvarez-Dolado, M., et al., *Fusion of bone-marrow-derived cells with Purkinje neurons, cardiomyocytes and hepatocytes.* Nature, 2003. **425**(6961): p. 968-73.

140. Weimann, J.M., et al., *Contribution of transplanted bone marrow cells to Purkinje neurons in human adult brains.* Proceedings of the National Academy of Sciences of the United States of America, 2003. **100**(4): p. 2088-93.

141. Ogle, B.M., M. Cascalho, and J.L. Platt, *Biological implications of cell fusion.* Nature reviews. Molecular cell biology, 2005. **6**(7): p. 567-75.

142. Nygren, J.M., et al., *Bone marrow-derived hematopoietic cells generate cardiomyocytes at a low frequency through cell fusion, but not transdifferentiation.* Nature medicine, 2004. **10**(5): p. 494-501.

143. Camargo, F.D., M. Finegold, and M.A. Goodell, *Hematopoietic myelomonocytic cells are the major source of hepatocyte fusion partners.* J Clin Invest, 2004. **113**(9): p. 1266-70.

144. Lagasse, E., et al., *Purified hematopoietic stem cells can differentiate into hepatocytes in vivo.* Nat Med, 2000. **6**(11): p. 1229-34.

145. Vassilopoulos, G., P.R. Wang, and D.W. Russell, *Transplanted bone marrow regenerates liver by cell fusion.* Nature, 2003. **422**(6934): p. 901-4.

146. Weimann, J.M., et al., *Stable reprogrammed heterokaryons form spontaneously in Purkinje neurons after bone marrow transplant.* Nat Cell Biol, 2003. **5**(11): p. 959-66.

147. Camargo, F.D., et al., *Single hematopoietic stem cells generate skeletal muscle through myeloid intermediates.* Nat Med, 2003. **9**(12): p. 1520-7.

148. Corbel, S.Y., et al., *Contribution of hematopoietic stem cells to skeletal muscle.* Nature medicine, 2003. **9**(12): p. 1528-32.

149. Ferrari, G., et al., *Muscle regeneration by bone marrow-derived myogenic progenitors.* Science, 1998. **279**(5356): p. 1528-30.

150. Rizvi, A.Z., et al., *Bone marrow-derived cells fuse with normal and transformed intestinal stem cells.* Proc Natl Acad Sci U S A, 2006. **103**(16): p. 6321-5.

151. Davies, P.S., et al., *Inflammation and proliferation act together to mediate intestinal cell fusion.* PLoS One, 2009. **4**(8): p. e6530.

152. Johansson, C.B., et al., *Extensive fusion of haematopoietic cells with Purkinje neurons in response to chronic inflammation.* Nature cell biology, 2008. **10**(5): p. 575-83.

153. Nygren, J.M., et al., *Myeloid and lymphoid contribution to non-haematopoietic lineages through irradiation-induced heterotypic cell fusion.* Nature cell biology, 2008. **10**(5): p. 584-92.

154. Harris, R.G., et al., *Lack of a fusion requirement for development of bone marrow-derived epithelia.* Science, 2004. **305**(5680): p. 90-3.

155. Lee, C.Y., et al., *Bone Marrow Cells in Murine Colitis: Multi-Signal Analysis Confirms Pericryptal Myofibroblast Engraftment without Epithelial Involvement.* PLoS One, 2011. **6**(10): p. e26082.

156. de Jong, J.H., et al., *Fusion of intestinal epithelial cells with bone marrow derived cells is dispensable for tissue homeostasis.* Scientific reports, 2012. **2**: p. 271.

157. Waterhouse, M., et al., *Horizontal DNA transfer from donor to host cells as an alternative mechanism of epithelial chimerism after allogeneic hematopoietic cell transplantation.* Biology of blood and marrow transplantation : journal of the American Society for Blood and Marrow Transplantation, 2011. **17**(3): p. 319-29.

158. McClanahan, T., et al., *Identification of overexpression of orphan G protein-coupled receptor GPR49 in human colon and ovarian primary tumors.* Cancer Biol Ther, 2006. **5**(4): p. 419-26.

159. Yamamoto, Y., et al., *Overexpression of orphan G-protein-coupled receptor, Gpr49, in human hepatocellular carcinomas with beta-catenin mutations.* Hepatology, 2003. **37**(3): p. 528-33.

160. Duran-Struuck, R. and R.C. Dysko, *Principles of bone marrow transplantation (BMT): providing optimal veterinary and husbandry care to irradiated mice in BMT studies.* Journal of the American Association for Laboratory Animal Science : JAALAS, 2009. **48**(1): p. 11-22.

161. Owen, D.G., *Parasites of laboratory animals*1992: Published for Laboratory Animals Ltd. by Royal Society of Medicine Services.

162. Hansen, A.K., *Handbook of Laboratory Animal Bacteriology*2000: CRC Press.

163. Shen, Z., et al., *Helicobacter rodentium sp. nov., a urease-negative Helicobacter species isolated from laboratory mice.* Int J Syst Bacteriol, 1997. **47**(3): p. 627-34.

164. Truett, G.E., *Preparation of genomic DNA from animal tissues*, in *DNA sequencing II: optimizing preparation and cleanup*, J. Kieleczawa, Editor 2006, Jones and Bartlett Publishers.

165. Muskhelishvili, L., et al., *Evaluation of cell proliferation in rat tissues with BrdU, PCNA, Ki-67(MIB-5) immunohistochemistry and in situ hybridization for histone mRNA.* J Histochem Cytochem, 2003. **51**(12): p. 1681-8.

166. Totty, B., *Mucins*, in *Theory and practice of histological techniques*, J.D. Bancroft and M. Gamble, Editors. 2002, Elsevier Science: London.

167. Otto, W.R., et al., *Identification of blottin: a novel gastric trefoil factor family-2 binding protein.* Proteomics, 2006. **6**(15): p. 4235-45.

168. Willenbring, H., et al., *Myelomonocytic cells are sufficient for therapeutic cell fusion in liver.* Nature medicine, 2004. **10**(7): p. 744-8.

169. Direkze, N.C., et al., *Multiple organ engraftment by bone-marrow-derived myofibroblasts and fibroblasts in bone-marrow-transplanted mice.* Stem Cells, 2003. **21**(5): p. 514-20.

170. Broekema, M., et al., *Bone marrow-derived myofibroblasts contribute to the renal interstitial myofibroblast population and produce procollagen I after ischemia/reperfusion in rats.* J Am Soc Nephrol, 2007. **18**(1): p. 165-75.

171. Verstappen, J., et al., *Preferential recruitment of bone marrow-derived cells to rat palatal wounds but not to skin wounds.* Arch Oral Biol, 2011.

172. Direkze, N.C., et al., *Bone marrow-derived stromal cells express lineage-related messenger RNA species.* Cancer research, 2006. **66**(3): p. 1265-9.

173. Poulsom, R., et al., *A robust method for isotopic riboprobe in situ hybridisation to localise mRNAs in routine pathology specimens.* Eur J Histochem, 1998. **42**(2): p. 121-32.

174. Goldenring, J.R., et al., *Expression of trefoil peptides in the gastric mucosa of transgenic mice overexpressing transforming growth factor-alpha.* Growth factors, 1996. **13**(1-2): p. 111-9.

175. Jeffrey, G.P., et al., *Spasmolytic polypeptide: a trefoil peptide secreted by rat gastric mucous cells.* Gastroenterology, 1994. **106**(2): p. 336-45.

176. Chinery, R., et al., *Localization of intestinal trefoil-factor mRNA in rat stomach and intestine by hybridization in situ.* The Biochemical journal, 1992. **285 (Pt 1)**: p. 5-8.

177. Marty, G.D., *Blank-field correction for achieving a uniform white background in brightfield digital photomicrographs.* Biotechniques, 2007. **42**(6): p. 716, 718, 720.

178. Schmidt, P.H., et al., *Identification of a metaplastic cell lineage associated with human gastric adenocarcinoma.* Laboratory investigation; a journal of technical methods and pathology, 1999. **79**(6): p. 639-46.

179. Goldenring, J.R., et al., *Reversible drug-induced oxyntic atrophy in rats.* Gastroenterology, 2000. **118**(6): p. 1080-93.

180. Nomura, S., et al., *Spasmolytic polypeptide expressing metaplasia to preneoplasia in H. felis-infected mice.* Gastroenterology, 2004. **127**(2): p. 582-94.

181. Menheniott, T.R., et al., *A novel gastrokine, Gkn3, marks gastric atrophy and shows evidence of adaptive gene loss in humans.* Gastroenterology, 2010. **138**(5): p. 1823-35.

182. Nam, K.T., et al., *Mature chief cells are cryptic progenitors for metaplasia in the stomach.* Gastroenterology, 2010. **139**(6): p. 2028-2037 e9.

183. Yamada, Y. and H. Mori, *Multistep carcinogenesis of the colon in Apc(Min/+) mouse.* Cancer Sci, 2007. **98**(1): p. 6-10.

184. Barker, N., et al., *Identification of stem cells in small intestine and colon by marker gene Lgr5.* Nature, 2007. **449**(7165): p. 1003-7.

185. Brittan, M., et al., *Bone marrow cells engraft within the epidermis and proliferate in vivo with no evidence of cell fusion.* The Journal of pathology, 2005. **205**(1): p. 1-13.

186. Brown, L.F., et al., *Osteopontin expression and distribution in human carcinomas.* The American journal of pathology, 1994. **145**(3): p. 610-23.

187. Hayashi, Y., et al., *The transdifferentiation of bone-marrow-derived cells in colonic mucosal regeneration after dextran-sulfate-sodium-induced colitis in mice.* Pharmacology, 2007. **80**(4): p. 193-9.

188. Wood, J.A., et al., *Distinct contribution of human cord blood-derived endothelial colony forming cells to liver and gut in a fetal sheep model.* Hepatology, 2012.

189. Zavros, Y., et al., *Chronic gastritis in the hypochlorhydric gastrin-deficient mouse progresses to adenocarcinoma.* Oncogene, 2005. **24**(14): p. 2354-66.

190. Zavros, Y., et al., *Treatment of Helicobacter gastritis with IL-4 requires somatostatin.* Proceedings of the National Academy of Sciences of the United States of America, 2003. **100**(22): p. 12944-9.

191. Donnelly, J.M., et al., *Sonic hedgehog mediates the proliferation and recruitment of transformed mesenchymal stem cells to the stomach.* PloS one, 2013. **8**(9): p. e75225.

192. Lee, H.J., et al., *Gene expression profiling of metaplastic lineages identifies CDH17 as a prognostic marker in early stage gastric cancer.* Gastroenterology, 2010. **139**(1): p. 213-25 e3.

193. Nozaki, K., et al., *Altered gastric chief cell lineage differentiation in histamine-deficient mice.* American journal of physiology. Gastrointestinal and liver physiology, 2009. **296**(6): p. G1211-20.

194. Nam, K.T., et al., *Spasmolytic polypeptide-expressing metaplasia (SPEM) in the gastric oxyntic mucosa does not arise from Lgr5-expressing cells.* Gut, 2011.

195. Cervantes, A., et al., *Molecular biology of gastric cancer.* Clinical & translational oncology : official publication of the Federation of Spanish Oncology Societies and of the National Cancer Institute of Mexico, 2007. **9**(4): p. 208-15.

196. Qiao, X.T., et al., *Prospective identification of a multilineage progenitor in murine stomach epithelium.* Gastroenterology, 2007. **133**(6): p. 1989-98.

197. Uede, T., *Osteopontin, intrinsic tissue regulator of intractable inflammatory diseases.* Pathology international, 2011. **61**(5): p. 265-80.

198. Vetrone, S.A., et al., *Osteopontin promotes fibrosis in dystrophic mouse muscle by modulating immune cell subsets and intramuscular TGF-beta.* The Journal of clinical investigation, 2009. **119**(6): p. 1583-94.

199. Wada, T., et al., *Functional role of CD44v-xCT system in the development of spasmolytic polypeptide-expressing metaplasia.* Cancer science, 2013. **104**(10): p. 1323-1329.

200. Ogawa, M., et al., *Altered metaplastic response of waved-2 EGF receptor mutant mice to acute oxyntic atrophy.* American journal of physiology. Gastrointestinal and liver physiology, 2006. **290**(4): p. G793-804.

201. Oshima, H., et al., *Hyperplastic gastric tumors induced by activated macrophages in COX-2/mPGES-1 transgenic mice.* The EMBO journal, 2004. **23**(7): p. 1669-78.

202. Karam, S.M., C. Tomasetto, and M.C. Rio, *Trefoil factor 1 is required for the commitment programme of mouse oxyntic epithelial progenitors.* Gut, 2004. **53**(10): p. 1408-15.

203. Yan, F. and D.B. Polk, *Disruption of NF-kappaB signalling by ancient microbial molecules: novel therapies of the future?* Gut, 2010. **59**(4): p. 421-6.

204. May, F.E. and B.R. Westley, *Expression of human intestinal trefoil factor in malignant cells and its regulation by oestrogen in breast cancer cells.* The Journal of pathology, 1997. **182**(4): p. 404-13.